

Power Scaling of High Brightness Multi-kilowatt Coaxial CO₂ Lasers

Jochen Deile

Thesis submitted
as part of the Engineering Doctorate in Photonics
at Heriot-Watt University.

Prof. Denis R. Hall, Academic Supervisor
Heriot-Watt University, Edinburgh, United Kingdom

Dr. Francisco Villarreal, Industrial Supervisor
TRUMPF Inc., Farmington, CT USA

November 2012

The copyright in this thesis is owned by the author. Any quotation from the thesis or use of any of the information contained in it must acknowledge this thesis as the source of the quotation or information.

Abstract

The objectives of the work described in this thesis have been *first*, to develop a high brightness diffusion-cooled CO₂ laser based on the annular discharge geometry and *secondly*, to scale up the output power to provide multi-kilowatt operation.

A stable-unstable-hybrid resonator (helix-axicon resonator) serves as the starting point for the development. In order to address the brightness, polarization and temporal stability issues of this resonator several new features and concepts are introduced.

High brightness is achieved by ensuring fundamental mode operation without truncating the mode in a free-space configuration. This is achieved by the introduction of shaped electrodes.

The temporal stability problems are addressed by introducing a new resonator configuration in the unstable direction, by moving the unstable direction away from the boundary of stability in the ‘classical’ resonator stability diagram.

The polarization issues are addressed by introducing a new beam shaping telescope that includes polarization correction based on the use of a dielectric coating, which transforms the azimuthal polarization emitted by the resonator into linear polarization.

The overall outcome is the experimental demonstration of a laser with an output power of 2 kW, and a beam with M^2 values < 1.1 , exhibiting constant linear polarization and temporally stable beam characteristics.

In the second part of the thesis, the power scaling laws for diffusion-cooled lasers with annular geometry and free-space propagation are derived and the scaling limits are investigated.

A scaled-up version is realized by extending the discharge length and the introduction of distributed inductances to ensure a homogenous discharge distribution. A characterization of the laser confirms the conservation of all beam characteristics at higher output power levels. A maximum laser power level of about 4 kW was reached.

Dedication

To Sandra and Meo

Acknowledgements

I am grateful to Professor Denis R. Hall for giving me the opportunity to participate in the Engineering Doctorate Programme and for his guidance.

I also would like to thank Mr. Biekert and TRUMPF Inc. for providing the organizational support that enabled this work.

My special thanks go to Dr. Francisco Villarreal for taking on the industrial supervisor role and the many fruitful discussions over the past three years.

A big thank you also goes to Dr. Fernando Monjardin for the final proofreading.

I also thank all my colleagues in the Laser Development Department at TRUMPF Inc. for their support, contributions and discussions.

I am deeply grateful to my wife Sandra and my son Meo for their support during the last years and the sacrifices they made in order to provide me with the time and encouragement to successfully participate in this programme.

Table of Contents

Abstract.....	ii
Dedication.....	iii
Acknowledgements	iv
Table of Contents	v
List of Publications.....	ix
Chapter 1	1
1 Introduction	1
1.1 High Power Lasers in Industry	1
1.2 Organization of the Thesis	3
Chapter 2	4
2 Annular Coaxial RF Excited CO ₂ Lasers - Background	4
2.1 Introduction.....	4
2.2 CO ₂ Laser Kinetics and Gas Chemistry	4
2.2.1 Vibrational energy levels	4
2.2.2 Rotational energy levels	6
2.2.3 Transitions of the regular bands	6
2.2.4 Gas additives	8
2.2.5 Gas chemical processes in the discharge.....	9
2.3 Laser Gas Discharges.....	12
2.3.1 Introduction	12
2.3.2 RF discharges	13
2.3.3 The current-voltage characteristic	15
2.3.4 Reduced electric field strength - E/N	16
2.3.5 Discharge instabilities	16

2.4	Power Scaling	19
2.5	Resonators for Coaxial Media	21
2.5.1	General introduction helix-axicon resonator.....	23
2.6	Beam Formatting	28
2.6.1	Beam formatting requirements.....	28
2.6.2	Spatial filtering.....	29
2.7	Polarization Issues	31
2.8	Tools for Resonator Modelling.....	34
2.8.1	Geometrical optics.....	34
2.8.2	Gaussian beam propagation	35
2.8.3	Diffraction integral method.....	38
2.8.4	Diffraction integral method model for the helix-axicon resonator	39
2.9	Special Resonators	41
Chapter 3		44
3	Annular Laser Resonator Configuration.....	44
3.1	Introduction.....	44
3.2	Radial Direction	46
3.2.1	Optimization of constant gap configurations	49
3.2.2	Shaped electrodes for high brightness.....	53
3.2.3	Resonator alignment sensitivity	59
3.2.4	Suppression of waveguide modes	64
3.3	Azimuthal Direction.....	66
3.3.1	Magnification	66
3.3.2	Temporal stability of the unstable resonator	71
3.3.3	Mirror optimization.....	73
3.3.4	Parabolic slope	75
3.4	Polarization Correction	81
3.4.1	Correction of the state of polarization.....	83
3.4.2	Beam shaping telescope set-up	85
3.5	Summary	87
Chapter 4		89

4	Beam Characteristics of the Laser	89
4.1	Introduction.....	89
4.2	Unformatted Beam.....	89
4.3	Formatted Beam.....	92
4.4	Summary	96
	Chapter 5	97
5	Power Scaling Principles.....	97
5.1	Introduction.....	97
5.2	Thermal Laser Power Scaling Law	97
5.3	Power Scaling Limitations	99
	5.3.1 Free-space propagation	99
	5.3.2 RF system and longitudinal voltage distribution	101
5.4	Similarity Laws	102
	Chapter 6	104
6	Power Scaling: Design and Performance of the Scaled-up Laser	104
6.1	Design Options for the Scaled-up Version	104
6.2	RF and Discharge Distribution	105
6.3	Optical Resonator.....	111
	6.3.1 Verification of the radial direction.....	111
	6.3.2 Verification of the azimuthal direction	112
	Chapter 7	117
7	Resonator Optimization	117
7.1	Resonator parameters.....	117
	7.1.1 Helix slope optimization	117
	7.1.2 Helix mirror power maps	127
	7.1.3 Axicon mirror power maps	132
	7.1.4 Influence of the banking parameters	136

7.2	Additional Considerations	139
7.2.1	Resonator length.....	140
7.2.2	Thermal lensing.....	142
7.2.3	Summary	147
7.3	Characterization of the Scaled-up Laser	147
Chapter 8		152
8	Summary and Outlook	152
8.1	Summary of Main Achievements	152
8.2	Suggestions for Future Work.....	154
Appendix		156
A.1	OPT Input File	156
References		167

List of Publications

- 1 J. Deile, "*Diffusion-cooled laser system*", Patent US 6,879,616, 2005.
- 2 J. Deile and J. Schulz, "*Beam forming telescope with polarization correction*", Patent US 7,019,902, 2006.
- 3 B. Ehlers, J. Deile, S. Sumrain, V. Granson, F. Villarreal, V. Negoita, "*Experimental and theoretical study of a coaxial, hybrid-stable-unstable resonator for high-power lasers*", in *SPIE*, vol. 6452, 2007.
- 4 V. Granson, S. Sumrain, P. Daniel, F. Villarreal, J Deile, "*Power Scaling Issues of Diffusion Cooled Annular CO₂ Lasers in the Multi-Kilowatt Region*", in *SPIE*, vol. 6872, 2008.
- 5 F. J. Villarreal-Saucedo, J. Deile, S. Sumrain, V. Granson, and P. Daniel, "*Laser having distributed Impedances*", US Patent US7,778,303, Aug. 2010.
- 6 V. Granson, F. Villarreal, J. Deile, J. F. Monjardin, and S. Sumrain, "*Comprehensive Analysis of Thermal Lensing Effects on the Coaxial Resonator of a High Power RF-Excited CO₂ Laser*" in *SPIE*, vol. 8236, 2012.

Chapter 1

1 Introduction

1.1 High Power Lasers in Industry

Even though CO₂ lasers have come out of fashion in academia, they are still number one in industrial applications. Their beam quality, available laser power levels, efficiency, reliability and cost of ownership make them very attractive for industrial applications like laser cutting and laser welding. Their unique wavelength of 10.6 μm is particularly well suited for metal cutting and requires only simple enclosures to protect operators from stray radiation.

In recent years, thin disk and fiber lasers have been shown to be capable of power and beam quality rivalling those of carbon-dioxide lasers. These new lasers have been successful in many applications, and will doubtless be successful in many more. Nonetheless, the myriad advantages of carbon dioxide lasers will keep them competitive for a very long time, perhaps indefinitely. For this reason companies such as TRUMPF continue to develop CO₂ laser technology.

CO₂ lasers have been used in industrial applications starting in the late 1960s, but the main surge in applications and usage began to occur in the 1980s. Since then the technology has been improved continuously and sealed-off, diffusion-cooled CO₂ laser are available now up to 1000 W from companies like Coherent Inc. and Rofin Sinar UK Ltd. State of the art laser cutting machines utilize fast-flow lasers with up to 8 kW of laser power, while diffusion-cooled waveguide (slab) lasers with stable-unstable-hybrid resonators are available at power levels up to 8 kW. These diffusion-cooled lasers create laser beams with excellent beam quality and therefore excellent focusability. Nevertheless, this technology has never quite reached its full potential in laser cutting applications due to pointing problems of the stable-unstable-hybrid resonators used in these lasers. Pointing creates applications-related problems in the most widely used concept of 2D laser cutting machines, the so called flying-optics machines. In

applications that are less critical in regard to pointing, such as laser welding, high power diffusion-cooled waveguide lasers have been quite successful. In this work an alternative to the slab laser design, based on an annular electrode structure, is further developed with the goal to help diffusion-cooled lasers reach their full potential in 2D laser cutting of metals. Compared to the plate-like design (waveguide lasers with inter-electrode gap sizes of about 2 mm), the discharge area of the annular design is increased by a factor of π for the same electrode footprint. This additional discharge area can be used to either increase the output power, or to open up the inter-electrode gap size to allow free-space propagation at the same output power level. Basing the resonator on free-space propagation reduces the tolerance requirements in the electrode-mirror system and the electrode surface requirements since the electrodes are no longer part of the optical system (no waveguiding) creating a rugged laser suited for industrial applications.

Especially right now, with 1 μm lasers being in fashion, diffusion-cooled lasers are in a unique position. The cutting speeds in thin sheet metal, up to 5 mm, are not quite as fast as the speeds reached with fiber or thin disk lasers, but faster than those reached with fast-flow or DC excited CO_2 lasers. For thicker materials, the speeds are currently about equal, but in general the CO_2 laser produces the better cut quality. In thick material, e.g. values greater than about 12 mm, the performance of the CO_2 laser is unmatched. Solid state RF-generators and near-sealed off gas systems and the absence of any moving parts make diffusion-cooled lasers virtually maintenance free. The lower wall plug efficiency of the CO_2 laser is offset by the lower investment costs. These characteristics make the diffusion-cooled CO_2 laser a perfect match for applications that require flexibility in material thickness and high cut quality.

Achieving excellent performance in laser cutting of metals requires high brightness. Since the wavelength of fiber and thin disk lasers used in metal cutting applications is about 10 times shorter than the wavelength of CO_2 lasers, it is clearly imperative that the beam quality of the CO_2 laser must approach the diffraction limit to achieve the same brightness, at reasonable power levels, as multi mode fiber or thin disk lasers. At the same time, this perceived disadvantage is at least partially responsible for the superior cut quality in thicker material. The lower degree of absorption in metals of the 10.6 μm wavelength allows the laser beam to penetrate the work piece better. At the same time,

the Brewster angle at 10.6 μm is almost at normal incidence creating a vertical cut front, resulting in a smooth and burr-free cut edge.

In other applications, like the processing of plastics and organics, the longer wavelength of the CO₂ laser provides an advantage, or even enables the processing of these materials, due to the higher degree of absorption of the 10.6 μm wavelength in these materials.

1.2 Organization of the Thesis

The work in Part One of this thesis focuses on the required re-design of the helix-axicon resonator, (a cavity design which is suitable for annular discharge structures), so as to achieve the necessary high brightness and stable performance required by industrial applications. In Part Two, the principal topic covered is the power scaling of diffusion-cooled annular CO₂ laser using stable-unstable-hybrid/free space helix-axicon resonators.

Following this introductory chapter, previous work from the literature on the helix-axicon resonator will be reviewed in chapter 2. In chapter 3 the stable direction of the hybrid resonator is re-designed in order to ensure fundamental mode operation by the introduction of shaped electrodes. The linear slope on the helix mirror is replaced by a parabolic slope to ensure that the resonator operates as an unstable resonator in the azimuthal direction under thermal and mechanical loading. Additionally, a beam shaping telescope is introduced with the objective of transforming the general astigmatic beam extracted from the resonator into a stigmatic beam. The correction of the state of polarization within the beam shaping telescope is also discussed. Measurement data from a complete characterization of the beam properties is presented in chapter 4.

Chapters 5 and 6 focus on power scaling, while in chapter 5 the general power scaling law for diffusion-cooled lasers is modified so as to apply to free-space configurations and the scaling limits are discussed. A design configuration for the scaled-up version of the laser is described in chapter 6 which includes a discussion of the introduction of distributed inductances for discharge homogenization. An optimization of the resonator design is performed in chapter 7, which includes also a description of the experimental characterization of the beam properties. The last chapter concludes the thesis with a summary and future outlook.

Chapter 2

2 Annular Coaxial RF Excited CO₂ Lasers - Background

2.1 Introduction

This chapter provides appropriate background information relevant to the understanding of the annular coaxial RF excited CO₂ laser discussed in this theses.

The topics covered here range from the basic laser kinetics and gas chemistry of CO₂ lasers in section 2.2 to a summary of characteristics of special optical resonators in 2.9. Also included are an introduction to laser gas discharges in 2.3 and the basics of power scaling of diffusion-cooled lasers in 2.4.

Section 2.5 provides a basic introduction to resonators suitable for annular discharge geometries, with a particular focus on the helix-axicon resonator. Beam formatting and polarization issues of the helix-axicon resonator are discussed in section 2.6 and 2.7 respectively. Selected tools used for the modelling of the optical resonator are introduced in 2.8.

2.2 CO₂ Laser Kinetics and Gas Chemistry

2.2.1 *Vibrational energy levels*

The CO₂ molecule is a linear symmetric molecule with an axis of symmetry along the nuclei and a plane symmetry perpendicular to this axis. It is well documented that the emission wavelength spectrum of a CO₂ laser is determined by the low-lying vibrational and rotational energy levels of the CO₂ molecule. The normal modes of vibration of the CO₂ molecule are shown in Figure 2.1.

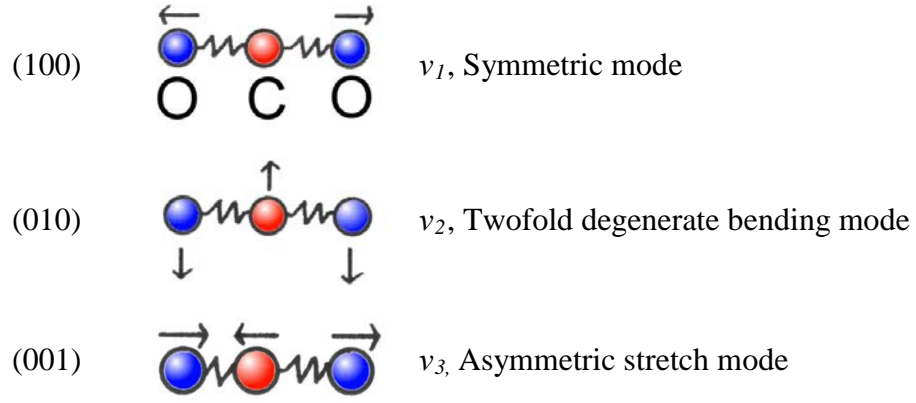


Figure 2.1 Normal modes of vibration of the CO_2 molecule.

One of the major technical breakthroughs for the CO_2 laser came with the improved excitation of the CO_2 molecule by the addition of Nitrogen to the laser gas mix [1]. Electric discharges excite the N_2 molecule very effectively, and since the N_2 molecule has two identical nuclei, its dipole radiation is forbidden, so that it can only decay by collision with the wall of the discharge vessel or by collision with other molecules. Moreover, the energy stored in the N_2 molecule can be easily transferred to the CO_2 molecule due to the close resonance of the N_2 vibration and V_3 vibration levels of the CO_2 molecule. The (00^01) level of the CO_2 is only $\Delta E = 18 \text{ cm}^{-1}$ higher than the vibrational level V_1 of Nitrogen. This energy difference is much smaller than the average kinetic energy so that during collisions the CO_2 molecules can easily draw the vibrational energy of the N_2 to excite the V_3 vibration [2], the upper laser level, as illustrated in Figure 2.2.

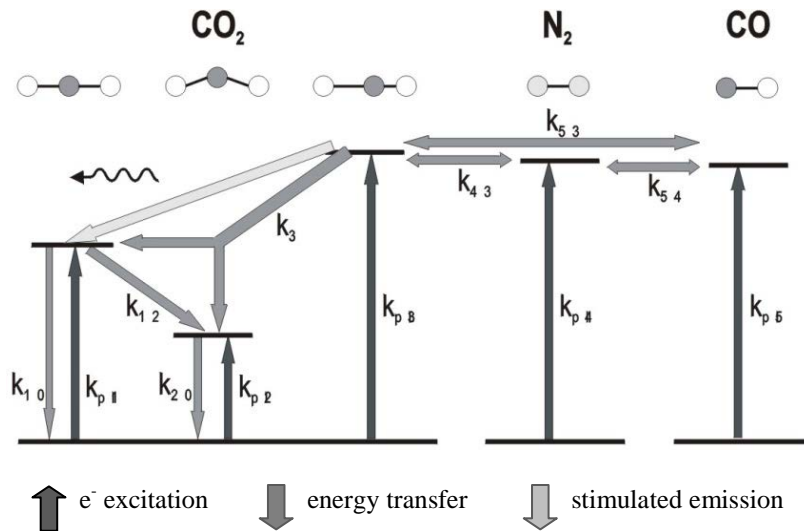


Figure 2.2 Vibrational energy levels of the CO_2 , CO and N_2 molecules.

There is a similar though smaller effect between the CO and CO₂ molecules in the gas mix. CO is produced in the discharge by dissociation from CO₂ or is often added to the laser gas mix of diffusion-cooled lasers. The cross section for vibrational excitation of the CO molecule in the electric discharge is rather large and the CO molecule can transfer energy to the V₃ vibration because the energy difference of the vibrational level of CO and the (00⁰1) level of CO₂ is $\Delta E = 170 \text{ cm}^{-1}$ which is smaller than the average kinetic energy. However, the energy transfer from CO to CO₂ is less efficient than the energy transfer from N₂ to CO₂, due to the larger energy difference of the energy levels and the fact that CO has a dipole moment and is therefore subject to spontaneous decay.

The energy transfer process via N₂ and CO to CO₂ is much more efficient than the direct excitation of the CO₂ molecule due to the much larger cross sections for vibrational excitation of N₂ and CO by electron impact. As shown in Reference [3] the vibrational excitation of the CO₂ molecule by electron impact is only efficient for a narrow range of electron energies, whereas the vibrational excitation of CO and N₂ by electron impact is quite efficient for a wide range of electron energies. For optimum excitation of CO and N₂ the electron energies should be in a range from 1 to 3 eV. Importantly, the range of electron energies can be adjusted by changing discharge conditions and especially the pressure and composition of the laser gas mix [2].

2.2.2 *Rotational energy levels*

Superimposed onto the vibration of the CO₂ molecule is its rotational motion. The energy of the rotational levels is in general much lower than the energy of the vibrational levels. The energy levels are given by

$$W_r = B \cdot J(J + 1) \quad 2.1$$

where B is the rotational constant and J is the quantum number for the rotational state. The higher the value for J the faster the molecule rotates in a classic mechanical model.

2.2.3 *Transitions of the regular bands*

The infra-red spectrum of the CO₂ laser results from the transitions between the vibrational-rotational levels and these transitions are governed by a set of quantum

mechanical selection rules. The selection rules are based on the conservation of spin or angular momentum and the symmetry properties of the wave function. The strongest allowed CO₂ laser emission lines result from the vibrational transitions (00⁰1) → (10⁰0) with a centre wavelength of 10.4 μm (10 μm band) and (00⁰1) → (02⁰0) with a centre wavelength of 9.4 μm (9 μm band). For these transitions in the regular band the following selection rules apply [2]:

$$\Delta J = \pm 1 \quad 2.2$$

Symmetric vibrations have only even j numbers and anti-symmetric vibrations have only odd j numbers. The transitions with $\Delta J = -1$ are called P-branch transitions and those with $\Delta J = +1$ are called R-branch transitions. One of the strongest emission line is named 10P20 indicating a transition in the 10 μm band with the lower rotational state $J = 20$. Different transitions have different energy differences and therefore different wavelengths. Figure 2.3 shows the calculated small signal gain of the regular bands of a typical CO₂ laser [4]. Both vibrational transitions have characteristic R and P branches due to the rotational levels superimposed onto the vibrational levels. The small signal gain is proportional to the population density difference of the upper and lower laser levels. For typical gas temperatures of $T = 400$ K the levels around $J = 19$ have the strongest population. Depending on the resonator design, gas mix, gas pressure and the reflectivity of the resonator mirrors CO₂ lasers emit on one or more lines of these regular bands. If no wavelength selective elements are included in the laser design it will emit around the 10P20 line at 10.59 μm. Typical values for the gain of a CO₂ laser range from 0.5 to 1.5 m⁻¹.

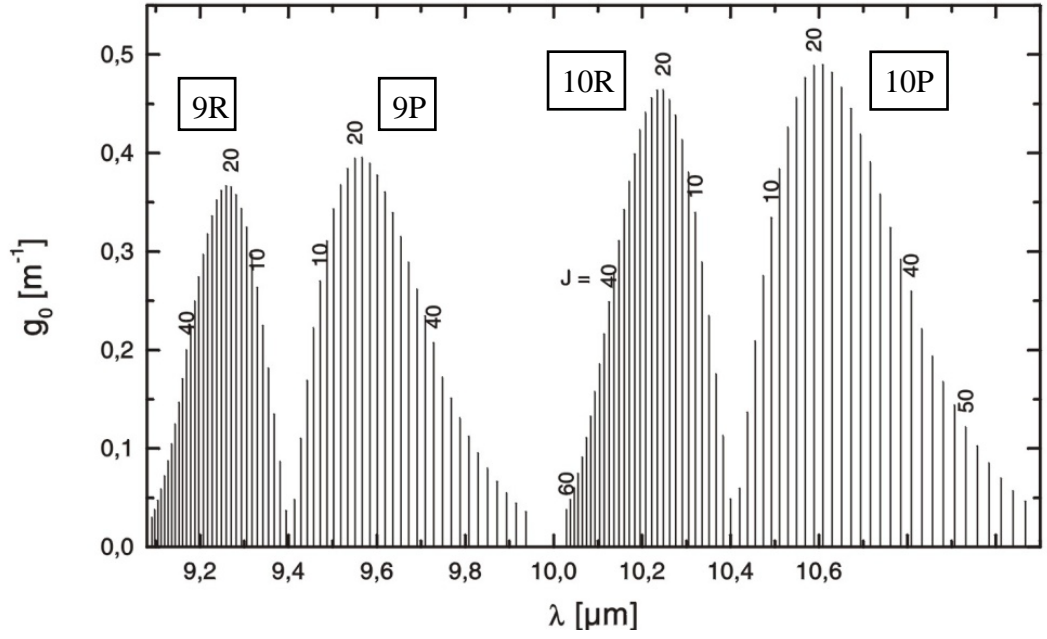


Figure 2.3 Small signal gain for the regular bands of the CO_2 laser at $T = 520$ K, RF-density: 5 Wcm^{-3} , $\text{He} = 73\%$; $\text{N}_2 : \text{CO}_2 = 2.75$ [4].

2.2.4 Gas additives

The gas mix of CO_2 lasers is usually a mix of CO_2 , N_2 and He, though in order to improve certain aspects of the laser performance CO, Xe and other gases are added as needed.

Due to its high thermal conductivity, which is about six times higher than the thermal conductivity of N_2 and CO_2 , Helium reduces the gas temperature since the temperature gradient between the laser gas and the cooled electrode surface is inverse proportional to the thermal conductivity. The thermal conductivity of Helium is $\kappa_{\text{He}} = 0.22 \text{ W/mK}$ at 500 K [5], and since the energy levels of Helium are all above 20 eV, then for a gas mix that is optimized for high laser power, namely electron energy levels in the range 1 to 3 eV, Helium does not influence the discharge significantly. Thus, the thermal conductivity of the gas mix is basically determined by the Helium content, resulting in improved heat removal and a reduction of the thermal population of the lower laser level. Also, the width of the gain profile is temperature-dependent and increases with decreasing temperature for a constant gas pressure. Helium also acts to stabilize the discharge since diffusion processes and thermal conductivity are important for discharge stability by acting to even out local in-homogeneities.

Gas mixtures for diffusion-cooled lasers typically contain Xenon (Xe). Three to five percent increase the output power and efficiency of the laser. The increased efficiency is due to the effect Xenon has on the electron energy distribution in the discharge. Xenon has a relatively low ionization energy of 12.1 eV, which is about 2 to 3 eV less than that of the other gas components. Therefore, the number of electrons with energies above 4 eV decreases and the number of electrons with energies below 4 eV increases [6]. This reduced average electron temperature has a favourable impact on the vibrational excitation of CO and N₂ as discussed above, and also leads to reduced dissociation of the CO₂.

Water (H₂O) has a strong influence on the laser performance. In low power, sealed-off lasers it is often added in order to suppress the dissociation of 2CO₂ molecules into 2CO and O₂. In most high power diffusion-cooled lasers with metal electrodes the amount of water vapour in the system is so large that it has a negative impact on the laser performance and it has to be removed. H₂O or H₂ contents above a critical level have a large effect on the relaxation of the upper laser level.

Water forms mono layers on the surfaces of the electrodes and the vacuum vessel. Removing the mono layers requires a baking process at high temperatures and low pressures. To prevent an increase of the moisture level over time in a laser system water adsorbers like zeolites can be added to the vacuum system of the laser.

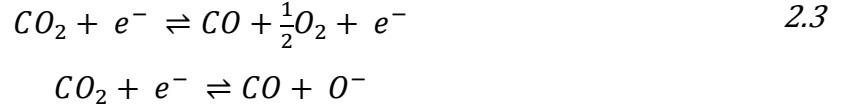
2.2.5 Gas chemical processes in the discharge

If failures due to mirror or electrode damage etc. are neglected, the lifetime of sealed-off CO₂ lasers is mainly determined by the long-term stability of the CO₂ partial pressure and the contamination of the laser gas by leaks and outgasing of the materials used in the construction of the laser. Analogously, the gas exchange frequency required for near-sealed-off lasers depends on the same factors [7], [8].

There is a strong tendency for the partial CO₂ pressure to change over time due to dissociation of the CO₂ molecules [9], [10], so if no special precautions are taken the initially reached equilibrium between CO₂, CO and O₂ is pushed further and further to the CO side until efficient laser operation is not possible anymore. The initial equilibrium

established is influenced by the gas mix, pressure, RF input power, electrode materials etc. Typically 50 – 70% of the CO₂ is dissociated when the initial equilibrium is reached.

The dissociation of the CO₂ molecule is triggered by electron impact in the gas discharge [11]:



There are several ways to stabilize the CO₂ partial pressure:

- Prevent the Oxygen generated in the gas discharge from being consumed by either oxidation or adsorption processes
- Use of catalysts like gold to accelerate the back reaction of CO and O₂ to CO₂ [10]
- Use of gas additives like H₂O and H₂ [2]
- Use of CO₂ donors [7]
- Use of a pre-dissociated gas mix

In order to conserve the CO₂ partial pressure the materials used in the construction of the laser are critical. According to the law of mass action the CO₂ partial pressure will decline if the O₂ partial pressure is reduced. The reduction of the O₂ partial pressure can be avoided by using non-oxidizing materials like quartz or ceramic, or by passivating the metallic materials used. For instance, the passivation of Aluminium electrode surfaces can be achieved by chemical reactions of the Aluminium with a strong oxidizer such as Nitric acid [7]. Other methods include anodizing and the application of conversion coatings [12].

The CO₂ partial pressure can also be conserved by accelerating the back reaction of CO and O₂ to CO₂ by the use of a catalyst. Gold has been studied as a catalyst by many groups [10], [9], [13]. Other materials like platinum [14] and Rutheniumoxid [15] have also been investigated, but are not used in commercial products. Gold is well suited as an internal catalyst since it is stable in the reactive environment of the CO₂ laser gas discharge. Gas phase reformation of CO₂ by CO and O is an improbable process in the bulk gas since the energy released during this reaction is larger than the dissociation

energy of CO_2 . A three body collision is necessary in order to remove the excess energy and facilitate the formation of CO_2 . In a typical laser discharge this three body collision is unlikely to occur in the bulk gas, and the walls of the discharge vessel are the most likely third-body candidate [16].



A Gold catalyst on the surface of the discharge vessel adsorbs CO, while the discharge produces the atomic Oxygen needed for the back reaction.

Another way to promote the reformation of CO_2 is the addition of H_2 or H_2O to the gas mix. The Hydrogen forms OH which in turn reacts with the CO molecule to $\text{CO}_2 + \text{H}$ [17].

Since catalysts are not easy to handle and often need activation and can be poisoned while H_2 and H_2O quench the upper laser level, methods to provide constant replenishment of the CO_2 have been investigated. Malz and Hubenreisser [18] investigated the use of molecular sieves (zeolites) as a CO_2 donor. The molecular sieves can adsorb large amounts of CO_2 and release it again when the partial CO_2 pressure decreases due to oxidation processes, O_2 adsorption or other chemical reactions.

The most common used method to stabilize the CO_2 partial pressure is the use of pre-dissociated gas mixes: CO and sometimes O_2 are added to the gas mix. This approach does not only avoid CO_2 dissociation but also the creation of O_2 . Avoiding the creation of O_2 is of interest since it quenches the upper laser level [19] and the excited N_2 molecule [20].

Most effective is of course the combination of two or more of these methods.

2.3 Laser Gas Discharges

2.3.1 *Introduction*

Even though some of the early research activities, like Patel's groundbreaking work, in the 1960s were carried out with RF discharges, DC excitation was mainly used for CO₂ lasers until the end of the 1970s only to be replaced again by RF excitation in the 1980s. The newly found advantages of RF excitation enabled new geometries that resulted in compact high power diffusion-cooled lasers. The main advantages of RF over DC excitation were the scalability of the discharge into large areas without the occurrence of arcing or filamentation, and the lower voltages across the electrodes. The lower voltages enabled transverse discharges with all-metal electrodes which improved the heat removal process from the gain medium significantly. RF excitation also helped to overcome major lifetime limiting issues caused by sputtering effects of the electrodes in DC discharges.

DC excited lasers are typically constructed with cylindrical glass tubes with electrodes (anode and cathode) attached at the two ends. This concept was used for sealed-off and slow-flow systems. The laser output power can be increased by increasing the current density in the discharge until thermal rollover occurs and the efficiency of the laser declines. In order to further increase the laser power the discharge length needs to be increased. Laser power was therefore limited to a few hundred Watts in linear systems, while folded set-ups were available commercially (e.g. from Ferranti Ltd who used a Herriott-Cell folded resonator) to produce power levels in the kilowatt range. Commercial DC excited lasers are (were) also available from companies like Sharplan, Wegmann-Baasel and others. Companies like Feha and Chinese manufacturers still offer DC-excited glass tube lasers since their production costs are extremely low. They are used in low power applications such as marking and medical procedures.

Some attempts were made to utilize AC discharges with excitation frequencies in the range between tens and hundreds of kHz. In this frequency range the discharge characteristics are quite similar to DC discharges. The main difference is, of course, the alternating polarity with each half cycle, and though this approach was still pursued by research groups into the 2000s, the technology has never been a commercial success.

2.3.2 RF discharges

RF discharges can be subdivided into inductively and capacitively coupled discharges. For diffusion-cooled lasers only the capacitively coupled discharge is relevant. There are two important forms of the capacitively coupled RF discharge which are named α - and γ -discharge according to the Townsend coefficients α and γ describing where the electrons are generated [21]. The main difference between them is the impedance of the sheaths / power dissipation in the sheaths and their current densities [22]. The two types can be easily distinguished by their intensity and luminosity distribution along the discharge length as shown in Figure 2.4. The γ -discharge is also called high current discharge since it can have an order of magnitude higher current density than the α -discharge, which in turn is called low current discharge.

α is the *first Townsend ionization coefficient*, expressing the number of secondary electrons generated per unit length by an electron moving through the discharge. γ is the *second Townsends ionization coefficient*, expressing the number of electrons generated by ion impact on the electrodes. Even though the α -discharge is the dominant discharge type in diffusion-cooled lasers, there is usually some γ -discharge present for discharges driven at low radiofrequencies (few tens of MHz) [23].

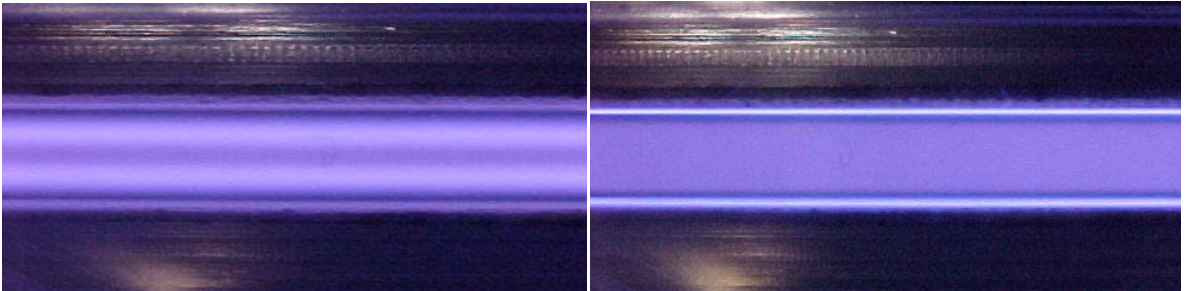


Figure 2.4 Left: Image of a typical α -discharge in a 6 mm inter-electrode gap; Right: typical γ -discharge in a 6 mm inter-electrode gap [24].

The α -discharge is self sustaining with cold electrodes. One of the characteristics of this discharge type is the positive sheath at the cathode and an electric field distribution that is high at the electrode surface and drops rapidly towards the centre of the gap. Since the discharge is alternating at radiofrequencies, the cathode and anode switch from one side to the other with each half cycle.

If the inter-electrode gap is large enough, a neutral plasma region with low electric field strength is formed between the areas with high electric field strength called the positive column [21], [23]. Efficient excitation of the vibrational energy levels of the N_2 and CO molecules occurs in the positive column. Compared to the sheaths, which are essential for the discharge stability, the positive column has only a marginal influence on the overall electrical and thermal characteristics of the discharge, and does not form if the sheaths fill the entire area between the electrodes.

The formation of the sheaths in RF discharges is due to the different mobility of electrons and ions in the plasma due to their different masses. The electron gas oscillates periodically around a middle point, as shown in Figure 2.5, with an amplitude that is inversely proportional to the RF frequency. Electrons that are closer to the electrodes than the amplitude of the oscillating electron gas hit the electrodes and are lost. As a result, the oscillating electron gas leaves a positively charged layer (sheath) in front of the electrodes with a total width of d_s [21].

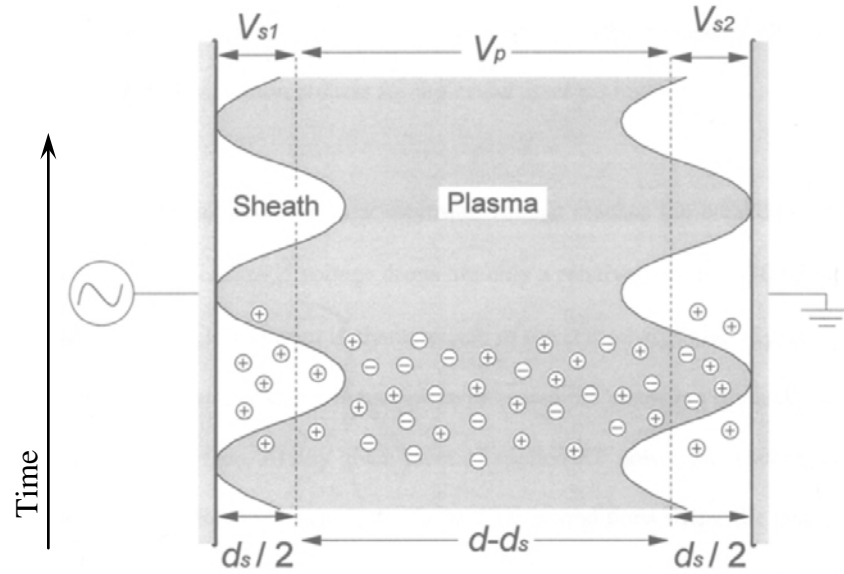


Figure 2.5 Cross-section and temporal structure of a α -discharge. d is the inter-electrode gap size and d_s the total width of the sheaths [25].

If the electric field across the sheaths reaches a sufficient level it accelerates ions up to a point where they have enough energy to cause secondary electron emission if they strike the electrodes. The electrons can then be accelerated in the electric field of the sheaths and can create electron-ion-pairs.

2.3.3 The current-voltage characteristic

During the ignition process of the discharge voltage and current increase proportionally to each other as the RF power is increased. As the voltage reaches a critical point breakdown occurs and the plasma ignites. The voltage drops and the current rises. At this point the plasma might not cover the entire electrode surface. To sustain a discharge over the entire electrode surface, A , a minimum current $I_{min} = j_{min} \cdot A$ is required. In cases of currents lower than I_{min} the discharge covers only an area where the minimum current density j_{min} can be sustained. With increasing current the voltage across the electrodes stays constant and the discharge spreads. Once the entire surface area is covered, the voltage and current density change in accordance to the CVC (current voltage characteristic) as shown in Figure 2.6. The normal current density j_{min} corresponds to a minimum voltage and increases with increasing gas pressure. The value of j_{min} also increases when the excitation frequency, f is increased. As a result, higher current densities can be achieved at higher frequencies.

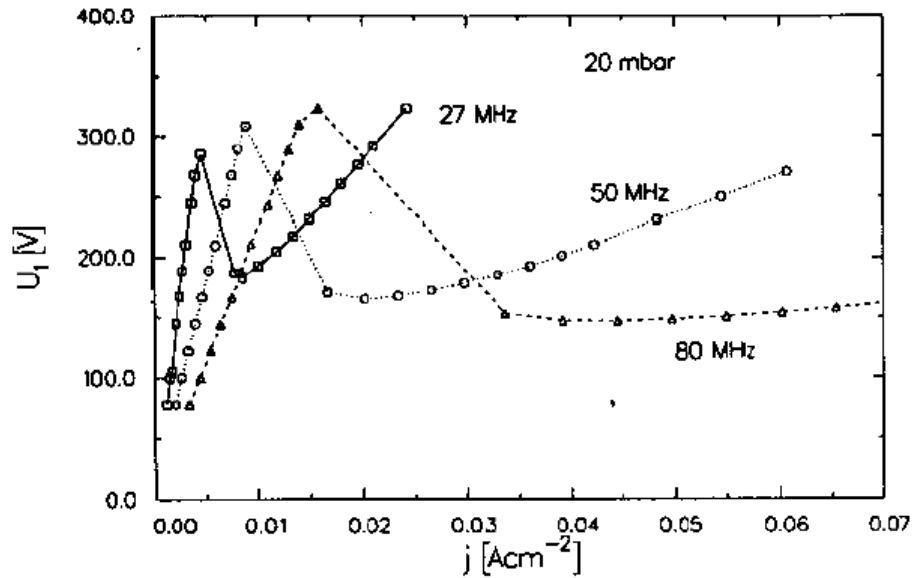


Figure 2.6 Calculated current density-voltage characteristic (CVC) for a gas mix of $\text{He:N}_2:\text{CO}_2 = 8:3:1$ at a gas pressure of 20 mbar and excitation frequencies of 27, 50 and 80 MHz [26].

With increasing gas pressures, p and inter-electrode gap sizes, d , the voltage drop in the sheaths increases. At a critical value of pd the sheath voltage becomes so large that breakdown occurs [21].

As the discharge current density is increased, the ion density in the sheaths increases resulting in a higher voltage in the sheaths. At sufficiently high voltages breakdown occurs. The current is self-sustained by ion-electron emission from the electrodes followed by charge multiplication during the electron flight through the sheath. An ionization wave travels toward the electrode, leaving behind a plasma and reducing the initial sheath thickness of the α -discharge to the much thinner sheath thickness of the γ -discharge creating optimal conditions for charge multiplication through secondary emission [27]. The discharge has transitioned from α to γ . With an increase of the excitation frequency the limiting values for the α -discharge increase. With an increase in frequency the thickness of the sheath decreases and a larger ion density is required for the voltage to reach a level where breakdown occurs.

2.3.4 Reduced electric field strength - E/N

The ratio of the electric field and the gas density (E/N) plays an important role both in the discharge behaviour and laser excitation. It relates to the mean free path of an electron between collisions per half cycle of the RF field. The larger the free mean path, the more energy electrons extract from the electric field and consequently the larger the average electron energy [2].

In a typical gas discharge for diffusion-cooled CO_2 lasers the optimum E/N for efficient excitation is about $(2.5 - 3.0)10^{-16} \text{ Vcm}^2$ in the bulk of the discharge [23]. For smaller values of E/N the losses due to elastic collisions are high while for larger values of E/N the cross sections for direct excitation of the CO_2 (001) level and the vibrational excitation of N_2 are reduced. And for even larger values losses due to ionization increase [2].

2.3.5 Discharge instabilities

Laser gas discharges are characterized by different temperatures of the electron gas and the heavy particles (ions). Within certain ranges of gas pressure and RF power density these discharges are stable and homogeneous. However, due to thermal imbalances certain conditions cause instabilities [23], [28]. Random local disturbances can reach catastrophic levels and transform the discharge into another regime. These other regimes

are in general highly undesirable and impact the laser performance in a negative way, and in practice, these instabilities can be detected visually. Different intensities in the glow of the discharge are due to different electron densities. As a conclusion, factors causing instabilities are closely related to factors governing electron density, electron production and annihilation, and transport mechanisms [21]. Figure 2.7 shows how changes in the electron or gas density can lead to either stabilizing or destabilizing effects in the electron density in the discharge.

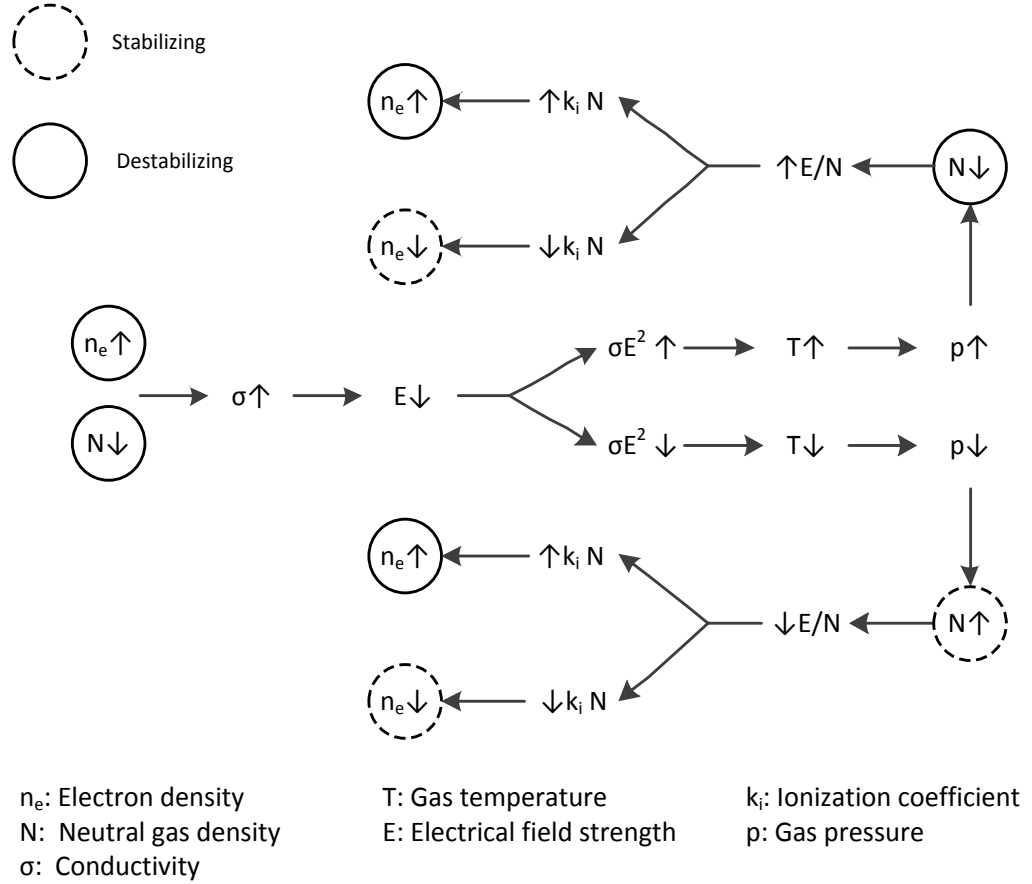


Figure 2.7 Mechanism of thermal instabilities in gas discharges [23].

For example, one way of understanding this diagram is as follows. The plasma conductivity, σ is proportional to the electron density, n_e and inversely proportional to the neutral gas density, N . Therefore, the conductivity increases when the gas pressure decreases or the electron density increases. The electric field strength, E in general decreases with increased conductivity. The power density, σE^2 will increase or decrease depending on which mechanism is stronger.

The temperature increases as the power density is increased resulting in a local expansion of the gas which in turn results in higher pressure. Since this does not change the E -field strength directly the corresponding reduced field strength, E/N increases. Then, since the electron-ionization frequency increases with E/N , therefore the electron production increases, so that the ‘disturbance’ in the discharge is further amplified [23]. This process can start at any point. For example, an increase in temperature yields higher conductivity and higher currents producing further increases in heat production.

$$\delta n_e \uparrow \rightarrow \delta(\sigma E^2) \uparrow \rightarrow \delta T \uparrow \rightarrow \delta N \downarrow \rightarrow \delta(E/N) \uparrow \rightarrow \delta T_e \uparrow \rightarrow \delta n_e \uparrow$$

The other paths in the diagram can be followed in a similar manner.

The following paragraphs describe the most relevant instabilities in more detail:

- **Filaments:** Thermal instabilities in discharges lead to filaments in the direction of the electric field vector. In the filaments the conductivity and the power density are enhanced. The origins of these inhomogeneities are local fluctuations of the neutral gas density and the electron density. The displacement current in the sheath is not sufficient to sustain filaments, they need electrons from the near vicinity, which explains the larger diameter of filaments on the electrode surface. Due to a field strength regulating effect, more filaments are created in characteristic distances. The strongly reduced E -field strength in an emerging filament also reduces the E -field strength in the close vicinity and the reduced net electron production rate results in lower electron densities. If the reduction of the local field strength is large enough the mechanism starts to act in the opposite direction. The lower electron density yields higher E -field strengths that propagate into the neighbouring areas creating a new filament [29], [30].
- **Arcing:** At higher power densities increases in the local electron density in the positive column increase the ion density in the sheaths resulting in a higher voltage in the sheaths. When a critical voltage is reached arcing occurs. If this arc is not extinguished immediately, the discharge can collapse and the entire current flows through this channel of ionized gas. This arc can move over the electrode surface, can stall and re-appear at a different position. The high current densities heat up the electrode locally and erode and evaporate the electrode material,

though the electrode itself stays cool. The main electron source is the thermal field emission effect [21] and may damage the electrode surface, with the erosion generating pitting in the electrode surface and the high temperatures may ‘crack’ the CO₂ molecules and cause carbon deposits on the electrode surface. Then, the carbon deposits may promote additional arcs since carbon has a relatively low ionization energy of 11.3 eV compared to the gases.

2.4 Power Scaling

As discussed in section 2.2, efficient removal of the waste heat from the gain medium and keeping its temperature below 600 K is key to efficient laser operation. Two types of industrial CO₂ laser designs on the market efficiently remove the heat from the active medium: fast-flow and diffusion-cooled lasers. In fast-flow designs, the gas is circulated with speeds of up to half the speed of sound through the discharge area. The gas is then cooled in heat exchangers before returning to the discharge area. In diffusion-cooled designs, the laser gas is in contact with cooled surfaces, and the heat is removed by diffusion of the hot gas molecules to the water-cooled electrodes. As discussed in section 2.2, Helium plays a key role in the heat removal process.

The first reported RF excited diffusion-cooled lasers were linear waveguide lasers with a square cross-section. The inter-electrode gap size was typically about 2 mm and the discharge length less than 500 mm [31]. The achievable laser power is about 1 Wcm⁻¹ and power levels up to 50 W are typical. Folding of the linear waveguides provided a way to increase the output power above fifty Watts, but it did not offer a path to multi-kilowatt lasers since this approach to power scaling is severely limited due to the coupling losses between the waveguides. The power scaling law for these linear waveguides can be expressed as

$$P = P_L L \tag{2.5}$$

where P_L is the characteristic power for a square cross-section gain medium and L the discharge length [32]. Typical values for P_L are in the range from 80 to 100 Wm⁻¹.

A path forward, to multi-kilowatt laser systems, was reported in [32] - large area scaling of RF excited discharges. By utilizing a two-dimensional discharge structure, a planar structure, the power scaling law changes to

$$P_A = P_L \frac{A}{d} f \quad 2.6$$

where A is the electrode surface area and d the inter-electrode gap size. The scaling factor f , takes into account the differences in two-dimensional heat flow in linear waveguides and one-dimensional heat flow in planar waveguides. A value of $20 \text{ kW}\cdot\text{m}^{-2}$ for P_A was reported in [32].

The $1/d$ power scaling was experimentally confirmed in [33] down to inter-electrode gap sizes of about 1.2 mm. In smaller inter-electrode gaps, the waveguide losses and ion sheath losses dominate and no further increase in laser power can be achieved as reported in [22].

When the discharge area and the inter-electrode gap size are used for power scaling, it is important to understand the limiting factors and to maintain the efficiency of the laser. Instability processes, limiting the RF power density in the discharge, were already discussed in section 2.3. In order to maintain the efficiency and a stable discharge the excitation frequency must be chosen carefully. In [34] and [35] frequency scaling was investigated initially and later *Similarity Laws* were introduced in [22] detailing the relationship between the excitation frequency and other discharge parameters and defining invariants for *similar* discharges. The most important invariant is the product of excitation frequency, f and inter-electrode gap size, d , which should equal about $280 \text{ mm}\cdot\text{MHz}$. The excitation frequency is key since the alpha to gamma discharge transition occurs when the threshold voltage in the sheaths is reached, which scales inversely with the frequency. Additionally, the electrical losses in the sheaths scale with $1/f^2$.

How powerful the excitation frequency is with regard to controlling laser efficiency is shown in Figure 2.8. The laser output power is plotted versus gas pressure for RF excitation frequencies in the range of 28 to 116 MHz. The input power is 100 W for all frequencies and the discharge has a volume of $6 \times 6 \times 386 \text{ mm}^3$. As predicted by the

similarity law the maximum output power is reached at about 50 MHz for an inter-electrode gap size of 6 mm.

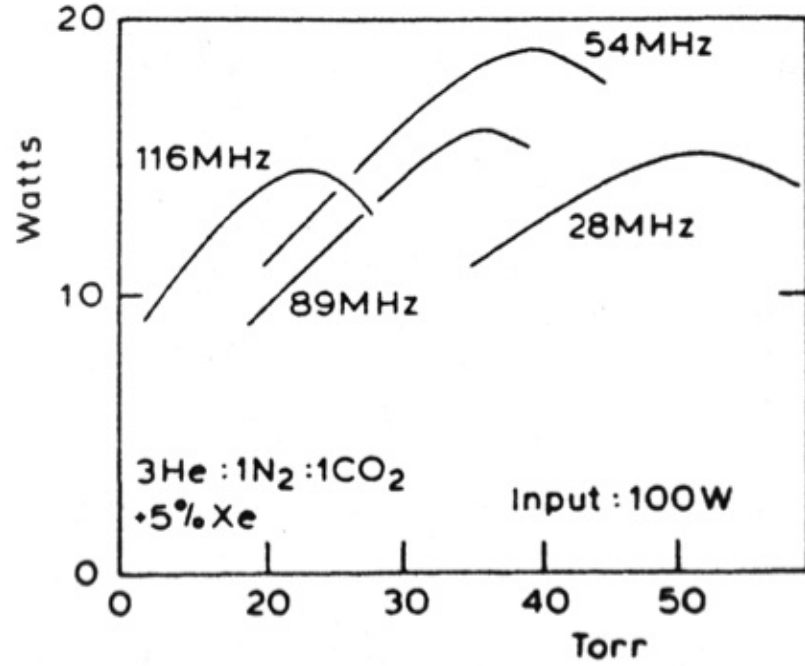


Figure 2.8 Laser output power vs. gas pressure for different excitation frequencies. Discharge volume: $6 \times 6 \times 386 \text{ mm}^3$ [35].

While large area discharges offer the potential for power scaling into the multi-kilowatt range, optical resonators are needed that can effectively utilize the gain medium. Such resonators are the subject of section 2.5.

2.5 Resonators for Coaxial Media

Over the past few decades numerous designs and resonator configurations for diffusion-cooled lasers were investigated. Planar waveguide designs were studied in detail by [33], [36], [37], [38], [39] and [40] to mention only a few and they are available as commercial products from Rofin Sinar, Coherent, Synrad, Universal Laser Systems and others. Coaxial waveguides were reported in [41], [42] and [43]. Several configurations with an annular discharge structure have been investigated: Multipass configurations by [43], [44] and [45], stable resonator configurations with rotational symmetric mirrors by [46], [47], [48], [49], [50] and [51], and stable-unstable-hybrid resonators with non-rotational symmetric mirrors by [52] and [4].

Coaxial waveguide lasers require mechanical tolerances for the electrode system that are extremely difficult and expensive to achieve, and multipass free-space configurations do not utilize the discharge volume efficiently, while configurations with rotationally symmetric optics yield only poor beam quality and are extremely alignment-sensitive. However, good utilization of the gain medium in combination with good beam quality can be achieved with the stable-unstable-hybrid configurations as described here.

New production technologies like the Fast-Tool-Servo [53] for ultra precision diamond turning enabled complex mirror surface fabrication and therefore the development of novel optical resonators for diffusion-cooled lasers with stable-unstable-hybrid resonators combined with coaxial electrodes. These resonators yield the same excellent beam quality as planar waveguides with stable-unstable-hybrid resonators, but exhibit better performance in regard of spatial beam stability and pointing. Such concepts were first studied by Ehrlichmann [52] and Habich [54].

One of the resonators investigated by Ehrlichmann [55] was a helix-torus resonator (see Figure 2.9). However, there are two major problems with this configuration: 1) no polarization selection and 2) short resonator length. Both of these problems were solved with the helix-axicon resonator investigated by Schulz [4]. In spite of these improvements the helix-axicon resonator still has some major shortcomings: limited brightness, insufficient polarization and reproducibility and stability problems. Nevertheless, this resonator is used as the starting point for the development of a multi-kilowatt diffusion-cooled laser with high brightness in the next chapters.

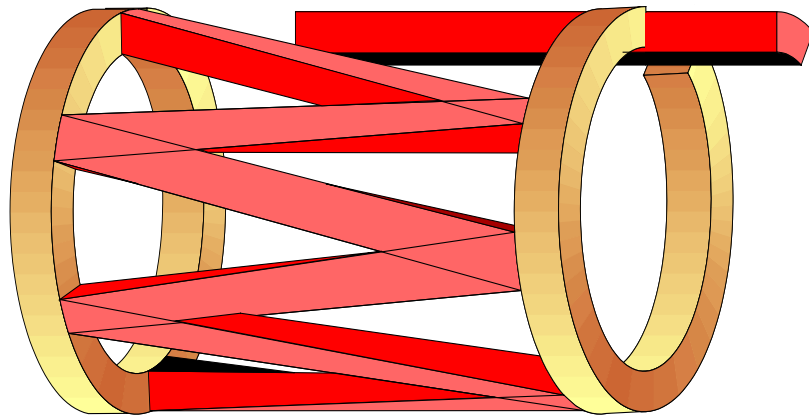


Figure 2.9 Raytracing representation of the helix-torus resonator. The helix mirror (on the right) drives the beam around the circumference until it reaches the output coupling window and exits the resonator.

2.5.1 General introduction helix-axicon resonator

The annular discharge geometry requires a stable-unstable-hybrid resonator, such as the helix-axicon resonator, in order to make efficient use of the discharge volume. A schematic representation of the helix-axicon resonator is shown in Figure 2.10. One mirror is a so called axicon which acts as a retro-reflector. This is an optic having the special property that a reflected beam is always parallel to the incident beam, irrespective of the angle of incidence. The axicon mirror folds the beam inside the resonator and therefore doubles the resonator length which lowers power fluctuations due to laser signature scanning to $\leq 1\%$. The second mirror, the helix mirror, acts as the ‘front’ and ‘rear’ mirror of the stable resonator. Since both, ‘front’ and ‘rear’, mirrors are manufactured on the same blank at the same time they are aligned to each other per definition. Misalignments of the helix mirror now result in very low amounts of power loss, mode degradation and beam steering [56].

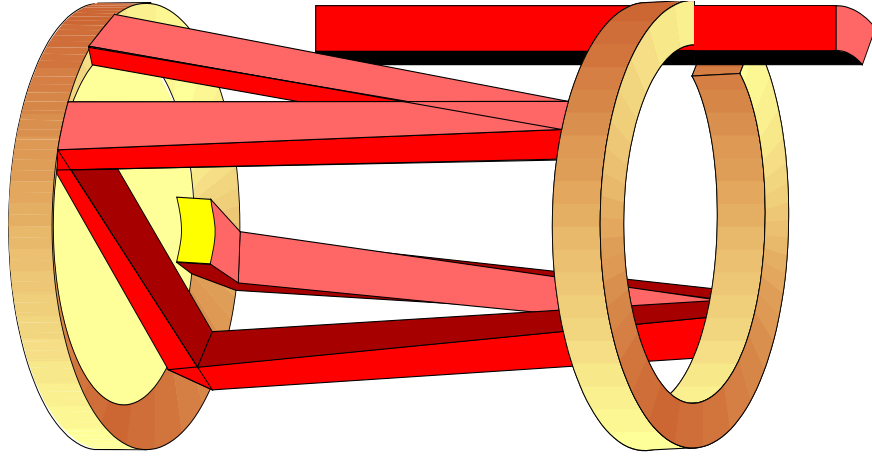


Figure 2.10 Raytracing representation of the helix-axicon resonator with the so called axicon mirror on the left and the helix mirror on the right.

The helix mirror has a slope in the azimuthal direction that drives the beam around the circumference until it reaches the output coupling window where the beam exits the resonator. How much of the overall resonator internal power is extracted is determined by the magnification, M . The magnification is defined as $M = 2\pi r / (2\pi r_s - W)$ with W being the size of the outcoupled beam and r_s the middle radius of the resonator. For a helix mirror with linear slope the beam size, W can be calculated using $4(2c\pi L)^{1/2}$ [52], [57] where L represents the resonator length and c defines the steepness of the slope on the helix mirror.

For a linear slope the shape of the helix mirror, $h(r, \phi)$ is given by [52], [57]:

$$h(r, \phi) = c\phi + \frac{(r - r_s)^2}{2r_h} - c\phi \frac{2}{r} (r - r_s) \quad 2.7$$

Figure 2.11 shows a cross section of the stable direction of the resonator. The radius of curvature in the stable direction, ROC_{helix} is given by r_h and r_s is the middle radius of the resonator.

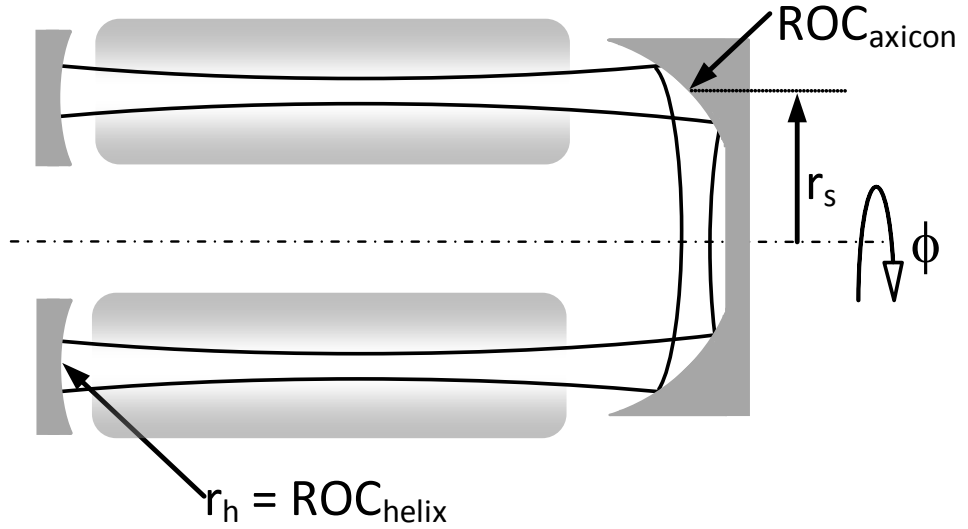


Figure 2.11 Cross section of the resonator defining the middle radius of the resonator, r_s and the radius of curvature on the helix mirror in the stable direction, ROC_{helix} . The ROC_{axicon} equals $2 \cdot \sqrt{2} \cdot ROC_{\text{helix}}$.

The helix mirror contour, as defined by Equation 2.7, is plotted in Figure 2.12. The main features are the radius of curvature (ROC) in the radial direction, the step in the azimuthal direction inside the output coupling window and the change of the vertex position of the ROC in the radial direction at about 180° , opposite from the output coupling hole.

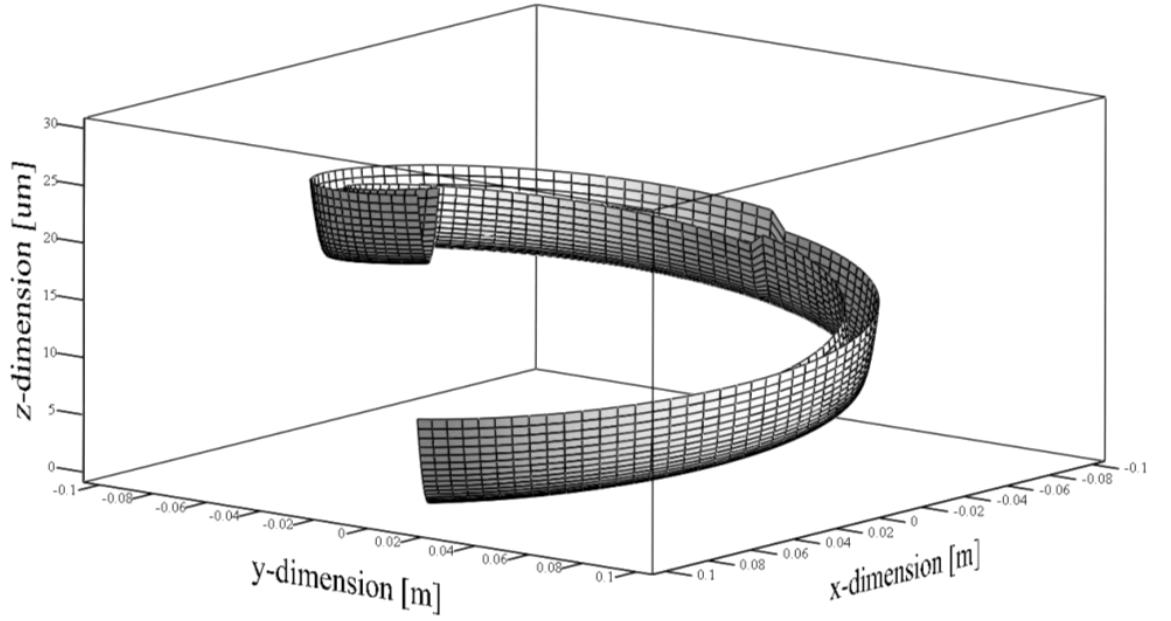


Figure 2.12 Representation of the surface contour on the helix mirror as determined by Equation 2.7 for a linear slope with $c = -3.3 \cdot 10^{-3} \text{ mm/rad}$.

The inter-electrode gap size in the radial (stable) direction is chosen to be suitable for free-space propagation. In general, it can produce a beam with good beam quality ($M^2 = 1.1$) but the divergence and beam size have to be corrected before it can be used for material processing. The unstable or azimuthal direction of the resonator produces a beam with lower beam quality ($M^2 \approx 10$). In order to improve the beam quality of the azimuthal direction spatial filtering is required. Spatial filtering, beam size and divergence correction are performed in a beam formatting telescope (see section 2.6).

Figure 2.13 shows a schematic representation of the coaxial electrode system with L being the electrode length, d the inter-electrode gap size and $2r_s$ the middle diameter of the inter-electrode gap.

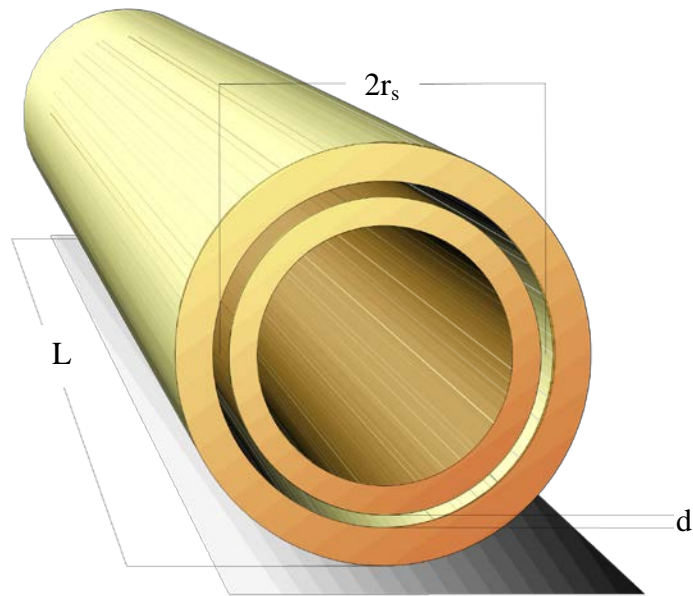


Figure 2.13 Schematic representation of the coaxial electrode system used with the helix-axicon resonator.

The immense rigidity and robustness of tubular structures allows the combination of several functions in the electrodes. The outer electrode, for instance, acts as the main mechanical structure, vacuum chamber, RF shield and it also provides cooling for the laser gas.

Figure 2.14 shows the mechanical construction of the coaxial laser. The two electrodes are held by two blocks, which also hold the resonator mirrors. A lid on each end closes the vacuum system. The Aluminium electrodes are in direct contact with the laser gas and are water cooled. The beam is extracted through a diamond window in the helix mirror lid.

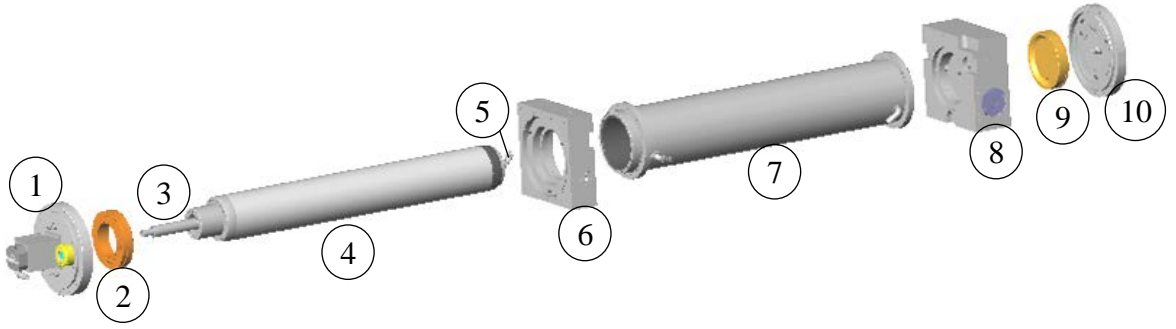


Figure 2.14 Exploded view of the mechanical structure of the coaxial laser with a helix-axicon resonator: 1: Helix lid with diamond window; 2: Helix mirror; 3: RF feed; 4: Inner electrode; 5: Termination; 6: Helix block; 7: Outer electrode; 8: Axicon block; 9: Axicon mirror; 10: Axicon lid.

The basic dimensions and parameters of the coaxial laser are listed in Table 2.1.

Discharge length L	1 m
Resonator radius r_s	77.5 mm
Distance helix mirror to electrodes x_1	29 mm
Distance axicon mirror to electrode x_2	90 mm
Excitation frequency f	27.12 MHz

Table 2.1 Basic parameters and dimensions of the coaxial laser with helix-axicon resonator.

Due to the relatively large inter-electrode gap size of about 6 mm the discharge can be excited at 27.12 MHz, a frequency that does not require any special management of the lossy transmission line if the electrodes are about 1 m in length or less [58]. Longer electrodes will require some additional management of the transmission line as discussed in chapters 5 and 6. For the one meter long coaxial laser the RF power is end-fed on the helix side and the lossy transmission line is terminated on the axicon end.

2.6 Beam Formatting

In general there are three different types of beams: stigmatic beams, simple astigmatic and general astigmatic beams [59]. A typical example of a stigmatic beam is a rotational symmetric Gaussian beam. If such a stigmatic beam is passed through a cylindrical lens, or is reflected off a cylindrical mirror it will be transformed into a simple astigmatic beam. A simple astigmatic beam has an elliptical intensity distribution, but the principal axes of the beam stay fixed relative to the laboratory coordinate system. If such a simple astigmatic beam is reflected off a second cylindrical optic or passed through a second cylindrical lens, which has its axis of symmetry not parallel or perpendicular to the first one, the beam is transformed into a general astigmatic beam. This concept can be used in reverse sequence to transform general astigmatic beams into stigmatic beams.

The beam extracted from a laser with a coaxial electrode configuration and a helix-axicon resonator is general astigmatic: it has an elliptical intensity distribution that rotates in a plane perpendicular to the beam axis during propagation.

2.6.1 *Beam formatting requirements*

In order to transform the general astigmatic beam extracted from a stable-unstable-hybrid resonator into a rotational symmetric, nearly diffraction limited beam it is shaped in a beam formatting telescope. The following functions need to be integrated into the telescope:

- Improvement of the beam quality in the unstable direction (spatial filtering)
- Transformation of the general astigmatic beam into a simple astigmatic beam
- Transformation of the simple astigmatic beam into a stigmatic beam

Figure 2.15 shows the intensity distribution of the unformatted beam in the stable and unstable direction at one and three meter distance from the output coupling window.

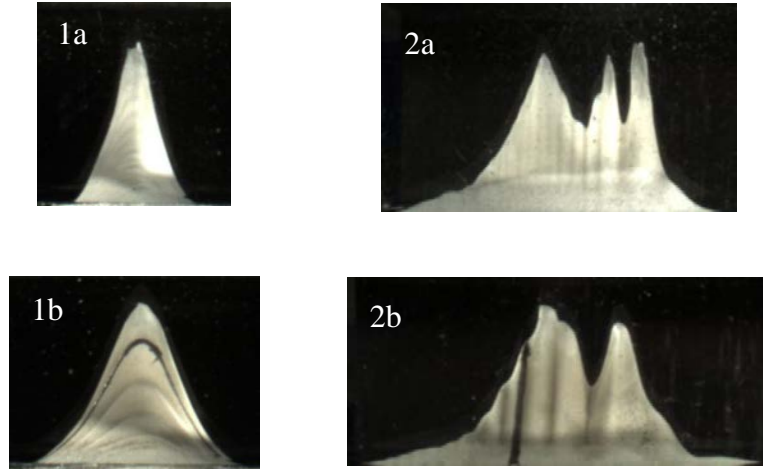


Figure 2.15 Intensity distribution of the unformatted beam in the stable (radial) and unstable (azimuthal) direction at one and three meter distance from the output coupling window. 1a: 1 m, radial; 1b: 3 m, radial; 2a: 1 m, azimuthal; 2b: 3 m, azimuthal.

2.6.2 Spatial filtering

A description of the spatial filtering process can be found in the literature in [4], [60] and [55] among others. Briefly summarized, first the laser beam is focused, and in our case the azimuthal direction is focused with a Cu mirror. The Fourier transform of the intensity distribution can then be found in the focal plane where the higher spatial frequencies in the beam separate from the main peak and can be filtered out [61]. The intensity distribution in the Fourier plane is similar to a sinc^2 function. After filtering, the intensity distribution of the remaining beam is similar to that of a Gaussian distribution.

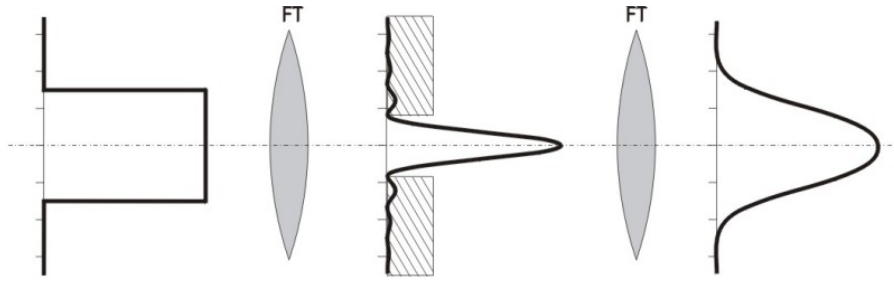


Figure 2.16 Visualization of the spatial filtering process. The intensity distribution of the unstable resonator is represented by a top hat. The focused intensity distribution is filtered in the Fourier plane and then collimated. The unfiltered intensity distribution in the focus is similar to a sinc^2 function. (picture taken from [4])

The position of the Fourier plane must be spatially and temporally stable for consistent filtering results. Changes in the far-field position by more than one Rayleigh length will change the intensity distribution dramatically and the higher frequencies will not be separated from the main peak anymore. Also, within one Rayleigh length the beam size increases by a factor of $\sqrt{2}$ and the beam would be severely truncated by the spatial filter if the position of the Fourier plane moves significantly. Movement in the lateral direction of the beam in the filter will result in insufficient filtering on one side and truncation of the beam on the other side.

One possible set-up for the beam formatting telescope, which integrates all functions discussed above, is shown in Figure 2.17. It comprises four optical elements (OE) and a spatial filter (SF). Two optical elements at the time form a telescope to adjust the beam diameter and divergence of the stable and unstable direction. In the stable direction a Galilean style telescope is used. The unstable direction uses a Kepler style telescope to create a Fourier plane for spatial filtering [62].

At least one of the optical elements is rotated so that its axis of symmetry is not parallel or perpendicular to the laboratory coordinate system in order to stop the rotation of the intensity distribution during propagation.

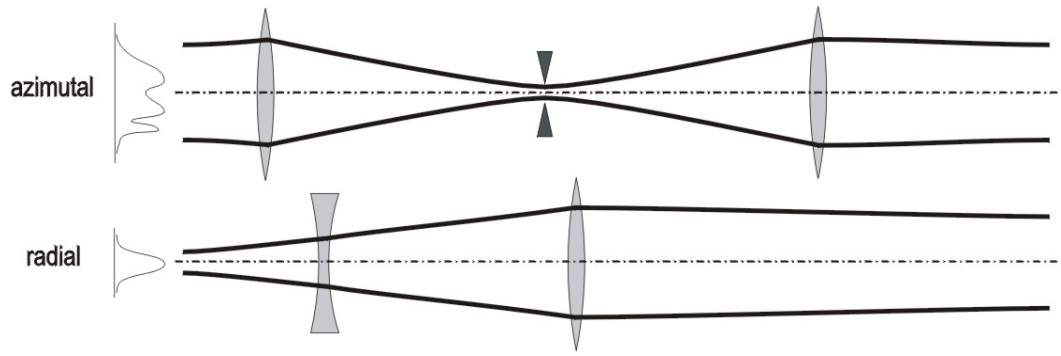


Figure 2.17 Top: Kepler style telescope for the formatting of the unstable direction; bottom: Galilean style telescope to format the stable direction. (Picture taken from [4])

2.7 Polarization Issues

Polarization is one of the most important characteristics of the laser beam for metal cutting. In order to have the same cutting performance independent of the cutting direction almost all laser cutting systems (laser cutting machines) use circular polarization. Since most lasers emit linear polarization, the linear state of polarization is converted into circular polarization using a $\lambda/4$ plate.

Schulz in [4] already reported that the helix-axicon resonator emits light with non-linear polarization that is in essence azimuthally polarized. The polarization inside the helix-axicon resonator is defined by the two 90° deflections in the axicon mirror. The reflectivity for s-polarization is slightly higher than for p-polarization ($R_{s-pol} = 99.8\%$; $R_{p-pol} = 99.6\%$ [63]). This minimal difference in reflectivity suffices to discriminate locally between s- and p-polarization. As a result, on a global level the polarization on the axicon mirror is mainly azimuthal.

The state of polarization on the helix mirror is different from that on the axicon mirror. A beam that propagates from the axicon to the helix mirror starts out with a pure azimuthal polarization, but due to the inclination of the beam in the azimuthal direction the beam and the state of polarization both shift. As the inclination of the beam increases as it moves along the azimuthal direction, the state of polarization changes its angle more and more. As the beam propagates back to the axicon, the angle is shifted again by the same amount. Only another reflection on the axicon surface, where the two states of polarization are completely discriminated, can re-establish the pure azimuthal polarization [4].

Figure 2.18 visualizes the inclination of the beam in the azimuthal direction.

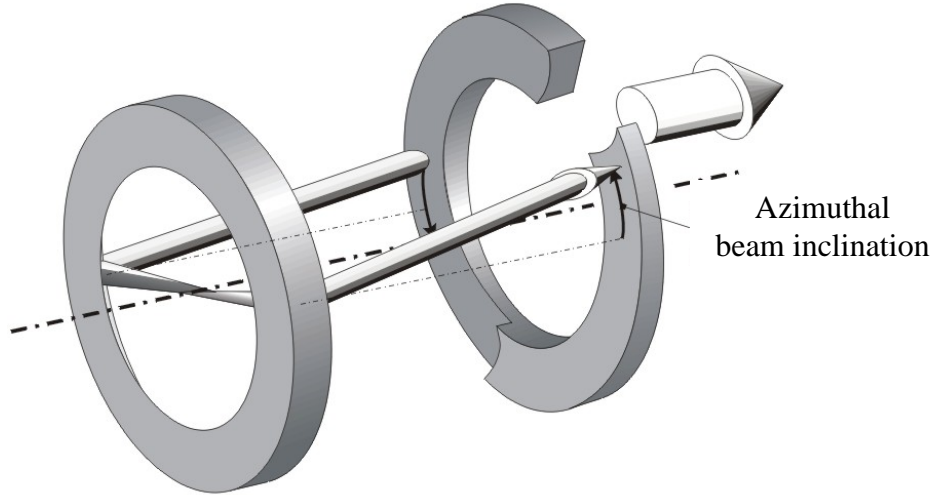


Figure 2.18 Visualization of the beam inclination in the azimuthal direction. (Picture taken from [4])

Figure 2.19 shows the calculated deviation of the state of polarization from pure azimuthal polarization on the axicon (left side) and the helix mirror (right side). With increasing azimuthal position of the beam on the helix mirror the deviation from pure azimuthal polarization increases.

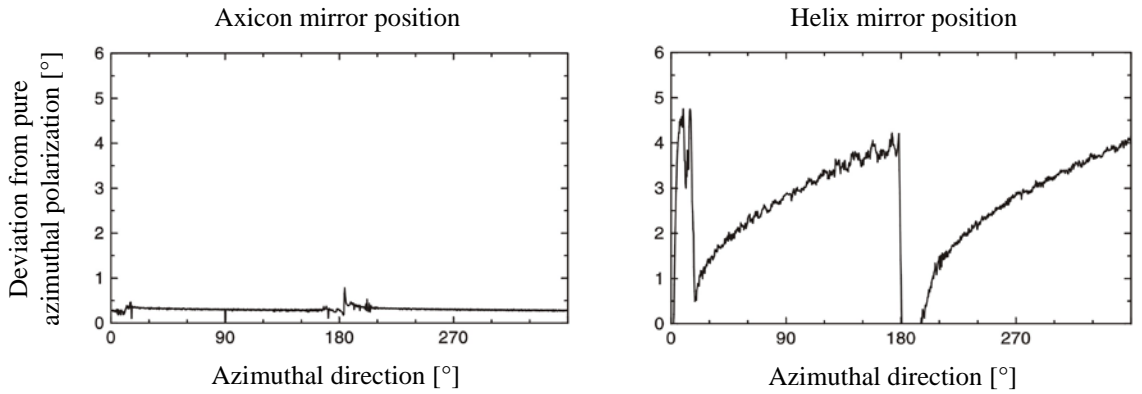


Figure 2.19 Deviation of the resonator internal state of polarization from pure azimuthal polarization on the helix and axicon mirrors [4].

The outcoupled beam has essentially azimuthal polarization that is slightly shifted. The outcoupled (unformatted or raw beam) and formatted beam both show this varying angle of the state of polarization across the beam. Figure 2.20 shows the measured state of polarization in the raw beam and formatted beam.

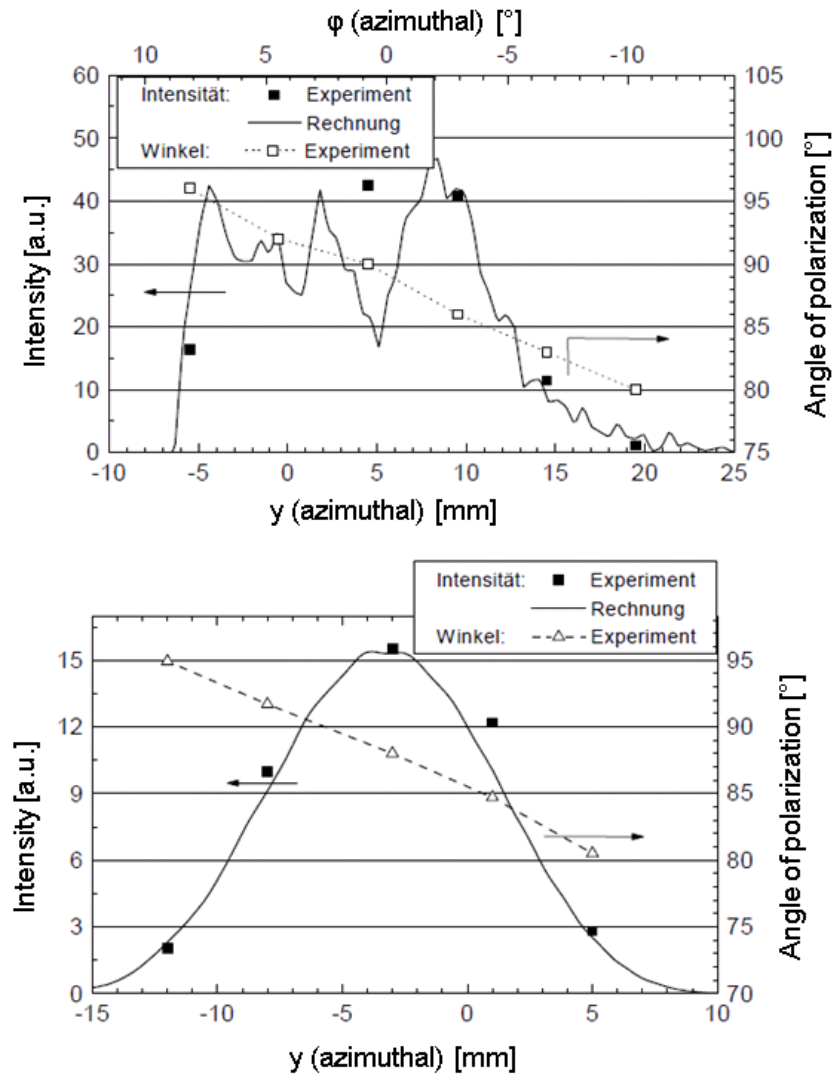


Figure 2.20 Polarization measurement across the beam. Top: unformatted beam; Bottom: formatted beam [4].

Figure 2.21 shows how a ring shaped beam (or a section thereof) is transformed via an axicon into a cylindrical beam. This transformation of the radiation field goes together with the transformation of the polarization. A purely azimuthal state of polarization is converted into a purely linear state of polarization.

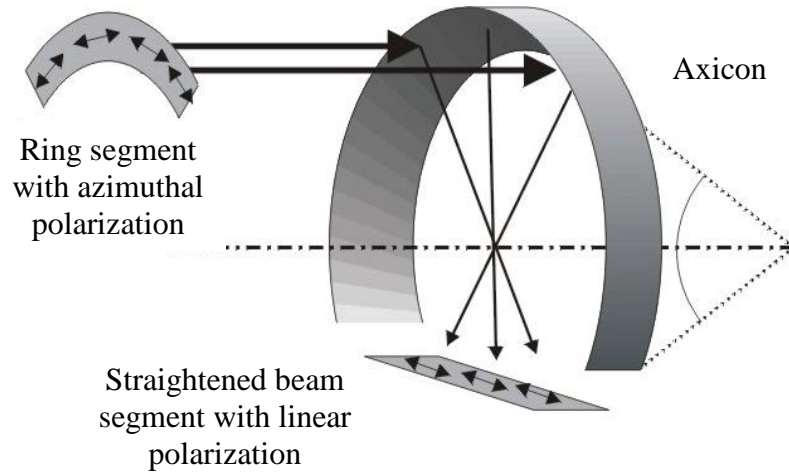


Figure 2.21 Transformation of an axial propagating field into a rectangular field with a focal line on the axicon axis and transformation of the polarization [4].

This effect can be used to correct the state of polarization of the beam extracted from the helix-axicon resonator. Anannev and others [64], [49] suggested accomplishing this transformation internal to the resonator. For the helix-axicon resonator, however, a transformation external to the resonator within the beam formatting telescope presents itself. Such an implementation is proposed in [65]. An axicon segment is used to transform a ring segment into a rectangle as shown in Figure 2.21. What is not considered in this solution is that the rotation of the azimuthal polarization (about 4°) cannot be corrected with this configuration. Therefore, a new concept is proposed in section 3.4.

2.8 Tools for Resonator Modelling

In this section three different modelling methods, which are used to investigate and optimize the properties of the helix-axicon resonator later on, are reviewed. The three different methods are: i) Geometrical optics (paraxial ray analysis) ii) Gaussian Beam Propagation (wave analysis) iii) Diffraction integral method. All three theories will be briefly discussed next.

2.8.1 Geometrical optics

Even though the paraxial ray analysis is not very accurate since it neglects the wave nature of the laser beam and diffraction effects, it can be useful to describe certain

properties of an optical system, such as the stability of an optical system or losses in an unstable resonator [66].

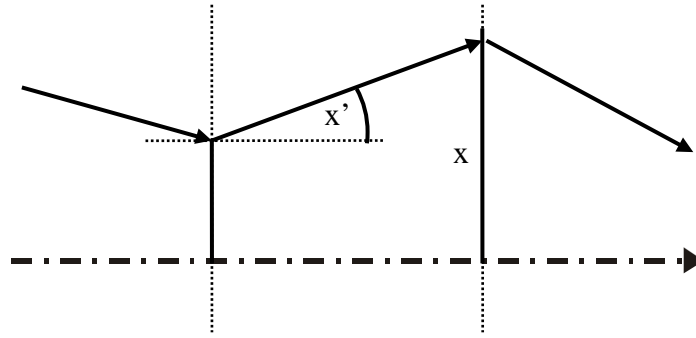


Figure 2.22 Paraxial ray propagation through a lens system.
 x : distance of ray to optical axis; x' : angle between ray and optical axis.

The propagation of paraxial rays through an optical system can be described by ray transfer matrices where the beam is characterized with its distance, X to the optical axis and its angle, X' in regards to it as defined in Figure 2.22. Ray transfer matrices are treated in detail in textbooks like [67], [68].

For paraxial rays the corresponding output quantities X_2 and X_2' are linearly dependent on the input quantities X_1 and X_1' as shown in Equation 2.8:

$$\begin{bmatrix} X_2 \\ X_2' \end{bmatrix} = \begin{bmatrix} A & B \\ C & D \end{bmatrix} \begin{bmatrix} X_1 \\ X_1' \end{bmatrix} \quad 2.8$$

The ABCD transfer matrix is related to the focal length, f and the distance between the principal planes of the optical system.

2.8.2 Gaussian beam propagation

Gaussian beam propagation takes the wave nature of the laser beams into account, but diffraction effects due to the finite size of apertures are neglected. This method is suitable for optical systems with relatively large apertures that truncate only negligible amounts of the beams.

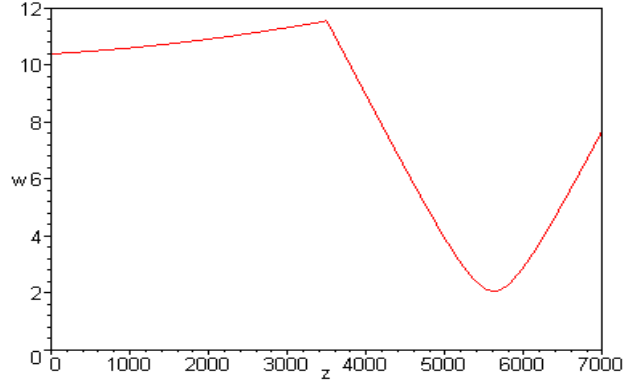


Figure 2.23 *Gaussian beam propagation: Paraxial ray propagation through a lens located at $z = 3500$ and forming a focus at $z \approx 5500$.*

The beam propagation inside a stable resonator can be modelled with the Gaussian beam propagation. It requires very little computational effort and provides a good general understanding of the beam size of the fundamental mode inside the resonator. For instance, the required inter-electrode gap size required for the helix-axicon resonator for fundamental mode operation can be calculated for a given resonator set-up if the optical resonator length, L and the g-parameters g_1 and g_2 are known. R_1 and R_2 represent the radius of curvature of the two resonator mirrors. ω_0 represents the beam radius at the waist, ω_1 and ω_2 represent the beam radii at the mirrors. The equations to calculate the waist size and beam sizes on the mirrors can be found in [69]:

$$\omega_0^2 = \frac{L\lambda}{\pi} \sqrt{\frac{g_1 g_2 (1 - g_1 g_2)}{(g_1 + g_2 - 2g_1 g_2)^2}} \quad 2.9$$

$$\omega_1^2 = \frac{L\lambda}{\pi} \sqrt{\frac{g_2}{g_1(1 - g_1 g_2)}} \quad 2.10$$

$$\omega_2^2 = \frac{L\lambda}{\pi} \sqrt{\frac{g_1}{g_2(1 - g_1 g_2)}} \quad 2.11$$

with

$$g_1 = 1 - \frac{L}{R_1}; \quad g_2 = 1 - \frac{L}{R_2} \quad 2.12$$

The free-space propagation of a laser beam can be simulated with Gaussian beam propagation, too. The equations and how they are derived can be found in any laser text book. The most widely used equations are the ones used to calculate the beam radius and the radius of curvature of the wave front as a function of the z position for the fundamental mode:

$$\omega^2(z) = \omega_0^2 \left[1 + \left(\frac{\lambda z}{\pi \omega_0^2} \right)^2 \right] \quad 2.13$$

$$R(z) = z \left[1 + \left(\frac{\pi \omega_0^2}{\lambda z} \right)^2 \right] \quad 2.14$$

The envelope of the beam is hyperbolic with asymptotes inclined to the axis at an angle of:

$$\theta = \frac{\lambda}{\pi \omega_0} \quad 2.15$$

This angle, θ is the far-field diffraction angle of the fundamental mode where at every given distance the beam intensity profile has a Gaussian shape.

The equations are simple for the fundamental mode. Even though some of them can be modified for higher order modes by replacing the wavelength, λ with the scaled wavelength, $M^2\lambda$ where M^2 is the beam quality of the laser, the equations become more complicated for higher order modes. The higher order modes can be described either in a Cartesian (x, y, z) or cylindrical (r, ϕ, z) coordinate system. In the Cartesian coordinate system the modes are described by the Hermite polynomials. The cylindrical coordinate system uses Laguerre polynomials. Some low order Hermite and Laguerre polynomials are listed in Table 2.2.

Low order Hermite polynomials	Low order Laguerre polynomials
$H_0(x) = 1$	$L_0^1(x) = 1$
$H_1(x) = x$	$L_1^1(x) = 1 + 1 - x$
$H_2(x) = 4x^2 - 2$	$L_2^1(x) = \frac{1}{2}(1 + 1)(1 + 2) - (1 + 2)x + \frac{1}{2}x^2$
$H_3(x) = 8x^3 - 12x$	

Table 2.2 Low order Hermite and Laguerre polynomials.

2.8.3 Diffraction integral method

The diffraction integral method takes into account both the wave nature of the laser beam and diffraction effects due to finite apertures. Optical systems with finite apertures are lossy and an electromagnetic field decays unless energy is supplied. This energy is supplied by the active medium in a laser. A method to compute the modes in a resonator with an active saturable gain medium was developed by Fox and Li [70], [71].

Analogous to what happens in a real resonator a field that is random at first is propagated back and forth between the resonator mirrors until it converges to a static field distribution. Diffraction losses, gain, mirror geometries and reflectivity, and outcoupling losses are considered during each iteration. The numerical calculation is usually performed with a computer program. The calculation is based on the Fresnel-Kirchhoff formulation of Huygens' principle. It is assumed that the dimensions of the resonator are large compared to the wavelength and the field is substantially transverse electromagnetic [72]. Since the mirror distance is large compared to the mirror size two linear states of polarization can be calculated and super positioned. The maximum laser power, P_{Lmax} that can be extracted from the laser medium is given by the volume integral of the product of small signal gain, g_0 and saturation intensity, I_0 . [69]. The ratio of the extracted laser power P_L and P_{Lmax} is the resonator extraction efficiency, η which is together with the beam quality one of the most important outputs of this simulation.

$$P_{Lmax} = \int_V g_0(\vec{r}) I_0(\vec{r}) \vec{dr} \quad 2.16$$

2.8.4 Diffraction integral method model for the helix-axicon resonator

The model used in the following chapters is created with a software package called OPT [73]. It uses the Fox and Li method to calculate the resonator properties as discussed above.

Figure 2.24 shows the conceptual set-up of the helix-axicon resonator in the model. All elements of the resonator such as mirrors, apertures and the gain medium etc are defined on grids. The grids are discrete elements and the radiation field is propagated from one grid to the next with propagators. In order to correctly represent the helix-axicon resonator in the model at least 5 Grids are needed.

- Grid 1: Axicon mirror
- Grid 2: Aperture of the electrodes on the axicon end
- Grid 3: Aperture in the centre of the electrodes
- Grid 4: Aperture of the electrodes on the helix end
- Grid 5: Helix mirror

The gain medium is represented with gain sheets which are located on grids 2, 3 and 4. The overall length of the gain sheets equals the electrode length. The gain sheet properties are defined by their small signal gain, saturation intensity and length.

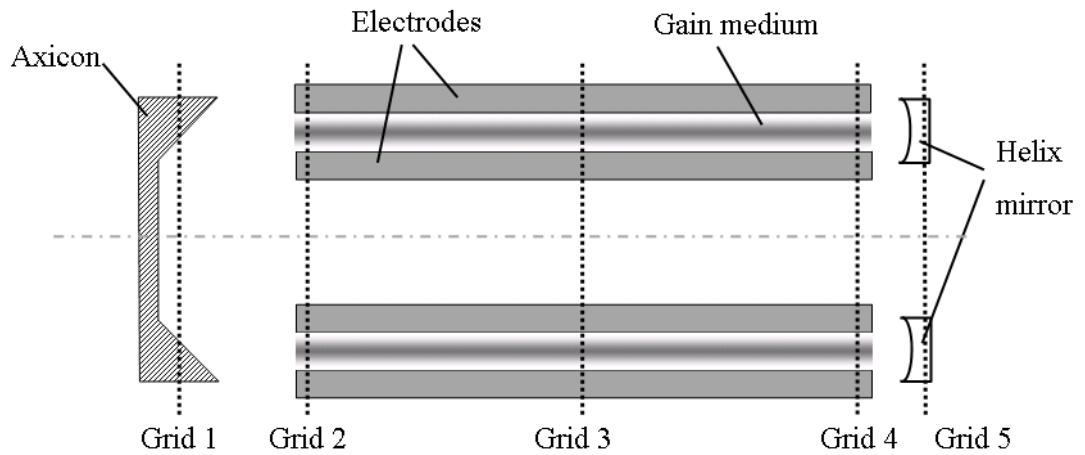


Figure 2.24 Schematic representation of the helix-axicon resonator in the model. Mirrors, apertures and the gain medium are defined on grids.

The short distance between the electrode ends and the mirrors makes the propagation between them extremely difficult since the grid size needs to be ten times larger than the

Fresnel number. Such large grid sizes make this calculation, even with today's fast computers, unpractical. For this reason the mirrors are defined on the same grids as the electrode ends reducing the number of grids from five to three. With this simplification the distance between the mirrors and the electrode ends is neglected. The resonator length is further reduced in the model since OPT does not take into account the beam propagation inside the axicon. The beam is switched from one side of the axicon to the other by a coordinate transformation. The phase is shifted, but the propagation length is neglected and therefore properties like the beam diameters and the radius of curvature of the wave front stay unchanged. This is a good approximation for resonators with a small diameter, but it creates less exact results with increasing resonator diameters.

There is another difference between the model and a real laser: Diffraction created by the finite apertures inside the resonator is not confined inside the model. If the propagation angles of the diffracted radiation are too large the radiation leaves the grids and is lost whereas the electrodes in a real laser trap it inside the resonator. This can lead to large discrepancies between simulation and real laser set-ups as shown in section 3.2.

The most relevant input parameters for the model together with typical values for them are listed in Table 2.3. Unless stated otherwise, the radius of curvature on the axicon mirror (ROC_{axicon}) is $2 \cdot \sqrt{2} \cdot ROC_{helix}$.

Parameter	Value
Slope type on helix mirror	Linear
Slope	$c = 4 \text{ } \mu\text{m/rad}$
ROC_{helix}	1.2 .. 2.4 m
ROC_{axicon}	$2 \cdot \sqrt{2} \text{ } ROC_{helix}$
Resonator length	1 m
Propagators	500 mm & 500 mm
Gain sheet length	300 mm / 400 mm / 300 mm

Table 2.3 *Input parameters for the diffraction integral method model of the helix-axicon resonator.*

Electrode materials and gas chemistry effects are not considered in the model. Gas mix, gas pressure and temperatures are indirectly considered in the properties of the gain sheets.

2.9 Special Resonators

As mentioned above, paraxial ray propagation can be used to investigate the stability of an optical system, such as an optical resonator. A laser beam propagating back and forth between the two mirrors of a resonator can also be described by a periodic system of focusing lenses. The ray transfer through n consecutive elements is described by the n^{th} power of the transfer matrix and can be evaluated by means of Sylvester's theorem [72]:

$$\begin{vmatrix} A & B \\ C & D \end{vmatrix}^n = \frac{1}{\sin \theta} \cdot \begin{vmatrix} A \sin n\theta - \sin(n-1)\theta & B \sin n\theta \\ C \sin n\theta & D \sin n\theta - \sin(n-1)\theta \end{vmatrix} \quad 2.17$$

where

$$\cos \theta = \frac{1}{2}(A + D) \text{ and } \sin \theta = \sqrt{1 - \frac{1}{4}(A + D)^2} \quad 2.18$$

A periodic optical system can be classified as either stable or unstable. It is stable when the trace $(A+D)$ obeys the inequality

$$-1 < \frac{1}{2}(A + D) < 1 \quad 2.19$$

so that the rays are focused periodically. For unstable systems, the trigonometric functions in that equation become hyperbolic indicating that the rays become more and more dispersed the further they pass through the sequence.

A laser resonator with spherical mirrors of equal curvature is a typical example of a periodic sequence that can either be stable or unstable [66]. The ray path through the optical system is folded in case of the resonator and unfolded in case of the periodic lens system. The focal length of the lenses is the same as the focal length of the resonator

mirrors ($f_1 = R_1/2$; $f_2 = R_2/2$), and the spacing, L of the lenses is the same as the spacing of the resonator mirrors. The stability condition can now be written as [72]:

$$0 < \left(1 - \frac{L}{R_1}\right) \left(1 - \frac{L}{R_2}\right) < 1 \quad 2.20$$

with $g_1 \equiv 1 - L/R_1$ and $g_2 \equiv 1 - L/R_2$.

With the knowledge of g_1 and g_2 each resonator can be plotted in the Stability Diagram shown in Figure 2.25.

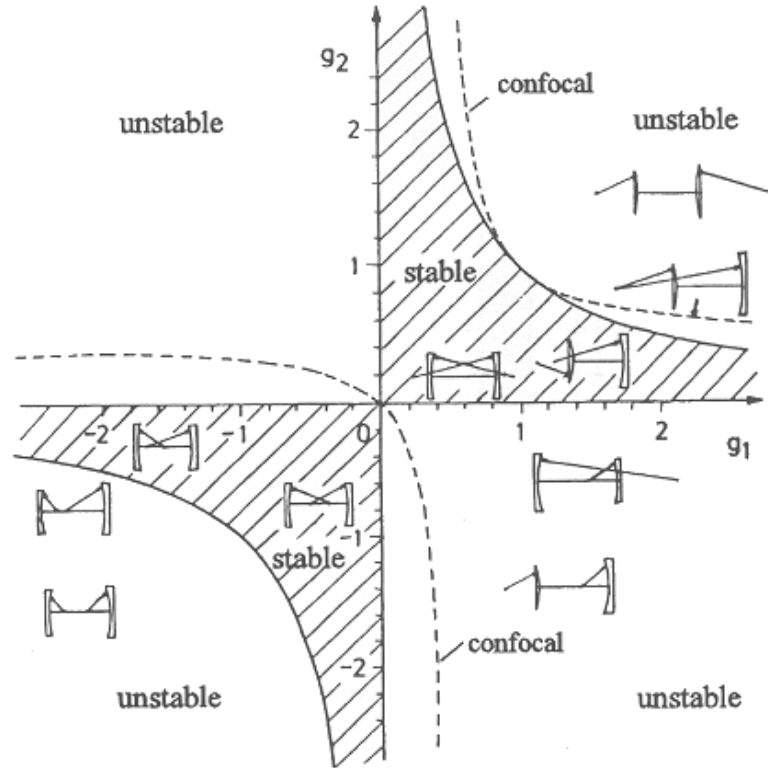


Figure 2.25 Stability diagram for a resonator with spherical mirrors.

Within the stability diagram a few special resonators can be found which will be relevant in chapter 3.

In the planar configuration the ROC of the mirrors is ∞ and $g_1 = g_2 = 1$. At this point and beyond the Gaussian theory fails. Planar and long-radius resonators have a large mode volume and utilize the gain medium well. Nevertheless, they are to be avoided since the alignment is very difficult. Also the production and mounting of the mirrors is difficult.

Manufacturing tolerances and mirror deformations due to the thermal load or mounting forces can be of the same order of magnitude as the contour (sag) on the mirrors.

The near-concentric configuration, for which the resonator length, L is less than the sum of the radii of the two resonator mirrors by ΔL , sits right at the edge of the stability diagram where $g_1 = g_2 = -1 + \Delta L/R$. It can produce large beam diameters on the mirrors in conjunction with very small waist sizes. With $R \approx L/2$ the mirror centres of curvatures are very close to each other in the middle of the resonator and small tilts of the mirrors result in large misalignments of the optical axis [69].

In the symmetric confocal configuration g_1 and g_2 equal zero. The focal points of the two mirrors coincide in the centre of the resonator ($R_1 = R_2 = L$) and the mirrors are spaced by exactly two Rayleigh lengths. The confocal resonator has the overall smallest average beam diameter along its length of any stable resonator [69]. Other resonator configurations can generate smaller waist diameters, but smaller waist diameters also result in larger diameters on the mirrors. The confocal resonator has a minimum alignment sensitivity since a tilt of one of the mirrors leaves the centre of curvature of the mirror on the surface of the other ($R = L$) and merely displaces the optical axis of the resonator by a small amount. In order to operate the resonator in fundamental mode only, good mode control is needed since the small average mode size is not efficient in utilizing gain mediums that are larger than the mode volume of the fundamental mode. The confocal resonator is only stable in the symmetric configuration. For all asymmetric combinations, the resonator is unstable. There is a second stable confocal resonator configuration for $g_1 = g_2 = 1$. In this case the focal points coincide at infinity and we have a planar resonator.

Chapter 3

3 Annular Laser Resonator Configuration

3.1 Introduction

Cutting of metals is an important industrial application for lasers, which impose demanding requirements on the properties of the laser beam. The laser power level and its stability, the beam spatial distribution and its stability and the beam polarization are all critical parameters, which impact the efficiency of the cutting process. In order to achieve good cutting performance the optical resonator must be carefully designed so as to achieve suitable values for these parameters. The brightness, B is a very useful measure of (both) the power and focusability of a laser beam and is defined as the power emitted per unit surface area per unit solid angle. The M^2 parameter is a measure of the beam quality, but the brightness, B is a crucial parameter since it defines the maximum intensity that can be achieved at the work piece, and can be expressed as:

$$B \cong \frac{P_L}{M_x^2 \times M_y^2 \times \lambda^2} \quad 3.1$$

where M_x^2 and M_y^2 are the beam quality factors for the two principal axes of the laser beam and λ is the wavelength.

Mode and mode stability are also critical since they define the intensity distribution at the work piece temporally and spatially. It has been recognised for many years that in order to obtain uniform, non-directional cutting results the intensity distribution must be rotationally symmetric. Also, the existence of any additional rings around the central lobe in the beam pattern causes interference with the cutting process and limits performance with regard to speed and/or quality. Moreover, asymmetric features in the mode profile limit cutting performance and reduce cut quality.

In order to obtain non-directional cutting performance, not only must the mode and intensity distribution be rotationally symmetric, but also the effective absorption in the metal must be constant for all directions. This requirement can be achieved if the state of laser beam polarization is such that the beam is absorbed equally for all cutting directions. Most state-of-the-art laser metal cutting systems achieve this requirement by the utilisation of circular polarization, which ensures uniform absorption. A circularly polarized beam is most commonly generated by converting the linear state of polarization emitted by the laser itself into circular polarization with a phase shifter positioned in the beam delivery system. Polarization issues are discussed in more detail in section 3.4.

Even though annular resonators with helical mirrors have been previously investigated by Ehrlichmann [52] and Schulz [4], none of the previously known annular resonator designs have been able to meet all laser beam requirements for efficient cutting performance. Thus the helix-torus resonator reported in [52] only meets the power level requirements for processing of metals, while power stability, beam spatial distribution and its stability and the beam polarization requirements are not met. In fact, the helix-torus resonator has no polarization defining element and therefore the polarization is unstable and fluctuates between azimuthal and radial states. Moreover, the short resonator length of about 1m (and therefore large longitudinal mode spacing) causes laser power fluctuations in the range of 10 - 15% due to scanning of the longitudinal mode signature when the mechanical resonator structure expands [74]. Both these problems (instability in power and polarisation) were resolved by the introduction of the helix-axicon resonator described in [4]. The replacement of the torus mirror with an axicon mirror more than doubles the resonator length and thereby reduces the power fluctuations. Also, since the reflectivity in the axicon is slightly different for s- and p-polarization, the helix-axicon resonator emits a beam with stable azimuthal polarization. However, the beam quality (mode and mode stability) is inadequate and therefore the brightness requirements are not met by this resonator design.

Resolving these key beam issues was identified as a major task for the present work, and in this chapter, mode stability and brightness issues are investigated and a new configuration of the stable-unstable-hybrid resonator based on the helix-axicon resonator is defined. In section 3.2 issues relating to the stable (or radial) direction of the resonator

are addressed, while in 3.3 those relating to the unstable (or azimuthal) direction are considered. Polarization is treated in 3.4.

3.2 Radial Direction

In the previous work on annular resonators for high power lasers, both Ehrlichmann [52] and Schulz [4], used the Fresnel number, N_f as the main design parameter for the stable direction of the resonator to ensure fundamental mode operation. As predicted by laser beam theory [69], fundamental mode operation is achieved by choosing a combination of resonator length, L and inter-electrode gap size, d ($2a$) yielding Fresnel numbers $N_f < 1$ for a specific wavelength, λ as follows:

$$N_f \equiv \frac{a^2}{L\lambda} \quad 3.2$$

The resonator Fresnel number is a measure of the order of transverse modes that ‘fit’ into the resonator before higher order modes are significantly truncated by the aperture edges [69]. Depending on the magnitude of the g -parameters of the resonator, the resonator Fresnel number needs to be more or less below unity to ensure operation in the fundamental mode [69]. Table 3.1 shows the calculated Fresnel numbers for three different inter-electrode gap sizes and a resonator length of 1 m. The inter-electrode gap sizes are constant over the entire length of the electrodes (constant gap) and the configurations are typical of the work presented by Schulz [4].

Inter-electrode gap size [mm]	Fresnel number N_f
6.0	0.85
6.5	1.00
7.0	1.16

Table 3.1 Fresnel numbers for three different inter-electrode gap sizes for a 1 m long resonator at a wavelength of 10.6 μm .

The exact transverse modes for these configurations can only be calculated numerically, by using for instance, the Fox and Li method (see section 2.8.3). Figure 3.1 shows the simulated, resonator internal intensity distribution for three different inter-electrode gap

sizes. The simulations of the resonator modes are carried out in OPT for a resonator length of 1 m, an electrode radius of 77.5 mm and a ROC of 2 m. For each configuration the internal intensity distribution is plotted in two sections, from 0 - 180° and 181 - 360°, and two views are shown, namely a colour plot with the colours representing the intensity and a cut through the azimuthal direction. The results obtained here are identical with the results presented in [4]. With increasing inter-electrode gap size there is a transition from the fundamental mode (Figure 3.1 top) to a mix of higher order modes (Figure 3.1 middle), and then to a mix of higher order modes with two maxima (Figure 3.1 bottom) in the intensity distribution in the stable direction of the resonator. This indicates that the beam quality becomes progressively worse as the electrode separation (aperture) becomes larger.

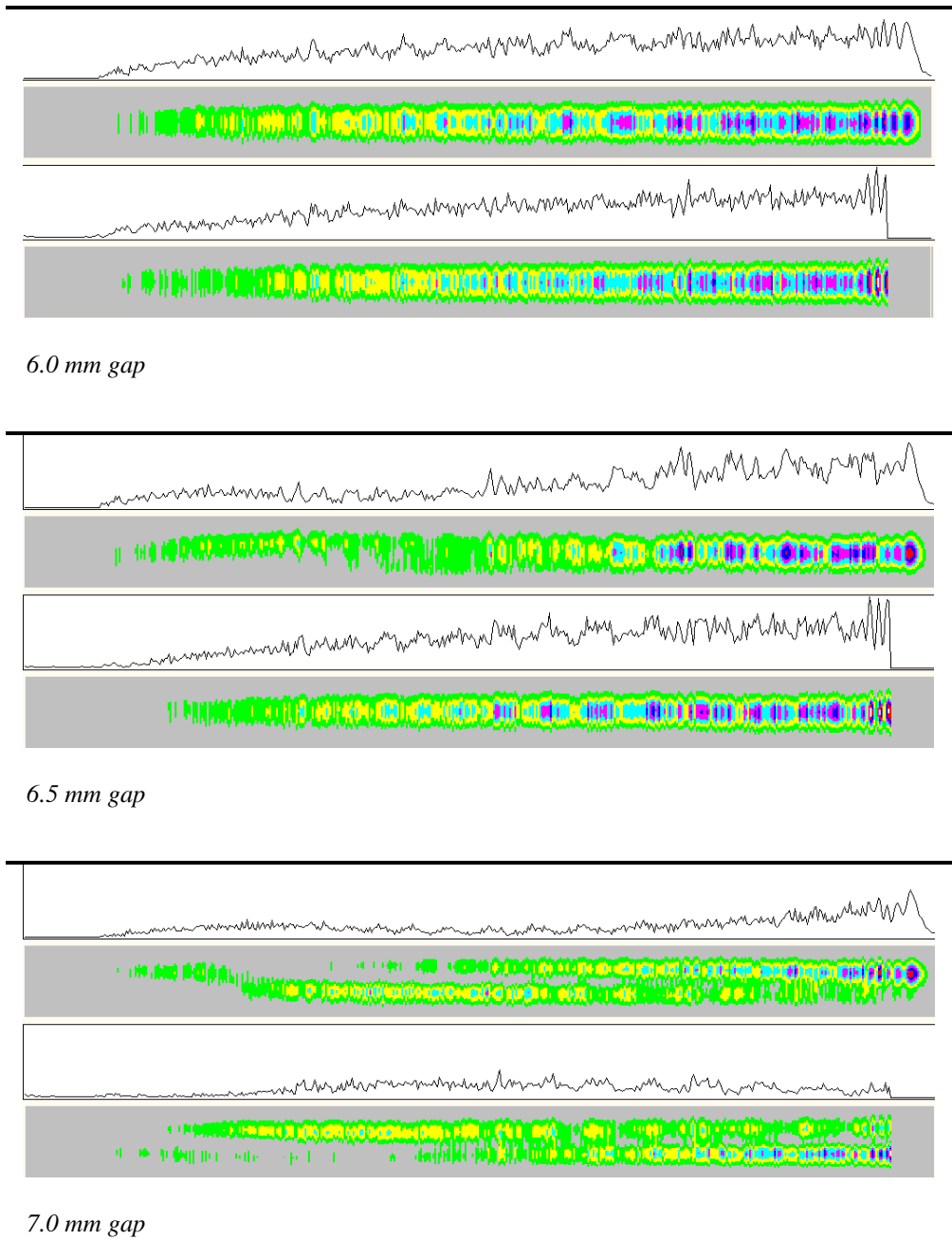


Figure 3.1: Simulated intensity distributions inside the optical resonator for three different inter-electrode gap sizes (6.0 mm, 6.5 mm and 7.0 mm). For each configuration the internal intensity distribution is plotted in two sections, from 0 - 180° and 181 - 360°, and two views are shown, a colour plot with the colours representing the intensity and a cut through the azimuthal direction. The inter-electrode gap is constant over the entire length of the electrodes; the ROC of the mirrors is 2 m; the distance between the mirrors is 1 m; the electrode radius is 77.5 mm.

After testing these three configurations in the lab, it was clear that the criterion that the Fresnel number should be less than unity to ensure fundamental mode operation is a necessary but not a *sufficient* condition for the generation of a diffraction-limited, high brightness beam. Figure 3.2 shows the beam intensity distributions in the stable direction

measured at a distance of 1 m from the output-coupling window for the 6.0, 6.5 and 7.0 mm inter-electrode gap size configurations. Even though the Fresnel number of the 6 mm configuration is 0.85 (i.e. < 1) and the intensity distribution shown in Figure 3.1 suggests a single lobe somewhat similar to fundamental mode operation, Figure 3.2a shows an intensity distribution that differs significantly from the expected Gaussian shape of the TEM_{00} fundamental mode. The main differences observed are the ‘broad pedestals’ in the diffraction pattern surrounding the main peak.

These broad pedestals in the diffraction patterns do not appear in the OPT simulations, because the diffraction effects created by the finite apertures are not contained inside the resonator in the simulation and are lost (see section 2.8.4). The intensity distributions in Figure 3.2b and c, though they are not perfect, do provide a better match to the simulation results given in Figure 3.1. In these cases, almost no edge-diffraction is present, but in any case since the Fresnel numbers are larger (1.0 and 1.16 for the 6.5 mm and 7.0 mm gap respectively), the resonator is not expected to operate in the fundamental mode and the beam quality is correspondingly reduced (M^2 is larger).

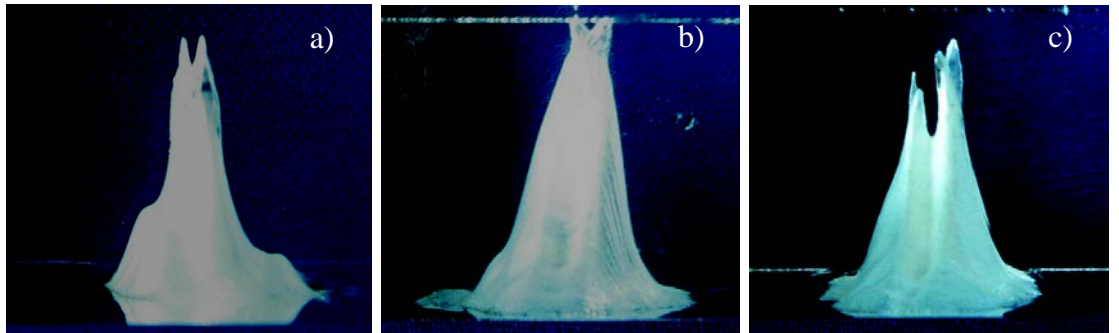


Figure 3.2 Intensity distribution of the unformatted beam at 1 m distance from the outcoupling window. a) for a 6.0 mm inter-electrode gap b) for a 6.5 mm inter-electrode gap c) for a 7.0 mm inter-electrode gap.

3.2.1 Optimization of constant gap configurations

In the previous section, the configurations employed differed in terms of the inter-electrode gap sizes, but used a mirror of fixed ROC of 2.0 m and an inter-electrode gap that is constant along the entire electrode length (see Figure 3.3). It is clear that none of these configurations produces an ideal diffraction-limited beam. Although the configuration with an inter-electrode gap size of 6.0 mm has a Fresnel number < 1 (thereby ‘obeying’ the rule-of-thumb for fundamental mode operation), the beam profile

shows significant deviation from the expected Gaussian intensity distribution. Moreover, the configurations with larger inter-electrode gap sizes, 6.5 mm and 7.0 mm, have Fresnel numbers that are certainly too large to ensure fundamental mode operation in combination with the chosen ROCs of the optical resonator.

As stated above, depending on the resonator g-parameters, the ‘rule-of-thumb’ is that the resonator Fresnel number should be slightly below unity to ensure fundamental mode operation [69]. In order to see whether it is possible to obtain fundamental mode operation with a minimum of high order diffraction effects, without a re-design of the overall physical structure, a simulation experiment was conducted to investigate the effect of varying the ROC on the helix and axicon mirrors using the OPT software for a 6.0 mm and 6.5 mm inter-electrode constant gap electrode system, and for the parameters shown in Table 3.2. The simulation was used to evaluate the resonator extraction efficiency, η and the beam quality parameter, M^2 as measures of laser power and beam quality. The results are shown in Figure 3.4 and Figure 3.5.

Slope type on helix mirror	Linear
Slope	$c = 4 \text{ } \mu\text{m/rad}$
$\text{ROC}_{\text{helix}}$	1.4 .. 3.0 m
$\text{ROC}_{\text{axicon}}$	$2 \cdot \sqrt{2} \text{ ROC}_{\text{helix}}$
Resonator length	1 m
Electrode diameter	155 mm
Propagators	500 mm & 500 mm

Table 3.2 Parameters for OPT simulation.

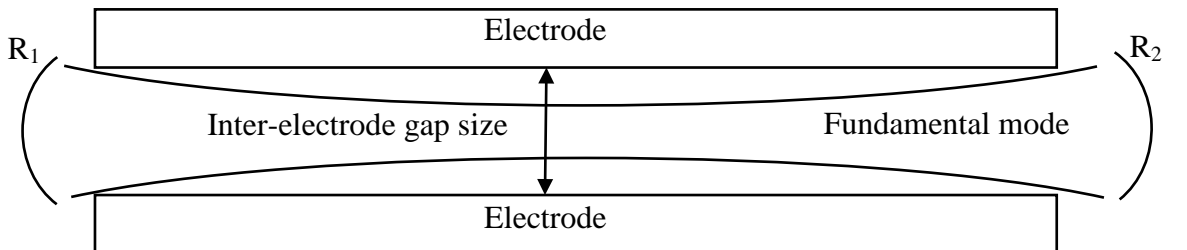


Figure 3.3 Schematic representation of one leg of the resonator in the stable direction with a constant gap electrode configuration.

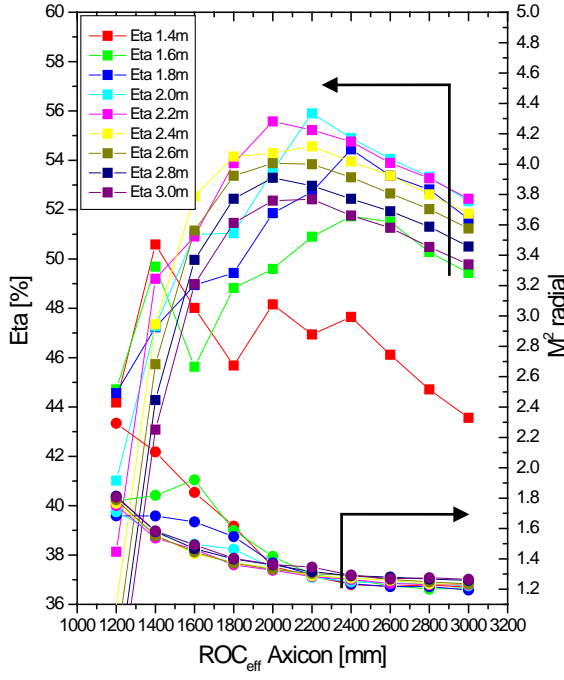


Figure 3.4 Beam quality and resonator efficiency for a 6.0 mm constant gap ($N_F = 0.85$) for different mirror combinations and a linear slope.

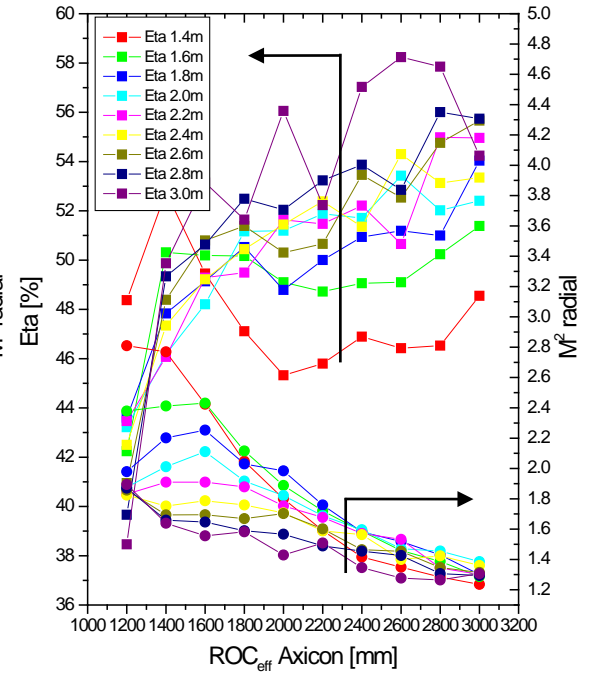


Figure 3.5 Beam quality and resonator efficiency for a 6.5 mm constant gap ($N_F = 1$) for different mirror configurations and a linear slope.

Figure 3.4 and Figure 3.5 show plots of the predicted beam quality (circles) and resonator extraction efficiency (squares) versus the radius of curvature of the axicon mirror for ROCs of the helix mirror from 1.4 to 3.0 m (represented by the different colours). As expected, symmetrical configurations give the best results in terms of extraction efficiency. With increasing ROC the extraction efficiency increases until the optimum ROC combination is reached, where the mode volume best matches the gain volume. As the ROC is increased beyond this optimum ROC combination, the mode volume exceeds the gain volume, whereupon the fundamental mode is too ‘large’ for the inter-electrode gap size, and the resonator extraction efficiency drops. Even though the extraction efficiency drops with further increasing ROCs the beam quality still increases. This confirms the well-known ‘conflict’ between achieving maximum extraction efficiency and best beam quality in electrode configurations with a constant gap.

Figure 3.6 and Figure 3.7 show the resonator internal intensity distribution for different mirror combinations for the 6.0 mm and 6.5 mm inter-electrode gap configurations respectively.

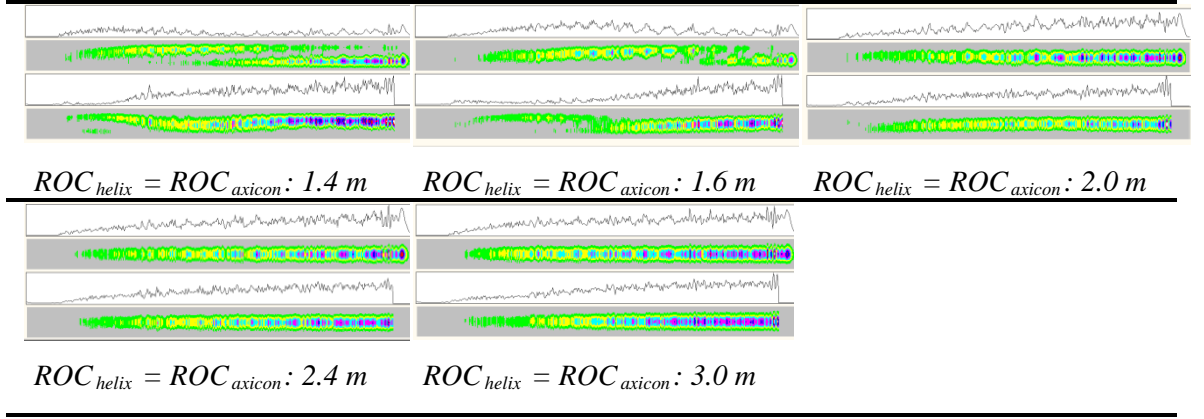


Figure 3.6 Resonator internal intensity distribution for a 6.0 mm constant gap configuration and different ROCs. For each configuration the internal intensity distribution is plotted in two sections, from 0 - 180° and 181 - 360°, and two views are shown, a colour plot with the colours representing the intensity and a cut through the azimuthal direction.

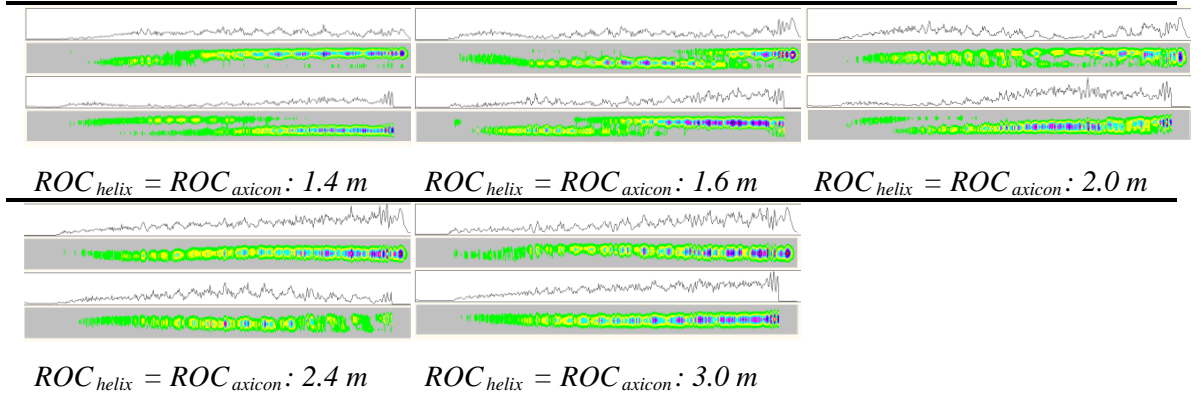


Figure 3.7 Resonator internal intensity distribution for a 6.5 mm constant gap configuration and different ROCs. For each configuration the internal intensity distribution is plotted in two sections, from 0 - 180° and 181 - 360°, and two views are shown, a colour plot with the colours representing the intensity and a cut through the azimuthal direction.

In general, the 6.0 mm and 6.5 mm constant gap configurations behave in a similar manner. Multimode operation results in low beam quality and low extraction efficiencies for small ROCs, and for large ROCs they generate mode apertures that exceed the inter-electrode gap size.

The set-up based on a 6 mm gap seems to be very sensitive to small changes in gap size or ROC, and no plateau is observed where resonator extraction efficiency and beam quality remain constant over a small change in the value of the ROC. The set-up based on a 6.5 mm gap seems to be more forgiving and there is a clear plateau in the extraction efficiency for ROCs between 2.0 and 2.6 m. Nevertheless, in contrast with the simulation,

empirical results in the lab show that the laser based on the 6.5 mm gap and a ROC of 2.4 m is very sensitive to resonator mis-alignment in spite of the wide plateau shown in Figure 3.5.

In summary, it can be stated that there are two main problems with the constant inter-electrode gap configurations:

- If the inter-electrode gap size is chosen to fit the fundamental mode size at the electrode ends, higher order modes are present due to a lack of mode discrimination.
- If the inter-electrode gap size is chosen to fit the fundamental mode size at the centre of the electrode, the fundamental mode aperture is too large at the ends of the electrodes resulting in unacceptable diffraction losses and diffraction patterns surrounding the main peak.

3.2.2 *Shaped electrodes for high brightness*

In section 3.2.1, laser configurations with a constant inter-electrode gap and different gap sizes were discussed. Since none of the configurations so far investigated yield acceptable performance, the use of a constant gap was abandoned. The new approach uses an inter-electrode gap shape that is shaped to be large enough at the ends to avoid diffraction, but small enough in the centre to discriminate higher order modes – in other words, ideally the gain volume should match the fundamental mode volume. Figure 3.8 shows a schematic representation of one leg of the stable direction of the resonator to visualize this. The shape of the electrode, and therefore the shape of the gain medium, matches the shape of the fundamental mode of the resonator.

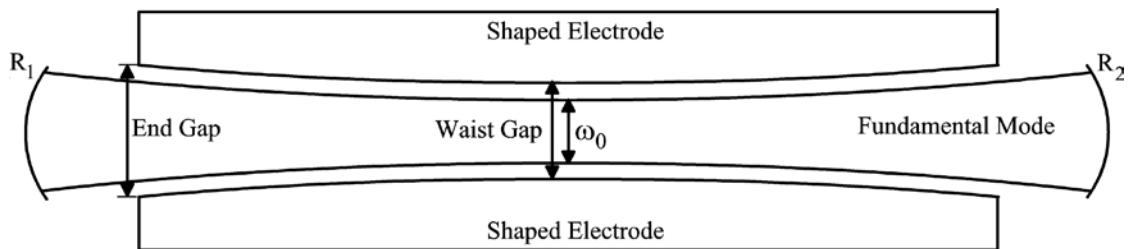


Figure 3.8 *Schematic representation of one leg of the resonator in the stable direction. The electrodes are shaped to provide a gain medium that matches the mode volume in shape.*

For a first approximation of the electrode shape Equations 2.10 to 2.12 are used to determine the inter-electrode gap size along the resonator length. In order to apply these equations to the stable direction of the helix-axicon resonator, a simpler, equivalent representation of the resonator is used: Since the axicon mirror is a folding mirror it can be represented by a lens in an unfolded version of the resonator as shown in [4]. The effective focal length, f_{eff} of this lens can be calculated with the equation for two compounded thin lenses. The focal lengths, f_1 and f_2 , are equal and given by the radius of curvature (ROC_{axicon}) in the radial direction of the axicon mirror and D is the diameter of the axicon mirror (distance between the two thin lenses).

$$\frac{1}{f_{eff}} = \frac{1}{f_1} + \frac{1}{f_2} - \frac{D}{f_1 f_2} \quad 3.3$$

with

$$f_1 = f_2 = \frac{ROC_{axicon}}{2} \quad 3.4$$

The beam size and shape in the left and right part of the unfolded resonator are symmetric, and therefore in the calculation it is only necessary to consider one-half of the resonator.

The effective resonator length, L_{eff} is the sum of the electrode length, L , the radius, $D/2$, of the resonator and the distance, x_1 and x_2 between mirrors and electrodes:

$$L_{eff} = L + \frac{D}{2} + x_1 + x_2 \quad 3.5$$

Figure 3.9 visualizes these simplifications of the resonator. The laser used in the laboratory has a discharge length of 1 m ($L = 1000$ mm). The distance between the mirrors and the electrodes are $x_1 = 29$ mm and $x_2 = 90$ mm respectively and the radius, $D/2$ of the laser is 77.5 mm. The value of the effective ROC_{axicon} is chosen so that the beam waist is located in the centre of the electrodes. The beam size along the electrodes for this configuration is shown in Figure 3.10 (top).

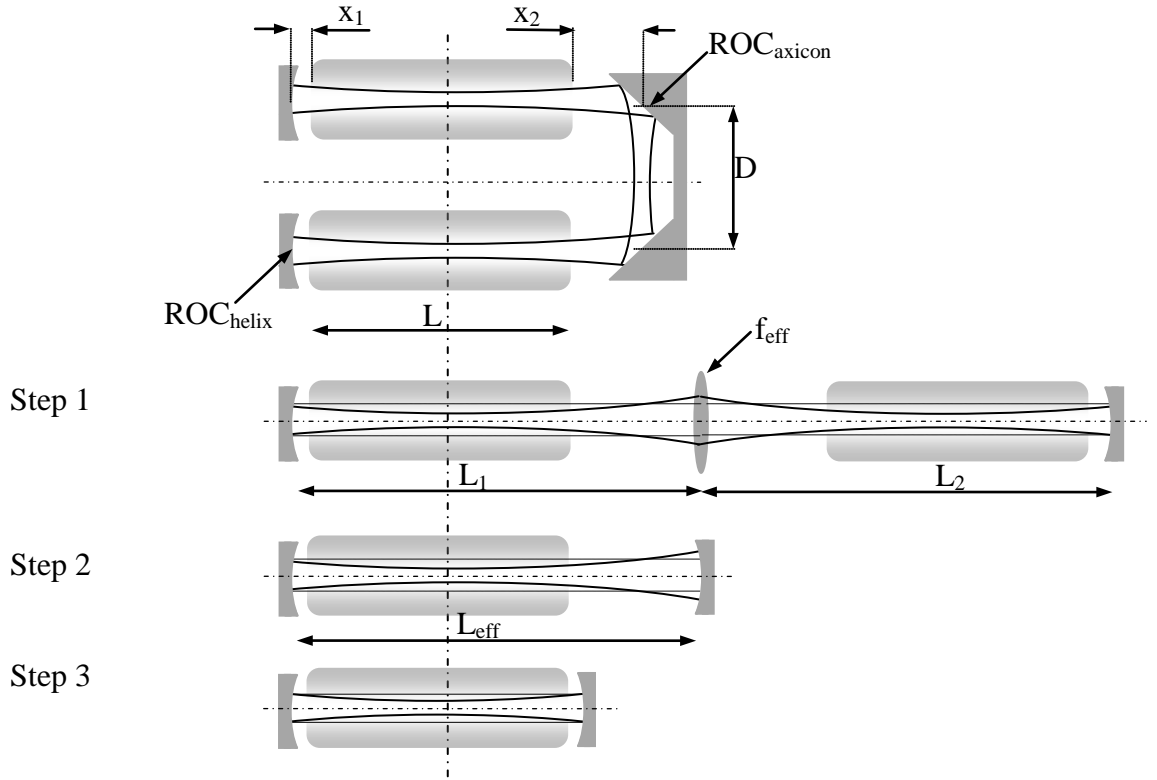


Figure 3.9 Step by step simplification of the helix-axicon resonator in the stable direction. Step 1: The axicon is represented with a lens ($f = f_{\text{eff}}$) and the resonator is unfolded; Step 2: One half of the resonator is removed since it is symmetrical around the lens. The lens is replaced again with a mirror; Step 3: The mirror is moved close to the electrodes.

The calculated inter-electrode gap size is 6.2 mm at the electrode ends and 5.4 mm in the centre. However, this result has limited value for several reasons. Not only does the simple Gaussian beam propagation calculation not consider the influence of apertures, in addition it takes no account of the azimuthal beam inclination due to the slope on the helix mirror. In order to factor in these effects the software package OPT has been used to produce a more accurate determination of the optimum inter-electrode gap size.

In order to reduce the complexity of the resonator model in OPT to a manageable level, simplifications are introduced. Since we are interested in the dimension of the inter-electrode gap size and not the beam diameter on the mirrors, the distance between the electrodes and mirrors is set to zero ($x_1 = x_2 = 0$), thereby reducing the number of propagations required between the different optical elements.

A basic understanding of the impact of this simplification can be obtained by applying Equations 2.10 to 2.12 to this simplified resonator configuration shown in Figure 3.9. x_1 and x_2 are set to zero and since the propagation inside the axicon is not considered in

OPT, the diameter, D is also set to zero. In order to keep the waist position of the beam in the centre of the electrodes the ROC_{axicon} must equal now $2 \cdot \sqrt{2} \cdot ROC_{helix}$ (see Step 3 in Figure 3.9). The resulting beam shape is shown in Figure 3.10 (bottom). The inter-electrode gap size is to a first approximation not affected by this simplification.

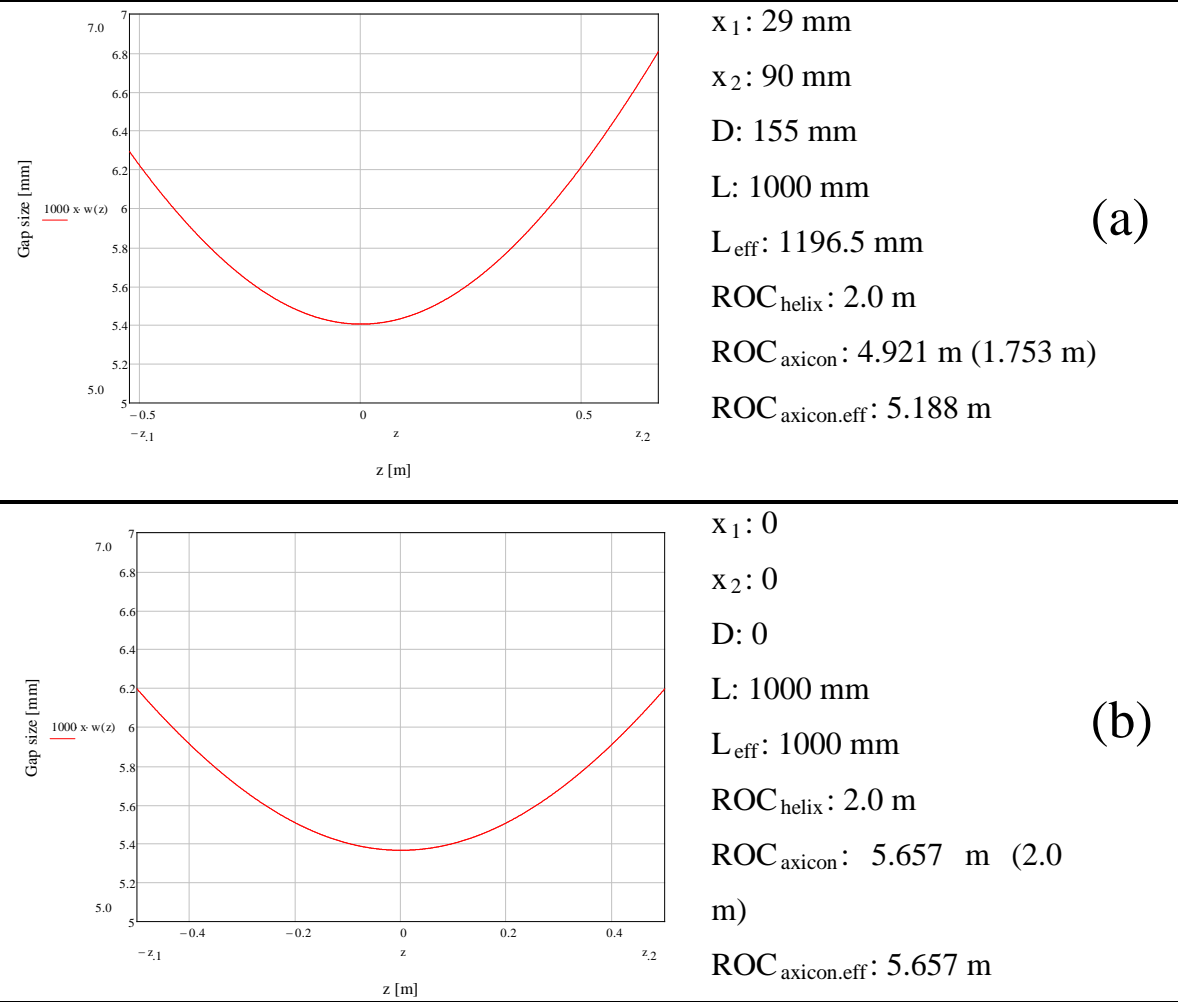


Figure 3.10 Predicted inter-electrode gap shape for the simplified resonator shown in Figure 3.9 along the length of the electrodes based on a simple Gaussian beam propagation calculation. (a) shows the original and (b) the simplified configuration where $x_1 = x_2 = D = 0$.

Table 3.3 shows the calculated gap sizes for the original (a) simplified (b) configuration based on Gaussian beam propagation. Both configurations yield the same inter-electrode gap sizes. The 100% beam diameter is represented by $\pi\omega$, the beam diameter on the helix mirror is $\pi\omega_{z1}$ and $\pi\omega_{z2}$ is the beam diameter on the axicon mirror. $\pi\omega_0$ is the waist beam diameter located at the centre of the electrodes and $\pi\omega_e$ represents the beam diameter at the ends of the electrodes.

	(a)	(b)
Beam diameter position	x_1 : 30 mm x_2 : 90 mm D: 155 mm	x_1 : 0 mm x_2 : 0 mm D: 0 mm
at helix: $\pi\omega_{z1}$	6.3 mm	6.2 mm
at axicon: $\pi\omega_{z2}$	6.8 mm	6.2 mm
at beam waist: $\pi\omega_0$	5.4 mm	5.4 mm
at electrode ends: $\pi\omega_e$	6.2 mm	6.2 mm

Table 3.3 A comparison of the beam diameters for the original (a) and simplified (b) resonator model shows that in a first approximation they are identical within the length of the electrodes.

OPT is now used for the verification of the inter-electrode gap size and shape using the parameters shown in Table 3.4. The inter-electrode gap size at the ends and in the centre are varied for a given set of resonator mirrors with $ROC_{helix} = 2.0$ m and $ROC_{axicon} = 5.657$ m. The end and centre gap sizes are varied from 5.6 to 7.6 mm and from 4.0 to 6.6 mm respectively. The resulting calculated extraction efficiencies and beam qualities are plotted in Figure 3.11.

The point where the losses start to increase, seen as reduced extraction efficiencies, is assumed to be the beam diameter, or the required inter-electrode gap size for fundamental mode operation.

Resonator length	1 m
$ROC_{helix} / ROC_{axicon}$	2 m / 5.657 m
Slope type	linear
Slope parameters	$c = 4 \mu\text{m/rad}$
Propagators	500 mm + 500 mm
Electrode diameter	155 mm

Table 3.4 Parameters for OPT simulation.

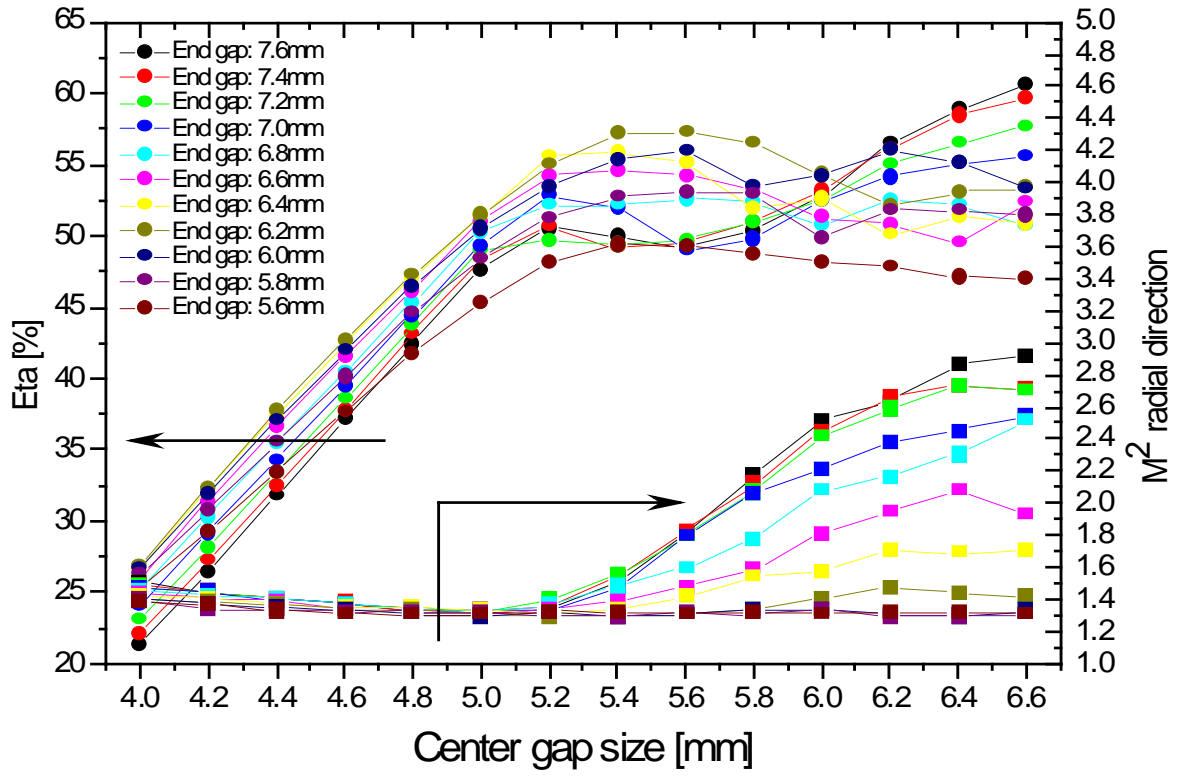


Figure 3.11 Optimization of the inter-electrode gap size for a ROC of 2.0 m / 5.657 m on the helix / axicon mirrors; slope: linear with $c = 4 \mu\text{m}/\text{rad}$. Plotted is the extraction efficiency, η and M^2 value for the radial direction versus the centre gap size. The different traces represent different electrode end gap sizes.

The optimum performance with regard to extraction efficiency and beam quality is achieved with an inter-electrode gap variation from 6.2 mm to 5.4 mm to 6.2 mm along the electrode length, which is the same inter-electrode gap size distribution as was predicted by the simple Gaussian beam propagation calculation.

Figure 3.12 shows the predicted resonator internal intensity distributions for different inter-electrode gap dimensions.

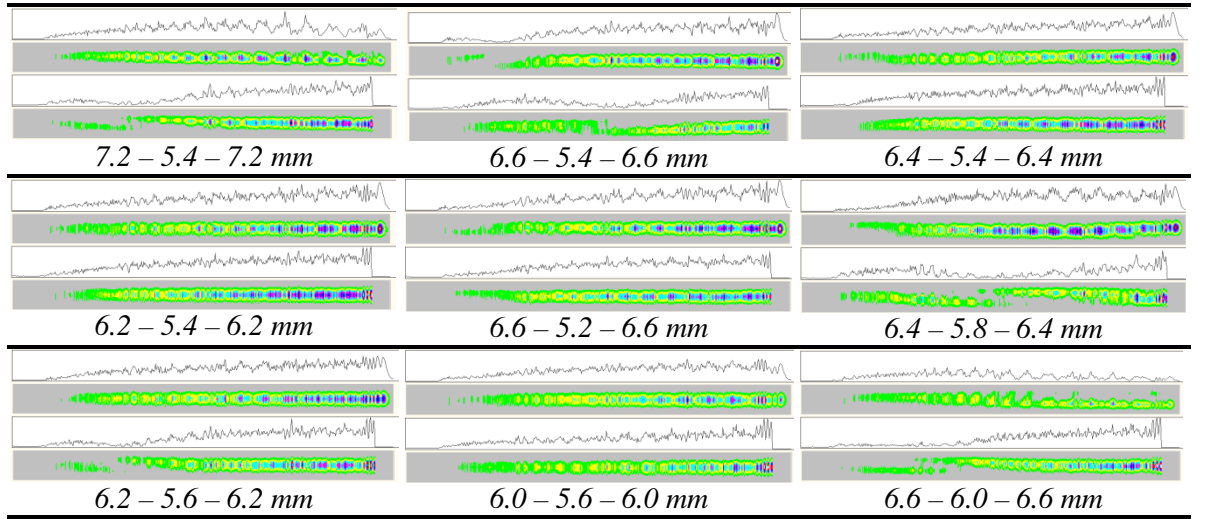


Figure 3.12 Resonator internal intensity distribution for different inter-electrode gap sizes. The ROC on the helix and axicon mirrors are 2.0 and 5.657 m respectively. For each configuration the internal intensity distribution is plotted in two sections, from 0 - 180° and 181 - 360°, and two views are shown, a colour plot with the colours representing the intensity and a cut through the azimuthal direction

The 6.2 - 5.4 - 6.2 mm gap produces the expected, straight intensity distribution with one maximum in the centre of the inter-electrode gap. For larger gap sizes, either at the electrode ends or centre or both, the intensity distribution does not remain centred in the gap.

3.2.3 Resonator alignment sensitivity

In section 2.8.1 the resonator stability diagram and a few special resonators were discussed. As a brief reminder their characteristics with regard to alignment sensitivity are restated here as described in the literature, for instance in [69]. Confocal resonators ($ROC = L$) are least sensitive to misalignment, near concentric resonators ($ROC = L/2$) are highly sensitive to misalignment, long-radius or planar resonators ($ROC \rightarrow \infty$) are to be avoided since the resonator alignment is very difficult.

In order to have symmetric electrode configurations only symmetric resonators are considered here. They lie along the 45° diagonal through the origin of the stability diagram (see Figure 2.25). For $g_1 = g_2 = 1$ the resonator is planar, for $g_1 = g_2 = 0$ confocal and concentric for $g_1 = g_2 = -1$.

When these configurations are discussed in text books the resonators have two optical elements, an output coupling mirror and a rear mirror, and the resonator length, L is

identical with the distance between the resonator mirrors. Table 3.5 shows the required ROCs to operate resonators in a confocal, near concentric and long-radius resonator configuration for a resonator length of 1000 mm.

	Confocal (ROC = L)	Long radius (ROC >> L)	Near concentric (ROC = L/2)
L [mm]	1,000	1,000	1,000
ΔL [mm]	-	-	50
ROC [mm]	1,000	18,000	550
g	0.0	0.94	-0.82

Table 3.5 Resonator g-parameters for a confocal, long radius and near concentric resonator. The radius of curvature (ROC) for the near concentric configuration is chosen so that $ROC = L/2 + \Delta L$.

If one would want to apply this classification of resonators to the helix-axicon resonator, the resonator length, L which represents the distance between output coupling and rear mirror in traditional two-mirror resonators, would have to be replaced with $2L$. This change is needed since the axicon mirror is only folding the resonator and the helix mirror is both output coupling and rear mirror at the same time. More specifically, one half acts as the output coupler and the second half as the rear mirror as discussed in section 2.5.1. In addition, the axicon acts as an optical element re-focusing the laser beam as it propagates back and forth between the two resonator mirrors. Resonators with additional optical elements, an internal lens for instance, were discussed in [75]. There, equivalent resonators with modified g-parameters are introduced in order to analyze the stability of these resonators. When the helix-axicon resonator is represented in an equivalent configuration as shown in Figure 3.9 step 1, then the resonator consists of the two resonator mirrors plus an internal lens. For a resonator with one additional internal lens the definition of the g-parameters changes to:

$$g_1 = 1 - \frac{L_2}{f} - \frac{L_0}{ROC_1} \quad 3.6$$

$$g_2 = 1 - \frac{L_1}{f} - \frac{L_0}{ROC_2}$$

where L_0 is defined as $L_1 + L_2 - (L_1 \cdot L_2 / f)$ and f is the focal length of the lens. L_1 and L_2 represent the distance between the mirrors and the internal lens. For a resonator with $L_1 = L_2 = 1$ m and a focal length, $f = ROC/2$ the g-parameters for five different

configurations are shown in Table 3.6. The resonator mirrors are symmetric and therefore $ROC_1 = ROC_2$. These five configurations represent special cases: The equivalent confocal resonator, the equivalent near concentric resonator, a long-radius configuration and the current helix-axicon resonator.

$L_{1,2}$ [m]	1.0	1.0	1.0	1.0	1.0
$ROC_{1,2}$ [m]	0.58	1.0	2.0	3.4	18.0
$g_{1,2}$	0	-1.0	-0.50	0	0.78

Table 3.6 *g-parameters for five symmetric resonators with an internal lens. L_1 and L_2 represent the distance between the mirrors and the internal lens. $ROC_{1,2}$ is the radius of curvature on the two resonator mirrors.*

Figure 3.13 compares the g-parameter values for a resonator with and without an internal lens. The resonator without internal lens has a length of 1 m; the resonator with internal lens has a distance between the mirrors and the lens, L_1 and L_2 of 1 m each and the focal length, f equals $ROC/2$.

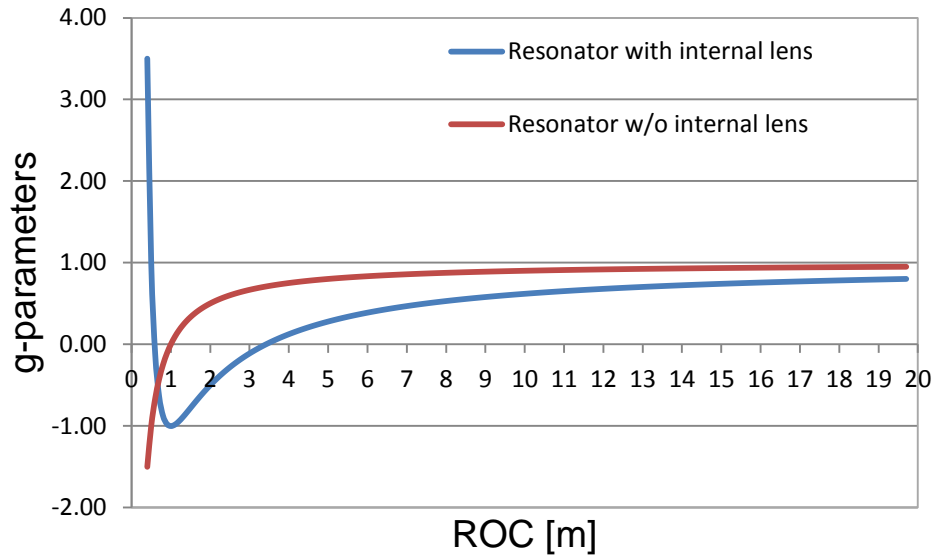


Figure 3.13 *g-parameters as a function of mirror radius of curvature for symmetric resonators with (blue) and without (red) an internal lens. The resonator without internal lens has a length of 1 m; the resonator with internal lens has a distance between the mirrors and the lens of 1 m each and the focal length, f equals $ROC/2$.*

The g-parameter trace in Figure 3.13 for the resonator without an internal lens crosses the abscissa only once while the trace for the resonator with an internal lens crosses it twice resulting in two ROC combinations that form a confocal configuration. Additionally,

there are some other interesting results. A mirror pair with a ROC of 1 m yields g-parameters of 0 in a standard resonator and g-parameters of -1 for a resonator with an internal lens ($f = 0.5$ m). A ROC of 0.5 m without and with a lens produces g-parameters of -1 and +1 respectively. The situation is similar for a ROC of 2.0 m. There the g-parameters are -0.5 and +0.5 for a resonator with and without a lens respectively.

In order to quantify the alignment sensitivity of the five different configurations the helix mirror is tilted around the X and Y axis in a simulation. In order to do that the inter-electrode gap size is optimized for fundamental mode operation first. The respective inter-electrode gap sizes are listed in Table 3.7.

ROC [m]	0.58	1.0	2.0	3.4	18.0
Gap size [mm]	7.0-2.8-7.0	7.4-3.8-7.4	6.5-5.7-6.5	8.0-6.3-8.0	9.6-9.0-9.6

Table 3.7 Inter-electrode gap sizes for fundamental mode operation with the corresponding ROC of the resonator mirrors.

Figure 3.14 shows the extraction efficiency versus mirror tilt for the five different configurations defined in Table 3.7. Here only the tilt around the X-axis is plotted since the result for a tilt around the Y-axis is closely similar.

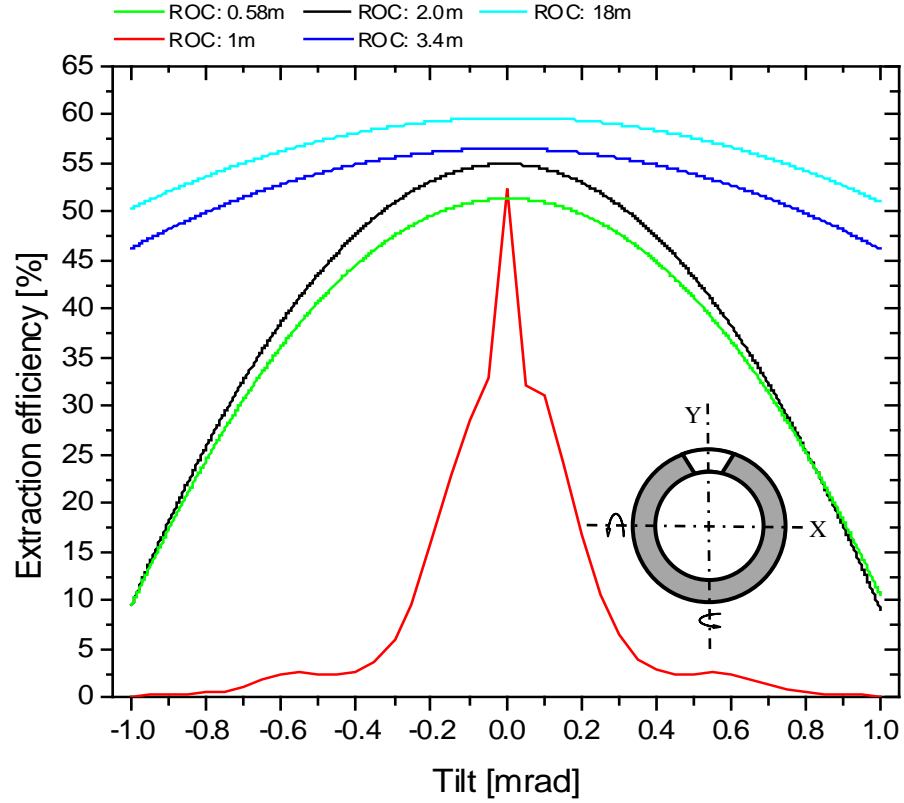


Figure 3.14 Resonator extraction efficiency versus tilt angle of the helix mirror around the X-axis. The variation for the tilt angle about the Y-axis looks closely similar.

The results of the tilt analysis in Figure 3.14 are not quite consistent with the expectations based on the g-parameter calculations with the equivalent resonator model. The long-radius resonator has g-parameters close to 1 but is least sensitive to misalignment. The configuration with a ROC of 1 m and g-parameters of -1 is highly sensitive to misalignment and in line with expectations based on the g-parameter values. The two configurations with $g = 0$ ($ROC = 3.4$ m and $ROC = 0.58$ m) behave very differently. One is as good as the long-radius configuration while the other one is almost identical in behaviour to the current helix-axicon configuration with an ROC of 2.0 m.

The main difference between the helix-axicon resonator and a standard resonator is that the output coupling and rear mirror are located on the same mirror. Therefore, a tilt in the helix mirror results in an opposing tilt for the two halves of the helix mirror. While a standard confocal resonator is least sensitive to a tilt of one of the resonator mirrors, the helix-axicon resonator is least sensitive to a tilt of the helix mirror in a long-radius configuration.

Thus to consider only the geometrical stability criteria (g-parameters) seems not sufficient in order to understand the sensitivity to misalignment of the helix-axicon resonator. When the resonator is operated in fundamental mode the ratio of the centre-to-end-gap size seems critical. A tilt of the helix mirror results in a tilt of the optical axis of the resonator and the mode experiences a lateral shift. If the centre gap is much smaller than the end gap the losses increase faster when the helix mirror is tilted compared to an inter-electrode gap shape where the change in gap size from the centre to the end is more moderate.

The current resonator with a ROC of 2 m seems to be a good compromise between sensitivity to misalignment and ROCs that can be manufactured and measured reliably with good accuracy.

3.2.4 Suppression of waveguide modes

So far in this chapter, the focus has been on issues involved in obtaining fundamental (TEM_{00}) mode operation in the stable direction of the resonator. To ensure this objective is achieved, the inter-electrode gap shape and size were adjusted to fit the size of the corresponding TEM_{00} mode. This results in Fresnel numbers, N_F close to unity. In general, if $N_F > 10$ the beam propagation can be considered to be "free-space" and waveguiding is negligible, whereas for $N_F < 0.5$ we have a waveguide system and TE and TM modes are supported. For values of $N_F \approx 1$, both free-space and waveguide propagation may occur, which is clearly undesirable. In order to suppress waveguide modes the electrode surface may be modified to increase the losses for TE and TM modes but not for TEM modes.

Waveguiding losses can be increased by increasing the roughness of the electrode surfaces, and while increased surface roughness can be achieved in many ways, only a few techniques are practical for the inside of a gas laser vacuum system. Although surface treatments such as glass bead or sand blasting create uniform roughed surfaces, it is difficult to avoid the sand and glass beads becoming embedded in the surface and therefore requiring extensive cleaning to avoid subsequent damage to the resonator mirrors in later laser operation. Since the electrode surface already requires machining to create the correct shape and dimensions, additional processes such as knurling can be

performed at the same time to create a surface structure that dramatically increases the losses for waveguide modes. The principal disadvantage of this approach however, is that such a surface is not sufficiently clean, due to the existence of burrs that may detach from the surface during laser operation. To overcome this problem, a very simple solution would be to produce a surface structure that is clean and burr free by the creation of a machined fine thread with a feature size that does not affect the discharge. Figure 3.15 shows a cross-sectional view of the outer and inner electrode assemblies (12, 14) and the inter-electrode gap (15). Upon each electrode surface (20, 22) there is a saw tooth shaped pattern which is formed by threading [76].

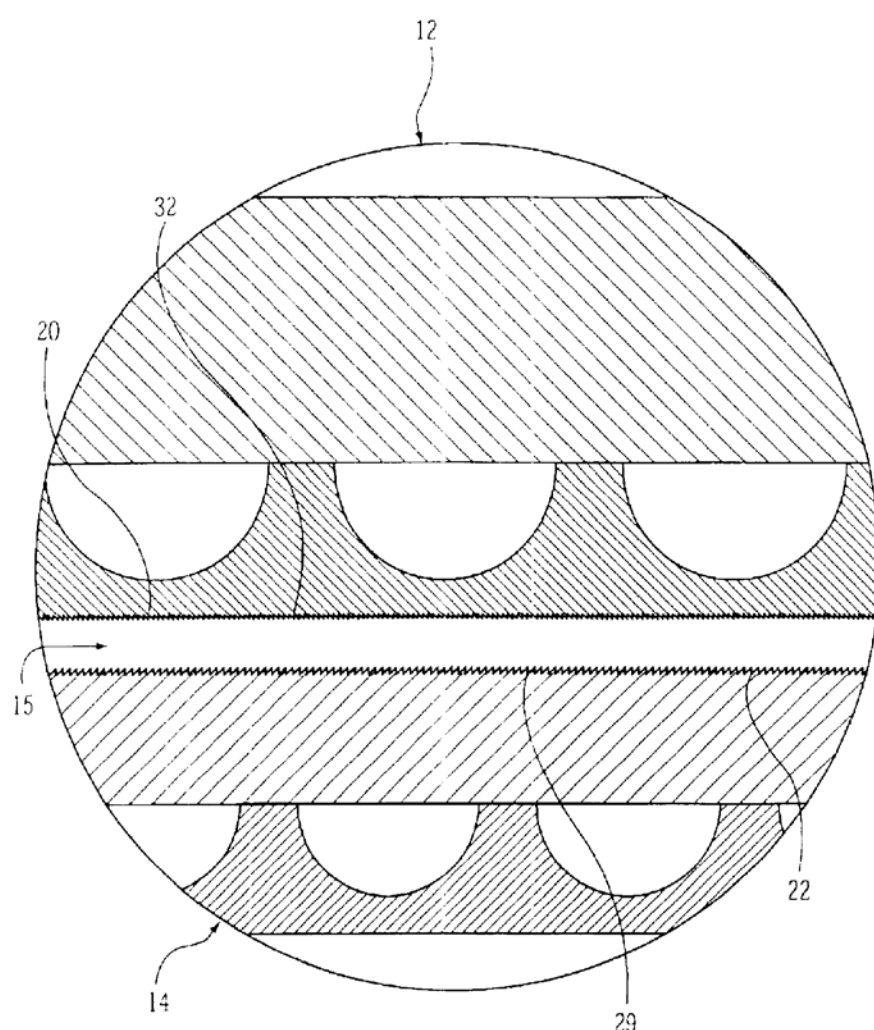


Figure 3.15 Cross-sectional view of the outer and inner electrode assemblies (12, 14) and the inter-electrode gap (15). Upon each electrode surface (20, 22) there is a saw tooth shaped pattern which is formed by threading [76].

This electrode surface meets all requirements. It provides a clean surface, which is easy to machine, it suppresses waveguide modes, minimises diffraction losses in case there is

interaction between the free-space modes and the electrode surface and extinguishes stray radiation.

3.3 Azimuthal Direction

The stable resonators discussed above have a long slender Gaussian-profile lowest order mode with a diameter of the order of a few times $(L\lambda)^{1/2}$. The ratio of the fundamental mode diameter to the aperture diameter of the laser medium is about the same as the resonator Fresnel number N_f (see equation 3.2). If N_f is much larger than unity, the fundamental mode will extract only a fraction ($\approx 1/N_f$) of the energy stored in the laser medium and therefore the laser oscillates in a mix of higher order modes to extract all the energy from the laser medium. Since the goal is to achieve high brightness, stable resonators are not suited for efficient energy extraction in the azimuthal direction.

Unstable resonators on the other hand are well suited for large gain area configurations with Fresnel numbers greater than unity. Unstable resonators are the optimum laser resonator for large gain areas because they combine nearly complete energy extraction with high beam quality. These characteristics make the unstable resonator a good fit for the azimuthal direction of coaxial discharge geometry of the coaxial laser.

3.3.1 Magnification

The resonator magnification, M determines the magnitude of the fractional output coupling, given approximately by $1-1/M$ in the one-dimensional case. The fractional output coupling or geometrical loss of an unstable resonator is therefore determined by the round-trip magnification. Note that the magnification is independent of the Fresnel numbers and resonator mirror sizes, and is given by the ratio of the initial and magnified beam size. For the case of the helix-axicon resonator, the magnification is given by:

$$M = \pi r_s / (\pi r_s - W) \quad 3.7$$

where W is the size of the extracted beam and r_s the radius of the mirrors. The parameters that determine the outcoupled beam size (W) in the helix-axicon resonator with a linear

slope is the scaling factor, c and the resonator length, L . The beam size is then given by [52]:

$$W = 4\sqrt{c2\pi L} \quad 3.8$$

In general, the far-field intensity distribution of the beam from an unstable resonator in the geometrical approximation is the Fraunhofer diffraction pattern of the uniformly illuminated region emerging from the output mirror. The far-field intensity distribution exhibits a central lobe that is surrounded by a number of diffraction rings or lines. For low magnifications, M a substantial fraction of the energy is contained in these rings [69].

However, for the case of the helix-axicon resonator the situation is different in that i) the aperture (outcoupling aperture) is not uniformly illuminated, and ii) the beam is coupled out immediately adjacent to (around) one hard diffracting edge.

In order to optimize the fractional output coupling a numerical optimization of the slope (scaling factor, c) is performed. For standard unstable resonators the optimum fractional output coupling depends on the gain, saturation intensity and the resonator losses [77], but for the helix-axicon resonator, an additional factor, associated with the diffraction losses due to the shadowing effect of the inner electrode, needs to be considered. With increasing magnitude of the fractional output coupling the inclination of the beam in the azimuthal direction increases, and at some point the inner electrode will start blocking the beam, thereby limiting the magnitude of the fractional output coupling.

Resonator length	1 m
ROC _{helix}	2.0 m
ROC _{axicon}	5.657 m ($2\cdot\sqrt{2}\cdot 2$ m)
Slope style	linear
Slope parameters	Varied from: $c = 1..14$ $\mu\text{m}/\text{rad}$.
Inter-electrode gap shape	6.2 mm – 5.4 mm – 6.2 mm

Table 3.8 Parameters for fractional output coupling simulation.

Figure 3.16 shows the extraction efficiency and beam quality for values of c between 1 and 14 $\mu\text{m}/\text{rad}$.

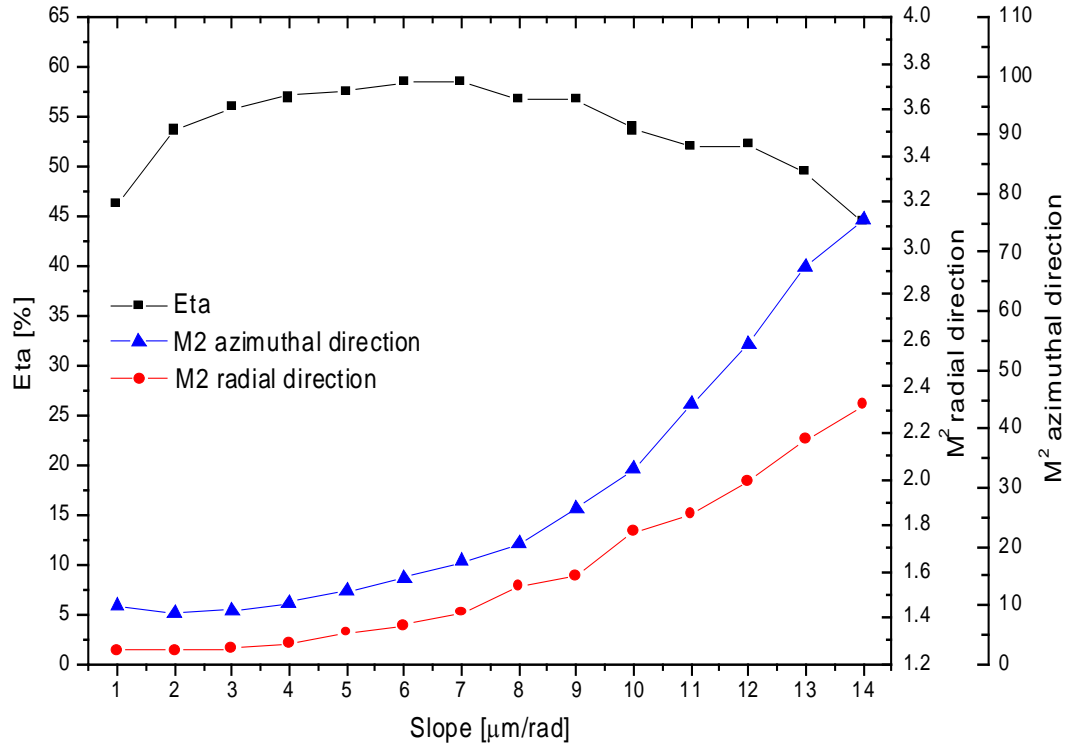


Figure 3.16 Calculated extraction efficiency and beam quality versus slope for an inter-electrode gap size of 6.2-5.4-6.2 mm.

Using Figure 3.16, it can be seen that for values of c in the range from about 3 - 7 $\mu\text{m/rad}$ the extraction efficiency changes only by a small amount from 56% to 58.5%, with the maximum of 58.5% being reached at 6 $\mu\text{m/rad}$. However, starting at about 3 $\mu\text{m/rad}$ the beam quality in both the radial and azimuthal direction starts to decrease. With increasing slope sizes the azimuthal beam inclination increases and the mode/mode mix in the azimuthal direction changes in order to minimize the losses caused by the shadowing effect. Figure 3.17 shows this shift in the energy distribution over the azimuthal mode orders for increasing values of c .

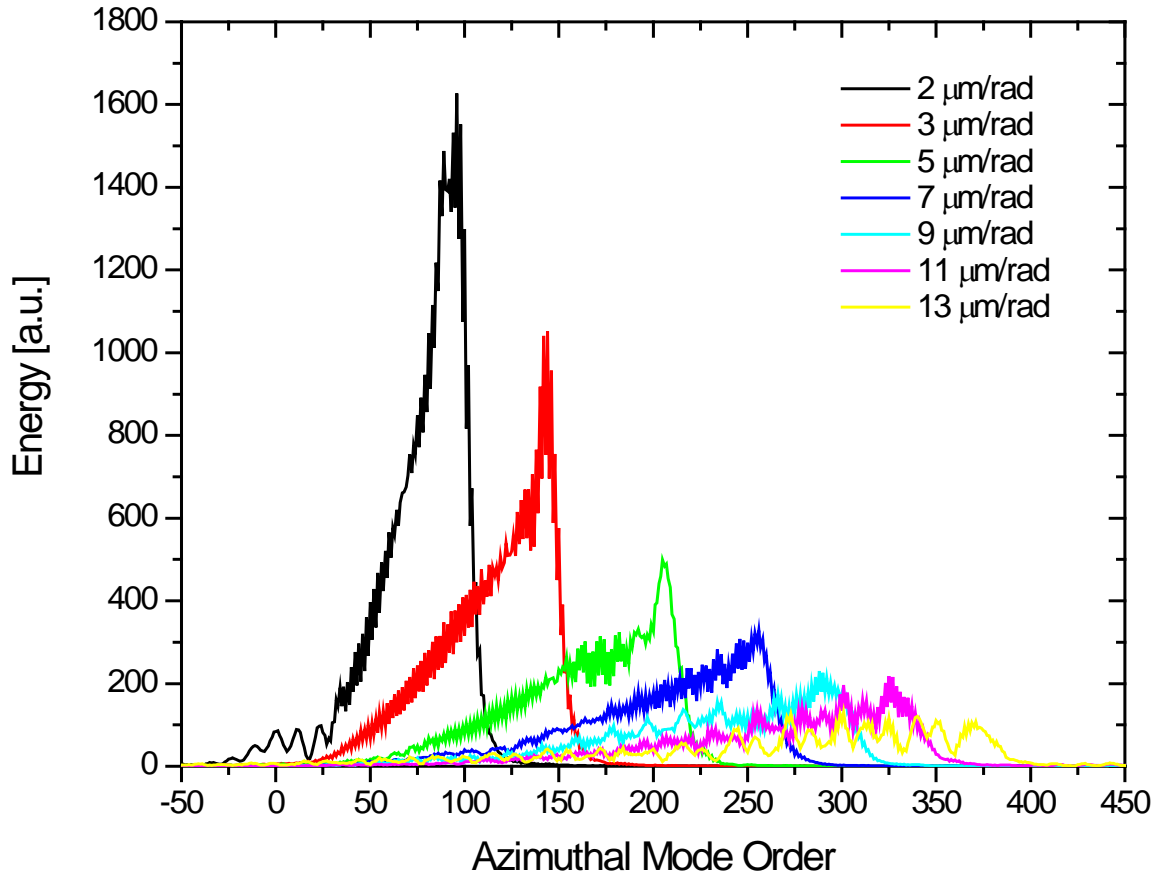


Figure 3.17 Calculated distribution of the resonator internal energy into different azimuthal mode orders for different slopes (c : 2..13 $\mu\text{m/rad}$; L : 1000 mm; ROC: 2.0 / 5.657 m; inter-electrode gap size: 6.2-5.4-6.2 mm).

This shift in the energy distribution over the azimuthal mode orders also has an effect on the far-field intensity distribution. Figure 3.18 shows the far-field intensity distributions corresponding to the resonator internal energy distribution over the azimuthal mode orders shown in Figure 3.17. With increasing values for the slope the size of the central peak of the far-field decreases in a manner which is consistent with the similarity property in Fourier transform theory.

For a slope of 2 $\mu\text{m/rad}$ the energy distribution of the azimuthal mode order is closest to a symmetric triangle. The Fourier transformation of a symmetric triangle is a sinc^2 function. This is for practical purposes also the case for the 2 $\mu\text{m/rad}$ trace in Figure 3.18. With increasing slope values the energy distributions in Figure 3.17 deviate more and more from a symmetric triangular shape and become more and more asymmetric resulting in a deviation from the sinc^2 function. This is quite a problem since the nulls are disappearing on the left hand side of the main peak making proper spatial filtering impossible. This

behaviour limits the maximum value for the slope and fractional output coupling. The current slope of $4 \mu\text{m}/\text{rad}$ represents a fractional output coupling of about 5.5% (ratio of outcoupled and internal power).

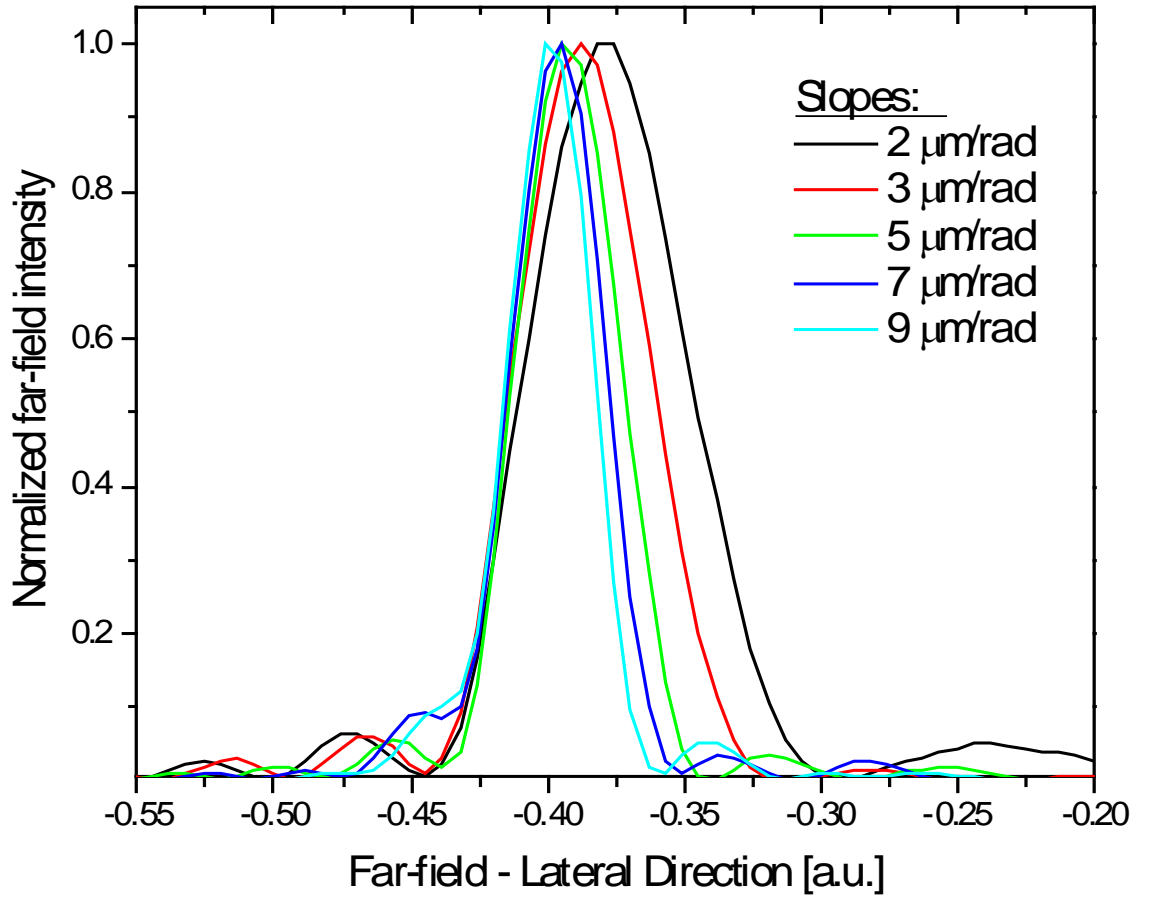


Figure 3.18 Far-field intensity distribution for different slopes (c : $2..9 \mu\text{m}/\text{rad}$; L : 1000 mm ; ROC : $2.0/5.657 \text{ m}$; inter-electrode gap size: $6.2\text{-}5.4\text{-}6.2 \text{ mm}$).

There are also limits on the low end of the slope values. For values of the slope which are too small, the gain utilization is poor resulting in low output power levels. Additionally, for small values of the slope the resonator internal power is highest. With increasing slopes values, the resonator internal power is decreasing, and therefore the heat load on the mirrors is reduced. The resonator internal power versus slope is shown in Figure 3.19. This figure also shows the increasing impact of the shadowing effect of the inner electrode with increasing values for the slope. The relative diffraction losses are defined as the ratio of absolute diffraction losses and internal power.

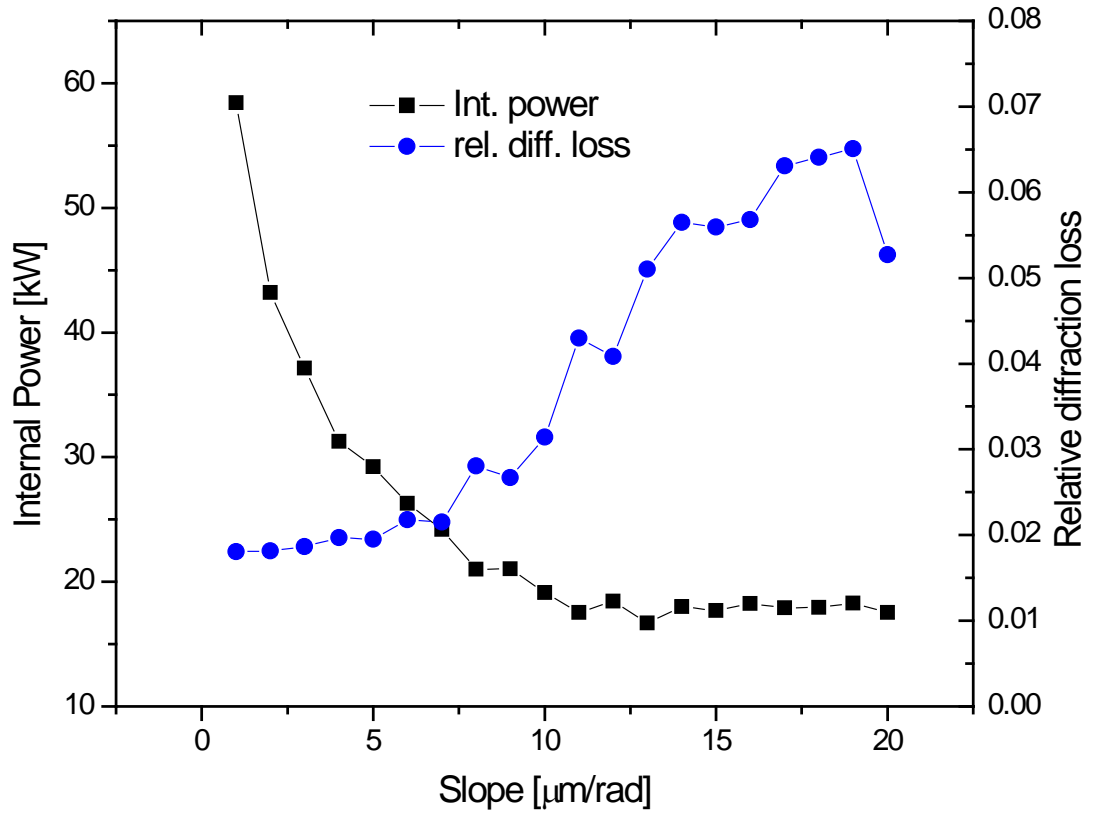


Figure 3.19 Internal resonator power and relative diffraction losses versus slope. (L : 1000 mm; ROC: 2.0 / 5.657 m; inter-electrode gap size: 6.2-5.4-6.2 mm).

3.3.2 Temporal stability of the unstable resonator

The azimuthal direction of the helix-axicon resonator was treated in [52], [4], and up to this point in this work also, as an unstable resonator. However, a closer examination of the resonator parameters reveals that the resonator is neither an unstable nor a stable resonator, but sits right at the border between the two resonator types in the stability diagram. In section 2.8.1 the stability criterion was discussed showing that stable resonators lie in the range from $0 \leq g_1 g_2 \leq 1$ with $g_1 = 1 - L/R_1$ and $g_2 = 1 - L/R_2$. Even though this stability diagram is valid for a simple two mirror resonator, the statement that the helix-axicon resonator sits right at the border between stable and unstable remains valid. This was shown in section 3.2.3, where the equivalent configuration of the helix-axicon resonator was used to calculate the g -parameters for a resonator with an internal lens. Equation 3.6 delivers g -parameters that are equal to 1 for ROCs approaching infinity ($R \rightarrow \infty$). The slope of the helix mirror defines the radii R_1 and R_2 for the calculation of the g -parameters in the azimuthal direction. For a linear slope the radii approach infinity and therefore g_1 and g_2 , and their product become 1. Hence, in the azimuthal direction,

the helix-axicon resonator can be more accurately described as the equivalent of a tilted planar resonator.

Planar resonators are known to be highly sensitive to misalignment and deformation of the mirrors. In order to determine the impact of the linear slope on the consistency, repeatability and stability of laser characteristics such as laser power and intensity distribution of the extracted beam, several mirrors with identical parameters were tested consecutively in one laser. In this arrangement the helix mirror remains constant in the laser while a series of different axicon mirrors were employed. The measurements indicated that while the laser power and general shape of the beam is repeatable from mirror to mirror, the temporal stability of the intensity distribution varies significantly from mirror to mirror.

These results are shown in Figure 3.20. The performance of the mirror pairings can be grouped in three categories: Mirror combinations that work well (green), mirror combinations that exhibit extreme hot-cold behaviour (red) and mirror combinations with only slight hot-cold behaviour (yellow). The term ‘hot-cold behaviour’ is used here to describe a change of the intensity distribution within the first few minutes of operating the laser – if a mirror pair shows hot-cold behaviour, the intensity distribution of the laser beam is different for the cold and warm (hot) state of the laser. The mode burn series in Figure 3.20 (left) represents the intensity distribution of the azimuthal direction. The graphs on the right hand side represent an electronic scan of the intensity distribution at different times [78].

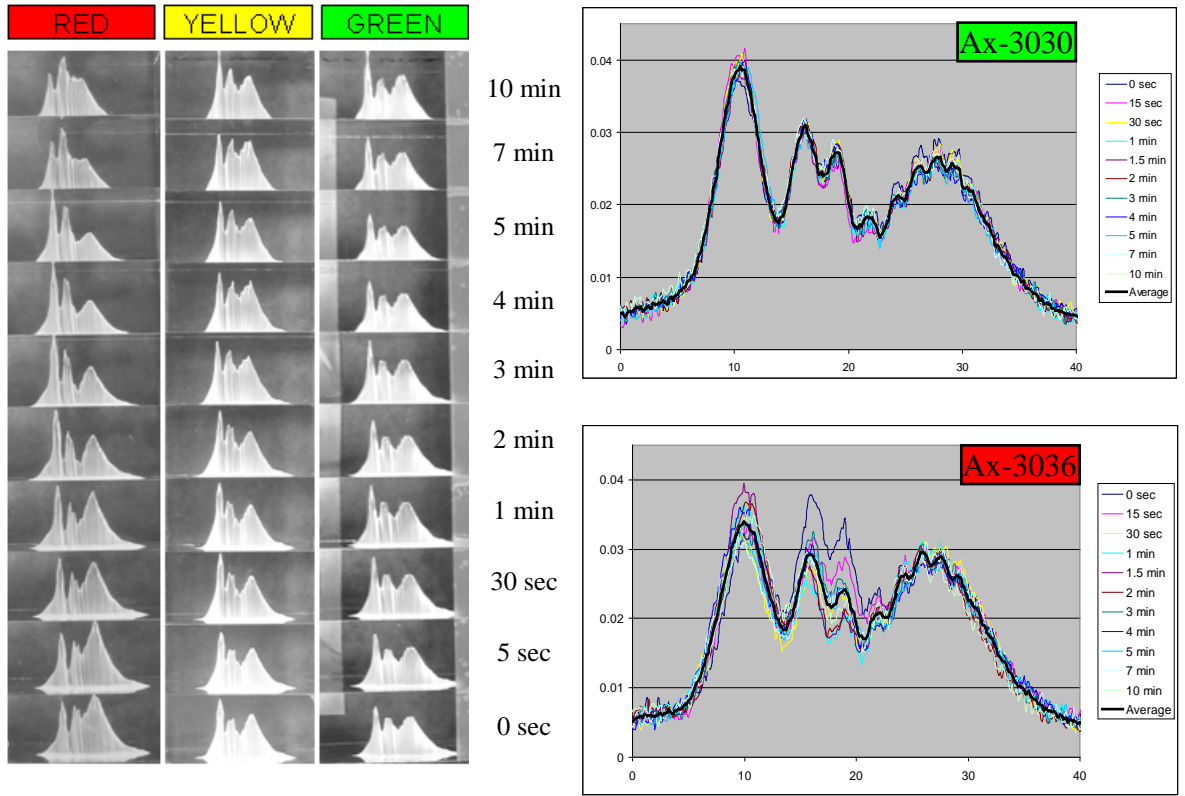


Figure 3.20 A configuration with a 6.5 - 6.0 - 6.5 mm shaped electrode configuration and a ROC of 2.0 m with a 4 $\mu\text{m}/\text{rad}$ linear slope is characterized with several nominally identical axicon mirrors to evaluate the consistency of the beam shape between the mirrors. The colour code indicates the temporal stability of the intensity distribution for the mirror combinations: Green: stable over time; Red: varying with time; Yellow: some change over time [78].

3.3.3 Mirror optimization

In 3.3.2 it is shown that the azimuthal direction of the helix-axicon resonator is equivalent to a tilted planar resonator and is therefore extremely sensitive to misalignment and mirror deformations. This can be seen in the hot-cold behaviour shown in Figure 3.20. In order to find the underlying cause of this hot-cold behaviour a finite element analysis of the axicon mirror was carried out. The result delivered by this analysis is the displacement of the mirror due to the various forces acting upon it. The main forces are the heat load on the optical surface, incoming cooling water pressure and mounting forces. Figure 3.21 shows a representative example of the displacement of the axicon mirror caused by the incoming cooling water pressure. It is clear from the result that the water feed points, positioned directly under the red area, are directly responsible for the displacement observed. When the mirror assembly is installed in the laser, the pressure

inside the laser is 0.07 bar, while on the outside the pressure is 1 bar. The water bellows have an inner pipe to connect the mirror to the water circuit; around this pipe there is a small gap where atmospheric pressure pushes directly on the bellow end thereby applying a force to the mirror. The maximum deformation of the conical surface in this case is about $1.2\text{ }\mu\text{m}$ [79].

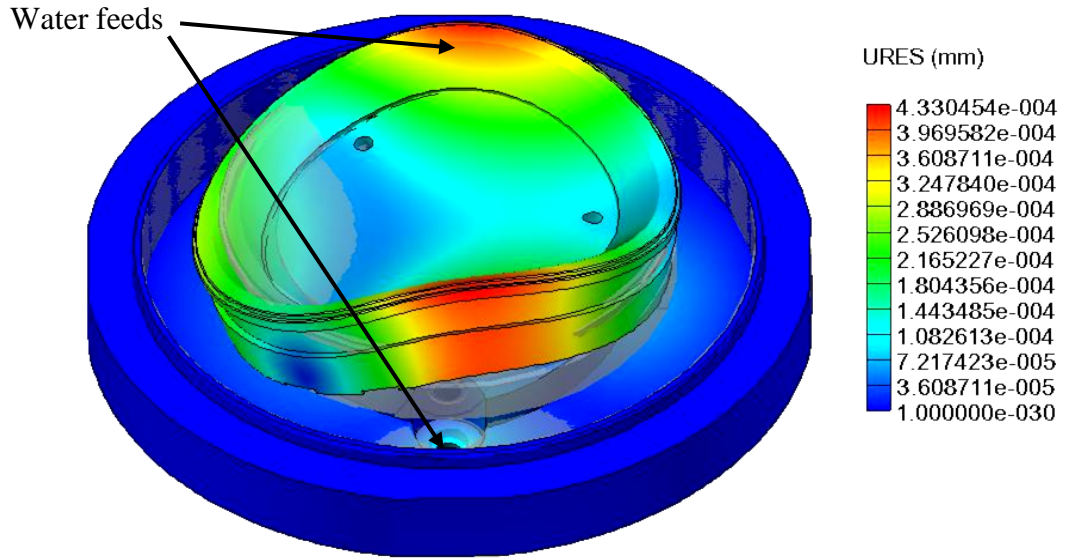


Figure 3.21 Finite element analysis of the axicon mirror. The colours indicate the displacement within the axicon mirror caused by the incoming cooling water pressure [79]. (URES = Displacement resultant)

This deformation of $1.2\text{ }\mu\text{m}$ is small in absolute terms, but compared to the structure height of the helix mirror in the azimuthal direction, it is significant. For a slope of $4\text{ }\mu\text{m/rad}$ the step height is $23.5\text{ }\mu\text{m}$. In addition to the deformation caused by the cooling water pressure there are additional deformations caused by the thermal load on the optical surface and mounting forces. Combined, these deformations can be up to $1.8\text{ }\mu\text{m}$ depending on the revision level of the mirror assembly [79]. (The optimization of the mirror assembly to minimize these distortions is not part of this thesis.)

As a result, the deformation of the mirror gives rise to regions which are locally stable or unstable in the azimuthal direction. The beam can become trapped in the stable regions of the resonator causing an increase in the thermal load and thereby further deformation of the mirror. This causes changes in the intensity distribution and heat load, then further deformation and an endless cycle starts, wherein the intensity distribution never reached a steady state, as demonstrated by many experiments carried out in the laboratory.

3.3.4 Parabolic slope

As concluded above, the tilted planar resonator of the azimuthal direction is not suited for industrial applications. A different resonator is needed, one that is less sensitive to the deformations of the mirrors. Therefore, the linear slope is replaced with one which is curved, by analogy to the positive and negative branch unstable resonators used in slab-like diffusion-cooled lasers. More precisely, a parabolic shaped slope is investigated.

Equation 3.9 describes the contour of the optical surface on the helix mirror. As discussed earlier, c is a scaling factor for the slope and its value defines the steepness of the incline of the linear slope.

$$h(r, \phi) = c(\phi) + \frac{(r - r_s)^2}{2r_h} - c(\phi) \frac{2}{r_s} (r - r_s) \quad 3.9$$

As shown in [52] this equation can be modified to accommodate any shape for the slope. For arbitrary shapes the scaling constant, c is replaced with $u(\phi)$. For a parabolic slope $u(\phi)$ is $-c_1 \phi - c_2 \phi^2$.

$$h(r, \phi) = u(\phi) + \frac{(r - r_s)^2}{2r_h} - u(\phi) \frac{2}{r_s} (r - r_s) \quad 3.10$$

A purely empirical optimization of c_1 and c_2 is prohibitive due to the cost, delivery times of the mirrors and the excessive testing effort required. Therefore, a numerical optimization is performed using a one-dimensional version of OPT. Figure 3.22 shows a comparison of a linear and parabolic slope. The difference of the structure height is plotted as Δh , and the simulation is performed for a range of Δh from -2 to +3 μm [80].

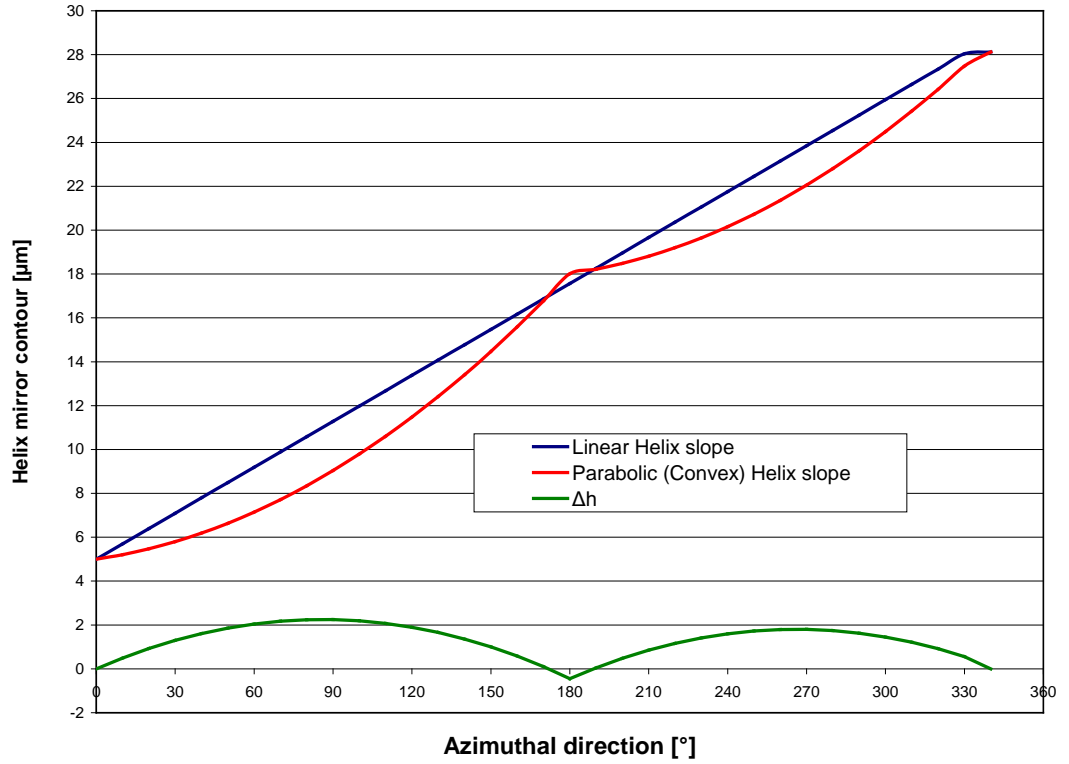


Figure 3.22 Comparison between linear (blue) and parabolic (red) slope. The difference (Δh) between them is plotted in green [80].

Figure 3.23 shows the results of the one-dimensional simulations, with each picture representing the result for one parameter set. The two graphs on the left within each picture show the internal intensity distribution on the mirrors, the top right graph shows the outcoupled intensity distribution, and the bottom right graph shows the intensity distribution in the far-field.

Slopes with a positive Δh represent a convex shape of the slope, negative Δh represent a concave shape of the slope, and for $\Delta h = 0$ the slope is linear. In the range of Δh from -2.00 to $-0.33 \mu\text{m}$ the intensity distribution on the mirrors is quite uneven and increases almost linearly as the beam travels along the azimuthal direction of the resonator. The outcoupled intensity distribution is observed to change significantly from parameter set to parameter set, while the far-field distribution is observed to be relatively unchanged. Once Δh equals or is larger than 0 the outcoupled intensity distribution is identical for all values of Δh , and with increasing values for Δh the intensity distribution on the mirrors becomes more even.

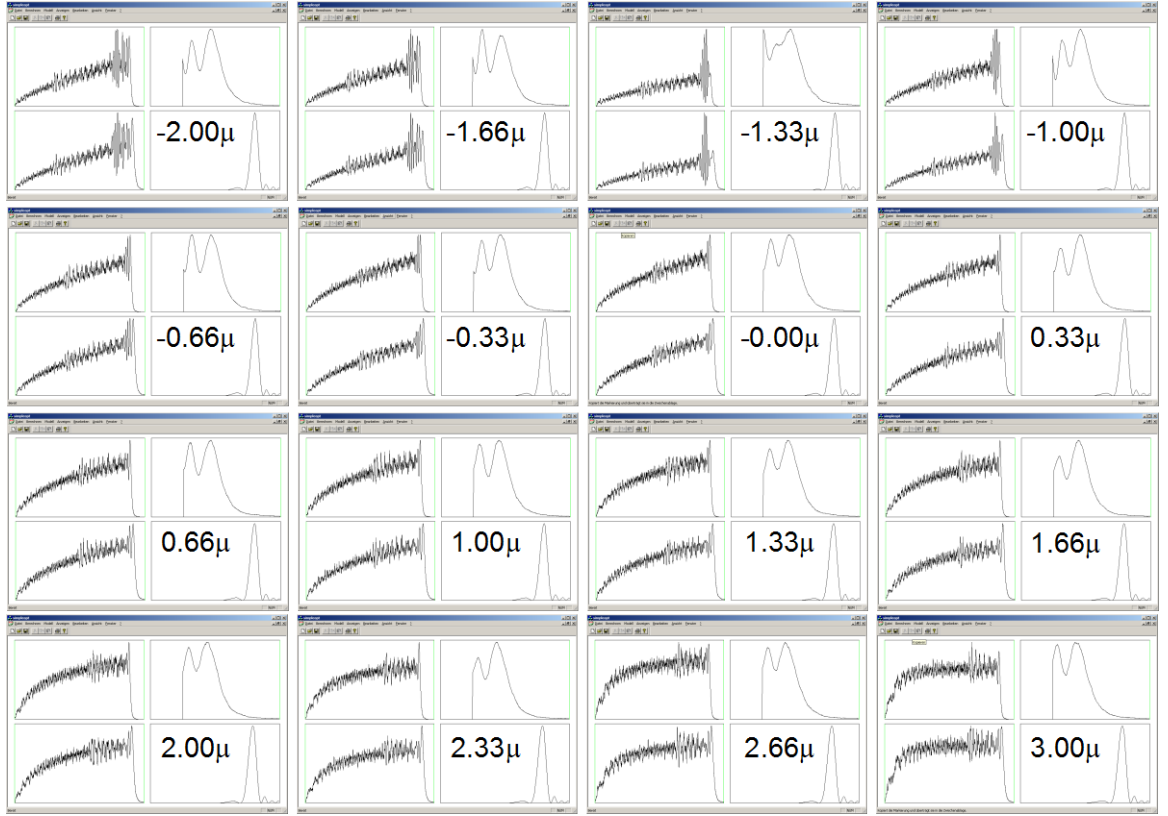


Figure 3.23 Results of a one dimensional simulation of the azimuthal resonator direction for different Δh values. The two graphs on the left within each picture show the internal intensity distribution on the mirrors, the top right graph shows the outcoupled intensity distribution, and the bottom right graph shows the intensity distribution in the far-field [80].

Empirical optimization of the parabolic shape in the range for Δh from 1 to 3 μm verifies the results of the simulation. The best performance with regard to laser power and mode stability is obtained for $\Delta h \approx 2.25 \mu\text{m}$.

The slopes used in the simulation are designed as indicated in Figure 3.22, where the parabolic shape is superimposed on the linear slope. For a structure height of $\Delta h \sim 2.25 \mu\text{m}$ the scaling constants c_1 and c_2 are $-1 \cdot 10^{-3} \text{ mm/rad}$ and $-1 \cdot 10^{-3} \text{ mm/rad}^2$ respectively.

In summary, the use of a parabolic (rather than linear) slope creates a real effective unstable resonator in the azimuthal direction, and the sensitivity of the resonator to deformations caused by the heat load and / or vacuum forces is reduced. With the parabolic slope, the resonator remains in the unstable zone on a local and global level even in the presence of some local deformations.

A direct comparison of the intensity distribution on the resonator mirrors for a resonator with a linear slope ($\Delta h = 0$) and a parabolic slope with $\Delta h = 2.25$ shows a more uniform distribution when the slope is parabolic. For the situation at the beginning of the contour ($\phi = 0$), the parabolic slope is less steep and therefore there are more reflections in this area (see Figure 3.24) causing the intensity to build up faster. With ϕ increasing, the angular separation between the reflections on the mirrors increases resulting in a more uniform intensity distribution.

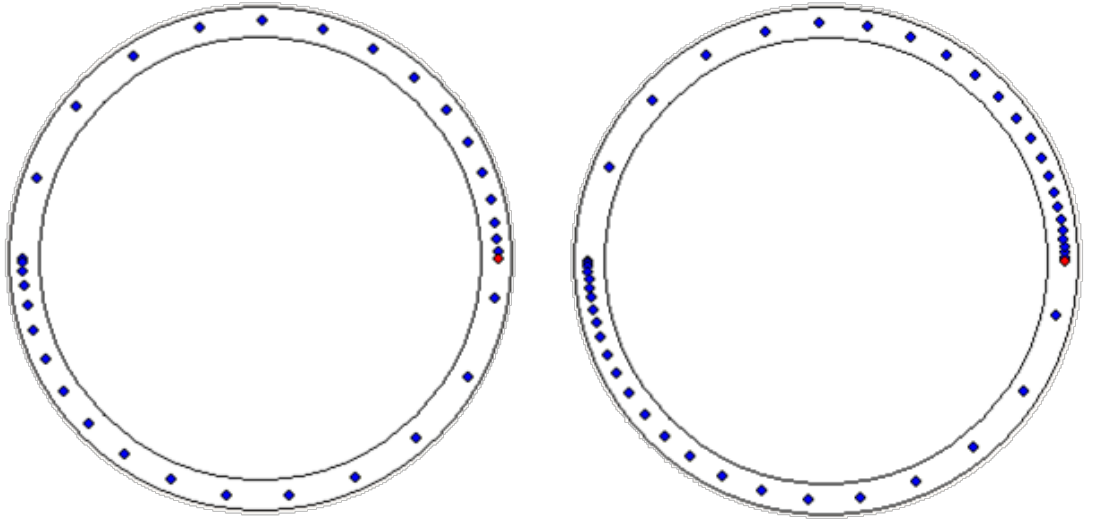


Figure 3.24 Comparison of the linear and parabolic slope with a ray tracing representation of the helix-axicon resonator. Every dot represents one bounce of a ray on the mirror. Left: Linear slope with $c = -4 \mu\text{m/rad}$; right: parabolic slope with $c_1 = -1 \cdot 10^{-3} \text{ mm/rad}$ and $c_2 = -1 \cdot 10^{-3} \text{ mm/rad}^2$.

A comparison of the internal intensity distribution for a resonator configuration with a linear and parabolic slope is shown in Figure 3.25. The more uniform intensity distribution is associated with reduced displacement of the mirror surface due to the more uniform thermal load.

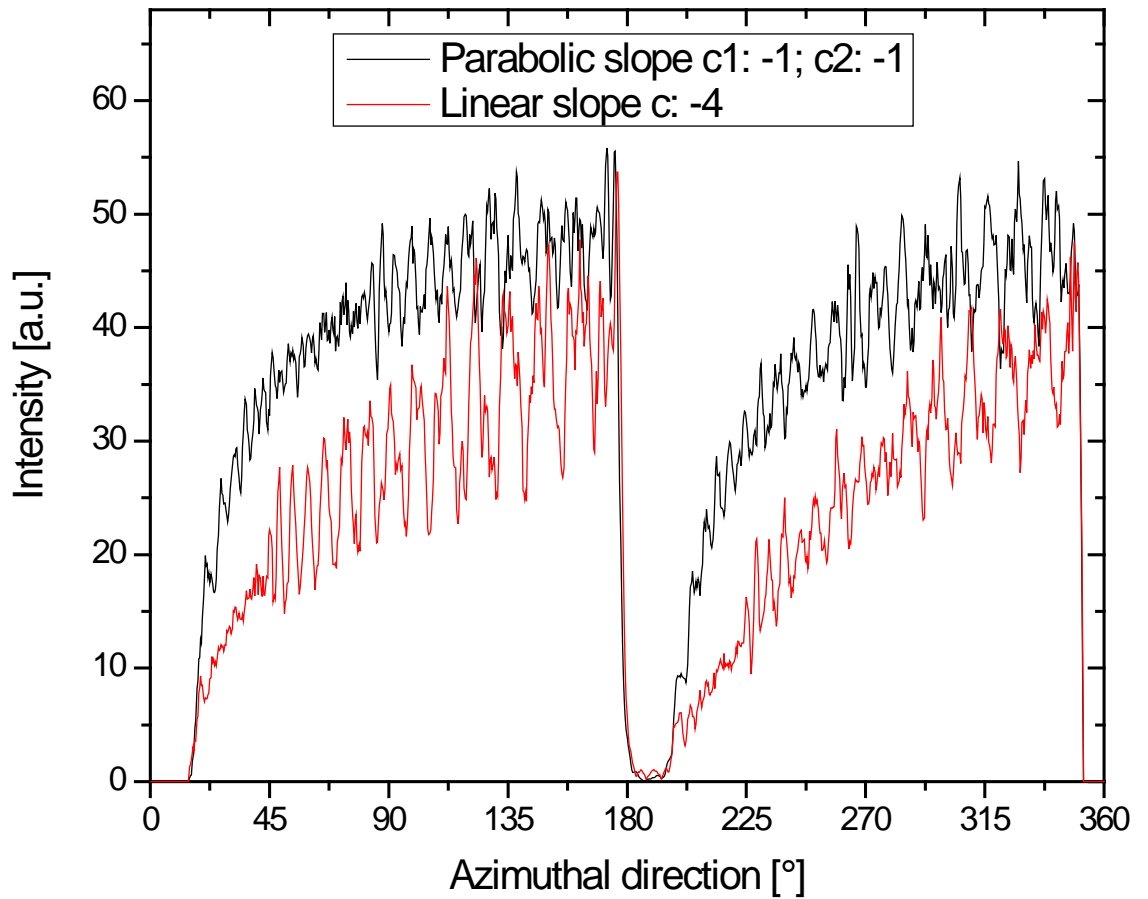


Figure 3.25 Intensity distribution on the helix mirror with a linear (red) and parabolic (black) slope.

For the case of a linear slope with $c = -4 \text{ } \mu\text{m/rad}$ the inter-electrode gap size was determined to be $6.2 - 5.4 - 6.2 \text{ mm}$ (end-centre-end along the electrode). Since the internal intensity distribution has changed significantly with the introduction of the parabolic slope the inter-electrode gap size now needs to be re-verified. The result of the relevant simulation shown in Figure 3.26 indicates a change in optimum predicted gap size to $6.6 - 5.6 - 6.6 \text{ mm}$. This increase in inter-electrode gap size can be explained by i) the faster build up of the intensity and ii) the overall higher intensity within the resonator.

This can be more easily understood if the resonator is considered as a combination of a seed and amplifier region. The initial few degrees represent the seed region where the radial mode becomes defined. Then with more rapidly increasing intensity and higher intensity levels in this area, the gap size can be increased without allowing higher order modes to oscillate. In the remaining (amplifier) zone a larger inter-electrode gap size enables a reduction in diffraction losses. Overall then, the better utilization of the gain medium and lower propagation losses result in higher output power levels. The model

predicts an additional output power in the range of 100 to 150 W for the parabolic slope, which is confirmed by the experimental results in the laboratory.

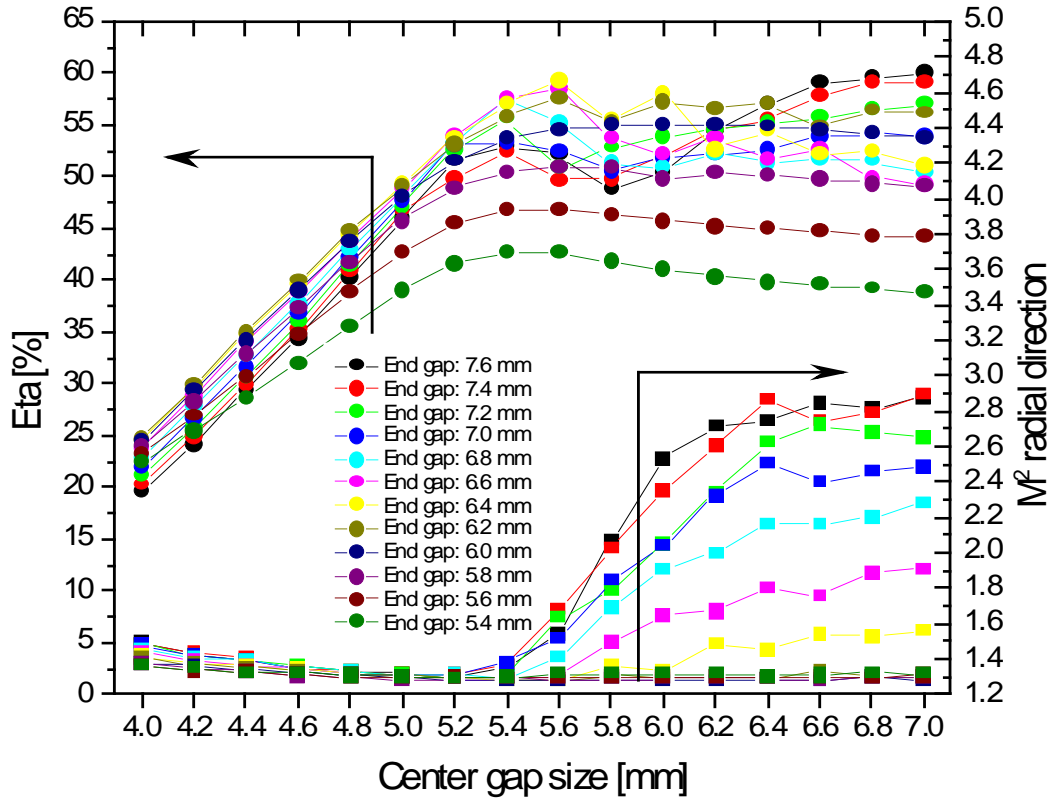


Figure 3.26 Optimization of the inter-electrode gap size for a slope with $c_1 = -1 \cdot 10^{-3} \text{ mm/rad}$ and $c_2 = -1 \cdot 10^{-3} \text{ mm/rad}^2$; ROC: 2.0 / 5.657 m; l : 500 + 500 mm.

Figure 3.27 shows the resonator internal intensity distributions for different inter-electrode gap sizes. The 6.6 – 5.6 – 6.6 mm gap has an even distribution and a slender, straight mode. If the centre gap is increased, e.g. to 6.0 mm the mode does not remain in the centre of the gap, and if both the centre and end gap sizes are increased, higher order modes begin to oscillate (see for example the case for 7.4 – 5.8 – 7.4 mm).

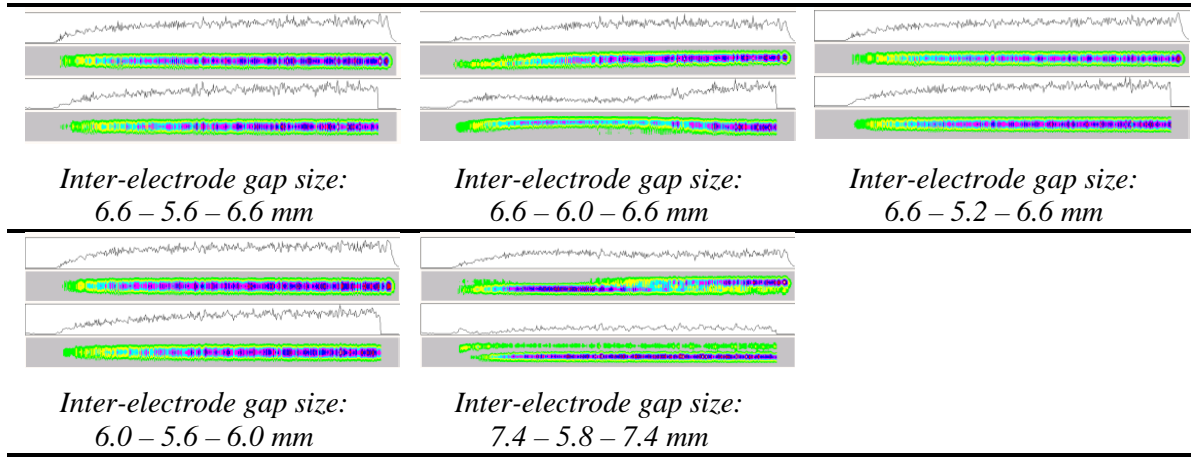


Figure 3.27 Resonator internal intensity distribution for different electrode configurations. For each configuration the internal intensity distribution is plotted in two sections, from 0 - 180° and 181 - 360°, and two views are shown, a colour plot with the colours representing the intensity and a cut through the azimuthal direction.

3.4 Polarization Correction

The absorption of a laser beam by the material depends on the properties of the material, the angle of incidence and the state of polarization as shown by the Fresnel equations for reflection and transmission. For metals, there is a significant difference in absorption for s- and p-polarization for angles of incidence in the range from 60° to 90°. During the cutting process, the angle of incidence is close to 90°. Therefore, in order to avoid a dependency of the absorption on the cutting direction, a state of polarization that ensures uniform absorption in all directions needs to be deployed. Radial, azimuthal or circular polarizations are the obvious choices. While promising results have been achieved with radial and azimuthal states of polarization, circular polarization remains the state of the art choice in metal cutting.

Since most commercially available lasers have linear polarized beams, circular polarization is generated with an external phase shifter that deflects the beam by 90° and retards the p-polarization against the s-polarization by 90°. If the laser beam is not linearly polarized, but for example has azimuthal polarization, or if a linearly polarized beam is incident on the phase shifter under an angle different from 45° in regard to the plane of incidence, elliptical instead of circular polarization is generated.

The helix-axicon resonator emits a beam with a state of polarization significantly different from the linear state of polarization as shown by [4] and depicted in Figure 2.20.

The emitted laser beam has the shape of a ring segment and the state of polarization is in essence azimuthal.

The azimuthal state of polarization is defined by the reflection of the beam on the axicon and the beam inclination in the azimuthal direction. At first, after the beam is reflected by the axicon mirror, the state of polarization is 100% azimuthal since the local reflectivity for s-polarization is higher than for p-polarization. As the beam propagates towards the helix side the polarization rotates due to the movement of the beam in the azimuthal direction (beam inclination). When the beam propagates back from the helix to the axicon mirror and is reflected again on the axicon, the small difference in reflectivity for s- and p-polarization cannot restore pure azimuthal polarization. By the time the beam reaches the output coupling window the rotation of the polarization is significant as shown in Figure 2.19 [4].

In summary, the state of polarization is azimuthal and rotated by about 4° against the horizontal. This makes it impossible to convert this state of polarization into circular polarization with a simple phase shifter. First, the state of polarization must be transformed into linear polarization with either horizontal or vertical orientation. This transformation includes two components: i) Changing the azimuthal state of polarization into a linear state of polarization and ii) rotate the linear state of polarization into the horizontal or vertical.

Beam shaping telescopes to perform this transformation have been proposed, for instance by Schulz [65]. The azimuthal state of polarization is transformed into linear polarization by ‘straightening’ it with an optical element that has the shape of an axicon segment. If the radius of curvature of the axicon segment is the same as the radius of the axicon used inside the resonator, the intensity distribution and polarization are straightened after one bounce (compare to Figure 2.21). However, this takes care of step 1 only, and there still remains an overall rotation of the linear polarization of about 4° . A deviation of 4° against the horizontal (or vertical) causes a significant deviation from the desired circular state of polarization. The ellipticity of the polarization was measured at about 0.8 for this set-up (ratio of the two principal axes). Whereas the minimum acceptable value for the circular polarization is 0.9.

3.4.1 Correction of the state of polarization

The azimuthal polarization can be separated into X- and Y-components in a Cartesian coordinate system as shown in Figure 3.28. Due to the dimensions of the ring segment, the bulk of its polarization is in the X-direction and only a small portion in the Y-direction. Note, the coordinate system in Figure 3.28 is rotated to compensate for the rotation of the polarization caused by the beam inclination.

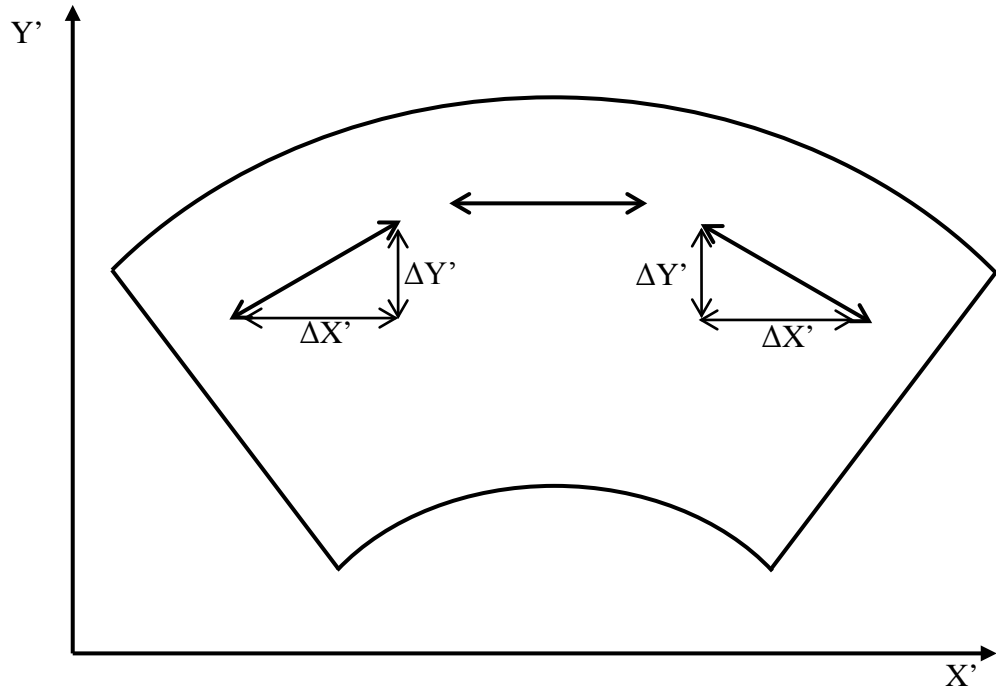


Figure 3.28 The polarization vectors are tangent to a circle and can be separated into their X- and Y-components in regard to a Cartesian coordinate system (X' , Y'). The $X'Y'$ coordinate system is rotated by 4° against the horizontal.

Figure 3.29 shows the calculated polarization components in the X (right) and Y (middle) directions and the superposition of the two (left). Based on measurements in the lab the Y-component represents about 2% of the overall laser power. In the simulation, the Y-component represents about 4%.

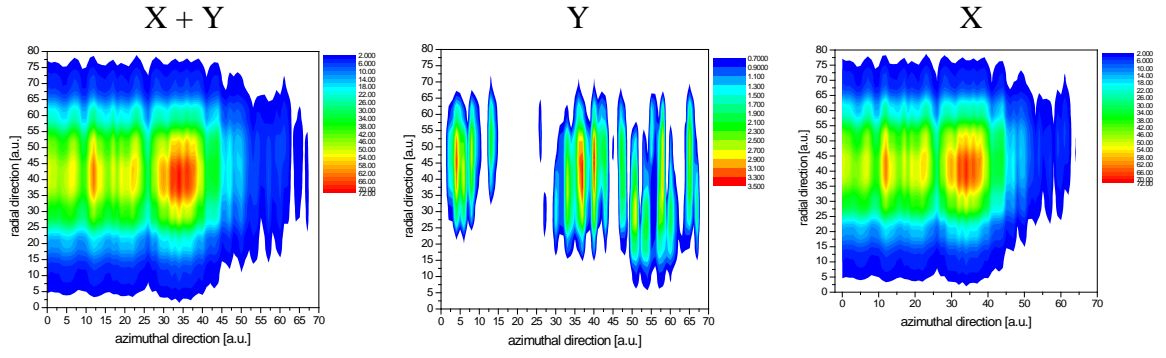


Figure 3.29 Calculated intensity distribution of the extracted beam: left: X- and Y-components; middle: Y-component only; right: X-component only. The Y-component comprises about 4% of the total power in the simulation. In reality, the Y-component comprises about 2%.

The approach chosen in [65] corrects the polarization by straightening the entire ‘beam’. Although it is necessary to correct the state of polarization of the beam, it is not necessary to transform the intensity distribution from a ring segment to a rectangular shape in order to achieve good application results. In that case, a dielectric coating absorbing the Y-component and reflecting the X-component of the polarization can transform the azimuthal state of polarization into linear polarization. This approach also corrects the 4° tilt of the overall polarization. The absorption and reflection characteristics for s- and p-polarization of such a coating are shown in Figure 3.31. This coating is designed for an angle of incidence of 45°. If a laser beam, with a non-linear state of polarization is deflected by 90°, so that the polarization component in the Y-direction is p-polarized and the X-component of the polarization is s-polarized with regard to the plane of incidence, the Y-component will be absorbed by the coating. The reflected beam therefore consists only of the X-component of the polarization and is, now, linear [62] (see Figure 3.30).

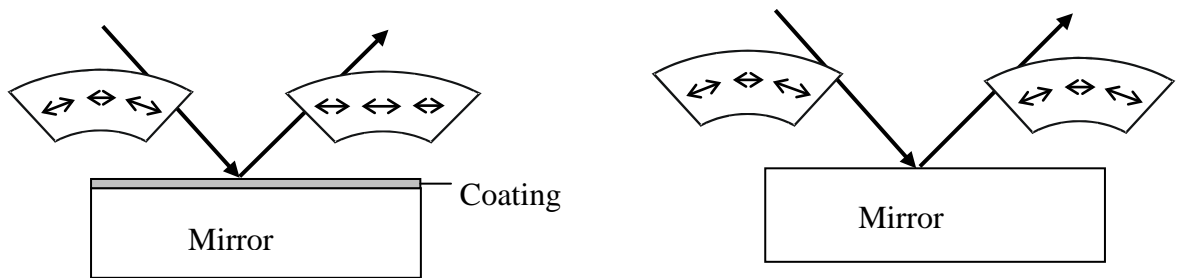


Figure 3.30 Right: Mirror with a high reflectivity, zero phase shift coating. It is only deflecting a beam without influencing its state of polarization. Left: The coating is absorbing the Y-component of the polarization.

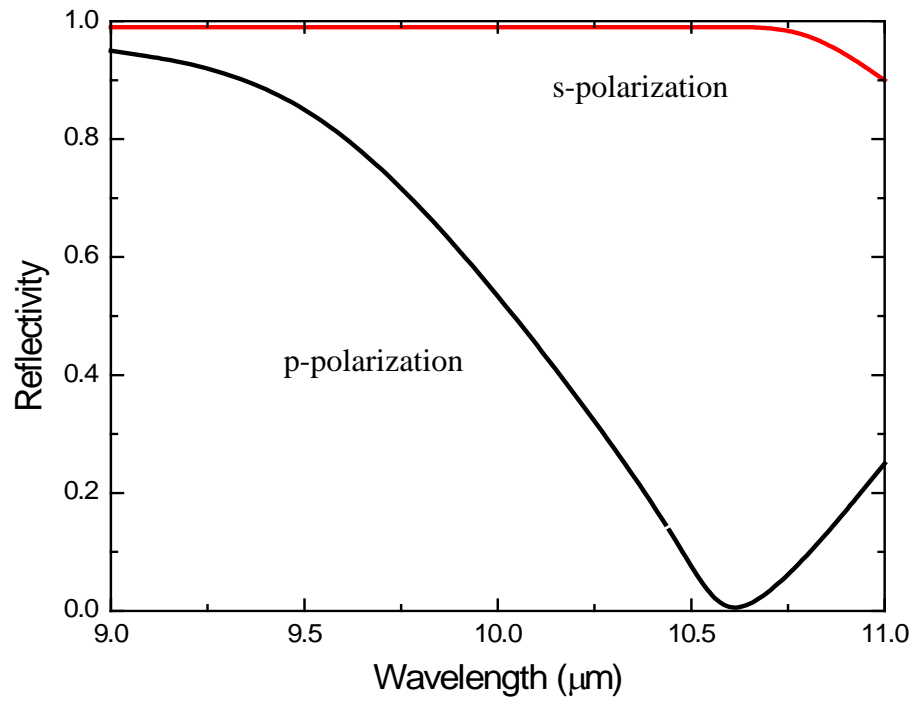


Figure 3.31 Characteristics of the polarization selective coating for an angle of incidence of 45° . The reflectivity for p-polarization approaches zero at a wavelength of $10.6 \mu\text{m}$ while the reflectivity for s-polarization stays at nearly 100% [63].

3.4.2 Beam shaping telescope set-up

Next, a set-up has to be defined that combines the functions required to transform the general astigmatic beam into a stigmatic beam and to transform the azimuthal state of polarization into linear polarization. One such set-up is shown in Figure 3.32. The beam shaping telescope has four optical elements (OE) and a spatial filter (SF). Two cylindrical optical elements at a time form a telescope to adjust the beam diameter and divergence of the radial and azimuthal direction. In the radial direction, a Galilean style telescope is used. The azimuthal direction uses a Kepler style telescope to create a far-field for spatial filtering. Once the beam has passed these optical elements, the general astigmatism is removed. The beam sizes in radial and azimuthal direction have been equalized and the waist position for the two directions is in the desired position. To correct the state of polarization OE 1 is coated with a polarization selective coating, for instance an ATFR coating from II-VI Inc. [63].

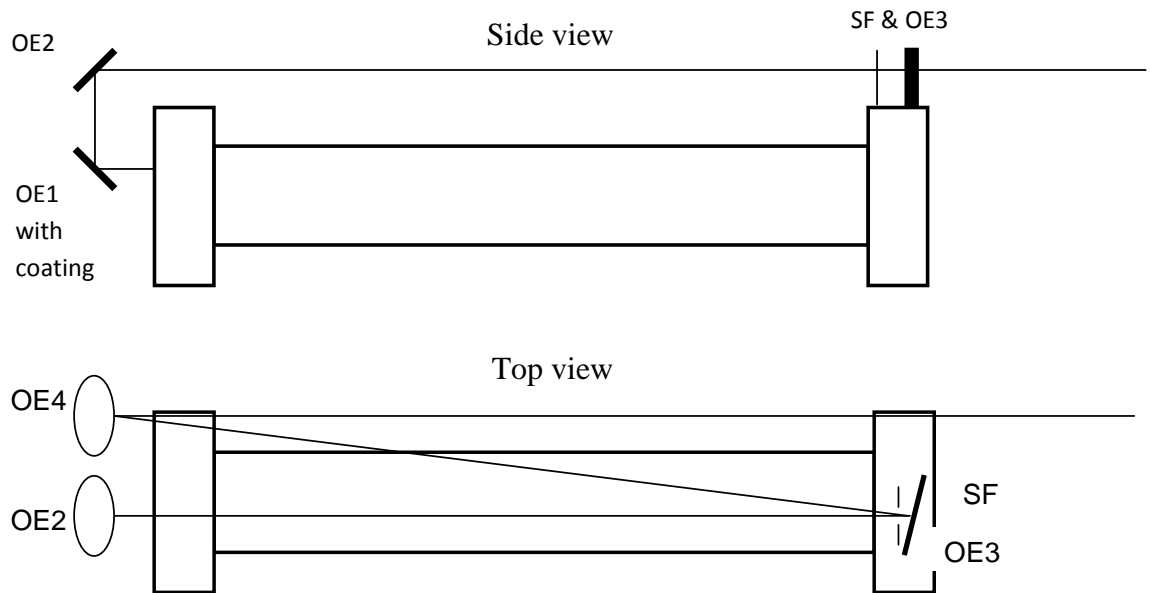


Figure 3.32 Side and top view of the mechanical design of the beam shaping telescope.

OE1 is right in front of the output coupling window and is coated with the polarization selective coating. It also focuses the beam in the azimuthal direction. The focus is generated right in front of OE3 where the spatial filter (SF) is located. OE4 is collimating the azimuthal direction. OE2 and OE3 form the Galilean telescope to adjust the beam size in the radial direction. The optical design is schematically shown as a lens equivalent in Figure 3.33.

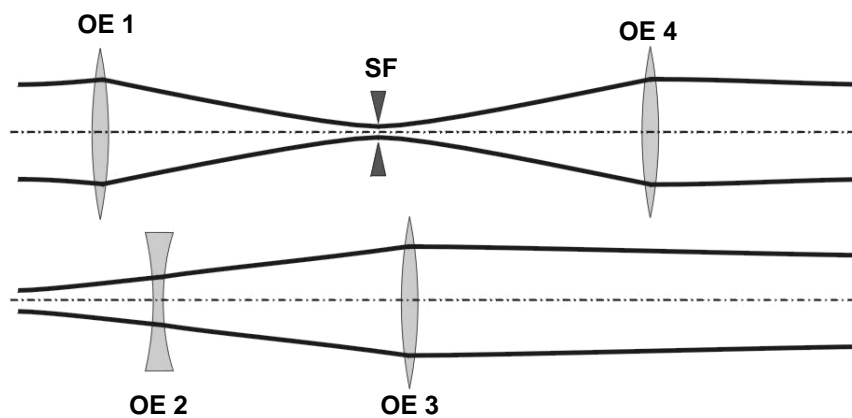


Figure 3.33 Lens equivalent representation of the beam shaping telescope. Top: azimuthal direction; bottom: radial direction [62].

Table 3.9 shows the ROCs of the optical elements and the respective substrate material.

Element	ROC [mm]	Substrate
OE 1	1975 concave	Cu
OE 2	2700 convex	Cu
OE 3	3700 concave	Cu
OE 4	2280 concave	GaAs
S. F.	1.6 mm filter size	Al

Table 3.9 Parameters of the cylindrical optical elements in the beam shaping telescope.

3.5 Summary

At the beginning of the chapter the importance of mode characteristics such as laser power stability, brightness, mode stability and intensity distribution were discussed.

In the radial direction, electrodes with a constant gap were replaced with shaped electrodes resulting in fundamental mode operation. Operating in the fundamental mode ensures spatial and temporal stability of the intensity distribution and high brightness. The beam quality was measured to be $M^2 = 1.1$ and the intensity distribution shows no side lobes.

In the azimuthal direction, the magnification of the optical resonator was optimized by optimizing the slope of the helix mirror. It was shown that the magnification has a direct impact on the intensity distribution in the far-field plane and therefore on the performance of the spatial filter.

The introduction of a parabolic slope created a real effective unstable resonator in the azimuthal direction eliminating a constant fluctuation of the intensity distribution in the azimuthal direction.

A simple solution for the transformation of the tilted azimuthal state of polarization of the helix-axicon resonator into linear polarization with a polarization selective coating was shown including a mechanical design that incorporates such a coating and also performs the formatting of the beam.

A full characterization of this telescope configuration, and the resonator, is performed in chapter 4.

Chapter 4

4 Beam Characteristics of the Laser

4.1 Introduction

In chapter 3 changes to the helix-axicon resonator were discussed to address issues with laser power stability, brightness, intensity distribution, mode stability and polarization. In this chapter, all optimized changes and modifications are consolidated in one laser and a characterization of the laser beam is carried out.

In the stable direction, the inter-electrode gap size is 6.6 mm at the electrode ends and 5.9 mm at the electrode centre. The electrode length is 1 m. The helix mirror has a parabolic slope with $c_1 = -1 \cdot 10^{-3}$ mm/rad and $c_2 = -1 \cdot 10^{-3}$ mm/rad². The ROC is 2.0 m and 5.657 m respectively for the helix and axicon mirror.

In section 4.2 the beam characteristics of the unformatted beam, pre telescope, are characterized and in 4.3 the beam characteristics of the formatted beam, post telescope, are characterized.

4.2 Unformatted Beam

The term unformatted beam is used to describe the laser beam at the exit of the optical resonator. This laser beam is then formatted in the telescope as described in section 3.4. First, the intensity distribution is characterized using mode burns (Plexiglas burns). The intensity distributions at distances of 1 and 3 m from the output coupling window are shown in Figure 4.1. The intensity distribution shows no signs of aperturing effects or any significant deviations from the expected Gaussian shape in the radial direction. This is a clear improvement over the constant gap configurations discussed in section 3.2.1 and a first indication that the selected inter-electrode gap shape is a good fit for the fundamental mode of the resonator in the radial direction. Another good indication for this is the relative insensitivity of laser power and beam shape to tilts of the resonator mirrors. Final

confirmation for this will be the post-telescope beam quality measurement described in section 4.3.

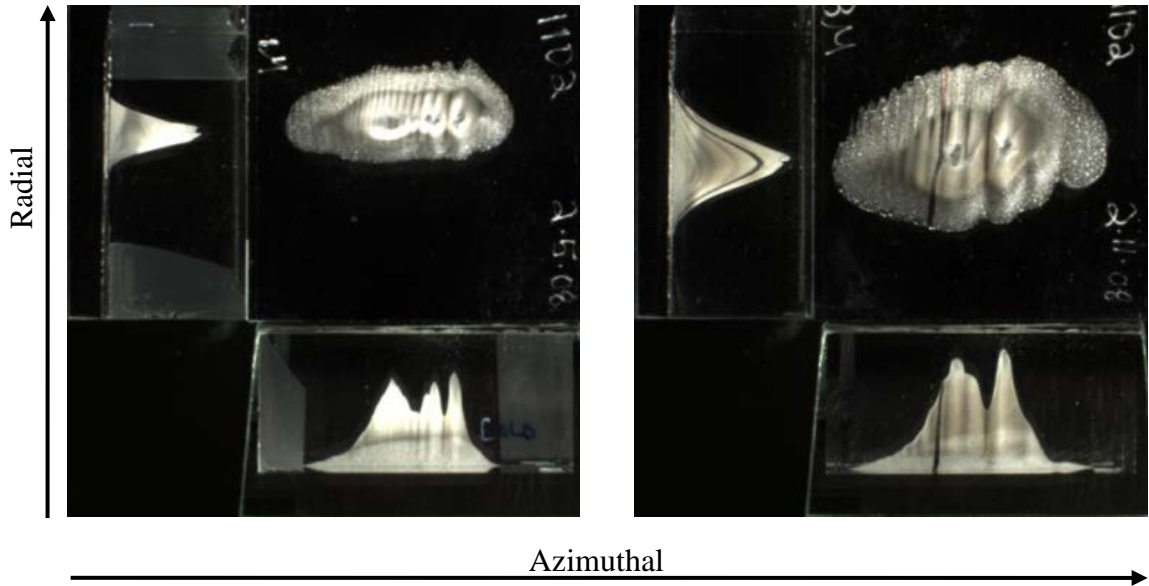


Figure 4.1 Intensity distribution of the unformatted beam at 1 m (left) and 3 m (right) from the output coupling window.

Figure 4.2 shows the temporal development of the intensity distribution in the azimuthal direction for times from 1 second up to 10 minutes after switch on. As expected, with the parabolic slope shape on the helix mirror, the intensity distribution is stable over time.

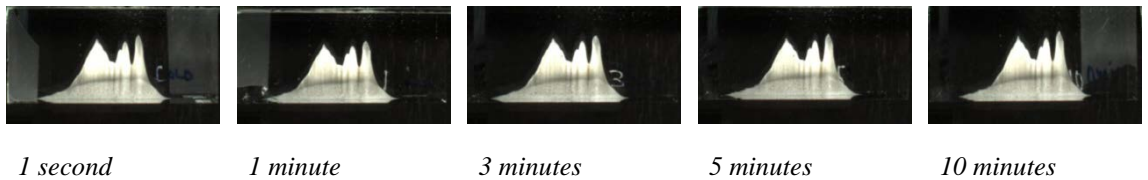


Figure 4.2 Intensity distribution of the unformatted beam in the azimuthal direction. The mode burns are taken at different times. 1 s, 1 min, 2 min, 3 min, 5 min and 10 min after tuning the laser beam on.

Next, the azimuthal direction is focused and the intensity distribution in the vicinity of the far-field is characterized with a Primes Focus-Monitor [81]. The beam formatting telescope, as shown in Figure 3.32, is used as the measurement fixture. OE2 is replaced with a flat Cu mirror and OE1 is used to focus the azimuthal direction (see Table 4.1 for mirror specifications). OE3 is removed and the Focus-Monitor is attached to the telescope

in the position of OE3. Figure 4.3 shows the measured intensity distribution in the far-field plane.

The PRIMES software includes a custom function that detects the null positions in the far-field intensity distribution and calculates the power in the side lobes representing the expected power loss in the spatial filter. Measurements are taken over a range of about 150 mm in 10 mm steps. The predicted power loss per plane is plotted in Figure 4.4. The clearest separation of the side lobes from the main peak is found in plane 7 (30 mm position). In the same plane, the predicted power loss reaches its minimum of about 7.5%.

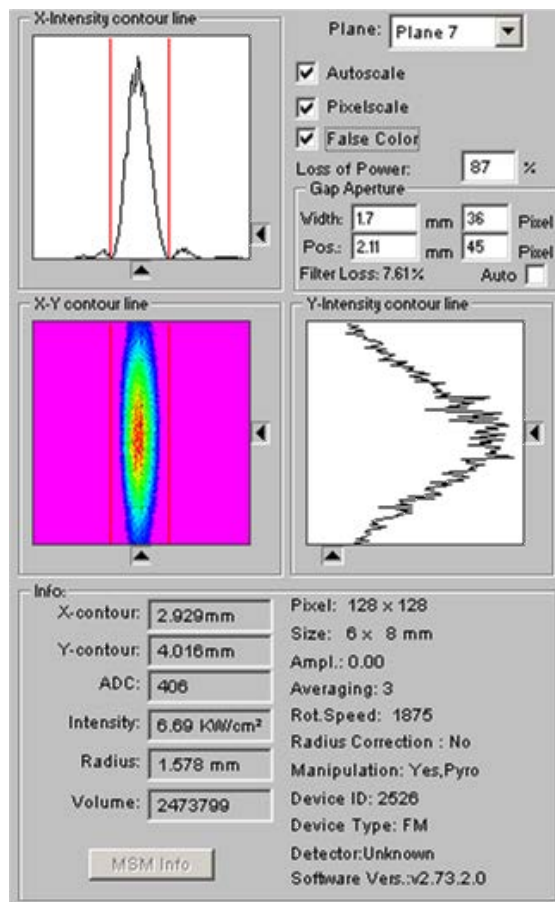


Figure 4.3 Measured intensity distribution in the far-field plane. The centre peak has a width of 1.7 mm and carries about 92% of the laser power.

The measurement is carried out with a Primes Focus-Monitor [81]. A custom function in the software calculates the expected laser power loss in the spatial filter.

The overall power measured in the unformatted beam is about 2500 W. A loss of 7.5% corresponds to a loss of about 200 W in absolute terms, which matches well with the empirically determined loss in the spatial filter (difference of measured power before and after filtering).

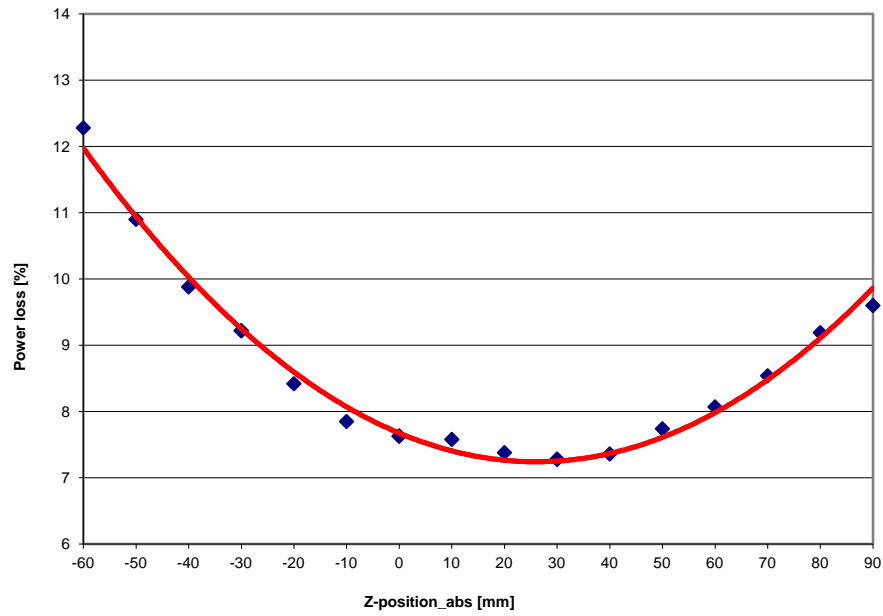


Figure 4.4 Predicted loss in the spatial filter for different measurement positions.

4.3 Formatted Beam

In order to characterize the laser beam post telescope the unformatted beam is aligned through the telescope (see Figure 3.32), filtered and then characterized in regard of intensity distribution, beam quality, astigmatism, ellipticity and polarization. The parameters of the optical elements in the telescope are shown in Table 4.1. The spatial filter has a width of 1.7 mm.

Optical element	Focal length [mm]	Substrate	Coating
OE1	1975 concave	Cu	ATFR
OE2	2700 convex	Cu	MMR-A
OE3	3700 concave	Cu	MMR-A
OE4	2280 concave	GaAs	AR; R = 99.7%

Table 4.1 Configuration of the beam formatting telescope.

Figure 4.5 shows the intensity distribution of the formatted beam from 0.1 to 7 m post telescope. The measured ellipticity is better than 0.85 in all distances and the laser beam is well collimated in both principal directions. The intensity distributions on the left side

in Figure 4.5 represent the former radial direction and the right ones the former azimuthal direction.

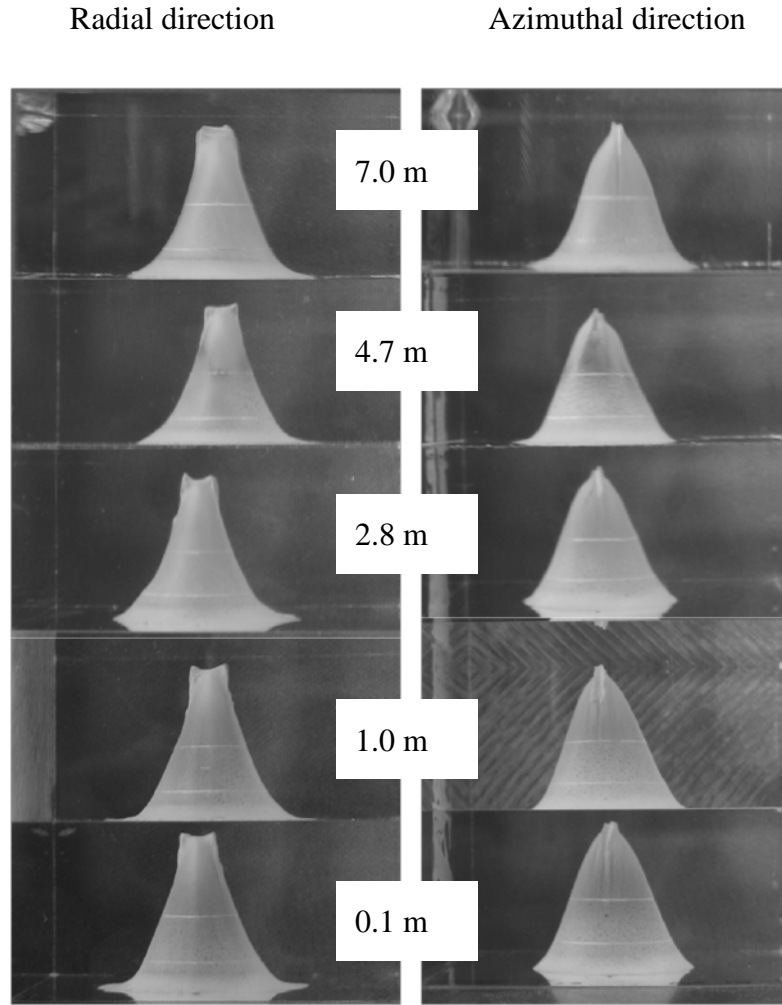


Figure 4.5 Intensity distributions of the formatted laser beam up to 7 m distance measured from the telescope exit. Left: former radial direction; right: former azimuthal direction [82].

The beam quality factors for the two principal axes are measured with a PRIMES Focus Monitor and a parabolic focusing mirror with a focal length of about 170 mm. Figure 4.7 shows the results screen of the PRIMES software. M^2 is measured to be 1.09 and 1.11 in the radial and azimuthal direction respectively. The astigmatic difference (ratio of the waist position difference in X and Y and the Raleigh length, Z_R) is 0.011 mm and ellipticity (ω_x/ω_y) varies between 0.93 and 1.00 in the different planes (see Figure 4.8). Based on the definitions of the ISO norm 11146 [83], the general astigmatic beam extracted from the resonator is now, after formatting and filtering, a stigmatic beam. The laser power stability of the formatted beam is within $\pm 1\%$ as shown in Figure 4.6.

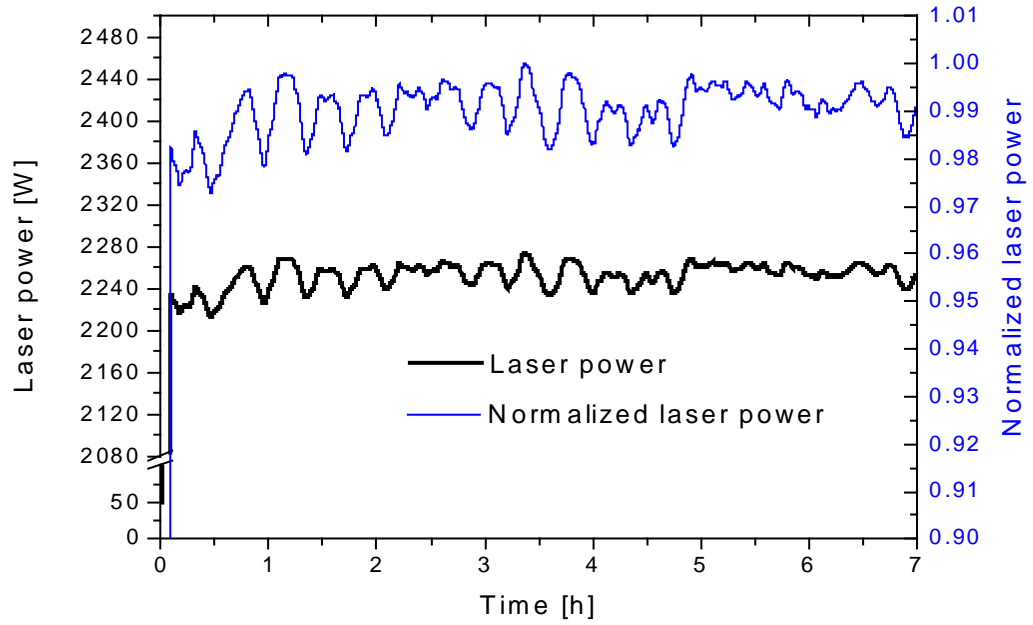


Figure 4.6 Laser power measurement over a time period of 7 hours. The normalized laser power trace shows the laser power stability within a range of $\pm 1\%$.

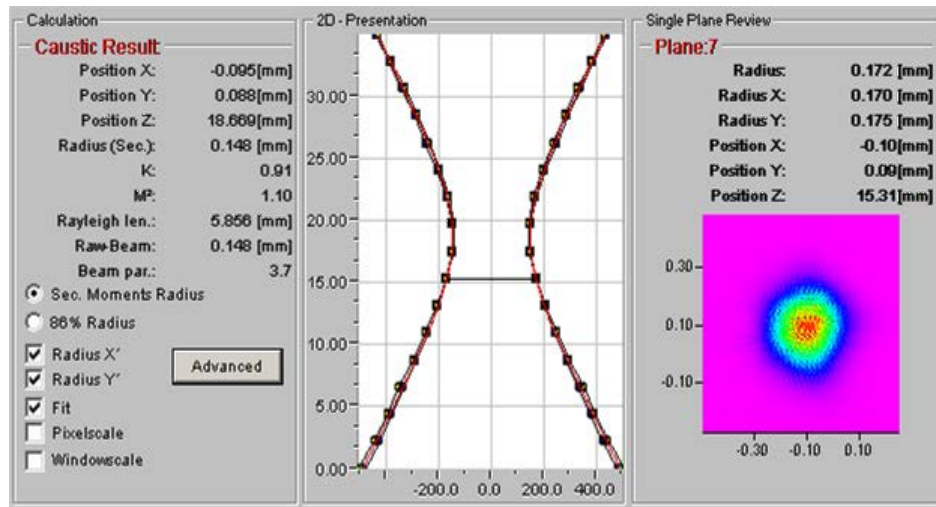


Figure 4.7 Beam quality factor measurement of the formatted beam ($f = 170$ mm): $M_x^2: 1.11$; $M_y^2: 1.09$; $Z_R: 5.9$ mm.

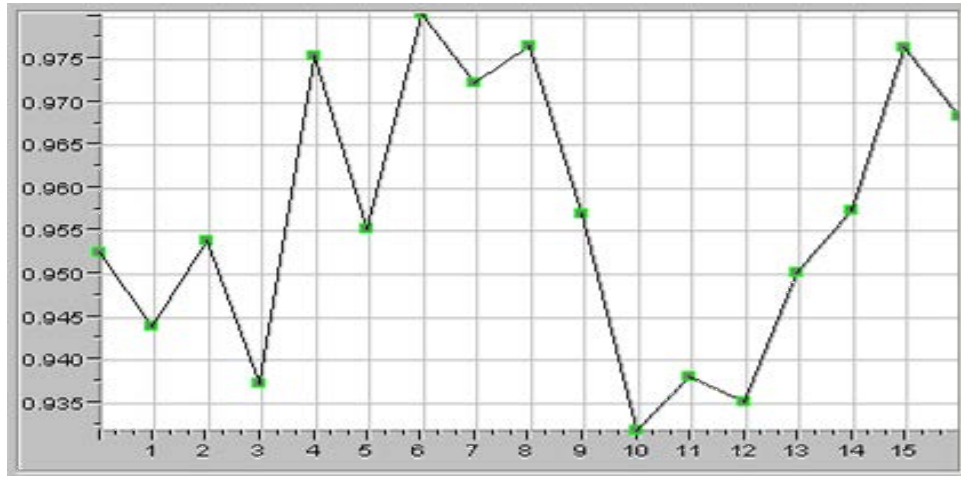


Figure 4.8 Ellipticity (ω_x / ω_y) of the formatted beam for all measurement planes. Data taken from beam quality factor measurement in Figure 4.7.

In order to measure the polarization of the formatted beam, a small portion of the beam is separated with a semi-transmissive mirror. The low power beam is deflected with a mirror that is coated with a polarization selective coating (ATFR coating). The mirror is then rotated $\pm 16^\circ$ around the beam axis and the reflected laser power is measured. The angle of the polarization rotates with the rotation of the mirror and the reflected power is a function of the angular position of the mirror.

Figure 4.9 shows the measured laser power versus the rotational position of the mirror (and power meter). The reference surface of the laser is measured with an electronic level to be at 0.3° . The lowest power level is found at an effective angle of 0.05° ($0.35^\circ - 0.3^\circ$) which is well within the resolution of the measurement. The fact that the laser power level reaches almost to zero is a good indication of the high degree of linear polarization achieved. The fact that the minimum is at zero degrees indicates that the orientation is horizontal. This result is supported by an additional polarization measurement after a 90° phase shifter where circular polarization of about 0.95 was measured.

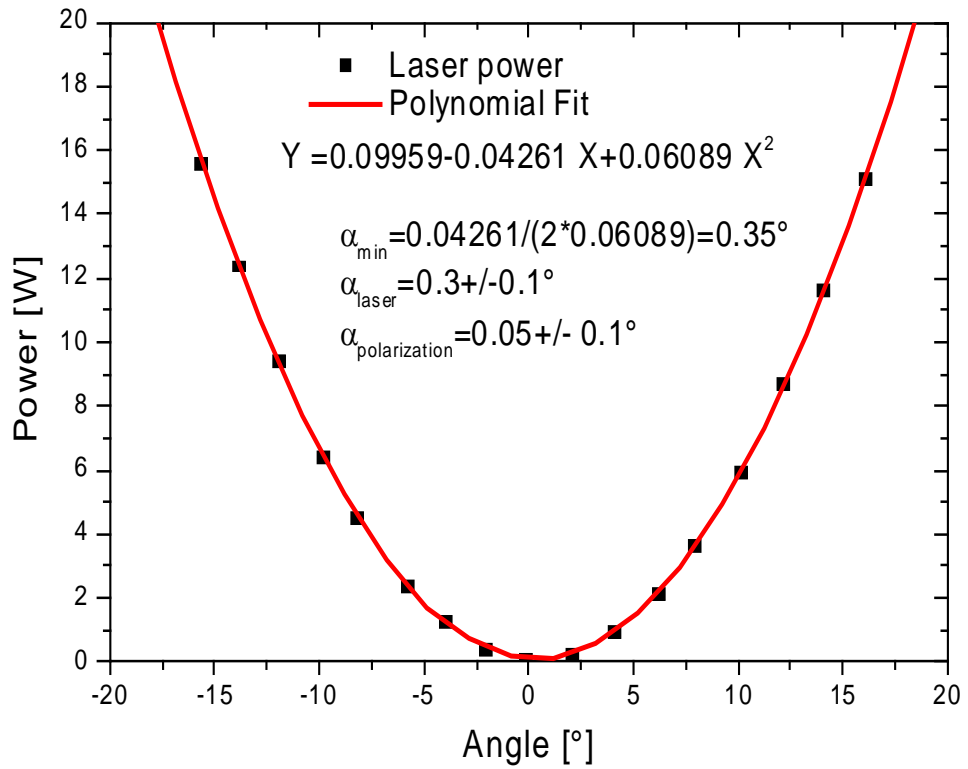


Figure 4.9 Polarization measurement of the formatted beam. The state of polarization is linear and its orientation is horizontal.

4.4 Summary

In section 3.1 the significant shortcomings of the basic helix-axicon resonator, as presented in [4], were stated, and in the following sections (3.2 to 3.4) solutions for these problems were proposed. In this chapter, the measured beam characteristics of a modified helix-axicon resonator incorporating each of these improvements have been presented.

Brightness issues were addressed by the introduction of shaped electrodes which eliminated side lobes. This was shown with mode burns of the formatted and unformatted beam and a beam quality measurement with an almost perfect result.

The chosen helix parameters yield a stable mode in the azimuthal direction and a ‘good quality’ far-field that can be filtered well.

Polarization was measured to be linear as proven in the polarization measurement in section 4.3.

Chapter 5

5 Power Scaling Principles

5.1 Introduction

In order to understand the power scaling concept of diffusion-cooled lasers based on the use of a coaxial electrode geometry and a free-space resonator, several different aspects of the design must be considered. Most importantly, the capacity to remove heat from the active medium requires evaluation. This basic thermal scaling law is discussed in section 5.2. Limitations for power scaling due to the free-space propagation and the radio-frequency (RF) excitation are discussed in section 5.3. In section 5.4, aspects of the laser efficiency are discussed in form of similarity laws, which provide a general guideline on how to maximize the electro-optical efficiency.

5.2 Thermal Laser Power Scaling Law

A basic understanding of the extractable output power of a diffusion-cooled CO₂ laser can be obtained by calculating how much heat, P_H can be extracted from the laser gas in the active region. Assuming that the temperature varies only in one direction in the active medium, for instance in x , where x represents the radial direction of the resonator (inter-electrode gap size), the extractable heat can be calculated by solving the one-dimensional thermal conduction equation, where κ is the thermal conductivity and T is the temperature.

$$P_H = -\kappa \cdot A \cdot \frac{\partial T}{\partial x} \tag{5.1}$$

P_H represents a heat flow through a cross-section A . How much heat is generated in the active medium depends on the efficiency, η of the laser and the RF input power level, P_{RF} used to excite the CO₂ laser gas mix, as shown in Equation 5.2. A limit for P_{RF} is given

by the maximum ‘allowable’ temperature of the laser gas, which is about 600 K [2], up to which the laser can still operate efficiently.

$$P_H = (1 - \eta) \cdot P_{RF} \quad 5.2$$

In the case of a coaxial electrode configuration, the cross-section A , through which the heat is flowing, is equal to the surface area of a cylinder with a radius, r_{av} equivalent to the average radius of the inner and outer electrode and length, L .

$$A = 4\pi r_{av} L \quad 5.3$$

The extractable laser power is then $P_L = \eta P_{RF}$. For a constant value of the thermal conductivity the extractable laser power can be calculated to be:

$$P_L = \frac{\eta}{(1 - \eta)} \cdot \kappa \cdot \frac{A}{d} \cdot \Delta T \quad 5.4$$

with d being the average inter-electrode gap size. Substituting A with Equation 5.3 leads to

$$P_L = \frac{\eta}{(1 - \eta)} \cdot \kappa \cdot \frac{4\pi r_{av} \cdot L}{d} \cdot \Delta T \quad 5.5$$

A typical value for the heat conductivity of the laser gas mix is about 0.1 W/(m K) at 300 K [84].

Combining some of the factors in Equation 5.4 in a single scaling constant, c_s leads to a simple version of the thermal power scaling law showing how the laser output power, P_L of diffusion-cooled CO₂ lasers with coaxial electrodes scales with its inter-electrode gap size, d and its electrode surface area, A .

$$P_L = c_s \cdot A/d \quad 5.6$$

5.3 Power Scaling Limitations

Equation 5.5 provides a basic understanding of the extractable laser power of a diffusion-cooled, coaxial laser. Depending on the chosen geometry and operating parameters of the gas discharge, limitations due to the free-space configuration and discharge uniformity need to be considered. The impact of the free-space configuration on laser power scaling is discussed in section 5.3.1, the impact of the discharge parameters in section 5.3.2.

5.3.1 *Free-space propagation*

A closer examination of the thermal power scaling law defined in Equation 5.6 reveals some limiting factors.

The electrode surface area, A can be scaled by either changing the electrode length, L or the electrode diameter, r_{av} . The total discharge length, L of the laser is in general limited by the electrical properties of the laser (see section 5.3.2). Increasing the electrode radius has more practical rather than physics based limitations. With increasing electrode diameters, the resonator mirrors become larger, more expensive and more sensitive to deformation.

If a resonator set-up with free-space propagation is chosen and fundamental mode operation is required, the inter-electrode gap size, $d(L)$ is determined by the size of the fundamental mode of the resonator and is therefore given for a specific set of g-parameters. Since the diameter of the beam is proportional to $(1+L^2)^{1/2}$, (see Equation 2.13) and the surface area, A scales only linearly with length ($A = 2\pi \cdot r \cdot L$), power scaling with discharge length is limited. After a certain electrode length is reached, a further increase in length does not yield additional cooling capacity.

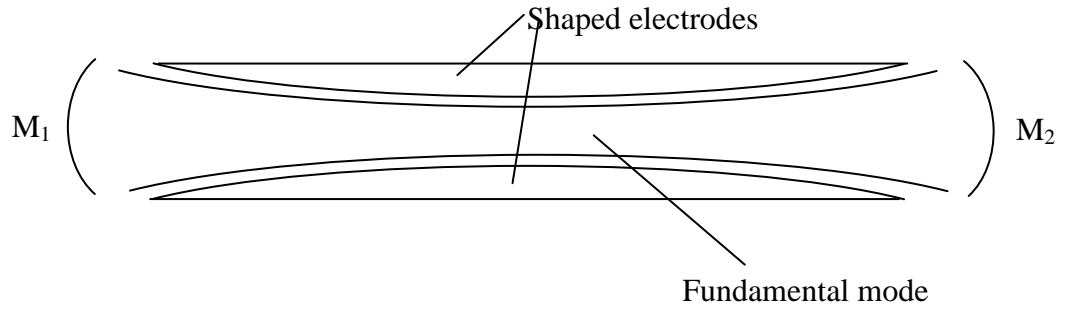


Figure 5.1 Stable resonator with free-space propagation and shaped electrodes.

If the resonator radius, r_{av} is kept constant the laser power scaling law can be re-written as

$$P_L = c_s^* \cdot L / d_{av} \quad 5.7$$

Since the inter-electrode gap size, d is not constant over the electrode length, L the average value of the gap size, d_{av} has to be used in Equation 5.7. Figure 5.2 shows the calculated ratio, L/d_{av} for discharge lengths between 0.5 and 3 m for the resonator configuration shown in Figure 5.1. It can be seen, that the ratio L/d_{av} is not increasing linearly with L but starts to roll over at a length of about 1.2 m. If the length is doubled, from 1 to 2 m, the increase in L/d_{av} is only about 50%. For an increase of 300% in length, from 1 to 3 m, L/d_{av} increases only by about 75%. For completeness, it should be mentioned that there is also a limit for the resonator length on the lower side. Even though for shorter electrode lengths the power scaling law is more favourable, laser power fluctuation will become an issue if the resonator is too short due to the growing longitudinal mode spacing. For the calculation, the M^2 factor is set to 1.1 and the g -parameters are kept constant for all resonator lengths.

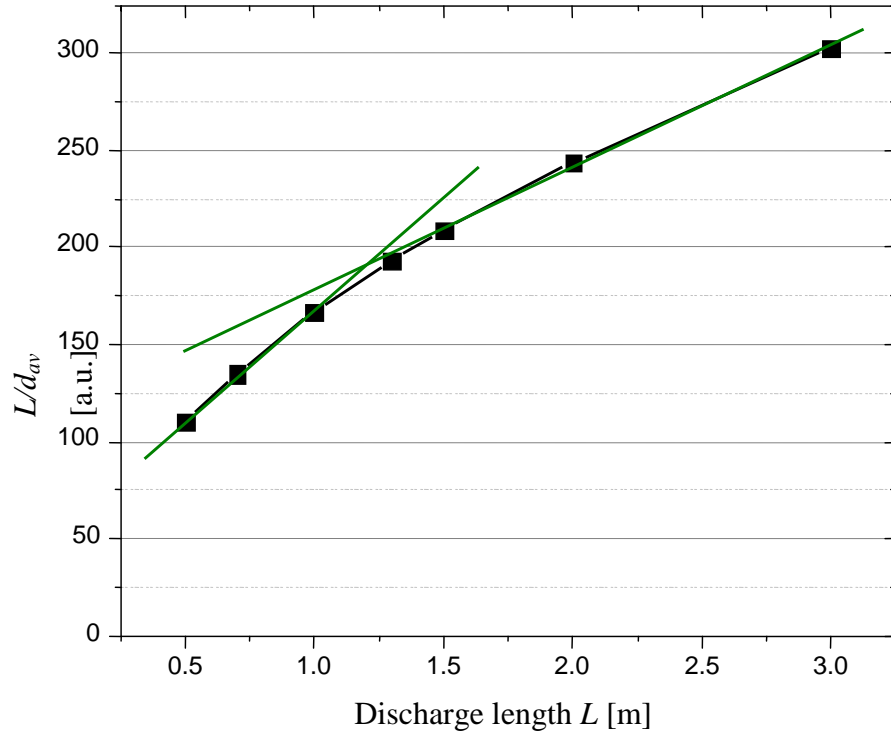


Figure 5.2 The L/d_{av} ratio is plotted versus electrode length showing the non-linear increase of cooling capacity with length.

5.3.2 RF system and longitudinal voltage distribution

The electrode system of RF excited CO₂ lasers can be described as a lossy coaxial transmission line, where a standing wave occurs with a variation of the electrical field along the resonator axis. The achievement of a uniform discharge distribution is dependent on producing a radial electrical field which is uniform along the electrode length. The most homogeneous voltage distribution is at the maxima or minima of the sinusoidal waveform. As a rule of thumb, the length of the laser should not exceed 1/8 of the RF wavelength [52], which is 1.38 m for an excitation frequency of 27.12 MHz.

In order to overcome uniformity problems of the discharge and to eliminate it as a limiting factor in power scaling, different approaches have been developed to reduce the variation of the E -field along the electrodes. The most common and obvious ones are listed below:

- **Multiple feeds:** In order to minimize the E -field variation along the length of the electrodes, the RF is fed into the electrode at multiple points. Controlling the

phase of the multiple feeds to avoid destructive interference between the feed points needs great care.

- **Segmented electrodes:** The electrodes are segmented and the length of the individual segments is much smaller than the wavelength.
- **Termination:** If the overall length of the electrodes is less than or about 1/8 of the RF wavelength, a reactive termination at the end of the electrodes can move the position of the stationary wave pattern over the electrode length to minimize the variation of the E -field strength along the electrodes [85], [86]. In combination with an end feed, one termination is needed at the opposite end of the feed [58]. With a centre-feed two terminations at both ends of the electrodes can be applied to further reduce the E -field variation.
- **Distributed inductances:** Distributed parallel inductors are added to the discharge structure in order to compensate for the capacitance of the electrode structure and create a long stationary wave over the electrode length [87]. The higher the frequency the higher is the number of inductors required per unit length.
- **Lower excitation frequency:** Lower excitation frequencies result in longer wavelengths and therefore less variation in the E -field distribution along the electrodes. However, lower excitation frequencies may be accompanied by serious downsides as discussed in section 5.4.

5.4 Similarity Laws

Maximizing the electro-optical efficiency of the laser is crucial for power scaling. A set of similarity laws, or invariant parameters, was developed in [22] to help in this effort. The parameters that are most relevant are summarized below.

The excitation frequency, f plays a crucial role in the operation of CO₂ lasers and RF discharges. According to [22] there is an excitation frequency, f_{opt} that optimizes the laser performance for a specific inter-electrode gap-size, d . According to this similarity law the product of excitation frequency and inter-electrode gap size is constant and should equal about 280 mm·MHz.

$$fd = 280 \text{ mm} \cdot \text{MHz} \tag{5.8}$$

Applying this similarity law to an average inter-electrode gap size of 6.5 mm results in an optimum excitation frequency of about 40 MHz. Likewise, the inter-electrode gap size for an excitation frequency of 27 MHz should be about 10 mm. In spite of this, the power scaling activities will be carried out at 27.12 MHz due to the availability of RF-generators at this frequency.

A second similarity law defined in [22] states that the product of laser gas pressure and inter-electrode gap size should be constant. The laser gas mix is easily optimized empirically in the laboratory by varying the gas pressure and gas mix. Optimizing the gas pressure satisfies the similarity law. Optimizing the laser gas mix optimizes the electron temperatures in the plasma and heat removal.

Two more aspects need to be considered when choosing the excitation frequency:

- Losses in the sheaths due to ohmic resistance are approximately inversely proportional to the square of the excitation frequency ($1/f^2$) [22].
- An increase in the RF power density to increase output power is not only limited by the heat removal capacity of the electrode system, but also by instability processes that disturb the spatial uniformity of the plasma. Instabilities in the discharge can lead to ineffective excitation processes or even to the destruction of the laser (see section 2.3).

Understanding these power scaling principles and limitations leads to a few conclusion for the design of the scaled-up version:

- The discharge length can only be increased moderately for several reasons: a) Significant increases in discharge length increase the average inter-electrode gap disproportionately. b) The size of the diamond window increases with resonator length increasing production costs. c) The maximum length of one-piece electrodes is limited by the working range of the turning machine to 1.4 m.
- Distributed inductances must be implemented to minimize the variation in the brightness distribution of the discharge along the electrode length.
- Since only RF-generators with a frequency of 27.12 MHz are available for this work the similarity laws will be violated and therefore only a sub-maxima for the laser power can be reached.

Chapter 6

6 Power Scaling: Design and Performance of the Scaled-up Laser

6.1 Design Options for the Scaled-up Version

In order to scale up diffusion-cooled CO₂ lasers to higher power levels, while preserving the extraction efficiency and free-space beam characteristics, and also keeping the excitation frequency invariant, it is necessary to increase the discharge area. Therefore, the average electrode radius, r_{av} and discharge length, L are the only two parameters available to change in order to scale laser power. Varying one or the other, or both, results in a number of physical and technological implications that have to be evaluated from a practical point of view. If both, r_{av} and L are increased, a completely new laser needs to be designed and the number of common parts between the different lasers is then small. The same holds true if only the radius, r_{av} is increased. An increase in the length, L provides an opportunity for a common structural platform for different power levels and brings with it a variety of practical commercial advantages: minimum number of parts, high flexibility in production and synergies in product development.

For these reasons, the scaled-up version of the annular laser is based on extending the *length* of the basic laser. The downside of this approach is that the limitations imposed by longer electrodes, as discussed in section 5.3, need to be overcome. The techniques used to overcome these limitations as well as other aspects of the resonator design for higher laser output power are discussed in this and the following chapter.

As a reminder, the power scaling activities are applied to the basic laser which has a discharge length of 1 m and an output power level of about 2.5 kW in the unformatted beam resulting in a power level of 2.2 kW in the formatted beam. For the scaled-up version the target output power is 3.5 kW post telescope which requires a power level of about 4 kW in the raw beam.

6.2 RF and Discharge Distribution

In order to reach the target output power of 3.5 kW it was decided to extend the electrode length in the scaled-up version by about 30 cm to 130 cm. It was determined that this modest extension provides enough additional cooling capacity for a significant increase in output power, but does not present serious problems in the manufacture of the one-piece electrodes and related requirements.

Figure 6.1 shows schematic representations of the basic and scaled-up version of the laser. The basic version, with a discharge length of 1 m, is short enough to be operated in an end-feed with termination configuration. The longer, scaled-up version requires distributed inductances in order to ensure a uniform distribution of the gas discharge along the electrodes.

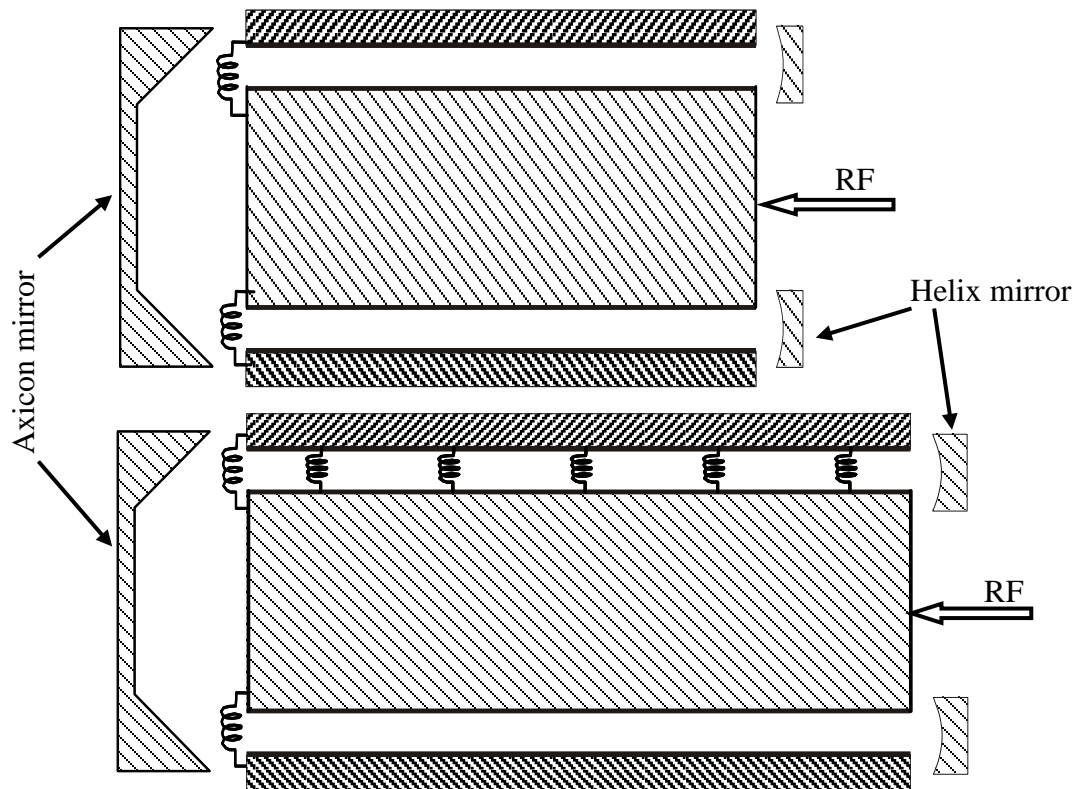


Figure 6.1 Schematic representation of the electrical configuration of the coaxial laser. Top: End-feed with termination for the basic version of the laser; Bottom: End-feed with termination combined with distributed inductances for the scaled-up version of the laser.

A general understanding of the electric properties, and therefore of the voltage and discharge brightness distribution along the electrodes, can be gained by representing the electrode system in an equivalent circuit model. The coaxial electrode structure can be

thought of as a lossy coaxial transmission line, and the equivalent circuit of a unit length of a lossy transmission line is shown Figure 6.2.

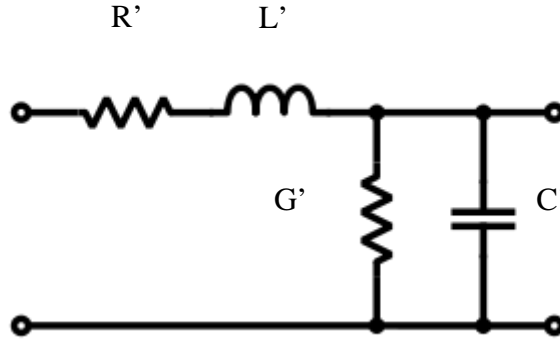


Figure 6.2 $R'L'C'G'$ equivalent circuit model of a unit length of the lossy transmission line.

According to transmission line theory [88] the voltage, $V(x)$ and current, $I(x)$ at any point along the length of the transmission line can be calculated using the basic differential equations for lossy transmission lines:

$$\frac{dV(x)}{dx} = -zI(x) \quad \frac{dI(x)}{dx} = -yV(x) \quad 6.1$$

and

$$\frac{d^2V(x)}{dx^2} - \gamma^2 V(x) = 0 \quad \frac{d^2I(x)}{dx^2} - \gamma^2 I(x) = 0 \quad 6.2$$

where $\gamma^2 = z \cdot y$ is the real part of the complex propagation constant. The series circuit elements R' and L' are the parasitic resistance and inductance per unit length and the parallel circuit elements, G' and C' are the conductance and capacitance per unit length of the lossy transmission line. It must be recognized that the capacitance per unit length, C' changes when the discharge is ignited, and this also influences the conductance per unit length, G' which represents the dielectric losses of the gas discharge.

The series and shunt elements z and y from Figure 6.2 can be expressed as

$$z = R' + j\omega L' \quad 6.3$$

$$y = G' + j\omega C' \quad 6.4$$

With those line parameters the complex propagation constant, γ and the complex characteristic impedance, Z_l of the transmission line can be calculated. C' and G' must be determined experimentally since the values are dependent not only on the electrode geometry, but also on the laser gas pressure and mixture, on the RF frequency and on the applied local RF power density and thus, the local voltage between the electrodes [89]. For the following analysis the parasitic resistance, R' will be neglected as justified in [86] and so

$$\gamma = \sqrt{zy} = \alpha + j\beta = \sqrt{j\omega L'(G' + j\omega C')} \quad 6.5$$

$$Z_l = \sqrt{\frac{z}{y}} = \sqrt{\frac{j\omega L'}{G' + j\omega C'}} \quad 6.6$$

The real part, α of the propagation constant, γ describes the attenuation due to resistive losses. The imaginary part, β describes the propagation properties of a wave as in a lossless line (phase constant).

The voltage along the transmission line, $V(x)$ then varies as given by

$$V(x) = V_0 \cos(-j\gamma x) \quad 6.7$$

where V_0 is the voltage at the end of the open ended transmission line ($x = L$). The voltage at the feed point is the voltage where $x = 0$.

The capacitance of the transmission line rotates the phase angle resulting in a voltage variation [86]. This voltage variation can now be addressed in two ways: i) use distributed inductances to rotate the phase angle back as shown in [90] or ii) use resonant distributed inductances as shown in [87]. In principle, the used electrical elements (distributed

inductors) required are the same for the two options, but the difference is in the values chosen for the distributed inductances. In ii) the values are chosen such that they form a resonant circuit with the capacitance of the electrodes at the RF excitation frequency when the discharge is ignited.

In order to better understand the distributed inductances a more detailed equivalent circuit is shown in Figure 6.3, the equivalent circuit is expanded to include the inductance, L_{DI} of the distributed inductance.

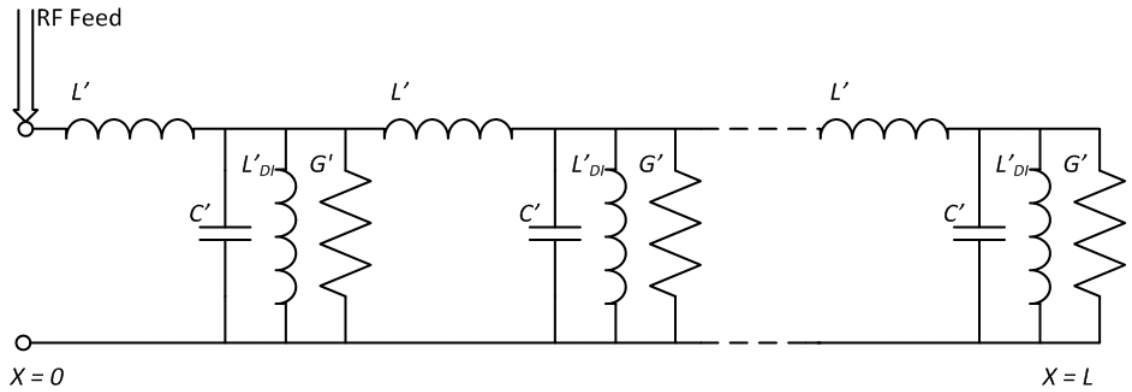


Figure 6.3 Equivalent circuit of the electrode structure including the distributed shunt inductance L'_{DI} . The electrodes have a length of L and the rf-feed is at $x = 0$

With the distributed inductances the net capacitance, C_{net} per unit length changes to

$$C_{net} = C' \left(1 - \frac{1}{\omega^2 L'_{DI} C'} \right) \quad 6.8$$

If now the values for the distributed inductances are chosen in a way such that for the excitation frequency, ω used $L'_{DI} = 1/\omega^2 C'$, then the typical voltage variation of a lossy transmission line is minimized. A small slope in the voltage remains due to the conductance G' , but for all practical purposes, the voltage distribution along the electrodes is uniform. In our case the distributed inductances rotate back the phase angle and compensate for the capacitance of the transmission line, but do not form a resonant circuit.

Due to the design of the optical resonator, there are two regions within the resonator volume with no circulating laser radiation. In these regions pockets are milled out so that

the inter-electrode gap size is increased and a discharge free volume is created. The inductors are positioned in these volumes to avoid damage caused by the laser radiation and/or the gas discharge. Figure 6.4 shows the schematic representation of the electrode system with the shunt inductors (distributed inductances). The inductance is realized with discrete inductors that connect the outer and inner electrodes. The inductance can be adjusted by changing the length of an aluminium sheet metal stripe outside the vacuum system.

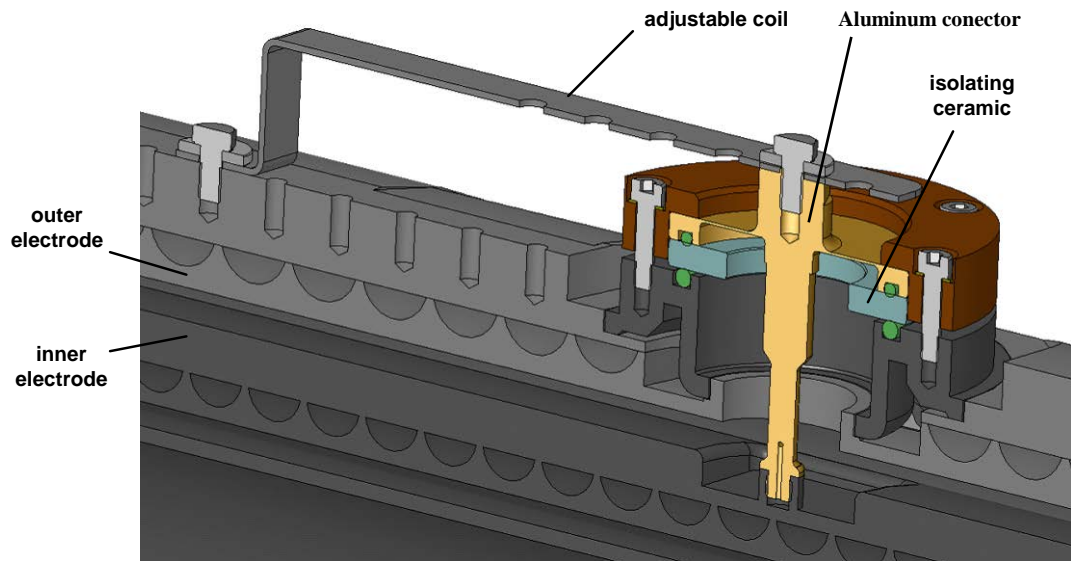


Figure 6.4 Schematic representation of the distributed inductances and their integration into the mechanical structure of the laser [91].

The value of the inductances and their spacing can easily be optimized empirically since the actual electrical elements that determine the inductance sit outside the vacuum system and are therefore easily accessible (see Figure 6.4).

In order to achieve a sufficiently uniform discharge distribution a minimum of two inductors are needed, one in the centre of the electrodes and a second one between the first one and the end of the electrodes, on the opposite side of the RF feed.

Figure 6.5 shows the measured brightness distribution of the gas discharge in Volts at five different positions along the electrodes (at the helix and axicon end, the middle and in between the middle and the two ends). (A) represents the scaled-up version with a termination only and (B) a combination of termination and distributed inductances. The brightness was measured with photodiodes. The variation of the discharge brightness is

greatly reduced when the distributed inductances are combined with the end-feed and termination configuration.



Figure 6.5 Measured brightness distribution of the gas discharge in Volts at five different positions along the electrodes (at the helix and axicon end, the middle and in between the middle and the two ends) for the scaled-up version of the laser with 30 kW RF input power [92]. The bar graphs show the signal of a photo diode for two different electrical configurations: (A): end-feed and termination; (B): end-feed and termination with distributed inductances (shunt inductors L'_{DI}).

A comparison of the laser performance with and without the shunt inductors shows that the distributed inductances not only enable a uniform distribution of the discharge in the longer (scaled-up) version, but also improved the electro-optical efficiency compared to the ‘basic’ version. Table 6.1 compares the laser output power and electro-optical efficiencies for the basic version and the scaled-up version at two different RF input power levels. The standard RF input power level for the basic version is 18 kW. When the scaled-up version is operated at the same input power level the electro-optical efficiency increases from 13.3 to 15.0% resulting in an additional 300 W in output power. When the RF input power level is increased until the electro-optical efficiency is reduced to the level of the basic laser the output power reaches about 4 kW. This is an increase of 60% in laser power with an increase in electrode length of 30%. It also means that the electro-optical efficiency of the basic version could also be increased significantly if distributed inductances were added to the termination with end-feed configuration at a discharge length of 1 m. However, this issue is not investigated further in this work, but since the

basic laser is only one meter in length, one element in the middle of the electrodes should suffice.

Length [m]	RF input power [kW]	Laser power [W]	Electro-optical efficiency [%]
1.0	18	2400	13.3
1.3	18	2700	15.0
1.3	30	4000	13.3

Table 6.1 Comparison of laser performance of the basic and scaled-up version at different RF input power levels.

6.3 Optical Resonator

One of the main reasons to scale up laser power by extending the electrodes was to maximize the number of common parts between the basic and scaled-up versions. In order to determine if the resonator mirrors of the basic version can also be used in the scaled-up version, tests and simulations are carried out to verify that the impact of the increased length on the performance of the resonator is acceptable. The performance of the optical resonator is judged by the extraction efficiency and beam quality in the radial direction and the far-field intensity distribution and fractional output coupling in the azimuthal direction.

6.3.1 Verification of the radial direction

In the basic version of the laser (with a length of one meter) the required inter-electrode gap size is 6.6 - 5.6 - 6.6 mm for the 2 m radius of curvature. Since the resonator length has now been increased the required gap size needs to be re-optimized. The results of the simulation are shown in Figure 6.6, and the predicted electrode gap sizes are 7.0 - 5.8 - 7.0 mm. Subsequent experimental results confirm that with this configuration good results can be achieved in terms of laser power and beam quality. Laser output power levels of up to 4 kW were realized and the measured M^2 values in the radial direction are around 1.1.

Based on the beam measurement results achieved for the radial direction, the current mirror pair can also be used for the scaled-up version. Next, the azimuthal direction is investigated.

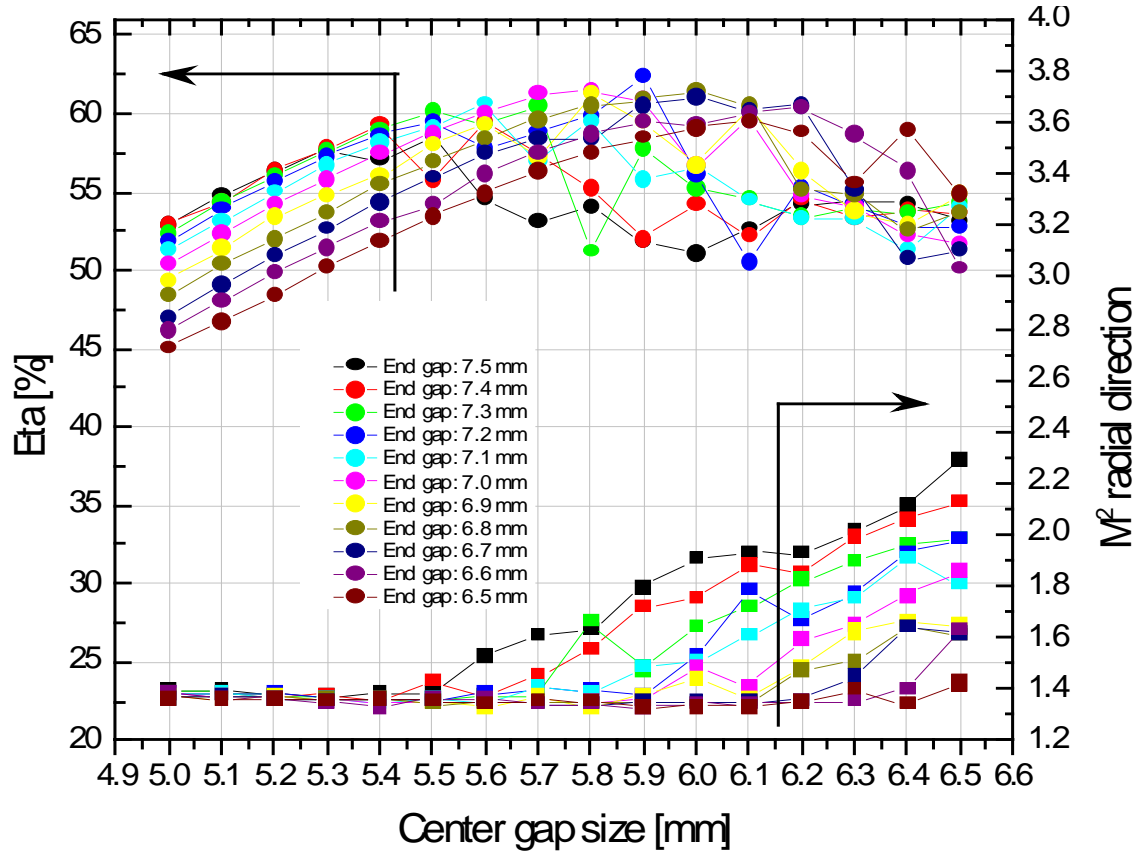


Figure 6.6 Inter-electrode gap size optimization for a resonator set-up with a ROC = 2.0 m and $c_1 = -1 \cdot 10^{-3}$ mm/rad and $c_2 = -1 \cdot 10^{-3}$ mm/rad². The end gap size is represented by the differently coloured lines; the centre gap is plotted on the x axis. The circles represent the extraction efficiency; squares represent the M^2 values in radial direction.

6.3.2 Verification of the azimuthal direction

The fractional output coupling is given approximately by $1-1/M$, where M is the magnification of the resonator. The magnification is a function of the size of the outcoupled beam size (see Equation 3.7) which in turn is a function of the resonator length, L . Since the resonator length was increased significantly it has to be verified that the current values for c_1 and c_2 yield the maximum output power (extraction efficiency) and a far-field intensity distribution that can be filtered effectively.

Figure 6.7 shows the calculated extraction efficiency and beam quality versus fractional output coupling for a resonator configuration with a ROC of 2.0 m, a resonator length of

1300 mm and an inter-electrode gap size of 7.0 - 5.9 - 7.0 mm. The fractional output coupling is defined as the ratio of the extracted power to the internal circulating power. In the simulation, the fractional output coupling is varied from about 2.5 to 9% corresponding to a range of c parameters from $-0.4 \cdot 10^{-3}$ to $-1.2 \cdot 10^{-3}$ mm/rad. The values of c_1 and c_2 are set to be equal.

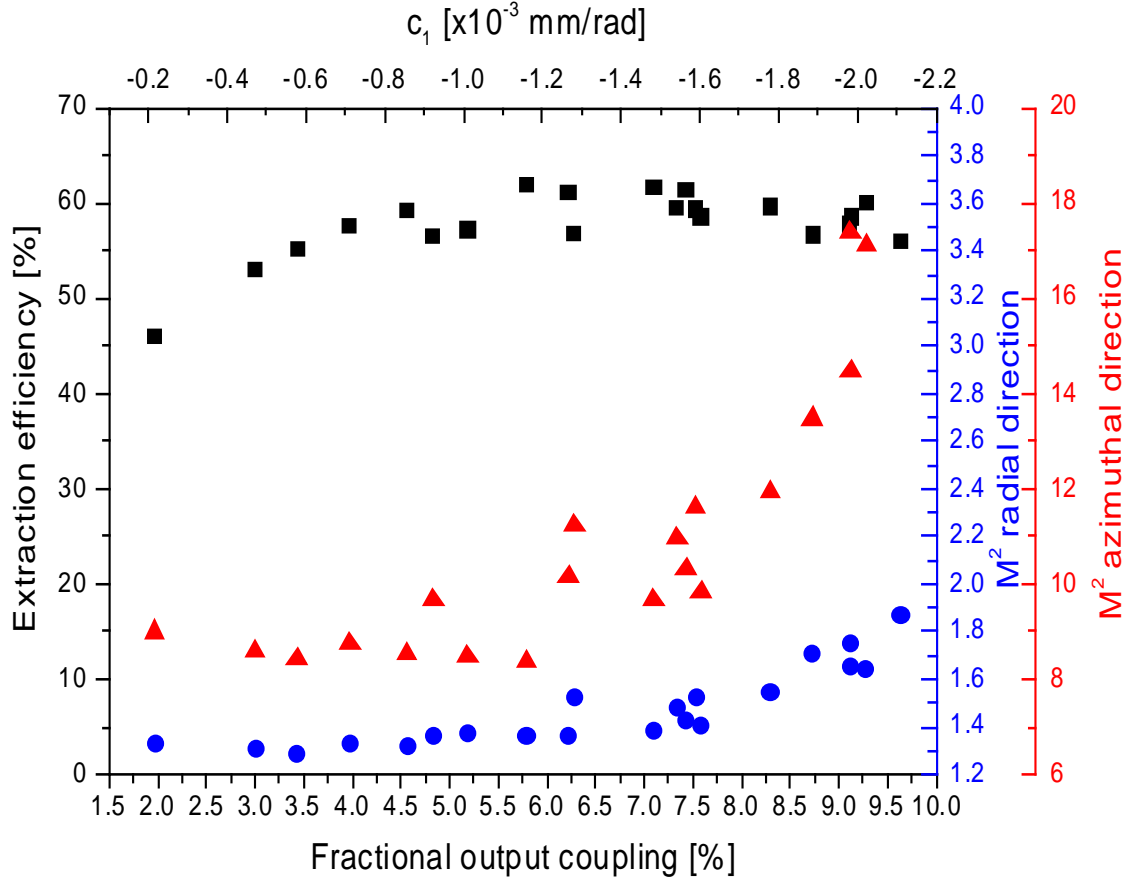


Figure 6.7 Extraction efficiency and beam quality vs. fractional output coupling for a resonator configuration with $ROC = 2.0$ m; $L = 1300$ mm; gap size: 7.0 - 5.9 - 7.0 mm.

Judging by the calculated extraction efficiency and radial beam quality, the current values for the c parameters ($c_1 = -1 \cdot 10^{-3}$ mm/rad and $c_2 = -1 \cdot 10^{-3}$ mm/rad²) used in the basic laser should also yield good performance in the scaled-up laser, since both the extraction efficiency and the radial beam quality are at or close to their optimum. The resulting fractional output coupling of this mirror pair in the scaled-up version is about 5.2%.

Figure 6.8 shows the simulated cross sections of the far-field intensity distribution for the same range of fractional output coupling values. As expected, with a decrease in fractional output coupling, the width of the main peak increases. But more importantly, for a fractional output coupling of 5.2%, which corresponds to the current c parameters

($c_1 = -1 \cdot 10^{-3}$ mm/rad and $c_2 = -1 \cdot 10^{-3}$ mm/rad²), the null in the far-field intensity distribution used for spatial filtering has disappeared. For fractional output coupling values higher than about 8% the first side maximum and the main peak merge and are indistinguishable. However, a fractional output coupling value of 4% produces a far-field intensity distribution with clear nulls. Fractional output coupling values that are too small are also problematic, since the extraction efficiency decreases and the energy in the side lobes increases.

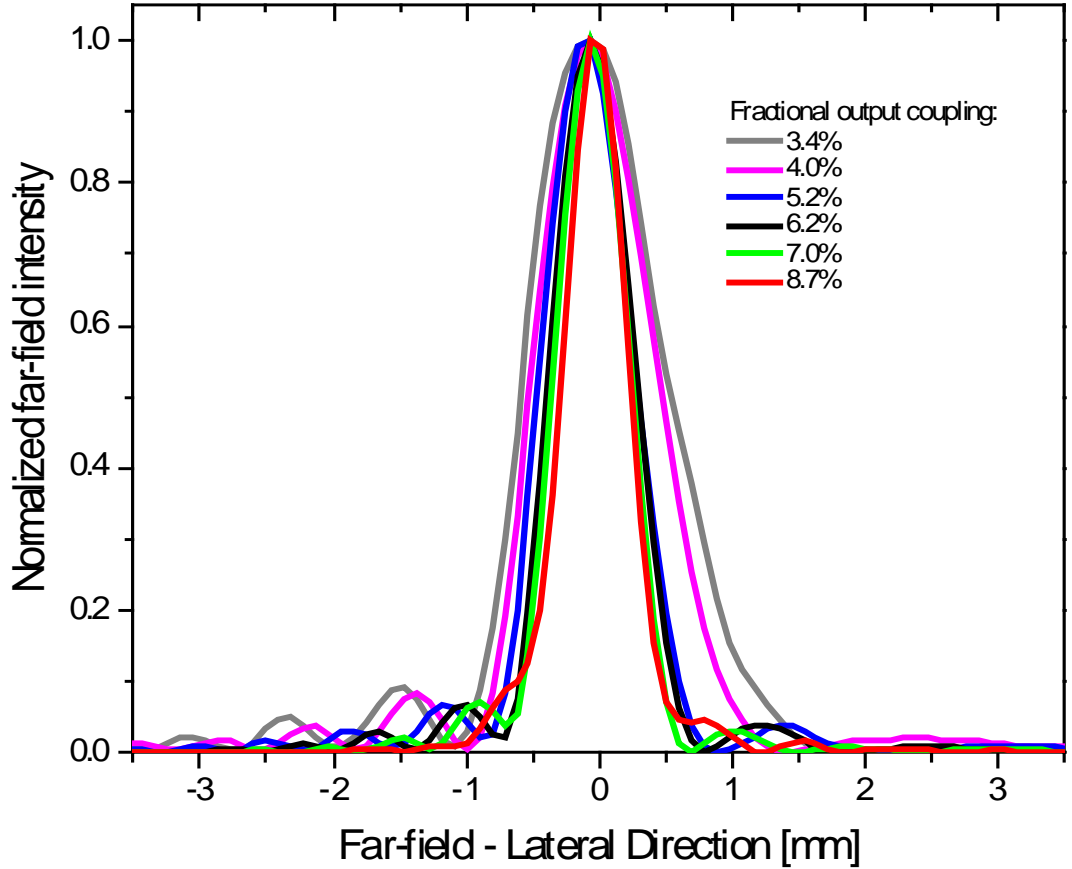


Figure 6.8 Cross section of the far-field intensity distributions for different fractional output coupling values (same resonator configuration as in Figure 6.7).

In order to better visualize how the main peak and first side maxima merge with increasing fractional output coupling values the data from Figure 6.8 is plotted in a 2D plot in Figure 6.9.

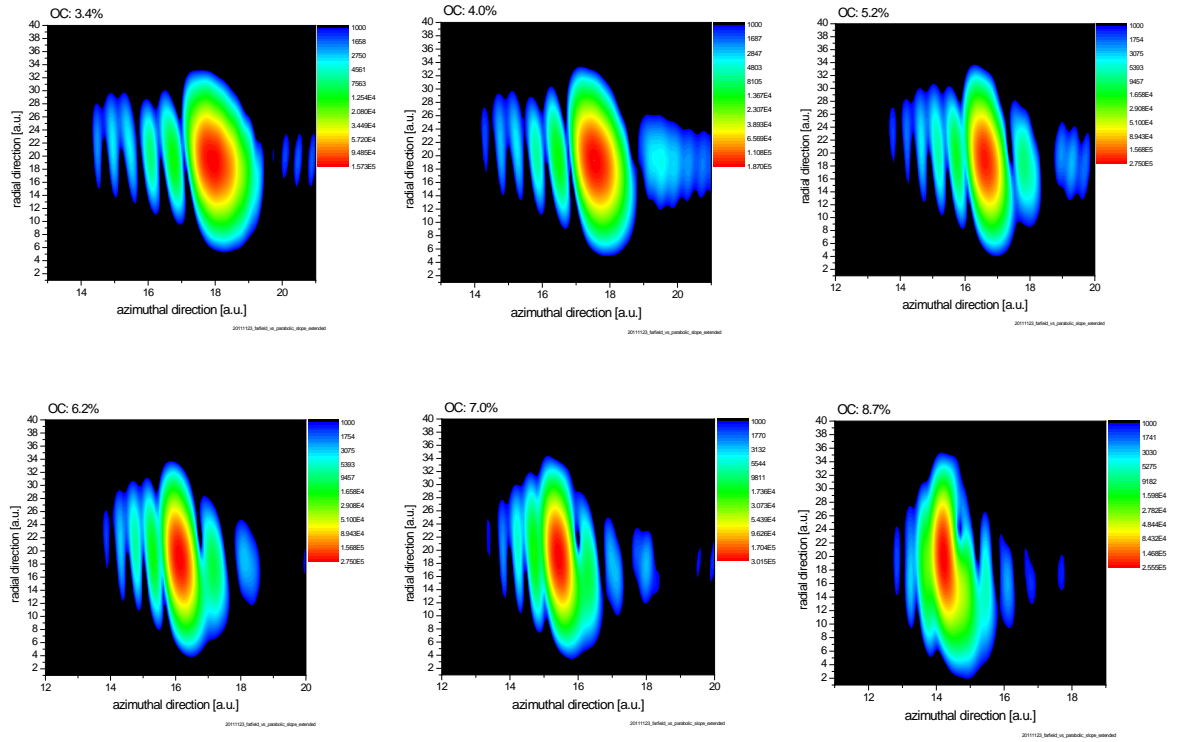


Figure 6.9 2D representation of the far-field intensity distribution (same data as in Figure 6.8); the fractional output coupling values are 3.4%, 4.0%, 5.2%, 6.2%, 7.0%, 8.7% starting from top left.

Of course, the disappearance of the nulls has a severe impact on the spatial filtering result. Again, with the helix mirror used in the basic version of the laser the fractional output coupling of the scaled-up version is about 5.2%. Even though the measured beam quality after spatial filtering reaches acceptable M^2 values of 1.1, the near-field intensity distribution of the formatted beam shows undesired features. The final confirmation that the spatial filtering is compromised with this arrangement is derived from application trials with the laser (laser cutting of metals). Whereas the cutting results with the basic version show no signs of directionality, the cut quality achieved with the scaled-up version shows clear signs of ‘cut-quality directionality’. Thus what is observed when cutting a square is that three sides are good and one side has increased roughness. Figure 6.10 shows two parts of the same material and thickness. The upper part represents the one side with increased roughness, the lower part the three other (good) sides.



Figure 6.10 Cutting results in 1/4" steel processed with O_2 . The upper part shows increased roughness while the lower part has a very smooth surface finish.

This leads to quite an important conclusion; the scaled-up version cannot utilize the exact same helix mirror as the basic version. Of course, the mirror blank can still be the same, but the final machining needs to be different, the value of fractional output coupling needs to be reduced in order to generate a far-field intensity distribution that has clear nulls for spatial filtering.

Chapter 7

7 Resonator Optimization

7.1 Resonator parameters

7.1.1 *Helix slope optimization*

In section 3.3.4 the impact of the helix slope on the far-field intensity distribution was discussed. In that section a linear slope was compared to a parabolic slope. The parabolic slope not only assured that the resonator in the azimuthal direction is really unstable, even in the presence of minor local mirror deformations, but created a more uniform intensity distribution on the mirrors. Even though the intensity distribution is greatly improved with the parabolic slope it is still not uniform. Now, since the thermal load on the mirrors is increased for the scaled-up version this topic is re-visited with the intention to further homogenise the intensity distribution on the mirror surface.

When the parabolic slope was introduced the focus was on reducing the impact of local deformations on the mirror shape and a parabolic shape was superimposed on the linear slope. Now the focus is shifted to the intensity distribution on the mirror surface. The remaining asymmetry of the intensity distribution is a result of the still slow build-up of the intensity from the starting point of the beam. In order to increase the rate of intensity build-up the beam must be kept longer in the low-intensity area. This can be achieved by modifying the parabolic slope so that the initial steepness of the slope is reduced. Figure 7.1 compares the original slope (parabolic shape superimposed on the linear slope) with slopes that start out flat ($\Delta h/\Delta \phi = 0$).

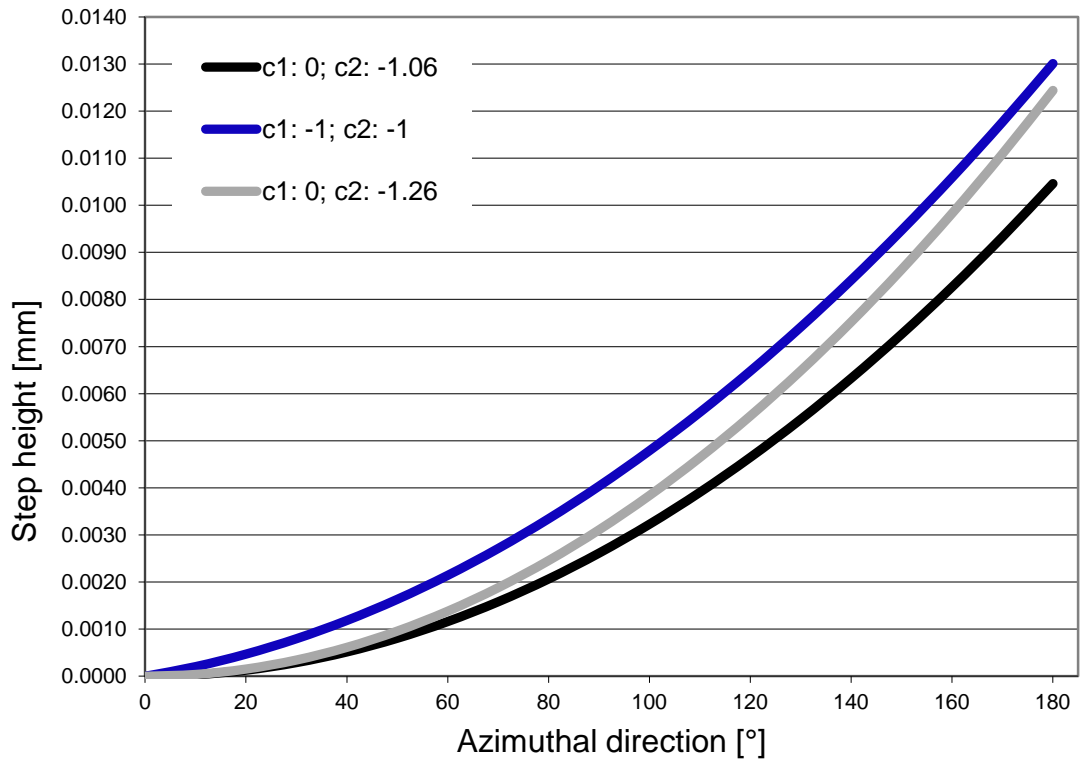


Figure 7.1 Original slope (parabolic shape superimposed on the linear slope) is compared with slopes that start out with zero slope ($\Delta h/\Delta\phi = 0$). Blue: $c_1 = -1 \cdot 10^{-3} \text{ mm/rad}$ and $c_2 = -1 \cdot 10^{-3} \text{ mm/rad}^2$; Grey: $c_1 = 0$ and $c_2 = -1.26 \cdot 10^{-3} \text{ mm/rad}^2$; Black: $c_1 = 0$ and $c_2 = -1.06 \cdot 10^{-3} \text{ mm/rad}^2$.

The slope parameters used in Figure 7.1 are listed in Table 7.1. The slopes with a starting condition where $\Delta h/\Delta\phi = 0$ have a value for c_1 of zero. The original slope has a value of $-1 \cdot 10^{-3}$ for both c parameters.

c_1 [10^{-3} mm/rad]	c_2 [10^{-3} mm/rad^2]	Step height [μm]
0	-1.06	10.4
0	-1.26	12.4
-1	-1	13.0

Table 7.1 Helix mirror parameters and the corresponding step height of the slope in the azimuthal direction.

Figure 7.2 shows the simulated resonator internal intensity distribution for the two different versions of the parabolic slope. The absolute step height has no significant influence on the intensity distribution. What have a big impact on the intensity distribution are the starting conditions of the beam. Keeping the beam longer in the low

intensity area accelerates the intensity build-up resulting in a more uniform load on the mirrors.

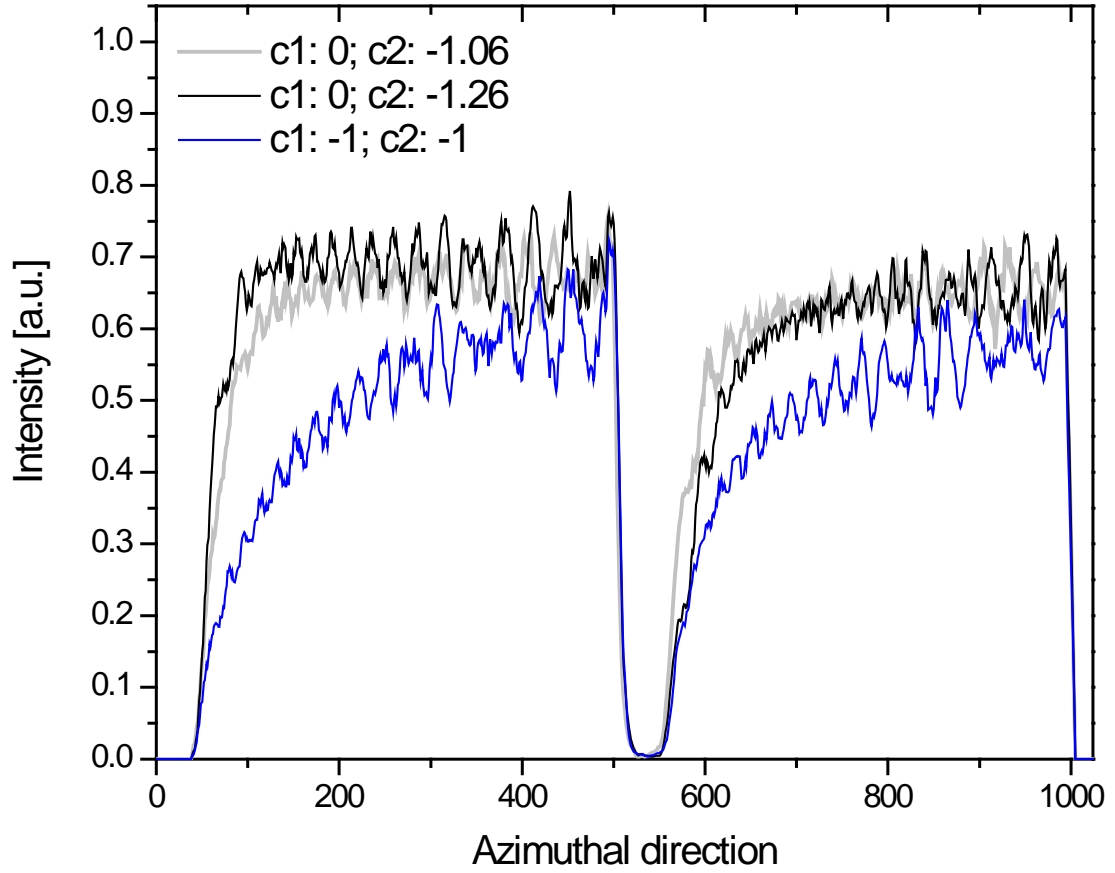


Figure 7.2 Intensity distribution inside the resonator for different helix mirror slope parameters. Blue: $c_1 = -1 \cdot 10^{-3} \text{ mm/rad}$ and $c_2 = -1 \cdot 10^{-3} \text{ mm/rad}^2$; Grey: $c_1 = 0$ and $c_2 = -1.06 \cdot 10^{-3} \text{ mm/rad}^2$; Black: $c_1 = 0$ and $c_2 = -1.26 \cdot 10^{-3} \text{ mm/rad}^2$.

After this modification to the helix mirror shape is introduced the optimization of the fractional output coupling is repeated. Figure 7.3 shows the calculated extraction efficiency and beam qualities versus fractional output coupling for a resonator configuration with $c_1 = 0$, ROC = 2.0 m, a resonator length of 1300 mm and an inter-electrode gap size of 7.0 - 5.9 - 7.0 mm.

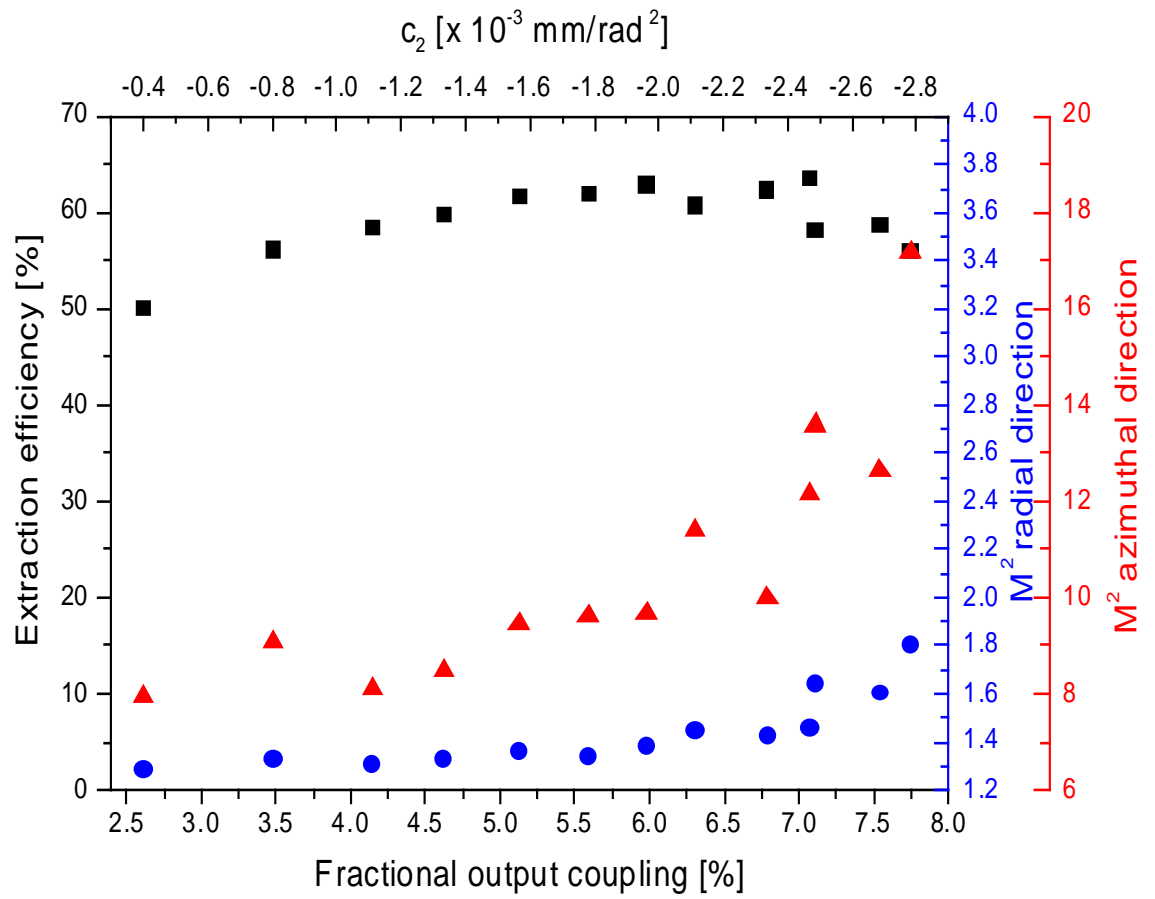


Figure 7.3 Extraction efficiency and beam quality vs. fractional output coupling for a resonator configuration with $c_1 = 0$; the other parameters are: ROC = 2.0 m; $L = 1300$ mm; gap size = 7.0 - 5.9 - 7.0 mm.

For some of the values of fractional output coupling the corresponding far-field intensity distributions are shown in Figure 7.4.

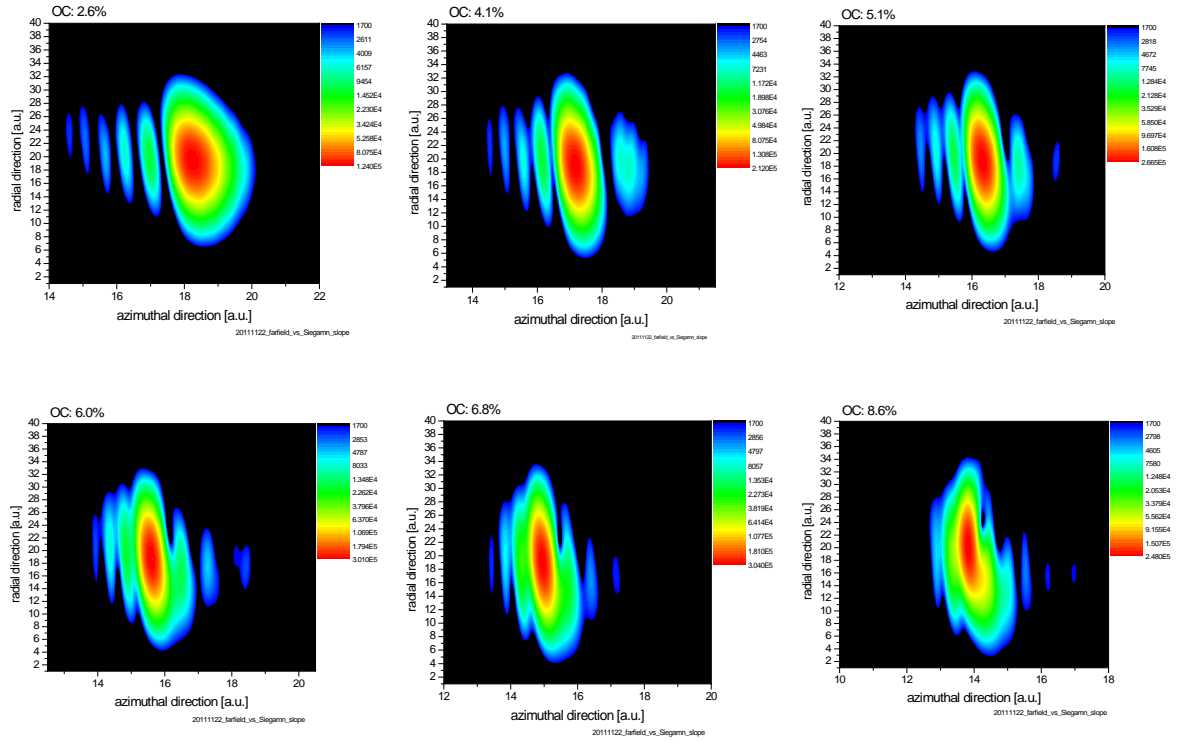


Figure 7.4 2D representation of the far-field intensity distribution for a configuration with a helix mirror slope where $c_1 = 0$; the fractional output coupling values are 2.6%, 4.1%, 5.1%, 6.0%, 6.8%, 8.6% (starting from top left).

In general, the change in the helix mirror shape does not influence the ‘deterioration’ of the far-field intensity distribution (compare to Figure 6.9). For values of fractional output coupling above 5% the nulls start to disappear.

A laser with a fractional output coupling of 4.2% ($c_1 = 0$; $c_2 = -1.06 \cdot 10^{-3} \text{ mm/rad}^2$) has been tested on a 2D laser cutting machine. The result is as expected, a clear separation of the higher order frequencies from the main peak is evident which allows proper spatial filtering to be achieved, which in turn results in cutting results without any directional dependencies.

The deterioration of the far-field intensity distribution seems to be mainly related to driving the beam faster and faster around the circumference with steeper and steeper slopes which come with increasing fractional output coupling. In order to confirm these assumptions, two configurations are compared with each other. The first one has a helix mirror with $c_2 = -1.32 \cdot 10^{-3} \text{ mm/rad}^2$ the second one $c_2 = -0.91 \cdot 10^{-3} \text{ mm/rad}^2$ (in both cases $c_1 = 0$). For both of them the centre gap size is reduced systematically. Figure 7.5 shows the influence of the centre gap size on the simulated extraction efficiency and

beam qualities. Figure 7.7 shows the same for the smaller value of fractional output coupling. For both configurations, the end gap size is 7.0 mm and the ROC is 2.0 m. Figure 7.6 and Figure 7.8 show the corresponding far-field intensity distributions.

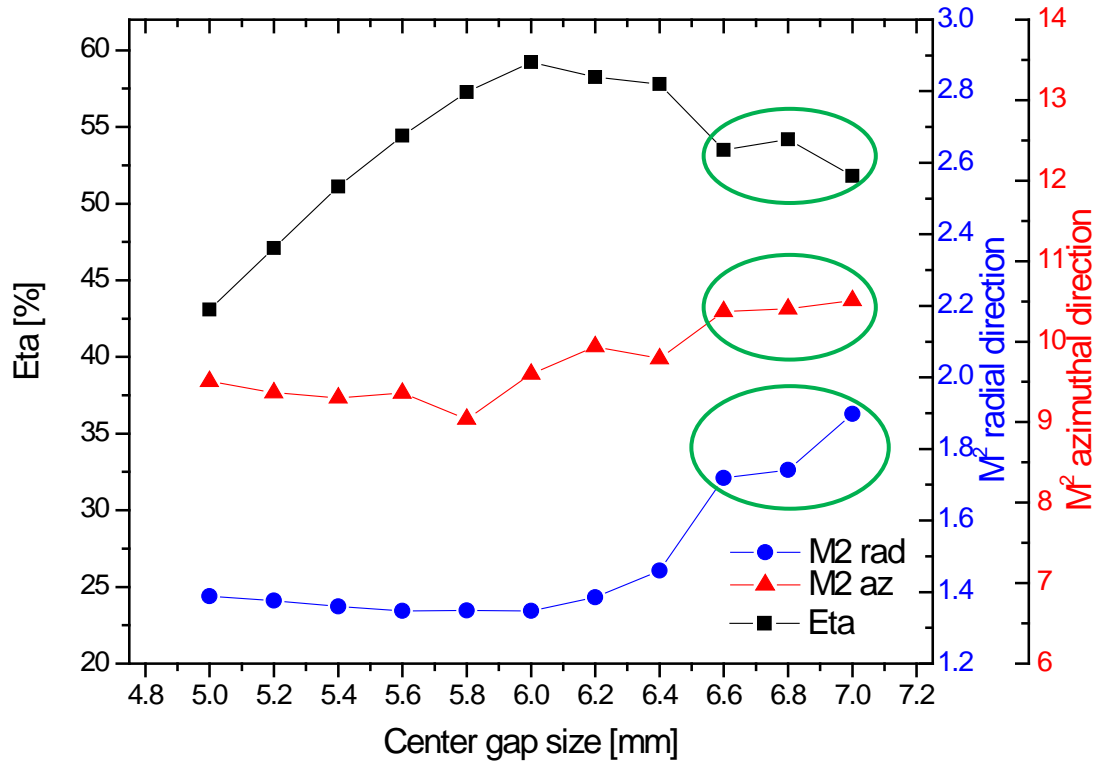


Figure 7.5 Extraction efficiency and beam quality for different centre gap sizes. Set-up: ROC = 2.0 m; $c_2 = -1.317 \cdot 10^{-3} \text{ mm/rad}^2$; $L = 1300 \text{ mm}$; end gap size = 7.0 mm.

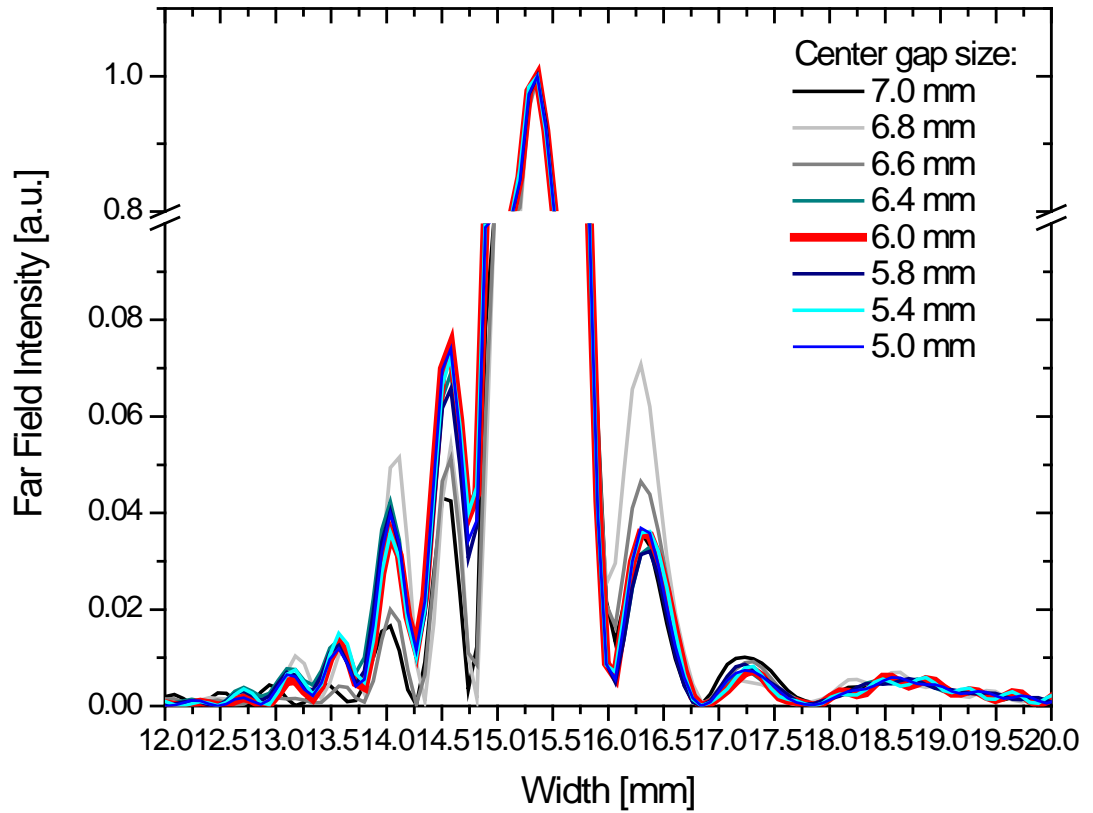


Figure 7.6 Intensity distribution in the far-field for different centre gap sizes plotted in a way that shows the side lobes. Set-up: ROC = 2.0 m; $c_2 = -1.317 \cdot 10^{-3} \text{ mm/rad}^2$; $L = 1300 \text{ mm}$; end gap size: 7.0 mm.

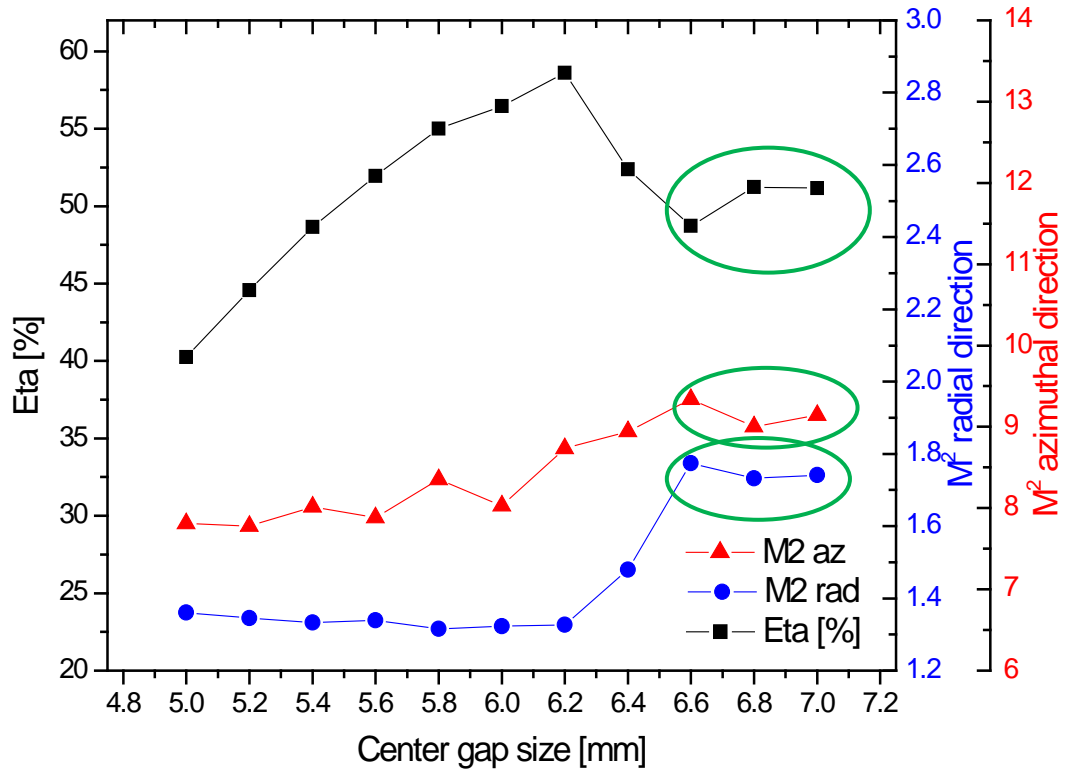


Figure 7.7 Extraction efficiency and beam quality for different centre gap sizes. Set-up: $ROC = 2.0\text{ m}$; $c_2 = -0.912 \cdot 10^{-3}\text{ mm/rad}^2$; $L = 1300\text{ mm}$; end gap = 7.0 mm .

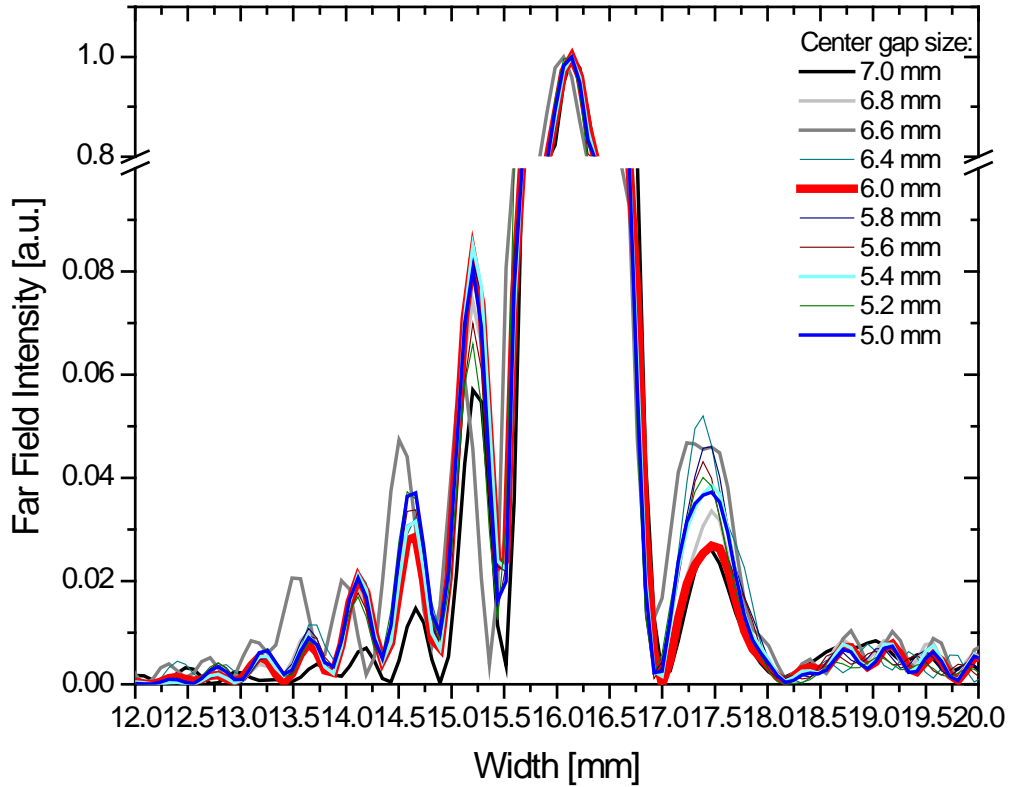


Figure 7.8 Intensity distribution in the far-field for different centre gap sizes plotted in a way that shows the side lobes. Set-up: $c_2 = -0.912 \cdot 10^{-3}\text{ mm/rad}^2$; $ROC = 2.0\text{ m}$; $L = 1300\text{ mm}$; end gap size: 7.0 mm .

There is a clear change in the shape of the intensity distribution for centre gap sizes of 6.6 mm and smaller: The intensity distribution in the minimum to the left of the main peak increases. Note however, that this increase does not occur gradually but rather happens in steps and corresponds with a change in extraction efficiency and beam quality as shown in Figure 7.5 (see highlighted data points). The changes in extraction efficiency and beam quality in the azimuthal direction are clear indicators for a different mode mix in the resonator with a different Fourier transform.

For the smaller value of the fractional output coupling ($c_2 = -0.9 \cdot 10^{-3} \text{ mm/rad}^2$) the impact of the centre gap size on the far-field intensity distribution is much reduced. Even though in general the same change in the intensity distribution can be seen as for the larger fractional output coupling value, the intensity in the minimum to the left of the main peak is only about 50% of what it is with the larger fractional output coupling value.

Figure 7.9 shows the measured intensity distributions of a scaled-up laser with two different helix mirrors. One has a smaller, the other a larger magnification with $c_2 = -1.060 \cdot 10^{-3} \text{ mm/rad}^2$ and $c_2 = -1.317 \cdot 10^{-3} \text{ mm/rad}^2$ respectively (in both cases $c_1 = 0$).

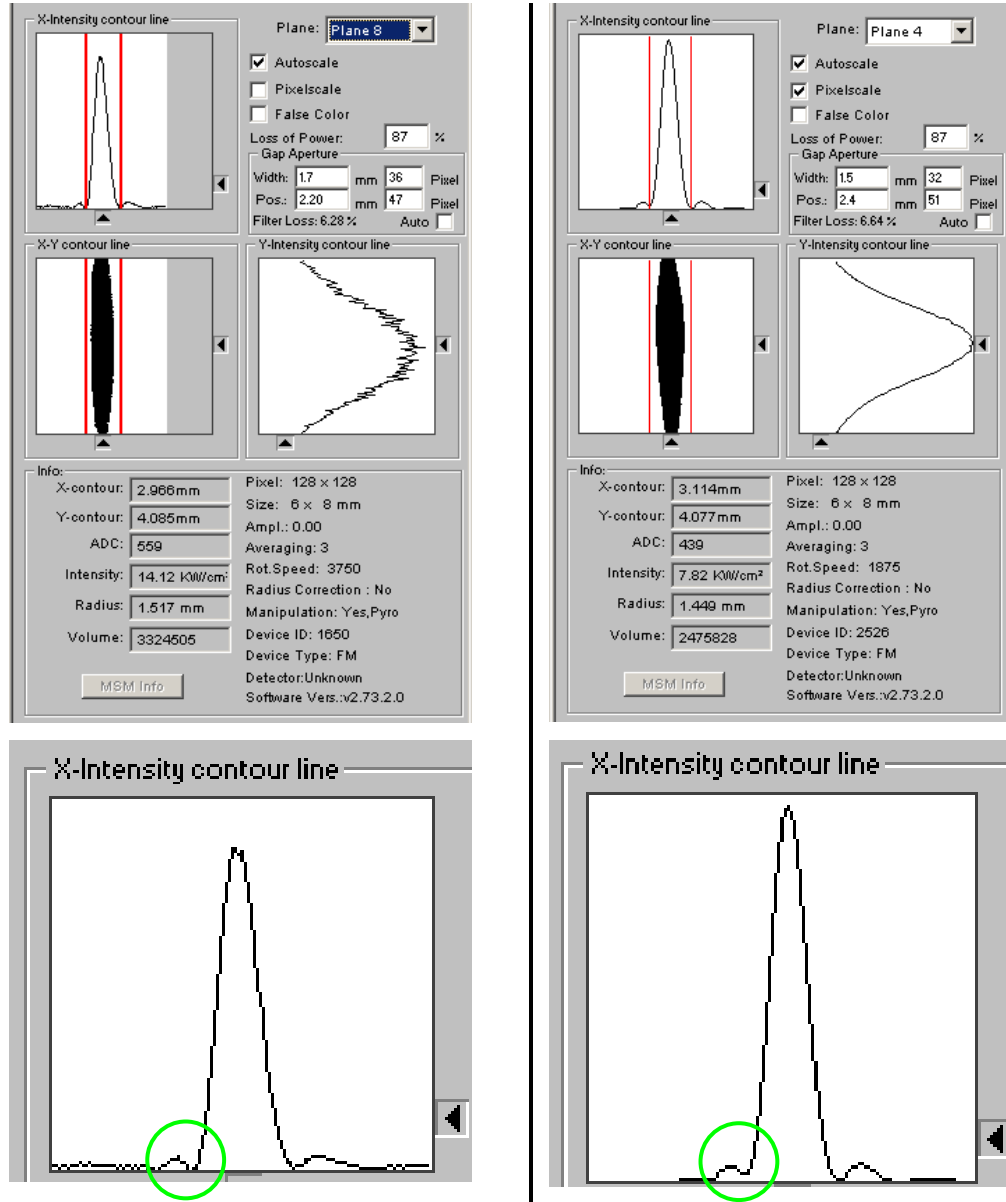


Figure 7.9 Measured intensity distribution in the far-field plane for two different helix mirrors. Left: $c_2 = -1.060 \cdot 10^{-3} \text{ mm/rad}^2$; Right: $c_2 = -1.317 \cdot 10^{-3} \text{ mm/rad}^2$ (The measurement is carried out with a PRIMES focus monitor).

The measurements confirm the impact of the fractional output coupling on the ‘quality’ of the far-field intensity distribution. For the smaller value of c_2 the higher spatial frequencies are clearly separated from the main peak, whereas for the larger value of c_2 the nulls disappear as predicted by the simulation. As a reference, the fractional output coupling is about 4.7% for the configuration with $c_2 = -1.31 \cdot 10^{-3} \text{ mm/rad}^2$ and about 4.2% with $c_2 = -1.06 \cdot 10^{-3} \text{ mm/rad}^2$ (the fractional output coupling is defined as the ratio of outcoupled to resonator internal power). As mentioned before, the disappearance of the nulls (as indicated in Figure 7.9 with a circle) has a severe impact on the spatial filtering result. Even though the measured beam quality after spatial filtering reaches M^2 values of

1.1, the near-field intensity distribution shows undesired features resulting in a significant reduction of the cut quality (roughness) in one direction of beam travel.

The measurements also confirm the change in width of the main peak in the far-field plane for different levels of fractional output coupling. Reducing c_2 from $-1.317 \cdot 10^{-3}$ to $-1.060 \cdot 10^{-3}$ mm/rad² increases the width of the main peak in the far-field from 1.5 to 1.7 mm.

7.1.2 *Helix mirror power maps*

Power maps are a useful diagnostic tool to get a better understanding of the alignment behaviour of the resonator and to determine how sensitive a particular resonator is to misalignment and tolerances in the electrode-mirror system. Power maps are misalignment experiments where for each alignment position of the resonator the laser power, and if desired the intensity distribution of the output beam, is measured. Since the generation of power maps is time consuming and the availability of electrodes with different inter-electrode gap sizes is limited, it is more practical to generate power maps by simulation experiments over a wide range of gap sizes and to perform experimental verification for a few selected sizes.

In the simulation the helix mirror is tilted around the X and Y-axes of the mirror from -250 to +250 μ rad in 21 steps in each direction and the ROC is kept constant for all electrode size combinations. Figure 7.10 and Figure 7.12 show simulated power maps for a resonator configuration where $c_1 = -1 \cdot 10^{-3}$ mm/rad, $c_2 = -1 \cdot 10^{-3}$ mm/rad² and $c_1 = 0$ and $c_2 = -1.06 \cdot 10^{-3}$ mm/rad² respectively. The corresponding experimental results are shown in Figure 7.11 and Figure 7.13. The horizontal direction represents end gap sizes and the vertical direction centre gap sizes (all numbers in mm).

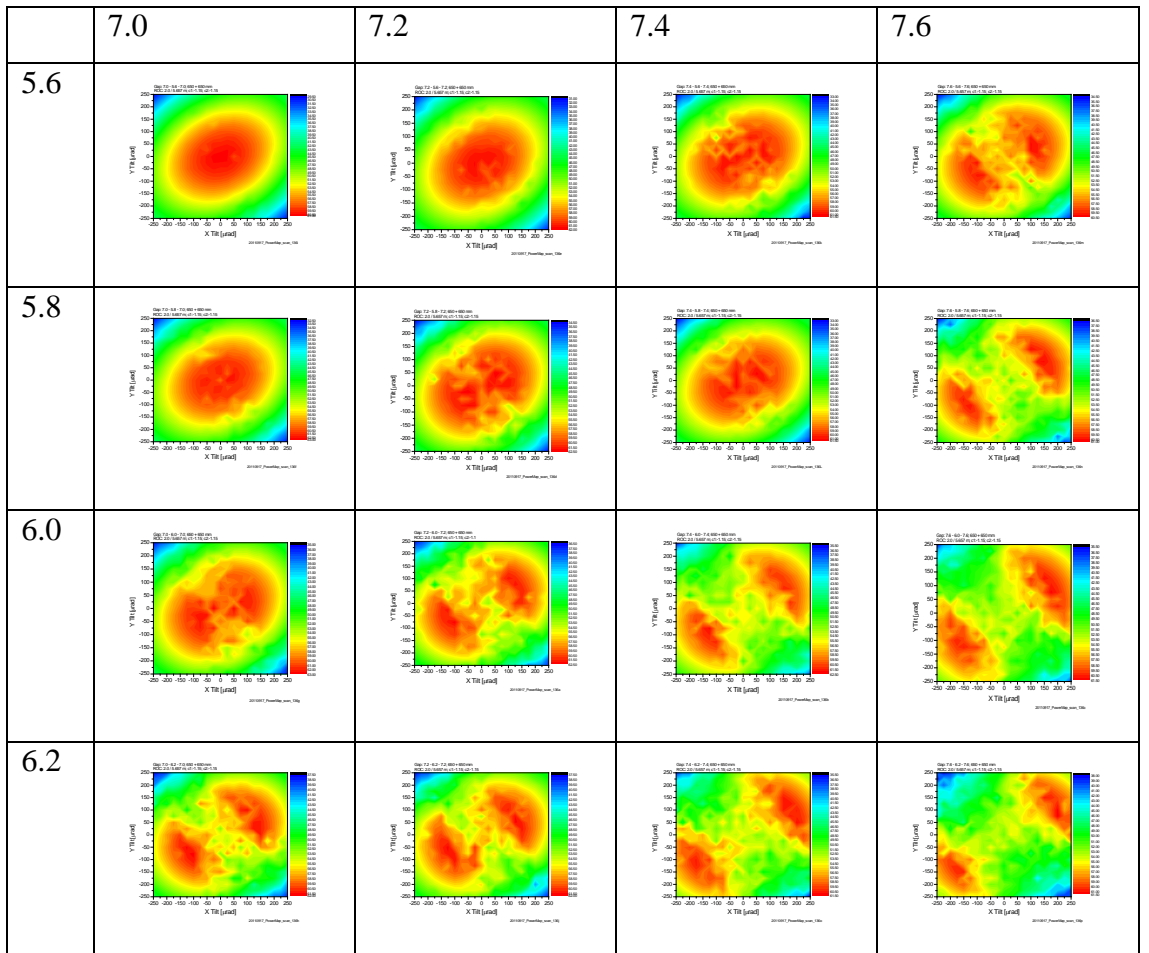


Figure 7.10 Simulated power maps for inter-electrode end gap sizes from 7.0 to 7.6 mm (shown in the horizontal direction) and centre gap sized from 5.6 to 6.2 mm (shown in the vertical direction). Resonator parameters: $c_1 = -1 \cdot 10^{-3}$ mm/rad and $c_2 = -1 \cdot 10^{-3}$ mm/rad²; ROC = 2.0 m; L = 1300 mm.

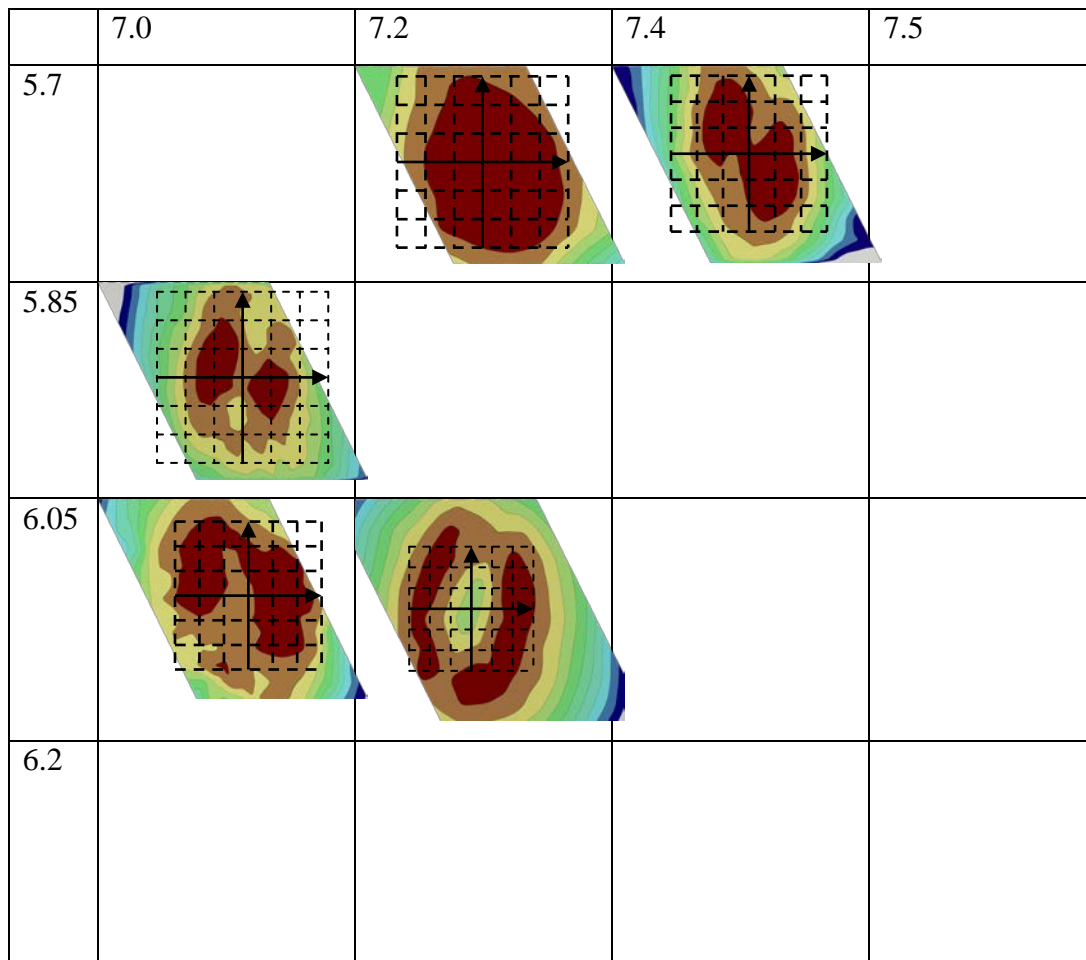


Figure 7.11 Experimentally derived power maps for a resonator configuration with $c_1 = -1 \cdot 10^{-3} \text{ mm/rad}$, $c_2 = -1 \cdot 10^{-3} \text{ mm/rad}^2$, a ROC of 2.0 m and a resonator length of 1300 mm. End gap sizes are varied from 7.0 to 7.4 mm (horizontal direction) and centre gap sizes are varied from 5.7 to 6.05 mm (vertical direction).

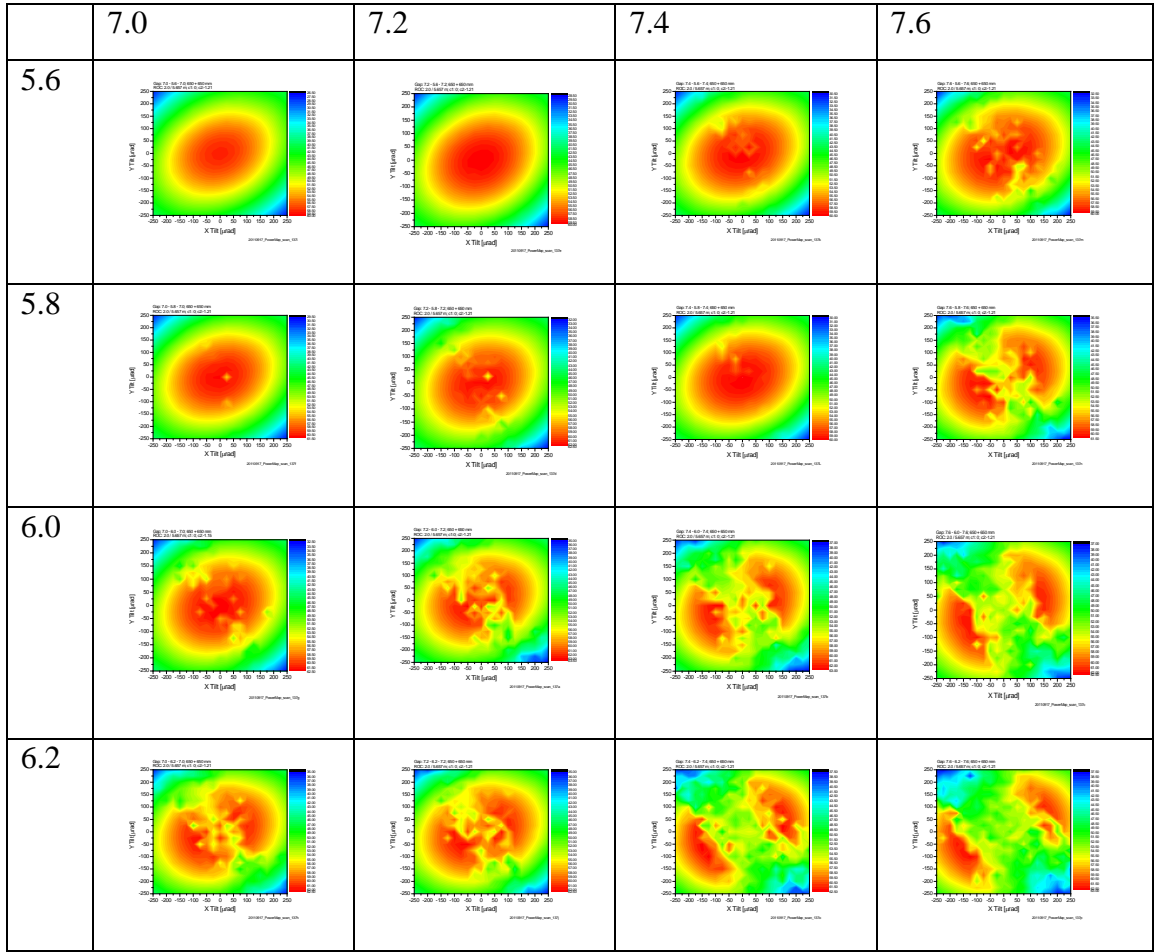


Figure 7.12 Simulated power maps for inter-electrode end gap sizes from 7.0 to 7.6 mm (shown in the horizontal direction) and centre gap sized from 5.6 to 6.2 mm (shown in the vertical direction). Resonator parameters: $c_1 = 0$ and $c_2 = -1.06 \cdot 10^{-3} \text{ mm/rad}^2$; $ROC = 2.0 \text{ m}$; $L = 1300 \text{ mm}$.

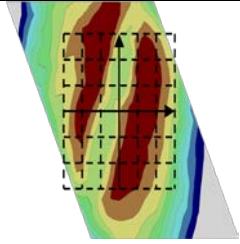
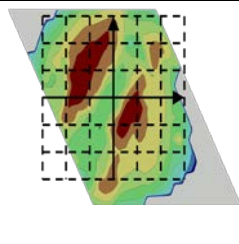
	7.0	7.2	7.4	7.5
5.7				
5.85				
6.05				
6.2				

Figure 7.13 Experimentally derived power maps for a resonator configuration with $c_1 = 0$; $c_2 = -1.06 \cdot 10^{-3} \text{ mm/rad}^2$, a ROC of 2.0 m and a resonator length of 1300 mm. End gap sizes are varied from 7.0 to 7.2 mm (horizontal direction) and the centre gap size is fix at 6.2 mm.

The shapes of the simulated and experimentally derived power maps are in general quite similar. The differences in orientation are caused by the use of different coordinate systems in the simulation and in the laboratory. Regarding absolute dimensions of the inter-electrode gap sizes, there is a small offset of 0.1 to 0.2 mm between the simulated and experimental results.

For both sets of slope parameters the power maps show a split in the intensity distribution for inter-electrode gaps exceeding a certain size. The split can be elicited by either an increase in the centre or end gap size. As shown in Figure 7.14, with increasing inter-electrode gap sizes the maximum extraction efficiency increases. For power maps with a split, this maximum value is, of course, not in the centre of the power map where the tilt is zero but in the ‘islands’. If the gap size is further increased beyond where the split occurs, multimode operation in the radial direction will take place if the resonator is operated in the centre of the power map. If the resonator is aligned to operate in one of the high power regions within the islands, multimode operation can be avoided.

One would think that a power map without split is desirable. In reality, the best overall results are achieved with configurations that show a small split. The resonator is least sensitive to misalignment, output power is increased and the resonator operates in fundamental mode. Operating the resonator in a configuration without a split in the power map can lower the output power significantly. For example, with an inter-electrode gap size of 7.2 - 5.7 - 7.2 mm the output power was about 3500 W which is about 300 to 400 W below what is achieved with gap sizes of about 7.0 - 6.0 - 7.0 mm.

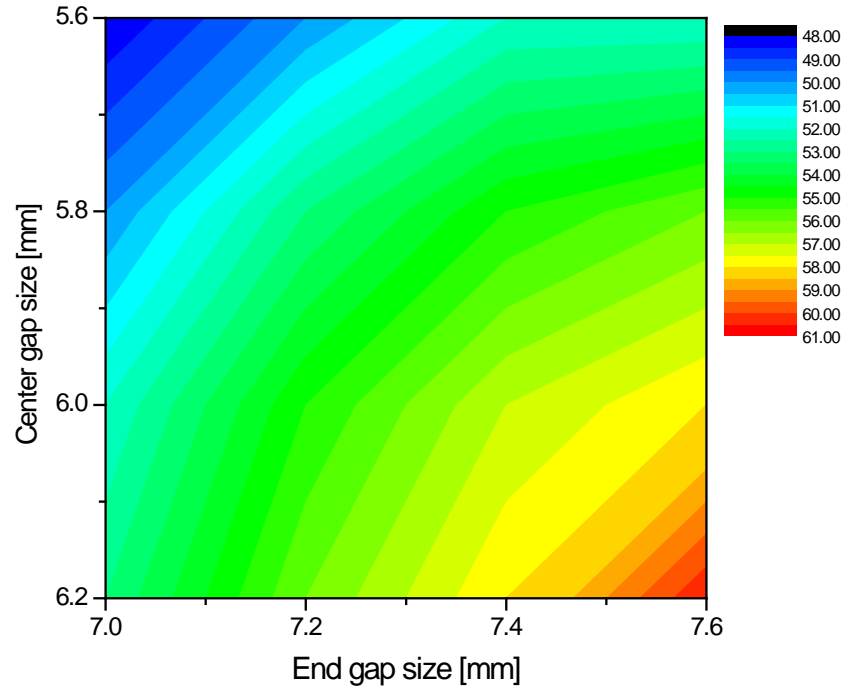


Figure 7.14 Maximum extraction efficiency (representing output power) for different inter-electrode gap size combinations.

7.1.3 Axicon mirror power maps

The same exercise, creating power maps as shown in section 7.1.2, has been repeated for the axicon mirror. Even though the axicon mirror is not actively aligned, but is only mechanically referenced, all machining processes are subject to tolerances and therefore axicon power maps serve as a tolerance analysis tool. Since there is good agreement between the simulated and experimentally created helix power maps and the axicon mirror assembly has no alignment screws, the axicon power maps are not experimentally confirmed. Figure 7.15 shows axicon power maps created for a configuration with a ROC of 2 m, $c_1 = 0$ and $c_2 = -1.06 \cdot 10^{-3} \text{ mm/rad}^2$.

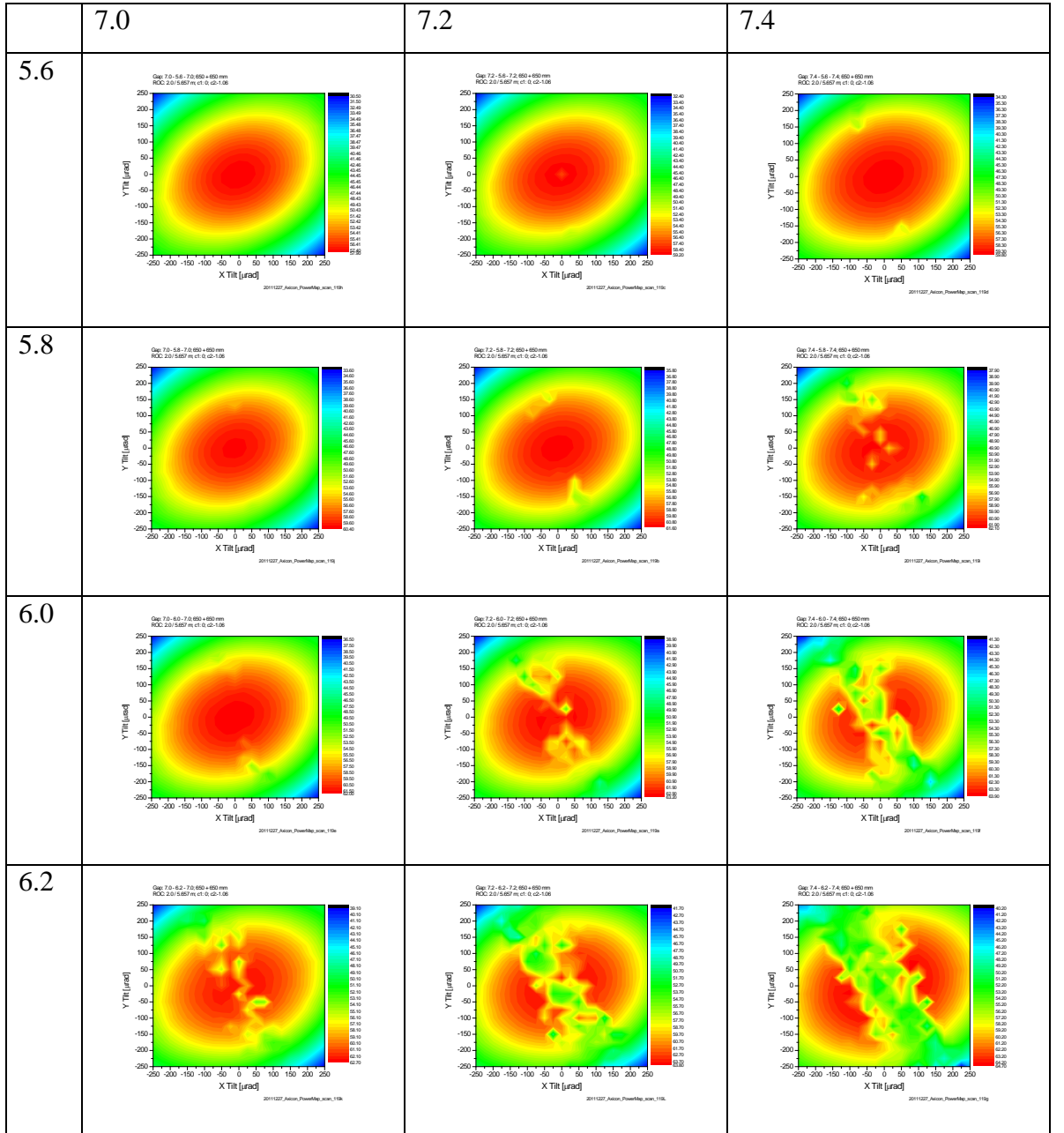


Figure 7.15 Axicon power maps for different inter-electrode gap size combinations. End gap sizes are varied in the horizontal direction from 7.0 to 7.4 mm and centre gap sizes in the vertical direction from 5.6 to 6.2 mm. Helix mirror parameters: ROC: 2.0m; $c_1=0$; $c_2 = -1.06 \cdot 10^{-3}$ mm/rad; $c_2 = -1.06$ mm/rad².

The overall shape of the axicon power map is identical to the shape of the helix power map. If the inter-electrode gap size is not chosen carefully a split occurs in the power map. The split emerges for about the same gap-size combinations as in the helix power maps.

In a second step, the same data is analyzed differently to determine the impact of an axicon mirror tilt on the centring of the beam in the inter-electrode gap. Figure 7.16 shows a typical resonator internal intensity distribution, which is compiled of 1024 planes

in the azimuthal direction. For each plane the first moments can be calculated. They represent the centre of gravity of the beam inside the resonator. The deviation of the first moments from their nominal position in the centre of the inter-electrode gap is plotted for different configurations and used as an additional criterion to judge the sensitivity of the resonator to a tilt of the axicon mirror and inter-electrode gap size changes.

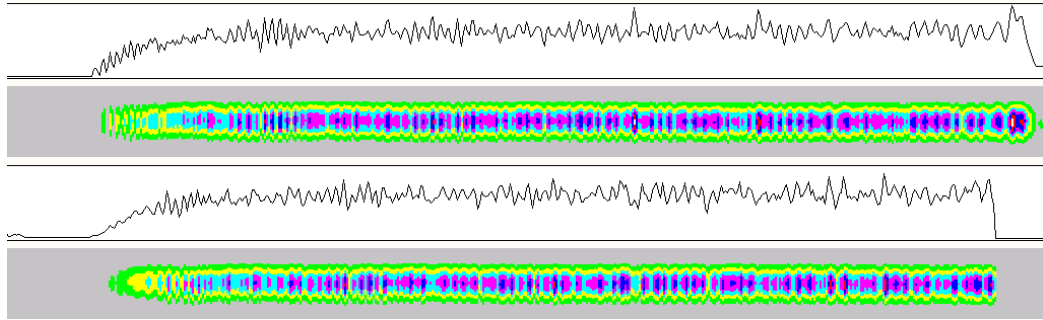


Figure 7.16 Typical resonator internal intensity distribution. The azimuthal direction (horizontal direction) is compiled of 1024 planes. The first moments of each plane are used to compare the centreline position of the intensity with its nominal position in the centre of the gap.

Figure 7.17 shows the deviation of the first moments from the centreline of the inter-electrode gap in the azimuthal direction for three different gap sizes. On the left side, tilts around the Y-axis are shown and on the right side tilts around the X-axis. The different traces represent tilts from -0.25 to +0.25 mrad. The big spike at about 180° is an artefact of the calculation. It is located just opposite the output coupling hole of the helix mirror.

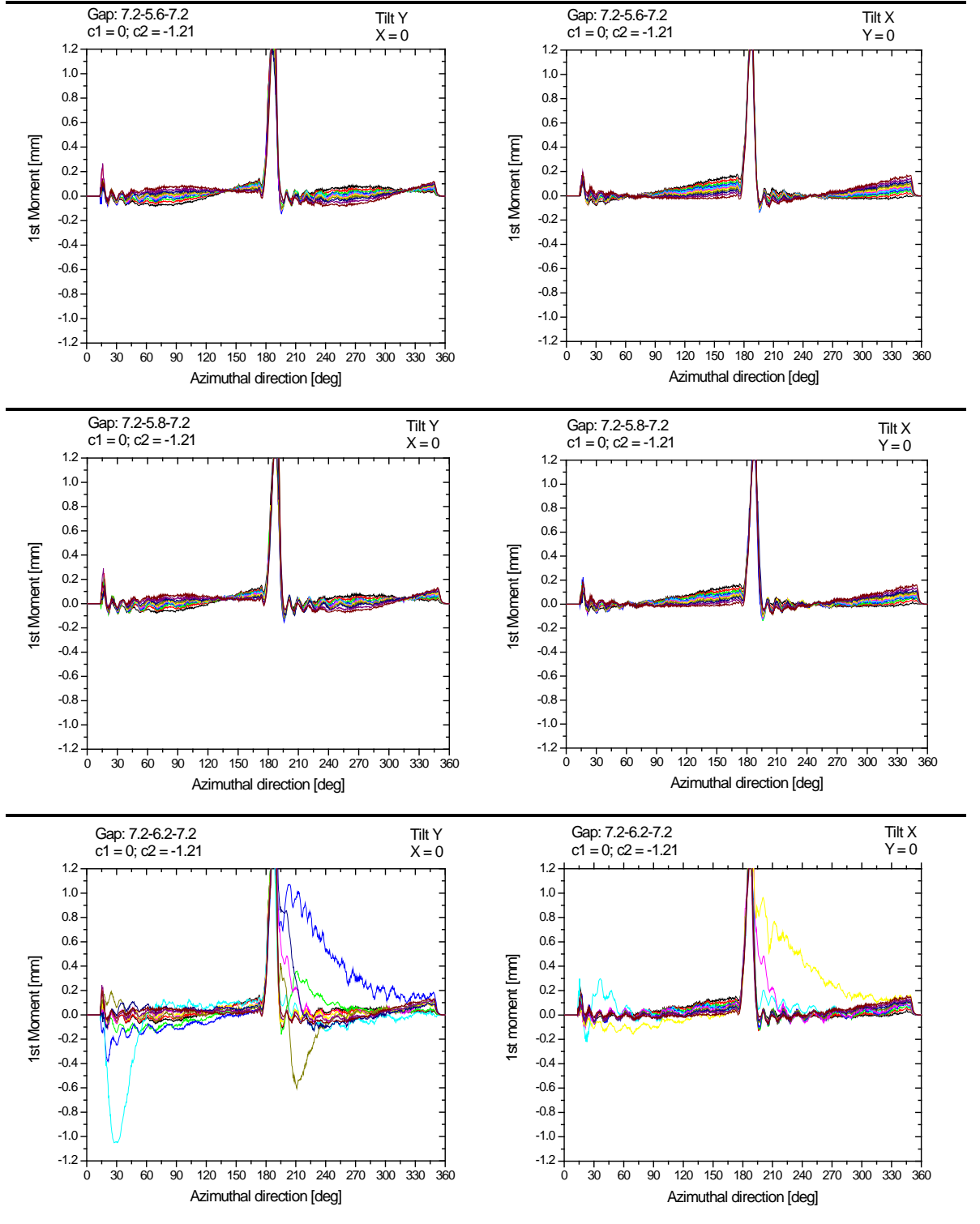


Figure 7.17 Simulated axicon mirror tilt from -0.25 to $+0.25$ mrad around the X-axis (left) and Y-axis (right) for three different inter-electrode gap sizes. Top: 7.2-5.6-7.2 mm; Centre: 7.2-5.8-7.2 mm; Bottom: 7.2-6.2-7.2 mm. Plotted is the deviation of the first moments from the centre position. The helix mirror parameters are: $c_1 = 0$; $c_2 = -1.21 \cdot 10^{-3} \text{ mm/rad}^2$; $\text{ROC} = 2.0\text{m}$.

Tilts in the range from -0.25 to $+0.25$ mrad around the X and Y-axis do not have a significant impact on the centring of the beam unless the resonator is operated with an electrode configuration that shows a significant split in the power map. Then, significant

deviations of the first moments from the centre position occur. Of course, this only happens when the helix mirror is in its nominal position. In a real laser, the alignment of the helix mirror will minimize the deviation of the first moments from the nominal position.

In conclusion, it can be said that operating the laser with an inter-electrode gap size that does not show the split in the power map results in high losses and therefore lower laser output power levels. Operating the laser with a configuration that has a split requires that the resonator needs to be ‘misaligned’ on purpose for best performance. Since resonator alignment is required regardless, and the deviation from the nominal position of the helix mirror is small when aligned for maximum output power and there is no visible asymmetry in the mode, this is not a real problem.

7.1.4 Influence of the banking parameters

“Banking” is part of the helix mirror shape and has the purpose of keeping the beam centred in the inter-electrode gap just like the banking that is used in a race track to keep the race cars/cyclists on the track. So far, the banking parameters, n_1 and n_2 have been calculated automatically in the simulations using Equation 7.1. They are a function of the slope parameters, c_i and mirror radius, r_s as follows.

$$n_i = \frac{-2c_i}{r_s} \quad 7.1$$

Using Equation 7.1, the equation for the helix mirror with a parabolic contour (see Equation 3.10) can be modified to be

$$h(r, \phi) = -c_1\phi - c_2\phi^2 + \frac{(r - r_s)^2}{2r_h} - (n_1\phi + n_2\phi^2)(r - r_s) \quad 7.2$$

In this section the banking parameters are not calculated automatically, but are systematically varied in a simulation from $-20 \cdot 10^{-5}$ to $+20 \cdot 10^{-5}$ in combination with slope parameters of $c_1 = 0$ and $c_2 = -1.2 \cdot 10^{-3} \text{ mm/rad}^2$ and an inter-electrode gap size of 7.2 - 6.0 - 7.2 mm.

The results are shown in Figure 7.18 and Figure 7.19. Figure 7.18 shows the extraction efficiency and Figure 7.19 the beam quality as a function of the banking parameters.

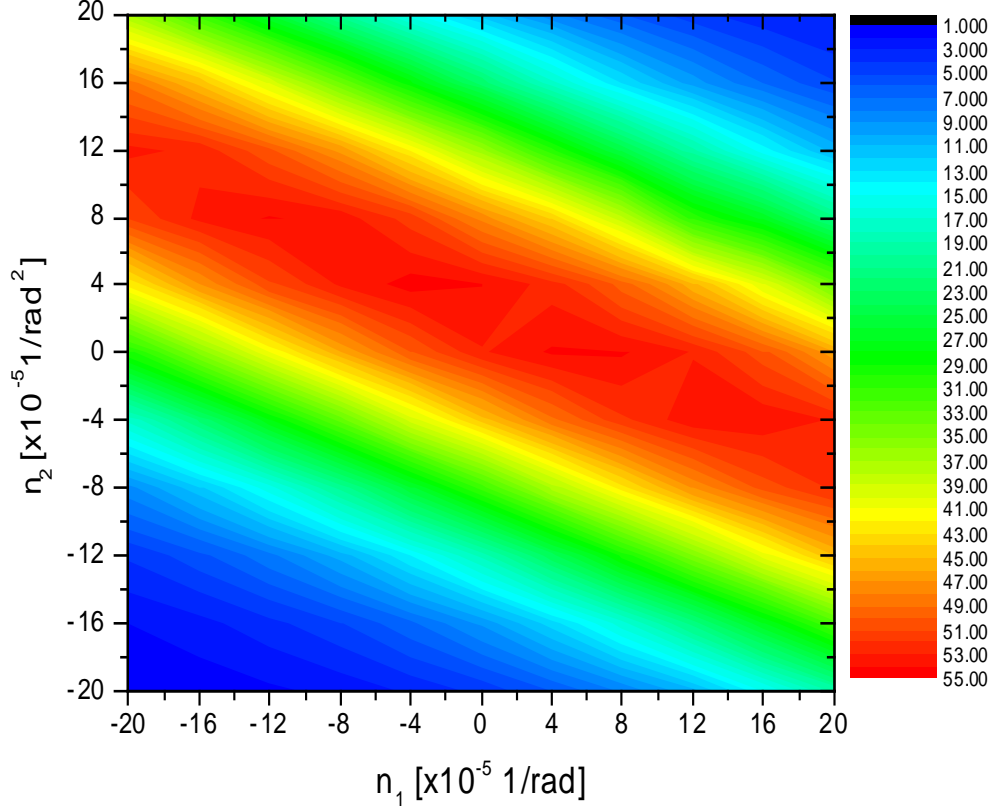


Figure 7.18 Extraction efficiency is plotted as a function of the banking parameters n_1 and n_2 . (ROC = 2.0 / 5.657 m; $L = 650 + 650$ mm; gap size: 7.2 – 6.0 – 7.2 mm; $c_1 = 0$; $c_2 = -1.2 \cdot 10^{-3}$ mm/rad²).

There is a corridor in which the extraction efficiency is constant for n_1 values from $-20 \cdot 10^{-5}$ to $+20 \cdot 10^{-5}$. Some of these combinations are listed in Table 7.2. For comparison, the standard values, calculated with Equation 7.1, for n_1 and n_2 in combination with slope parameters of $c_1 = 0$ and $c_2 = -1.2 \cdot 10^{-3}$ mm/rad² are 0 and $3.12 \cdot 10^{-5}$ 1/rad² respectively.

The beam quality (M^2 values for the azimuthal and radial direction) plots show the same general shape as the plot for extraction efficiency. There is a corridor in which the beam quality is constant for various combinations of n_1 and n_2 parameters.

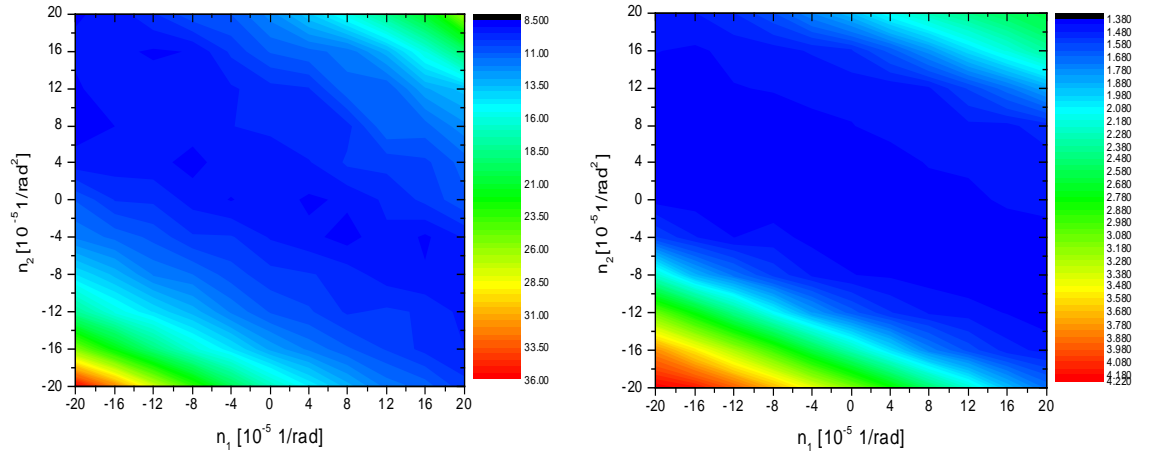


Figure 7.19 Left: M^2 values for the azimuthal direction as a function of n parameters. Right: M^2 values for the radial direction. (ROC = 2.0 / 5.657 m; $L = 650 + 650$ mm; gap size: 7.2 – 6.0 – 7.2 mm; $c_1 = 0$; $c_2 = -1.2 \cdot 10^{-3}$ mm/rad²).

The results for the extraction efficiency and beam quality indicate that banking is rather uncritical. Nevertheless, if the deviation of the first moments from the centre of the gap is plotted, which is a good measure for how well the beam is centred in the gap, a clear difference can be seen for different combinations of n_1 and n_2 parameters. The traces in Figure 7.20 represent these deviations from the centre for the combinations listed in Table 7.2 plus the standard value calculated with Equation 7.1.

n_2 [10^{-5} 1/rad ²]	+8	+4	0	-4	-4
n_1 [10^{-5} 1/rad]	-12	-4	+8	+8	+16

Table 7.2 Combinations of banking parameters which yield approximately the same extraction efficiencies in Figure 7.18.

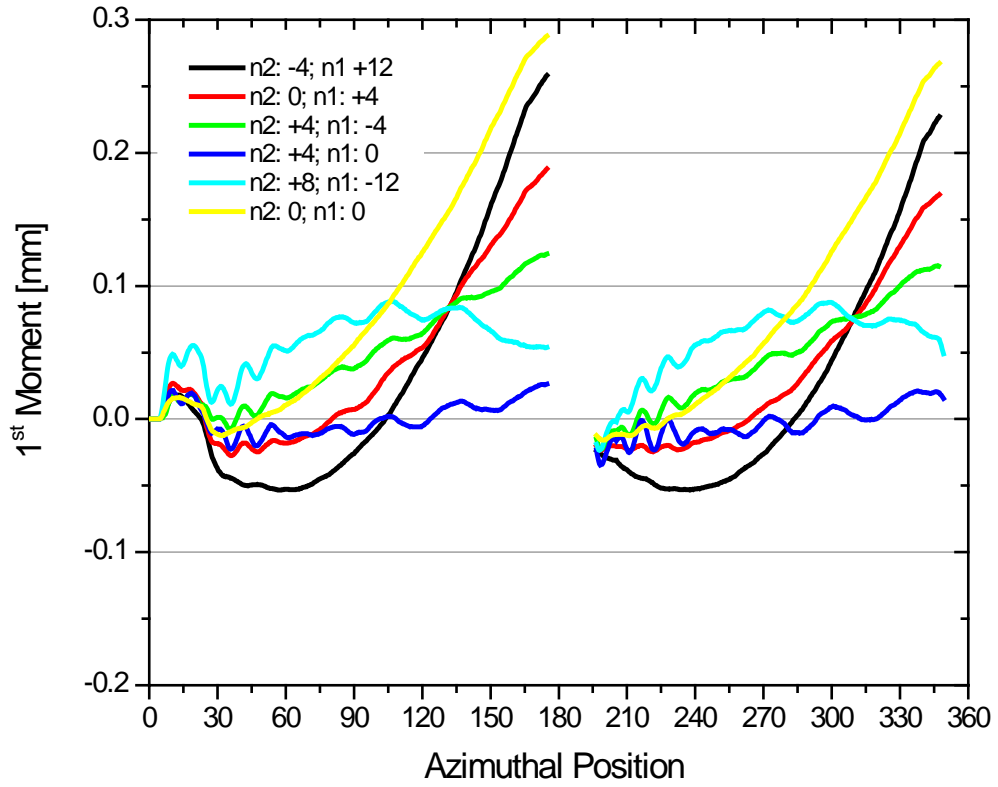


Figure 7.20 Deviation of the first moments from the centre of the inter-electrode gap for n_1 and n_2 combinations listed in Table 7.2. For $n_1 = n_2 = 0$ there is no banking.

The deviation of the first moments from the centre increases as the beam travels around the circumference. With banking parameters close to those calculated with Equation 7.1 the deviation is minimal while the deviation without any banking is maximal. Other combinations over or undercompensate in different sections of the circumference.

7.2 Additional Considerations

Even though there has been good agreement between the simulations and empirical results so far, the model used for the simulations included several assumptions and simplifications. Their justifications and impact on the inter-electrode gap size will be revisited here. Section 7.2.1 reviews the simplifications introduced regarding the resonator length, while in section 7.2.2 the impact of thermal lensing on the inter-electrode gap size is investigated.

7.2.1 Resonator length

The basic model of the resonator was introduced in section 2.8.4. There, two simplifications regarding the overall resonator length were introduced:

- In order to simplify the simulations the distance between the resonator mirrors and electrodes was neglected assuming that they are small compared to the overall resonator length.
- ii) Since in the model the beam is switched from one side of the axicon mirror to the other by a coordinate transformation, the propagation within the axicon is not considered resulting in a further reduction of the overall length.

Compared to the actual resonator length of 1496 mm, the length in the model of 1300 mm represents a reduction of almost 20% and is therefore not necessarily negligible. Using the correct resonator length for the simulation is important since Fresnel numbers, g -parameters, beam inclination and magnification are all a function of resonator length.

Different modifications could be made to improve the representation of the correct resonator length in the model. But in order to avoid additional and short propagators the missing length is simulated by scaling the magnification of the laser. In order to create the same magnification as in the 1496 mm long resonator in a resonator with a length of 1300 mm the slope parameters (c_1 and c_2) are scaled by a factor of $1496 / 1300 = 1.15$.

An inter-electrode gap size optimization is shown in Figure 7.21 for the original and *scaled magnification* model. Both end gap and centre gap sizes are systematically varied and extraction efficiency and beam quality in the radial direction are plotted.

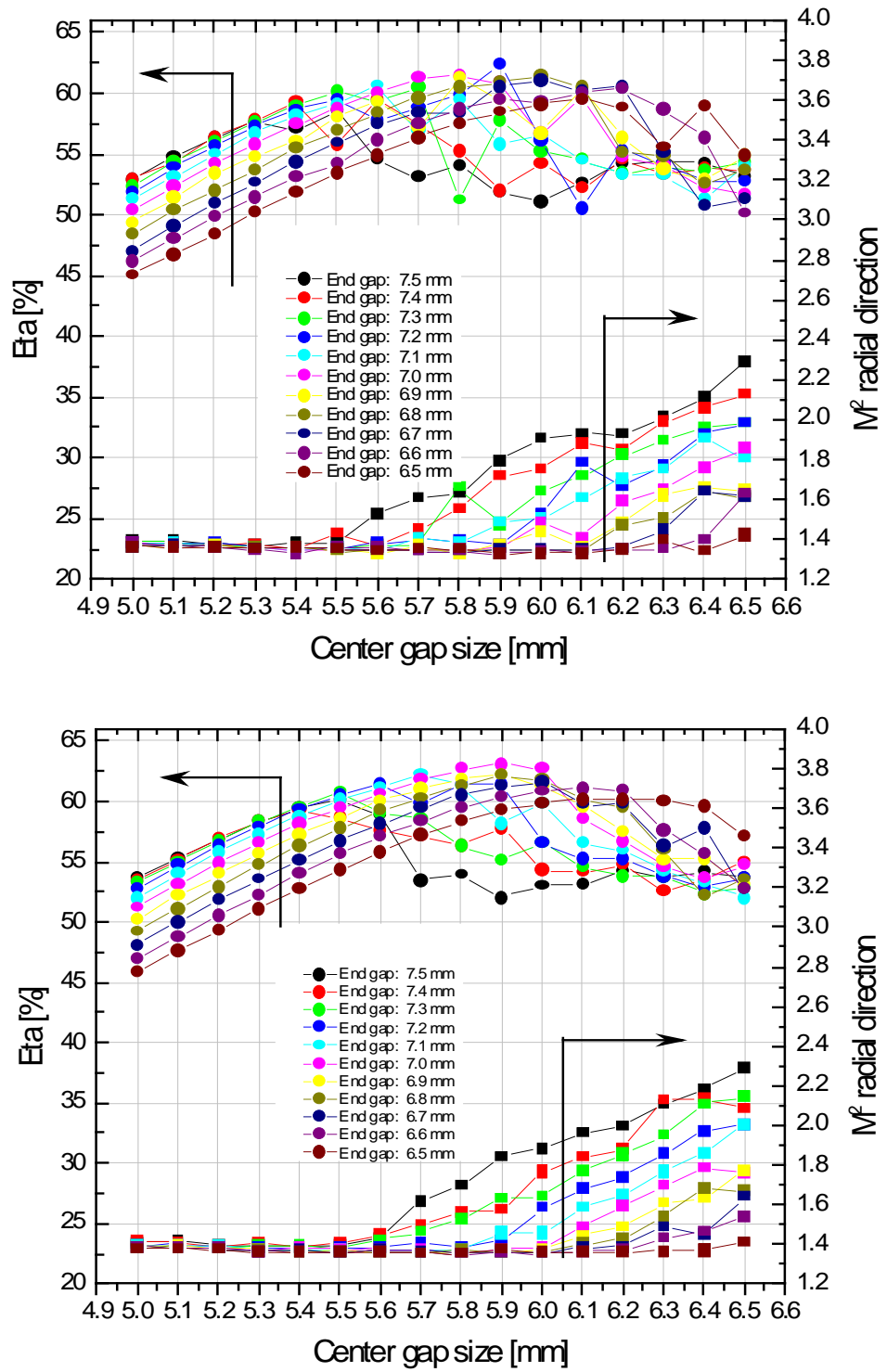


Figure 7.21 Inter-electrode gap size optimization with standard and scaled magnification model. Top: $c_1 = -1 \cdot 10^{-3} \text{ mm/rad}$ and $c_2 = -1 \cdot 10^{-3} \text{ mm/rad}^2$; Bottom: $c_1 = -1.15 \cdot 10^{-3} \text{ mm/rad}$ and $c_2 = -1.15 \cdot 10^{-3} \text{ mm/rad}^2$; for both $L = 650 + 650 \text{ mm}$.

The predicted optimum gap size with the scaled magnification model is now 7.0 – 5.9 – 7.0 mm whereas the original model predicted an initial inter-electrode gap size of 7.0 – 5.8 – 7.0 mm. Even though this increase in the centre gap size is small and within the accuracy of the simulation it is in agreement with the expected impact of the scaled magnification (longer resonator length) on the size of the inter-electrode gap size. In a longer resonator, the beam not only propagates further in the z direction but also further in the azimuthal direction (ϕ) requiring a larger centre gap size to avoid additional losses due to the shadowing effect of the inner electrode. This additional travel in the azimuthal direction is now considered in the *scaled magnification* model.

7.2.2 Thermal lensing

Thermal lenses have traditionally not been considered in the design of diffusion-cooled waveguide CO₂ lasers, since the impact is small. However, although Schulz in [4] estimated the focal length of a thermal lens in a *free-space* resonator configuration the impact it has on the resonator design or the resonator performance was not investigated further.

For an average inter-electrode gap size of 6.5 mm and a discharge length of 1.3 m the average RF power density in the discharge is about 4.5 Wcm⁻³ for 18 kW of input power and about 8 Wcm⁻³ for 30 kW of input power.

A comparison of the measured beam diameter in the radial direction of the unformatted beam shows a clear difference in size at these two different RF input power levels, thereby confirming the presence of a thermal lens. In order to incorporate a thermal lensing element in the laser model, the shape and value of the lens must be determined for the operating conditions of the laser. Reference [93] describes a technique for the calculation of the focal length of a thermal lens for different RF input power levels, specific gas mixes and inter-electrode gap sizes and indicates how the calculated values compare with experimentally derived values.

The starting points are the one-dimensional time independent heat equation and the transversal distribution of the power density (Joule heat release). The power density distribution is based on luminosity distribution measurements of the α -discharge. With

this information, the refractive index of the laser gas and the index profile across the inter-electrode gap can be calculated and converted into a ROC profile of the thermal lens.

Since the ROC profile for the refractive index is relatively flat in the centre of the gap, where the majority of the beam is located, and the intensity is low where the profile reaches extreme values towards the electrode surfaces, the radius of curvature profile, $ROC(x)$ is approximated by a single value to minimize the complexity of the model. Figure 7.22 shows the calculated refractivity distribution together with the constant ROC approximation and the intensity distribution of the fundamental mode as reported in [93].

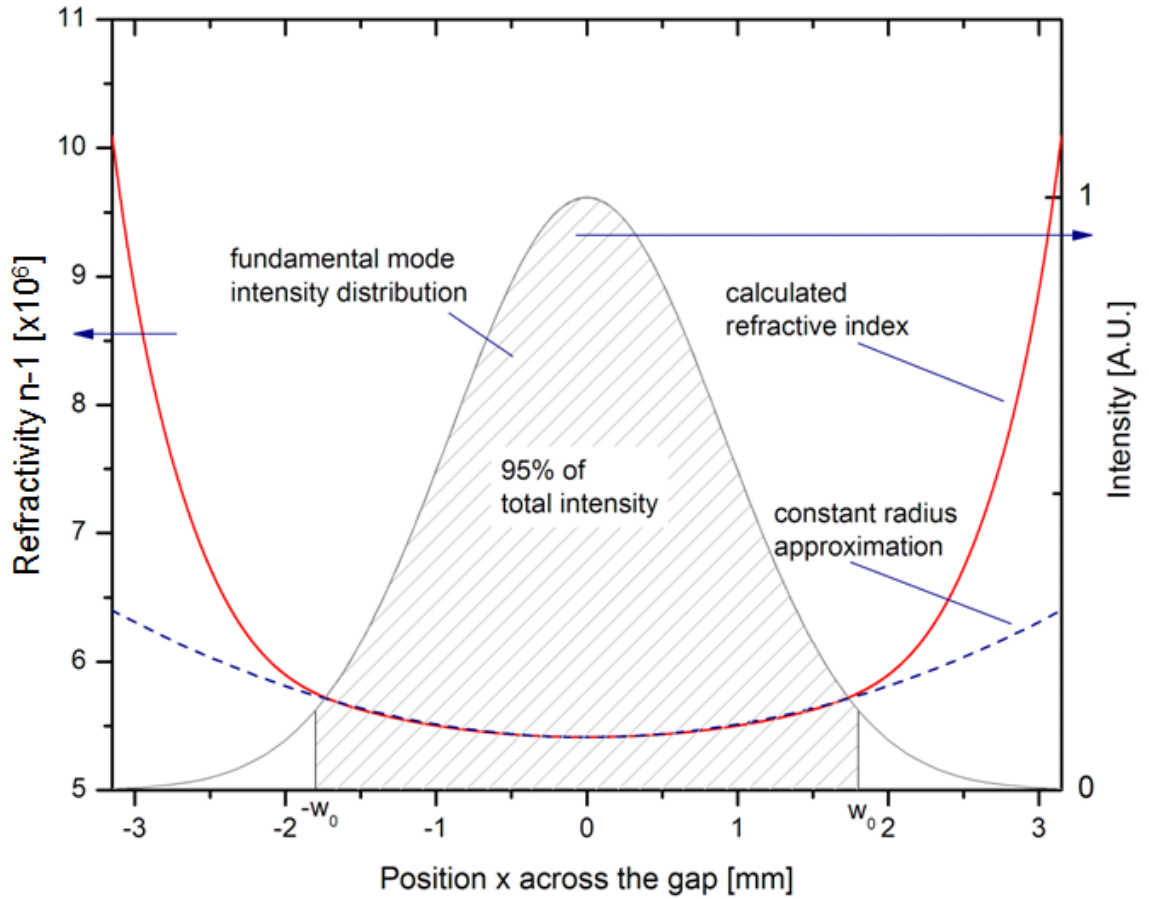


Figure 7.22 Comparison of the fundamental mode size and the refractivity profile across the inter-electrode gap for a gas pressure of 90 hPa [93].

A comparison of the calculated and measured thermal lens values is shown in Figure 7.23. The ROC of the experimentally derived thermal lens is determined by sending a probe beam through a discharge chamber and measuring the beam size of the transmitted beam for different RF input power levels.

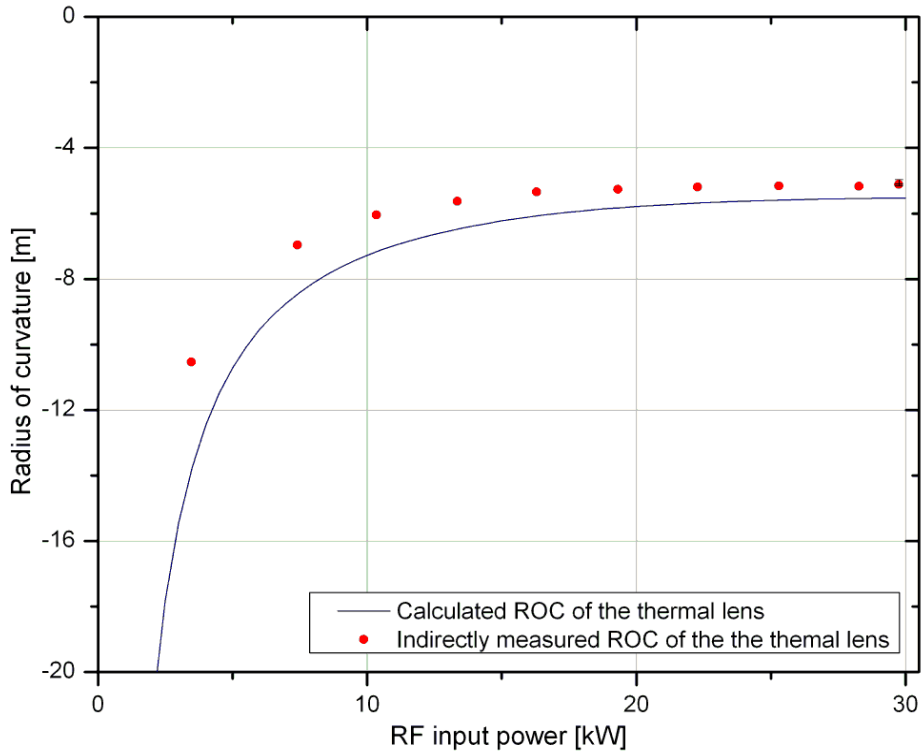


Figure 7.23 The calculated radius of curvature of the thermal lens versus RF input power in a discharge cell is found to be within 10% of the measured values [93].

In order to get a better quantitative understanding of the impact of the thermal lensing effect on the resonator design, the resonator model is expanded. The focal power, of what is a continuous thermal lens in the gain medium of a real laser, is split between three discrete ring shaped lenses on each gain sheet located on grid 2, 3 and 4. The split in focal power between the three lenses is proportional to the length of the gain sheets (400 mm for the left and right gain sheets and 500 mm for the gain sheets in the centre). The revised model is shown in Figure 7.24.

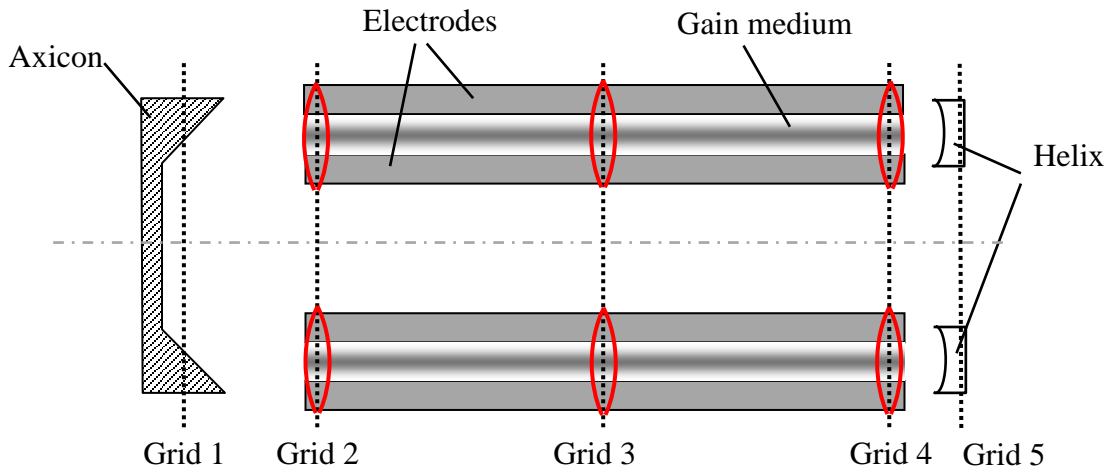


Figure 7.24 Revised resonator model with thermal lenses. The effective ROC of the thermal lens is distributed between three lenses proportional to the length of the gain sheets.

Figure 7.25 shows an inter-electrode gap size optimization including a thermal lens with an effective ROC of -10 m. The scaled magnification model is used to compensate for the shorter resonator length. Figure 7.21 shows the results for the same simulation but without the thermal lens.

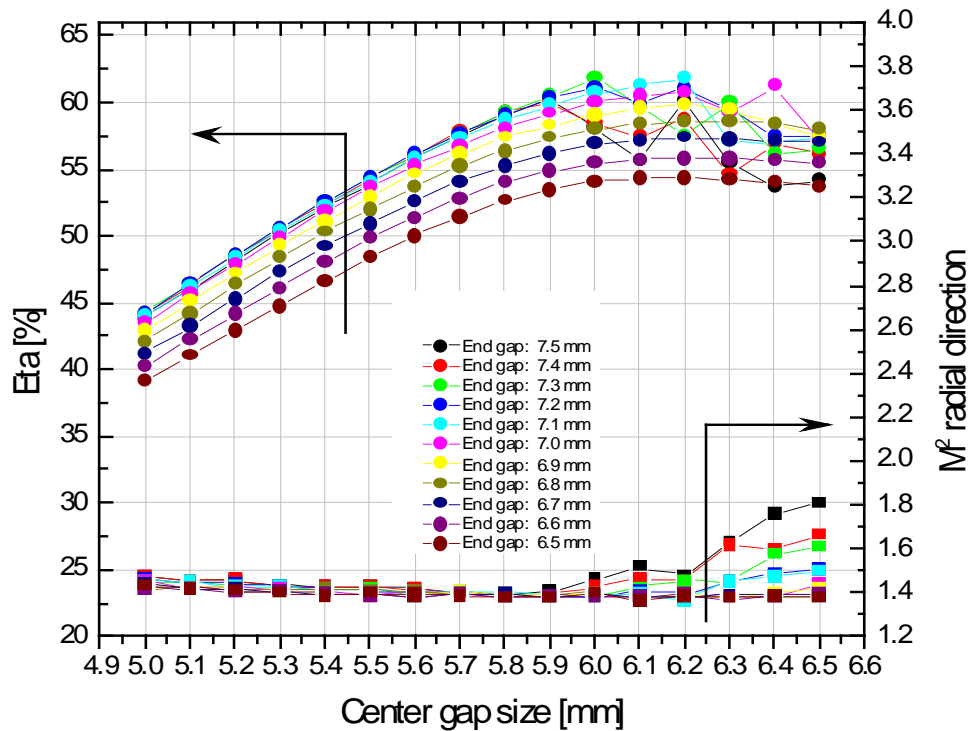


Figure 7.25 Inter electrode gap size optimization using an expanded model that includes a thermal lens with an average ROC of -10 m and scaled magnification. (ROC: 2.0 / 5.657.m; $c_1 = -1.15 \cdot 10^{-3}$ mm/rad and $c_2 = -1.15 \cdot 10^{-3}$ mm/rad²; $L = 1300$ mm).

For a thermal lens with a ROC of -10 m the optimum inter-electrode gap size changes from about 7.0 - 5.8 - 7.0 mm to 7.1 - 6.2 - 7.1 mm. It is interesting to note that the increase in the centre gap size is larger than the increase in the gap size at the ends of the electrodes. Of course, with decreasing values for the ROC of the thermal lens the inter-electrode gap size increases and vice versa.

A comparison of the calculated radial beam size of the extracted beam for a distance of three meters between the two simulations is shown in Figure 7.26.

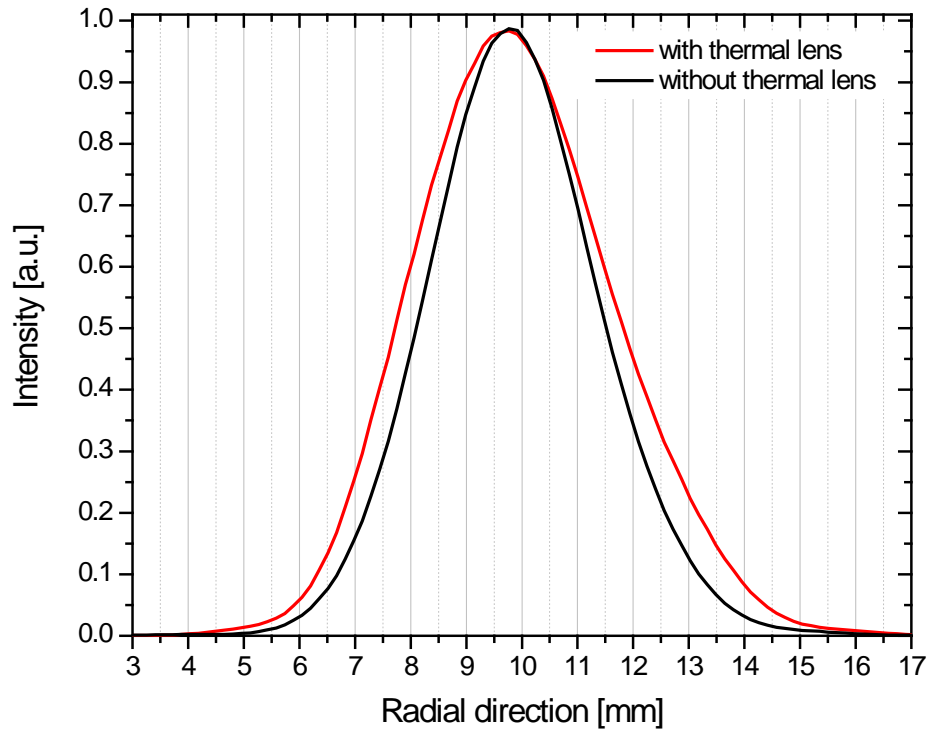


Figure 7.26 Beam size comparison of the unformatted radial beam at a distance of 3 m for a resonator with and without thermal lens. (ROC: -10m; scaled magnification model; $c_1 = 0$; $c_2 = -1.21 \cdot 10^{-3} \text{ mm/rad}^2$).

The results show that the thermal lens has a clear impact on the beam size in the radial direction. The change in size is about 1 mm which is in good agreement with the measured change in size.

Based on the data presented in [93] and in [4] the ROC of the thermal lens should be around -6 m. When effective values for the ROC between -4 and -8 m are used in the simulation the results are nonsensical. Sensible results are obtained with ROC values in the range of -10 to -12 m. This might be an indication that the approach of using a

constant ROC value for the thermal lens is too big a simplification or the size of the fundamental beam size in Figure 7.22 is too small.

7.2.3 Summary

Table 7.3 summarizes the simulation results of the inter-electrode gap size optimization with the expanded resonator model. Compared to the base line the scaled magnification model increases the centre gap size only slightly. Adding thermal lensing to the model has a significant impact on the inter-electrode gap size. A thermal lens with a ROC of -10 m increases the centre gap size by about 0.4 mm compared to the baseline, but the end gap size is less affected and increases only by about 0.1 mm.

Configuration	Gap size [mm]	Parameters
Baseline	7.0 - 5.8 - 7.0	$c_1 = -1 \cdot 10^{-3}$ mm/rad $c_2 = -1 \cdot 10^{-3}$ mm/rad ²
Scaled magnification	7.0 - 5.9 - 7.0	$c_1 = -1.15 \cdot 10^{-3}$ mm/rad $c_2 = -1.15 \cdot 10^{-3}$ mm/rad ²
Thermal lens	7.1 - 6.2 - 7.1	$c_1 = -1.15 \cdot 10^{-3}$ mm/rad $c_2 = -1.15 \cdot 10^{-3}$ mm/rad ² TL: 3 lenses distributed (ROC: -10 m)

Table 7.3 Summary of simulation results derived with different resonator models.

7.3 Characterization of the Scaled-up Laser

The characterization is unless stated otherwise carried out at a RF input power level of about 30 kW and an excitation frequency of 27.12 MHz. The laser gas pressure was optimized at 30 kW input power to 75 hPa. The laser gas mix is identical with the one used in the basic version of the laser.

Figure 7.27 shows a plot of the measured laser output power (unformatted beam) and electro-optical efficiency versus RF input power. For an input power level of 29 kW the laser power reaches 4120 W corresponding to an electro-optical efficiency of 14.2%. The maximum efficiency of 15.8% is reached at an input power level of 21 kW.

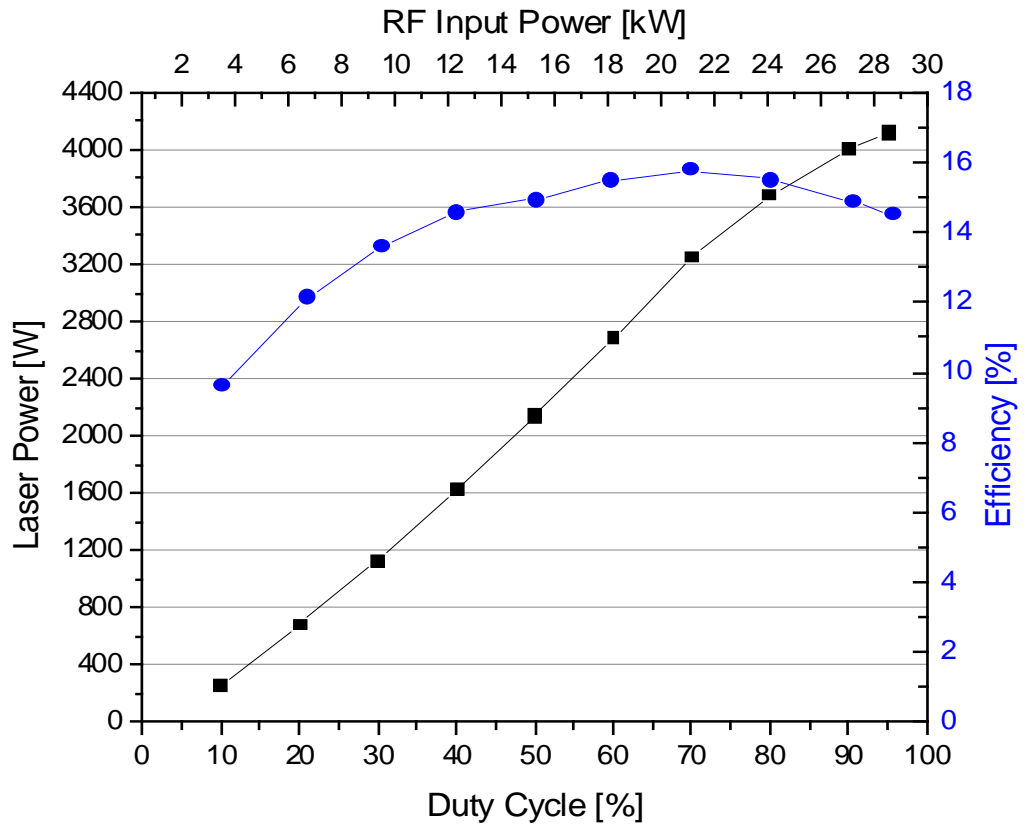


Figure 7.27 Laser output power and efficiency vs. RF input power. Set-up: Inter-electrode gap size: 7.0 – 5.9 – 7.0 mm; ROC: 2.0 / 5.657 m; helix slope: $c_1 = -1 \cdot 10^{-3}$ mm/rad and $c_2 = -1 \cdot 10^{-3}$ mm/rad².

Since the electro-optical efficiency is still fairly good at a RF input power level of 30 kW it is increased until the laser power does not increase any further. At an RF input power level of about 34 kW the laser power rolls over and there is almost no further increase in the laser power when the RF input power level is increased to 38 kW. The maximum output power is just below 4500 W at the standard cooling water temperature of 25°C.

Reducing the water temperature to 20°C does not increase the laser power significantly and the strong rollover effect at about 34 kW of RF input power remains. Additional laser power can be gained by reducing the cooling water temperature to 15°C. Even though this is no problem for laser operation in the laboratory it can create significant condensation problems in humid environments outside the laboratory and is therefore not pursued any further. Increasing the fractional output coupling also yields some extra laser power, but brings with it problems in spatial filtering as discussed above and is therefore also not pursued any further.

Figure 7.28 shows the intensity distribution of the unformatted beam at 1 m distance from the output coupling window for two different resonator configurations. On the left side the helix mirror has a slope with $c_1 = -1 \cdot 10^{-3}$ mm/rad and $c_2 = -1 \cdot 10^{-3}$ mm/rad² and an inter-electrode gap size of 7.0 - 5.9 - 7.0 mm and on the right side the helix mirror has a slope with $c_1 = 0$, $c_2 = -1.06 \cdot 10^{-3}$ mm/rad² and an inter-electrode gap size of 7.0 - 6.2 - 7.0 mm.

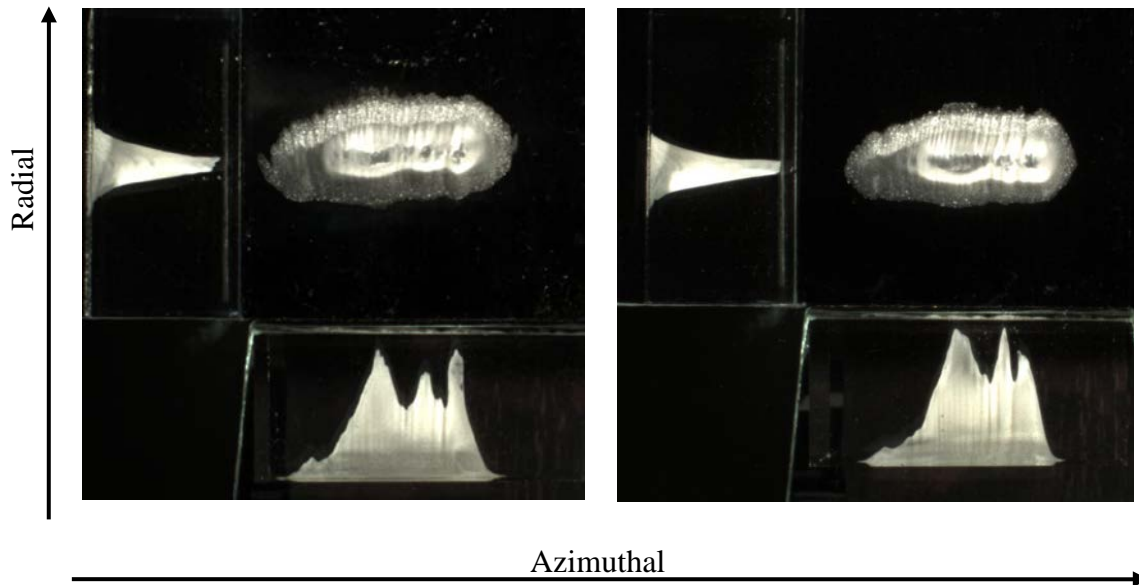


Figure 7.28 Radial and azimuthal intensity distribution in 1m distance from the output coupling window. The power level is about 4 kW. Left: $c_1 = -1 \cdot 10^{-3}$ mm/rad and $c_2 = -1 \cdot 10^{-3}$ mm/rad²; Right: $c_1 = 0$, $c_2 = -1.06 \cdot 10^{-3}$ mm/rad².

Increasing the inter-electrode gap size from 7.0 - 5.9 - 7.0 mm to 7.0 - 6.2 - 7.0 mm has no impact on the laser output power level. A clear difference between the two becomes visible in the power stability of the laser and how sensitive the resonator is to misalignment.

For both configurations the laser power stability is compared in Figure 7.29. While not all lasers with the smaller gap size exhibit power stability problems, many do.

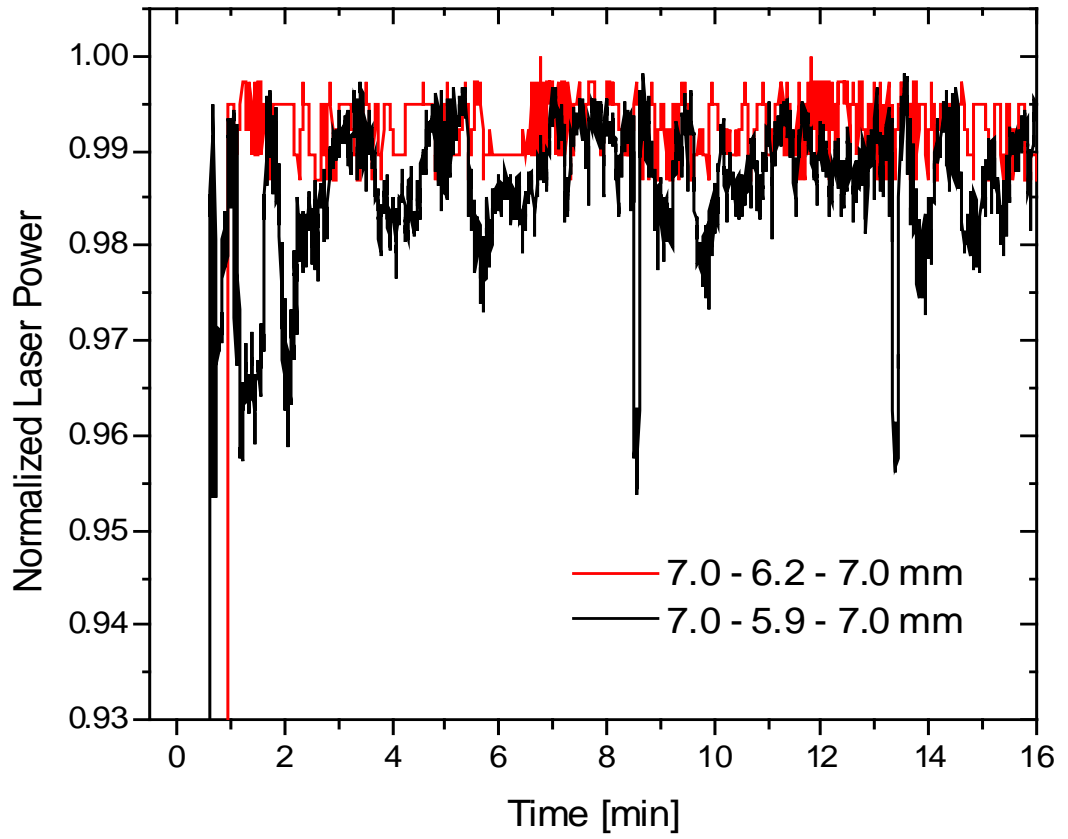


Figure 7.29 Power stability comparison for two configurations: Black: Standard inter-electrode gap size and $c_1 = -1 \cdot 10^{-3} \text{ mm/rad}$ and $c_2 = -1 \cdot 10^{-3} \text{ mm/rad}^2$; Red: Larger centre gap with $c_1 = 0$ and $c_2 = -1.06 \cdot 10^{-3} \text{ mm/rad}^2$.

Figure 7.30 shows the intensity distribution of the formatted beam at 1, 3 and 5 m distance from the laser. The corresponding beam quality measurement is shown in Figure 7.31. (Both results are obtained with an inter-electrode gap size of 7.0 – 5.9 – 7.0 mm and $c_1 = -1 \cdot 10^{-3} \text{ mm/rad}$ and $c_2 = -1 \cdot 10^{-3} \text{ mm/rad}^2$).

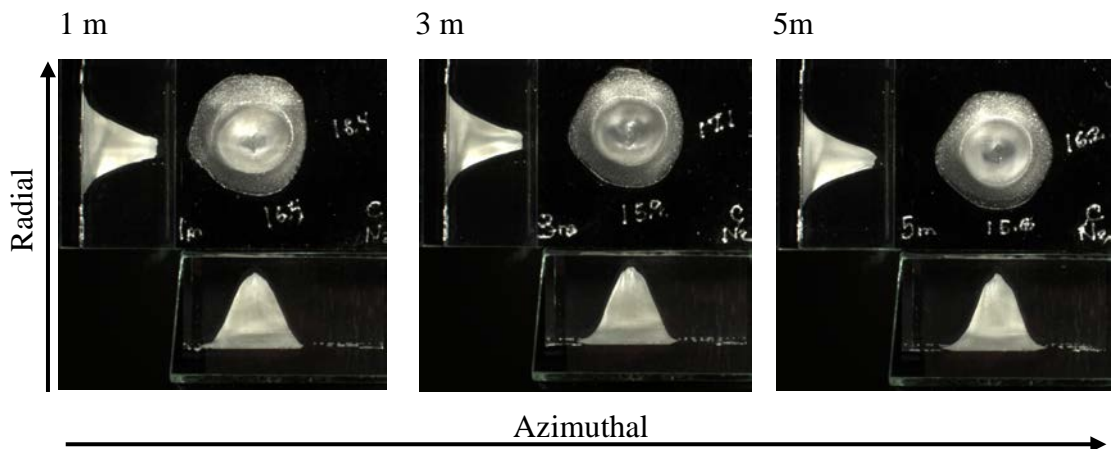


Figure 7.30 Intensity distribution of the formatted beam in 1, 3 and 5 m distance from the laser. Set-up: Inter-electrode gap size: 7.0 – 5.9 – 7.0 mm; ROC: 2.0 / 5.657 m; helix slope: $c_1 = -1 \cdot 10^{-3} \text{ mm/rad}$ and $c_2 = -1 \cdot 10^{-3} \text{ mm/rad}^2$.

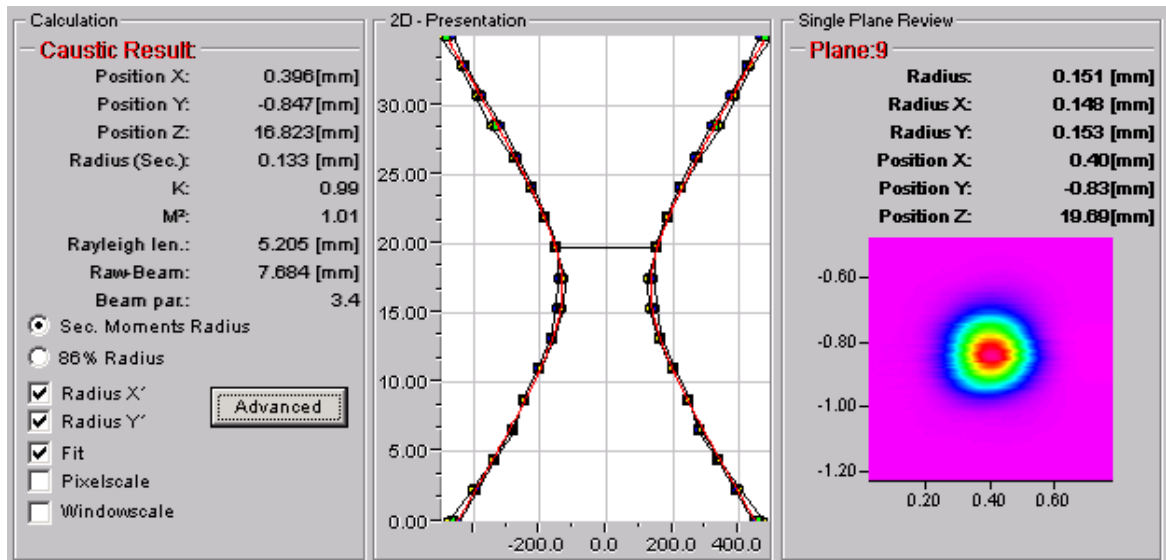


Figure 7.31 Beam quality measurement with a PRIMES focus monitor. Set-up: Inter-electrode gap size: 7.0 – 5.9 – 7.0 mm; ROC: 2.0 / 5.657 m; helix slope: $c_1 = -1 \cdot 10^{-3}$ mm/rad and $c_2 = -1 \cdot 10^{-3}$ mm/rad².

In summary, careful adaptation of the resonator designed has allowed the preservation of beam quality in the scaled-up version of the laser. The maximum laser power extracted was about 4500 W which is just enough to operate the laser as a 4 kW laser considering the losses in the beam formatting telescope. At this point though, the cooling capacity and the stability of the discharge are pushed to their limits. Therefore, a more moderate output power level in the range of 3.2 to 3.5 kW is recommended for use as an industrial product.

Chapter 8

8 Summary and Outlook

8.1 Summary of Main Achievements

The helix-axicon resonator, as introduced in [4], has some major shortcomings, notably low brightness, insufficient polarization control, reproducibility and poor stability of many beam characteristics.

In Part One of this thesis, the work focused on the re-design of the helix-axicon resonator to achieve high brightness, uniform polarization and stable performance, and in Part Two on the power scaling of a coaxial diffusion-cooled CO₂ laser with a helix-axicon resonator and free-space propagation.

In Part One, the stable direction of the resonator was re-designed in order to ensure fundamental mode operation. This was achieved by replacing the electrodes which had a constant inter-electrode gap with shaped electrodes. The shaped electrodes limit the gain volume to the size of the fundamental mode and successfully discriminate against higher order mode oscillation. At the same time, diffraction effects caused by the constant gap were eliminated since now all apertures match the mode size. This modification to the electrode system yields high brightness and Gaussian like intensity distributions in the radial direction. In combination with the use of a surface pattern to suppress (co-existing) waveguide modes a patent was obtained for the shaped electrode configuration.

In the other direction of the resonator, the unstable direction, the linear slope on the helix mirror was replaced with a parabolic slope to ensure that the resonator always operates as an unstable resonator. Even though in theory the linear slope is able to drive the beam around the circumference, imperfections in the shape, caused by the thermal load or cooling water pressure, create local areas of stability and the beam may be trapped, resulting in temporal fluctuations of the beam characteristics. A second major disadvantage of the linear slope is the asymmetric distribution of the load on the optical

surface due to the slow rise of the flux in the resonator. The introduced parabolic shape has a much steeper rise of flux, creating a more even load on the mirror. The departure from the linear slope on the helix mirror was one of the key elements in designing a stable-unstable-hybrid resonator that is suited for an industrial product.

The state of polarization was corrected by introducing a simple coated optic, thereby avoiding the use of complex optics that are expensive to produce and difficult to manufacture as proposed in [65]. The coating is absorbing the undesired components of the polarization resulting in a linear polarized beam at a minimal reduction in laser power. A patent was obtained for the combination of this polarization correction method and a configuration of the beam shaping telescope.

A complete characterization of the beam proved that the implemented changes result in a 2 kW laser with excellent beam quality and stable beam characteristics that are repeatable from one laser to another enabling the production of this laser in a serial production environment.

In part two the general power scaling law for diffusion-cooled lasers ($P = c \cdot A/d$) was modified for free-space configurations. Limitations for power scaling imposed by the discharge were overcome by introducing distributed inductances for discharge homogenization. Whilst the idea of distributed inductances was not new, a novel implementation of distributed inductances was patented for the use in annular configurations. The homogenization of the discharge not only enabled the power scaling to higher output powers but also increased the electro-optical efficiency of the laser.

A careful adaptation of the resonator parameters for the scaled-up version allowed the conservation of beam quality at higher output power levels. The maximum output power in the scaled-up version was 4.5 kW in the unformatted beam.

An advanced model of the resonator was developed in a software package that utilizes the Fox and Li method for the simulation of resonator modes. With the help of the model a much deeper understanding of the helix-axicon resonator was developed. The model allowed many parameters to be optimized in simulations where the cost and required time for an experimental optimization was prohibitive. The model was used to investigate the

influence of the extended length of the discharge on the resonator performance, the influence of different gap sizes, magnification and thermal lenses on the performance of the resonator. Additional investigations focused on the alignment sensitivity of the resonator for different configurations and the influence of the magnification on the spatial filtering process. Many results and conclusions were confirmed empirically in the laboratory.

8.2 Suggestions for Future Work

In addition to the limits for power scaling discussed in section 5.3 the output power is currently limited due to the fact that, for practical reason the optimum RF frequency for the particular discharge structure used has not been employed. Consequently, one of the crucial similarity laws for the optimised scaling of RF discharges formulated in [22] has not been followed. This similarity law links the inter-electrode gap size, d and the excitation frequency, f as stated in Equation 8.1:

$$f \cdot d = 280 \text{ mm} \cdot \text{MHz} \quad 8.1$$

Obeing this similarity law ensures maximum electro-optical efficiencies. For a 6.5 mm inter-electrode gap the optimum excitation frequency is about 40 MHz according to this law whereas the currently available excitation frequency of 27 MHz requires a 10 mm gap according to Equation 8.1.

Even though an output power level of 4 kW could be realized with the scaled up version of the laser simply by increasing the RF input power level and some further optimization, it becomes increasingly difficult to keep the discharge stable for RF input power levels above 30 kW.

In order to extend the power level to 4 kW and possibly above, which requires RF input power levels in excess of 30 kW, it is proposed to increase the RF excitation frequency from 27.12 to 40.68 MHz. The higher excitation frequency will not only increase the electro-optical efficiency but also increase the extractable laser power per volume and push the stability limits of the discharge to higher input power levels.

In the literature, for instance in [24] and [35], efficiency gains in the range of 15-20% have been demonstrated when the excitation frequency was increased from 27.12 to 40.68 MHz for an inter-electrode gap size of about 6 mm. Applying this efficiency gain to the demonstrated 4.5 kW of output power in section 7.3 results in a laser power level of about 5.2 kW.

The additional overhead in laser power and discharge stability at 40.68 MHz allows for an industrial 4 kW laser to be based on the scaled-up version of the laser.

Appendix

A.1 OPT Input File

Appendix A.1 shows a typical version of a xml-input file for the OPT simulations. It is compiled of different sections:

- Comments
- Definition of the simulation parameters (number of iterations, file-names etc.)
- Definition of the grids
- Definition of the optical elements
- Scan parameters
- Definition of the optical configuration

```
<?xml version='1.0' encoding='us-ascii'?>
```

```
<?comments
```

Description:

L-resonator = 1300 mm

Diameter = 155 mm

Gap = 7.0 - 5.9 - 7.0 mm

ROC Helix = 2.0 mm

ROC Axicon = 5.657 m

Slope = Parabolic

c1 = -1.15e-3 mm/rad

c2 = -1.15e-3 mm/rad²

Outcoupling: -9 deg to 15 deg (351 to 15)

Propagators = 2 x 650 mm

g0 = 0.947 1/m"

Is = 1.78e6 W/m²

Thermal Lens: 1 lens per gain sheet

```
/comments?>
```

```
<opt version="6.4">
```

```

<opt-parameter
    wellenlaenge="10.6e-3 mm"
    feldkomponenten = "1">
    <ausgabe
        device = "beide"
        filename = "OUTPUT"
        file-index = "3200_Master_"
        file-extension = ".txt"/>
    <ausgabe-if
        feld-aus-flag = "1"
    phase-aus-flag = "1"
        format = "rf_Ny"
        schritte_1 = "1"
        schritte_2 = "1"
        field-dump = "ja"
    dump-file-name = "3200_master"/>
    <ausgabe-nf
        feld-aus-flag = "1"
    phase-aus-flag = "1"
        format = "rf_Ny"
        schritte_1 = "1"
        schritte_2 = "1"/>
    <ausgabe-ff
        feld-aus-flag = "1"
    phase-aus-flag = "1"
        format = "xy_Ny"
        schritte_1 = "1"
        schritte_2 = "1"/>
    <steuerung
        iterationen = "500"
        mittelung = "50"
        fernfeld = "offline"
        normalize = "none"/>
    <anfangsverteilung

```

```

        type = "random"
    ausgabefile-name = "output_field"
        eingabefile-name = "3200_master"
    azim-ordnung = "1"
    feldstaerke = "1.0 V/mm"/>
</modelle> </modelle>
</opt-parameter>

<gitter>
    <grid name = "G2" type = "grid" gridtype = "zylindrisch">
        <grid-parameter
            Nr = "80"
            Nf = "1024"
            rmin = "73.9 mm"
            rmax = "81.1 mm"
            gauss-ordnung = "10"/>
    </grid>
    <grid name = "G2small" type = "grid" gridtype = "zylindrisch">
        <grid-parameter
            Nr = "80"
            Nf = "1024"
            rmin = "74.75 mm"
            rmax = "80.25 mm"
            gauss-ordnung = "10"/>
    </grid>
    <grid name = "GK1" type = "grid" gridtype = "kartesischFFT">
        <grid-parameter
            Nx = "80"
            Ny = "512"
            xmax = "20.0 mm"
            ymax = "20.0 mm"
            maske-jn = "n"/>
    </grid>
    <grid name = "FFGK2" type = "ffgrid" gridtype = "kartesischFFT">

```

```

    <grid-parameter
      Nx = "80"
      Ny = "512"
      xmax = "20.0 mm"
      ymax = "20.0 mm"/>
  </grid>
</gitter>

<optische-elemente>
  <element name = "TS1" type = "TorusSpiegel" gitter = "G2">
    <elem-parameter
      rs_1      = "77.5   mm"
      kr_1      = "2.0    m"
      Xc_1      = "-4.0e-3 mm/rad"
      c1_1      = "-1.15e-3 mm/rad"
      c2_1      = "-1.15e-3 mm/rad2"
      n1_1      = "2.9690e-5 1/rad"
      n2_1      = "2.96906e-5 1/rad2"
      phi-begin_1 = "15.0   grad"
      phi-end_1   = "195.0  grad"
      cont_12     = "0"
      rs_2      = "77.5   mm"
      kr_2      = "2.0    m"
      Xc_2      = "-4.0e-3 mm/rad"
      c1_2      = "-1.15e-3 mm/rad"
      c2_2      = "-1.15e-3 mm/rad2"
      n1_2      = "2.9690e-5 1/rad"
      n2_2      = "2.9690e-5 1/rad2"
      phi-begin_2 = "195.0  grad2"
      phi-end_2   = "351.0  grad"
      hoehen-profil-ausgabe = "helix_profile"
      loch-type    = "3"
      loch-par_1   = "0.0    mm"
      loch-par_2   = "100.0  mm"
    </elem-parameter>
  </element>
</optische-elemente>

```



```

        loch-par_3  = "351.0  grad"
        loch-par_4  = "15.0  grad"
        torus-ref   = "0.9985"
        loch-ref     = "0.0"
        loch-abs     = "0.0"
        verkipfung_x = "0.0"
        verkipfung_y = "0.0"
        spiegel-type = "auskoppelspiegel"/>
</element>
<element name = "DA1" type = "DoppelAxicon" gitter = "G2">
    <elem-parameter
        rs      = "77.50 mm "
        kr      = "5.657 m"
        delta-alpha = "0.0"
        loch-type  = "0"
        loch-par_1 = "0.0 mm"
        loch-par_2 = "0.0 mm"
        loch-par_3 = "0.0 grad"
        loch-par_4 = "0.0 grad"
        axicon-ref_r = "0.9965"
        axicon-ref_f = "0.9985"
        loch-ref     = "0.0"
        loch-abs     = "0.0"
        spiegel-type = "endspiegel"/>
</element>
<element name = "GS1" type = "GainSheet" gitter = "G2">
    <elem-parameter
        gain-laenge = "400.0 mm"
        gain-radius  = "85 mm"
        file-name-g0 = "none"
        g0           = "0.947 1/m"
        Is           = "1.78e6 W/m2"
        go-Is-aus-modell = "none"/>
</element>

```

```

<element name = "GS2" type = "GainSheet" gitter = "G2small">
  <elem-parameter
    gain-laenge = "500.0 mm"
    gain-radius = "85 mm"
    file-name-g0 = "none"
    g0          = "0.947 1/m"
    Is          = "1.78e6 W/m2"
    go-Is-aus-modell = "none"/>
</element>
<element name = "GS3" type = "GainSheet" gitter = "G2">
  <elem-parameter
    gain-laenge = "400.0 mm"
    gain-radius = "85 mm"
    file-name-g0 = "none"
    g0          = "0.947 1/m"
    Is          = "1.78e6 W/m2"
    go-Is-aus-modell = "none"/>
</element>
<element name = "P2lts" type = "Propagator" gitter1 = "G2" gitter2 =
"G2small">
  <elem-parameter
    prop-laenge = "650 mm"
    kernel-type = "Hankel"/>
</element>
<element name = "P2stl" type = "Propagator" gitter1 = "G2small" gitter2 =
"G2">
  <elem-parameter
    prop-laenge = "650 mm"
    kernel-type = "Hankel"/>
</element>
<element name = "ZK" type = "ZylToKart" gitter1 = "G2" gitter2 = "GK1">
  <elem-parameter
    x_0 = "77.5"
    y_0 = "0.0"

```

```

        winkel = "0.0"/>
    </element>
    <element name = "FFPK" type = "FFPropagator" gitter1 = "GK1" gitter2 =
"FFGK2" >
        <elem-parameter
            center_farfield = "ja"/>
    </element>
    <element name = "TL1" type = "TorusSpiegel" gitter = "G2">
        <elem-parameter
            rs_1      = "77.5   mm"
            kr_1      = "-32.3   m"
            Xc_1      = "-4.0e-3 mm/rad"
            c1_1      = "0   mm/rad"
            c2_1      = "0   mm/rad2"
            n1_1      = "0   1/rad"
            n2_1      = "0   1/rad2"
            phi-begin_1 = "0   grad"
            phi-end_1   = "360  grad"
            cont_12     = "0"
            hoehen-profil-ausgabe = "TL1_profile"
            loch-type    = "3"
            loch-par_1   = "0.0   mm"
            loch-par_2   = "100.0  mm"
            loch-par_3   = "0.0   grad"
            loch-par_4   = "0.0   grad"
            torus-ref    = "1.0"
            loch-ref     = "0.0"
            loch-abs     = "0.0"
            spiegel-type = "endspiegel"/>
    </element>
    <element name = "TL2" type = "TorusSpiegel" gitter = "G2small">
        <elem-parameter
            rs_1      = "77.5   mm"
            kr_1      = "-26.3   m"

```

```

Xc_1      = "-4.0e-3 mm/rad"
c1_1      = "0 mm/rad"
c2_1      = "0 mm/rad2"
n1_1      = "0 1/rad"
n2_1      = "0 1/rad2"
phi-begin_1 = "0 grad"
phi-end_1  = "360 grad"
cont_12    = "0"
hoehen-profil-ausgabe = "TL2_profile"
loch-type  = "3"
loch-par_1 = "0.0 mm"
loch-par_2 = "100.0 mm"
loch-par_3 = "0.0 grad"
loch-par_4 = "0.0 grad"
torus-ref  = "1.0"
loch-ref   = "0.0"
loch-abs   = "0.0"
spiegel-type = "endspiegel"/>
</element>
<element name = "TL3" type = "TorusSpiegel" gitter = "G2">
  <elem-parameter
    rs_1      = "77.5 mm"
    kr_1      = "-32.3 m"
    Xc_1      = "-4.0e-3 mm/rad"
    c1_1      = "0 mm/rad"
    c2_1      = "0 mm/rad2"
    n1_1      = "0 1/rad"
    n2_1      = "0 1/rad2"
    phi-begin_1 = "0 grad"
    phi-end_1  = "360 grad"
    cont_12    = "0"
    hoehen-profil-ausgabe = "TL3_profile"
    loch-type  = "3"
    loch-par_1 = "0.0 mm"

```

```

        loch-par_2  = "100.0  mm"
        loch-par_3  = "0.0  grad"
        loch-par_4  = "0.0  grad"
        torus-ref   = "1.0"
        loch-ref     = "0.0"
        loch-abs     = "0.0"
        spiegel-type = "endspiegel"/>
    </element>
</optische-elemente>

<scan>
    <scan-gruppe n-steps = "11">
        <scan-gruppen-element
            element = "opt/gitter/grid#name=G2/grid-parameter"
            attribute = "rmin"
            type     = "double"
            min      = "73.75 mm"
            max      = "74.25 mm">
        </scan-gruppen-element>
        <scan-gruppen-element
            element = "opt/gitter/grid#name=G2/grid-parameter"
            attribute = "rmax"
            type     = "double"
            min      = "81.25 mm"
            max      = "80.75 mm">
        </scan-gruppen-element>
    </scan-gruppe>
    <scan-gruppe n-steps = "16">
        <scan-gruppen-element
            element = "opt/gitter/grid#name=G2small/grid-parameter"
            attribute = "rmin"
            type     = "double"
            min      = "74.25 mm"
            max      = "75.0 mm">

```

```

</scan-gruppen-element>
<scan-gruppen-element
    element = "opt/gitter/grid#name=G2small/grid-parameter"
    attribute = "rmax"
    type = "double"
    min = "80.75 mm"
    max = "80.0 mm">
</scan-gruppen-element>
</scan-gruppe>
</scan>

```

```

<reihenfolge1>

```

```

    TL1    1
    GS1    1
    P2lts  1
    TL2    1
    GS2    1
    P2stl  1
    TL3    1
    GS3    1
    DA1    1
    GS3    -1
    TL3    -1
    P2stl  -1
    GS2    -1
    TL2    -1
    P2lts  -1
    GS1    -1
    TL1    -1
    TS1    1

```

```

</reihenfolge1>

```

```

<reihenfolge2>

```

```

    ZK      1
    FFPK    1

```

</reihenfolge2>

</opt>

References

- [1] C. K. N. Patel, "Selective Excitation through vibrational energy transfer and optical maser action in N₂-CO₂," *Physical Review Letter*, vol. 13, pp. 617-619, 1964.
- [2] W. J. Witteman, *The CO₂ laser*. Springer Verlag, 1987.
- [3] R. D. Hake and A. V. Phelps, *Phys. Rev*, vol. 158, pp. 70-84, 1967.
- [4] J. Schulz, "Diffusionsgekuehlte, koaxiale CO₂-Laser mit hoher Strahlqualitaet," RWTH Aachen Dissertation, 2001.
- [5] D. R. Lide, *Handbook of Chemistry and Physics*, 83rd ed. CRC Press, 2002.
- [6] M. Z. Novgorodov, A. G. Sviridov, and N. N. Sobolev, "Electron energy distribution in CO₂ laser discharges," *IEEE J. QE*, vol. 7, pp. 508-512, 1971.
- [7] P. Laakmann and K. D. Laakmann, "Sealed-off rf excited CO₂ lasers and method of manufacturing such lasers," U.S. Patent 4,393,506, 1983.
- [8] W. J. Witteman, "High-output powers and long lifetimes of sealed-off CO₂ lasers," *Appl. Phys. Let.*, vol. 11, pp. 337-338, 1967.
- [9] J. A. Macken, S. K. Yagnik, and M. A. Samis, "CO₂ Laser performance with a distributed Gold catalyst," *IEEE Journal of Quantum Electronics*, vol. 25, pp. 1695-1703, 1989.
- [10] M. B. Heeman-Ilieva, Y. B. Udalov, and W. J. Witteman, "Enhanced gain and output power of a sealed-off rf-excited CO₂ waveguide laser with gold-plated electrodes," *Appl. Phys. Let.*, vol. 64, p. 673, 1994.
- [11] A. L. S. Smith and J. M. Austin, "Dissociation mechanism in pulsed and continuous CO₂ lasers," *J. Phys. D: Appl. Phys.*, vol. 7, p. 314, 1974.
- [12] T. W. Jelinek, *Oberflaechenbehandlung von Aluminium*. Leuze Verlag, 1997.
- [13] S. N. Tskhai, W. J. Witteman, Udalov, P. J. M. Peter, and V. N. Ochkin, "The catalytic activity of gold-plated electrodes in a slab-geometry CO₂ laser," *Appl. Phys. B*, vol. 65, pp. 45-48, 1997.
- [14] C. Willis and J. G. Purdon, "Catalytic control of the gas chemistry of sealed TEA CO₂ lasers," *J. Appl. Phys*, vol. 50, pp. 2539-2543, 1979.
- [15] H. Kisch, "Oxidische Katalysatoren fuer die Niedertemperaturoxidation von Kohlenmonoxid," DE Patent DE19822280A1, 1999.

- [16] W. J. Wiegand, M. C. Fowles, and J. A. Benda, "Carbon monoxide formation in CO₂ lasers," *Appl. Phys. Lett.*, vol. 16, pp. 237-239, 1970.
- [17] W. J. Witteman and H. W. Werner, "The effect of water vapour and Hydrogen on the gas composition of a sealed-off CO₂ laser," *Physics Letters*, vol. 26, pp. 454-455, 1968.
- [18] R. Malz and U. Haubenreisser, "Use of zeolites for the stabilization of CO₂ partial pressure in sealed-off CO₂ waveguide lasers.," *J. Phys. D: Appl. Phys.*, vol. 24, p. 1060, 1991.
- [19] R. E. Center, "Vibrational relaxation of CO₂ by O atoms," *J. Chemical Physics*, vol. 59, no. 7, p. 3523, 1973.
- [20] R. J. McNeal, M. E. Whitson, and G. R. Cook, "Quenching of vibrationally excited N₂ by atomic Oxygen," *Chemical Physics Lett.*, vol. 16, pp. 507-510, 1972.
- [21] Y. P. Raizer, *Gas discharge physics*. Springer, 1997.
- [22] P. P. Vitruk, H. J. Baker, and D. R. Hall, "Similarity and Scaling in Diffusion-Cooled RF-Excited Carbon Dioxide Lasers," *Journal of Quantum Electronics*, vol. 30, pp. 1623-1634, 1994.
- [23] R. Wester, "Hochfrequenzgasentladungen zur Anregung von CO₂ Lasern," RWTH Aachen Dissertation, 1987.
- [24] M. Schwandt, "Untersuchung der Gasentladung in Abhaengigkeit von der Anregungsfrequenz bei diffusionsgekuehlten CO₂-Lasern," Diploma thesis, 2000.
- [25] P. P. Vitruk, H. J. Baker, and D. R. Hall, "The characteristics and stability of high power transverse radio frequency discharges for waveguide CO₂ slab laser excitation," *J. Phys. D: Appl. Phys.*, vol. 25, pp. 1767-1776, 1992.
- [26] R. Wester and S. Seiwert, "Numerical modelling of RF excited CO₂ laser discharges," *J. Phys. D: Appl. Phys.*, vol. 24, pp. 1371-1375, 1991.
- [27] Y. P. Raizer, M. N. Shneider, and N. A. Yatsenko, *Radio-Frequency Capacitive Discharges*. CRC Press, 1995.
- [28] W. L. Nighan, *Principals of laser plasmas*. Wiley, 1976.
- [29] R. Wester, S. Seiwert, and R. Wagner, "Theoretical and experimental investigations of the filamentation of high-frequency excited CO₂ lasers," *J. Phys. D Appl. Phys.*, vol. 24, pp. 1796-1802, 1991.
- [30] R. Wagner, "Einfluss des elektrischen Feldes auf die Hf angeregte CO₂

Lasergasentladung," RWTH Aachen Dissertation, 1992.

- [31] D. He and D. R. Hall, "A 30 Watt RF Excited CO₂ Waveguide Laser," *Appl Phys Lett*, vol. 43, p. 726, 1983.
- [32] K. M. Abramski, A. D. Colley, H. J. Baker, and D. R. Hall, "Power scaling of large-area transverse radio frequency discharge CO₂ lasers," *Appl. Phys. Lett.*, vol. 54, p. 1833, 1989.
- [33] C. Shackleton, H. J. Baker, and D. R. Hall, "Lateral and transverse mode properties of CO₂ slab waveguide lasers," *Optics Communications*, vol. 89, pp. 423-428, 1992.
- [34] D. R. Hall and D. He, "Frequency dependence in RF discharge excited waveguide CO₂ lasers," *IEEE Journal of Quantum Electronics*, vol. 20, pp. 509-514, 1984.
- [35] P. Vidaud, D. He, and D. R. Hall, "High efficiency rf excited CO₂ laser," *Optics Comm.*, vol. 56, pp. 185-190, 1985.
- [36] B. Wasilewski, H. J. Baker, and D. R. Hall, "Intracavity beam behaviour in hybrid resonator planar-waveguide CO₂ lasers," *Applied Optics*, vol. 39, pp. 6174-6187, 2000.
- [37] J. E. Goell, "A Circular-Harmonic Computer Analysis of Rectangular Waveguides," *The Bell System Technical Journal*, vol. 48, pp. 2133-2160, 1969.
- [38] J. Degnan, "The Waveguide Laser: A Review," *Appl. Phys.*, vol. 11, pp. 1-33, 1976.
- [39] A. Lapucci, A. Labate, F. Rossetti, and S. Mascalchi, "Hybrid stable-unstable resonators for diffusion-cooled CO₂ slab lasers," *Applied Optics*, vol. 35, p. 3185, 1996.
- [40] R. Nowack, H. Opower, and K. Wessel, "Diffusion-cooled compact CO₂ high power lasers," *Laser und Optoelektronik*, vol. 23, pp. 68-81, 1991.
- [41] J. W. Bethel, H. J. Baker, and D. R. Hall, "A new scalable annular CO₂ laser with high specific output power," *Optics Communications*, vol. 145, pp. 352-358, 1998.
- [42] D. Ehrlichmann, U. Habich, and H. -D. Plum, "High-Power CO₂ Laser with Coaxial Waveguide and Diffusion Cooling," *J Quantum Electronics*, vol. 29, pp. 2211-2219, 1993.
- [43] H. Bochum, "Koaxiale CO₂ -Wellenleiterlaser," DLR Dissertation, 1996.
- [44] J. G. Xin and D. R. Hall, "Compact, multipass, single transfer mode CO₂ laser," *Appl. Phys. Lett*, vol. 51, p. 469, 1987.
- [45] U. Habich, A. Bauer, P. Loosen, and H. D. Plum, "Resonator for coaxial slow-flow

- CO₂ lasers," in *SPIE*, vol. 1397, 1990, pp. 383-386.
- [46] A. Crocker and M. S. Wills, "Carbon-Dioxide Laser with High Power per Unit Length," *Electronics Letters*, vol. 5, pp. 63-64, 1969.
- [47] L. W. Casperson and M. S. Shekhani, "Mode properties of annular gain lasers," *Appl. Optics*, vol. 14, no. 11, pp. 2653-2661, 1975.
- [48] T. Tamida and J.-i. Nishimae, "Annular resonator with a Cassegrain configuration," *Applied Optics*, vol. 36, p. 5844-5848, 1997.
- [49] S. Anikichev, "Mode control in annular resonators," in *SPIE*, vol. 3267, 1998.
- [50] M. Endo, S. Yamaguchi, T. Uchiyama, and T. Fujioka, "Numerical simulation of the w-axicon type optical resonator for coaxial slab CO₂ lasers," *J. Phys. D: Appl. Phys*, vol. 34, pp. 68-77, 2001.
- [51] A. Lapucci, F. Rossetti, and P. Burlamacchi, "Beam properties of an R.F.-discharge annular CO₂ laser," *Optics Communications*, vol. 111, pp. 290-296, 1994.
- [52] D. Ehrlichmann, "Azimutal instabile Resonatoren und Ringresonatoren fuer Hochleistungslaser," RWTH Aachen Dissertation, 1994.
- [53] M. Weck and H. Oezmeral, "A fast-tool-servo system based on electrodynamic and piezoelectric actuators," *CIRP Annals. Manufacturing Technology 1*, 1995.
- [54] U. Habich, "Diffusionsgekuehlte CO₂ Laser fuer die industrielle Materialbearbeitung," RWTH Aachen Dissertation, 1992.
- [55] U. Habich, H. -D. Plum, and R. Poprawe, "Beam generation and beam shaping for a 1.5 kW diffusion cooled annular CO₂-laser," in *SPIE*, vol. 3267, 1998.
- [56] G. Markillie, et al., "Annular 2 kW diffusion cooled CO₂ laser operating with a novel hybrid-stable- unstable axicon resonator," in *CLEO Europe*, 2003.
- [57] D. Ehrlichmann, U. Habich, H. -D. Plum, P. Loosen, and G. Herziger, "Azimuthally Unstable Resonators for High-Power CO₂ Lasers with Annular Gain Media," *IEEE J of Quantum Elect.*, vol. 30, no. 6, p. 1441, 1994.
- [58] G. Markillie, J. Deile, and H. Schlueter, "Novel design approach benefits CO₂ laser users," *Laser Focus World*, vol. October, 2003.
- [59] G. Nemes, "Measuring and handling general astigmatic beams," in *Workshop on Laser Beam Characterization*, Madrid, 1993.
- [60] A. C. Heursch, "Laserstrahlformung mit nicht-orthogonalen optischen Systemen," Diploma thesis, RWTH Aachen, 1996.

- [61] J. W. Goodman, *Introduction into Fourier Optics*. New York: McGraw-Hill, 1996.
- [62] J. Deile and J. Schulz, "Beam forming telescope with polarization correction," Patent US 7,019,902, 2006.
- [63] II-VI Inc., *Optics catalog and reference guide*. 2008.
- [64] Y. A. Anan'ev, "Some new resonators for IR lasers," vol. 2502, pp. 96-102, 1995.
- [65] J. Schulz, "Koaxialer Laser mit einer Einrichtung zur Strahlformung eines Laserstrahls," EP Patent 1215774B1, Dec. 2000.
- [66] G. D. Boyd and H. Kogelnik, "Generalized confocal resonator theory," *Bell Sys. Tech. J.*, vol. 41, pp. 1347-1369, 1962.
- [67] E. Hecht, *Optik*. Oldenburg Verlag, 1999.
- [68] K. Hallbach, "Matrix representation of Gaussian Optics," *Am. J. Phys.*, vol. 32, p. 90-108, 1964.
- [69] A. E. Siegman, *Lasers*. University Science Books, 1986.
- [70] A. G. Fox and T. Li, "Resonant Modes in a Maser Interferometer," *Bell Sys. Tech. j.*, vol. 40, p. 453-488, 1961.
- [71] A. G. Fox and T. Li, "Effect of gain saturation on the oscillating modes of optical masers," *IEEE J. of Quantum Electronics*, vol. 2, p. 774-783, 1966.
- [72] H. Kogelnik and T. Li, "Laser Beams and resonators," *Applied Optics*, vol. 5, p. 287-299, 1966.
- [73] R. Wester, *OPT - Flexible Fresnel Program for Mode Calculations*. Aachen: Fraunhofer Institute for Laser Technology (ILT), 1998.
- [74] J. Deile, "Einfluss verschiedener Parameter auf die zeitliche und räumliche Fluktuation verschiedener Laserkenngrößen bei diffusionsgekühlten CO₂ Lasern mit koaxialen Elektroden," Diploma thesis, FH Heilbronn, 1998.
- [75] H. Kogelnik, "Imaging of optical modes - resonators with internal lenses," *Bell System Tech J.*, vol. 44, pp. 455-494, 1965.
- [76] J. Deile, "Diffusion-cooled laser system," Patent US 6,879,616, 2005.
- [77] W. Rigrod, "Saturation effects in high gain lasers," *J. Appl. Phys.*, vol. 36, p. 2487, 1965.
- [78] H. Benz, "Influence of mirror design on the mode stability of a 2 kW diffusion cooled CO₂ laser," Diploma thesis, Farmington, 2005.

- [79] P. Daniel, "TRUMPF Test report 0504".
- [80] V. Negoita, "Test report 0504," 2005.
- [81] PRIMES. PRIMES Focus Monitor. [Online]. <http://www.primes.de>
- [82] H. Benz, "TRUMPF Test report hb0502," 2005.
- [83] ISO11146, International Organization for Standardization (ISO), "Optics and Optical Instruments/ Lasers and Laser Related Equipment/ Test Methods for Laser Beam Parameters: Beam Width, Divergence Angle and Beam Propagation Factor," vol. ISO/TC 172/SC9/WG1 N80, 1995.
- [84] E. F. Plinski and J. S. Witkowski, "Prediction of thermal properties of CO₂, CO and Xe laser media," *Optics & Laser Technology*, vol. 33, pp. 61-66, 2001.
- [85] A. L. Lapucci, F. Rossetti, M. Ciofini, and G. Orlando, "On the longitudinal Voltage distribution in radio frequency discharged CO₂ lasers with large-area electrodes," *J. of Quantum Electronics*, vol. 31, pp. 1537-1542, 1995.
- [86] D. He and D. R. Hall, "Longitudinal voltage distribution in transverse rf discharge waveguide lasers," *J. Appl. Phys.*, vol. 54, p. 4367, 1983.
- [87] P. P. Chenausky and L. A. Newman, "Uniformly excited RF waveguide laser," Patent US 4,443,877, 1984.
- [88] H. H. Skilling, *Electric Transmission Lines*. New York: McGraw-Hill, 1951.
- [89] R. Engelbrecht, R. Schulz, G. Siebert, J. Hagen, and P. Schmid, "Gas discharge impedance and transmission line voltages in a RF excited CO₂ slab laser," *Frequenz*, vol. 59, pp. 154-157, 2005.
- [90] G. A. Griffith, "RF pumped waveguide laser with inductive loading for enhancing discharge uniformity," US Patent 4352188, 1982.
- [91] F. J. Villarreal-Saucedo, J. Deile, S. Sumrain, V. Granson, and P. Daniel, "Laser having distributed Impedances," US Patent US7,778,303, Aug. 2010.
- [92] S. Knupfer, "Optimization of the gas discharge characteristics on a high power CO₂ laser," Diploma thesis, TRUMPF Inc., Farmington, 2007.
- [93] V. Granson, F. Villarreal, J. Deile, J. F. Monjardin, and S. Sumrain, "Comprehensive Analysis of Thermal Lensing Effects on the Coaxial Resonator of a High Power RF-Excited CO₂ Laser," in *SPIE*, vol. 8236, 2012.